Doctoral Dissertation

Novel Si-based Solar Cells with an Al-induced Charged Oxide Inversion Layer Formed by a Wet Chemically Grown Ultrathin Al-doped SiO_x

Hiroki Nakajima

Supervisor: Keisuke Ohdaira

Japan Advanced Institute of Science and Technology
Division of Advanced Science and Technology

Materials Science

March 2024

Referee in Chief:

Professor Keisuke Ohdaira
Japan Advanced Institute of Science and Technology

Referees:

Associate Professor Masashi Akabori
Japan Advanced Institute of Science and Technology

Professor Toshikazu Suzuki
Japan Advanced Institute of Science and Technology

Professor Hiroshi Mizuta
Japan Advanced Institute of Science and Technology

Dr. Hitoshi Sai
National Institute of Advanced Industrial Science and Technology

ABSTRACT

Carrier-selective passivating contacts would realize excellent surface passivation for crystalline Si (c-Si) solar cells with a high conductivity without direct metal electrode contacts, causing a deterioration of the interface properties. Hence, it would be a breakthrough technology to access a practical limit of solar cell performance.

This thesis addresses using a simple process to realize low-cost and high-efficiency c-Si solar cells with a simple device structure of carrier-selective passivating contacts whose emitter is induced by external electrostatic charges.

The main major contribution of this work is developing a novel surface passivation method using a simple wet chemical process, which does not require vacuum, high temperature, or hydrogen treatment processes, which are essential processes in industrial c-Si solar cells. The process is just immersing Si wafers into a hot aluminum nitrate ($Al(NO_3)_3$) aqueous solution to form an ultrathin Al-doped SiO_x layer possessing hole selectivity. On a planar n-type c-Si surface, the maximum effective surface recombination velocity ($S_{eff,\,max}$) reached as low as 16 cm s^{-1}. The analyzed saturation current density (J_0) of 65 fA cm^{-2} and contact resistivity (ρ_c) of 20 mΩ cm^2, the hole selectivity (S_{10}) value could be estimated to be 13.3 which is competitive to other selective contacts created using vacuum and high-temperature process. Since the process eliminates the complexity of solar cell fabrication processes with an excellent carrier-selective passivating contact property, this study suggests that a wet chemical process using an aqueous solution of $Al(NO_3)_3$ can be an industrial solar cell fabrication process. In addition, the mechanism of the hole-selective passivating contact property was revealed. The field-effect passivation is mainly attributed to the surface passivation.

The second contribution of this work is a demonstration of the device operation of a novel device structure with an inversion layer induced by the negative fixed charges existing in ultrathin Al-doped SiO_x. This result implies that the charge-induced inversion layer acts as a p^+ emitter formed by a simple wet chemical process. Hence, using a surface charge-induced emitter, this type of solar cell realizes high-throughput, low-cost p^+ emitter formation by a simple wet chemical process. This novel solar cell was named an Al-induced charged oxide inversion layer (Al-COIL) solar cell. The conversion efficiency (η) of >10% was achieved for the device fabricated on a pyramidal textured Si substrate. In particular, an excellent FF of 0.794 was realized using a fine Ag grid electrode on the emitter side. The reduction due to a high emitter sheet resistance could be mitigated by improving carrier collection through a fine Ag grid electrode covering a relatively larger emitter surface area. However, still low J_{sc} and V_{oc} were confirmed. PC1D simulation implies that the reductions might originate from carrier recombination at the emitter surface due to the large number of interface states and the increased minority carrier (electron) density by the diminished fixed charge density (Q_f) less than -1×10^{11} cm^{-2}.

The third contribution of this work is a discovery that surface passivation, and the sheet resistance of ultrathin Al-doped SiO_x/Si improve by the light illumination, which is the variable for addressing the origin of the hole-selective passivating contact property. The significant increment of these properties implies that the excited electron trapping in the Al-induced acceptor states existing in the Al-doped SiO_x layer forms negatively charged AlO_4^- structures and enhances field effect passivation induced by the fixed charges.

Lastly, achieving an excellent surface passivation quality on a pyramidal textured c-Si surface was crucial. The lower $S_{eff,\,max}$ was confirmed as low as 13.3 cm s^{-1}, corresponding to iV_{oc} of 682 mV and J_0 of 59 fA cm^{-2}, respectively. The light-trapping enhancement and slight space charge region compression compensate for the relatively enormous amount of interface state density due to the surface area increment on the textured Si surface, reducing surface recombination velocity and increasing solar cell performance. Hence, this study provides insight into the novel surface passivation mechanism on a practical surface structure for the c-Si solar cell. It requires a suitable surface structure design with a nano-scale size for increasing a hole-selective passivating contact by effectively exploiting electron trapping and space charge region compression.

Keywords: c-Si solar cells, carrier-selective passivating contacts, electrostatic charges, ultrathin Al-doped SiO_x, wet chemical oxidation

ACKNOWLEDGMENT

I am immensely grateful to my supervisor, Professor Keisuke Ohdaira, for his invaluable guidance and support during my Ph.D. research. His thoughtful guidance and generous financial and mental assistance enabled me to focus and do my best for this research work. Without his help, I would not have been able to complete my Ph.D. thesis successfully.

I would like to express my gratitude to Professor Yoshifumi Oshima, my vice-supervisor, for advising me on my research proposal. I appreciate our productive discussions, which helped me achieve my research goals.

I would like to express my heartfelt gratitude to Professor Shinya Maenosono for his supervision of my sub-theme research on Al-doped h-WO_3 nanoparticles. I truly appreciate his enthusiastic guidance and valuable advice on my research policy and approach while conducting this study.

I am grateful to Assistant Professor Mari Takahashi. Her careful guidance was valuable for particle synthesis, TEM, and XRD measurements.

I would like to express my gratitude to Associate Professor Masashi Akabori for his guidance and support in the clean room of CNMT in JAIST. I am also thankful for taking time out of his busy schedule to review my thesis.

I would also like to acknowledge Professor Toshikazu Suzuki for taking time out of his busy schedule to serve as a reviewer for this thesis.

I would also like to acknowledge Professor Hiroshi Mizuta for taking time out of his busy schedule to serve as a reviewer for this thesis.

I would also like to acknowledge Dr. Hitoshi Sai from the Global Zero Emission Research Center, AIST, for taking time out of his busy schedule to serve as an external reviewer for this thesis.

I would like to express my gratitude to Dr. Tatsuya Murakami from CNMT, JAIST, for his assistance in performing XPS measurements and obtaining valuable data. Additionally, my sincere appreciation goes to Dr. Koichi Higashimine from CNMT, JAIST, for conducting TEM-EDS measurements and providing crucial data for this research.

I express my gratitude to Dr. Ayako Okano from Technical Service Office for Pure and Applied Science, University of Tsukuba, for her assistance in performing SPM measurements to discuss the surface passivation mechanism from the surface potential on a pyramidal textured Si surface.

I also express my gratitude to Dr. Katsuto Tanahashi and Dr. Tomihisa Tachibana from the Fukushima Renewable Energy Institute, AIST, for their assistance in evaluating the surface passivation quality of my samples using PV-2000A.

Moreover, I acknowledge Dr. Takuya Matsui from the Global Zero Emission Research Center, AIST, for his valuable advice during our discussion on this study.

I am extremely grateful for the opportunity to conduct research at the Ohdaira laboratory, where I received valuable assistance from its members. I express my sincere appreciation to Assistant Professor Huynh Thi Cam Tu for her guidance and support throughout my research. I would also like to extend my gratitude to the researchers, Mr. Shinichiro Hayashi and Ms. Tomoko Hori, for their assistance in my research activities. I am also thankful for the help extended by the students in the Ohdaira laboratory, Mr. Zheng Wang, Mr. Shuntaro Shimpo, Mr. Ryota Ohashi, Mr. Pengyu Yang, Mr. Yuhi Ito, Mr. Mitsunori Nagahara, Mr. Chenxi Li, and Mr. Baitong Li. I extend my gratitude to the following Ohdaira lab graduates: Dr. Yuli Wen, Mr. Ryoichi Ishikawa, Mr. Wenbo Cao, Mr. Dequin Wu, Mr. Yujia Liu, Mr. Toshiki Itasaka, Mr. Yudai Yanagi, and Mr. Kuan Liu. I express my gratitude to former research assistant Ms. Miyuki Katagiri in Ohdaira lab.

I acknowledge my previous supervisors at SANKEN, Osaka University: Professor Hikaru Kobayashi, Professor Masao Takahashi, Associate Professor Taketoshi Matsumoto, and Associate Professor Kentaro Imamura. During my master's program, I worked on the topic of surface passivation by nitric acid oxidation and gained extensive knowledge and experience in wet chemical processes under their guidance. This led me to the concept for my current research. I would also like to express my appreciation to Professor Kazuyuki Edamoto at Rikkyo University, whose instruction on XPS and AES was beneficial for my research. Without their guidance, I could not have developed this research program.

This Ph.D. study was supported by JST SPRING, Grant Number JPMJSP2102. I would like to acknowledge their financial support.

TABLE OF CONTENTS

CHAPTER 1

INTRODUCTION

It is commonly recognized that CO_2 emissions are the primary factor of global warming [1], resulting in rising sea levels due to melting icebergs [2], intense storms like hurricanes [3], droughts causing significant crop injury [4], and the like. Since 1850, the cumulative CO_2 emissions reached 2400 ± 240 $GtCO_2$ in 2019 [1]. In response, the Intergovernmental Panel on Climate Change (IPCC) announced that 45% of global CO_2 emissions must be reduced by the end of 2030 to keep the temperature increase below 1.5 °C [1]. Otherwise, an unchecked scenario will await our future.

Most of the CO_2 emission comes from coal, gas, and oil, which are energy sources [1]. Thus, one of the promising solutions is using sustainable energy such as solar, wind, and waterpower because these energy sources are inexhaustible and have extremely low CO_2 emissions. In particular, solar energy is a widely accessible energy source because the sunshine is evenly distributed worldwide [5]. Researchers in Bell laboratories demonstrated the first practical silicon (Si) solar cell in 1954 [6]. Fortunately, solar cells are commercially available nowadays, and the market is dominated by wafer-based crystalline Si (c-Si) solar cells with a 95% share [7]. Over several decades, the dramatic cost reduction has reached a comparable cost with fossil fuel, resulting in explosively rising photovoltaic (PV) installation and surpassing 1 TW as a cumulative PV module shipment in 2022 [8]. However, further cost reduction and initiating more PV installations will be essential to achieve our next goal of cutting 45% off greenhouse gas emissions by the end of 2030 [9].

1.1 Conventional crystalline Si solar cells and the recent trend

The several types of conventional c-Si solar cell structures are shown in Figure 1.1. The mainstream c-Si solar cell technology is the Passivated Emitter and Rear Cell (PERC) emerged in 1989. This technology has allowed us to obtain high solar cell efficiency compared with Al-BSF solar cells with a structure of fully Al-diffused and creating back surface field (BSF) at the rear Si surface due to the rear design of surface passivation and local Al-diffused contact area [10]. According to the calculation by Institut für Solarenergieforschung in Hameln (ISFH), the PERC cell efficiency limit will be 24.5% [11]. Since the theoretical c-Si solar cell efficiency limit is 29.43% [12], 4.93% can be improved by other novel cell architectures using state-of-the-art technologies. The following upcoming technologies that can be mainstream are expected to be tunnel oxide passivating contact (TOPCon) [13] or Si heterojunction (SHJ) [14] solar cells due to the higher theoretical efficiency limit of 28.7% and 27.5%, respectively [11]. Such high performance can be realized by minimizing surface carrier recombination, which reduces direct contact between metal electrodes and Si surface while selecting carrier types at the surface using field effect passivation, called passivating contact [15]. The 1.2% difference is mainly derived from parasitic absorption loss in the amorphous Si (a-Si) front surface passivation layer used in the SHJ structure [16]. In TOPCon structure, high bandgap materials with excellent optical transparency, such as aluminum oxide (Al_2O_3) and Si nitride (SiN_x), can be applied as a surface passivation layer on boron (B) diffused p^+ front emitter, realizing very low parasitic absorption loss of < 0.1 mA cm^{-2} on the front surface [17]. Recently, the Chinese PV manufacturer LONGi recorded cell efficiency of 26.81% using SHJ technology [18], and Jolywood has accomplished 26.7% using TOPCon technology [19]. Since TOPCon process cost is lesser than SHJ mainly due to lower Ag consumption and the absence of a transparent conductive oxide (TCO) layer such as indium tin oxide (ITO) for the TOPCon fabrication process, the market share of TOPCon is almost double compared with SHJ, 15% in 2022 [20]. Moreover, TOPCon's market share is expected to be dominated by 60%, while SHJ will be 19% in 2033 [20].

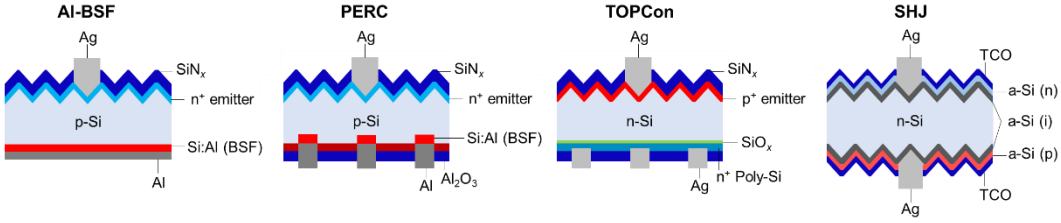

Fig. 1.1 Device structures of Al-BSF, PERC, TOPCon, and SHJ solar cells.

1.2 Promising solution for the cost-effective crystalline Si solar cells

In general, however, the B-diffused p^+ emitter surface is challenging to be passivated, causing relatively high energy loss of ~0.4 mW cm^{-2} at the p^+ emitter [21], compared with ~0.1 mW cm^{-2} for SHJ [18]. Previous research showed that the B-diffusion process forms the boron-rich layer (BRL). Since thermal B-diffusion forms misfit dislocations and causes recombination centers [22, 23], BRL would be lifetime killers. Thus, the BRL removal process is necessary, and several additional processes have been developed, as reported elsewhere [22, 23]. Moreover, the energy state level created by the boron oxygen (B-O) complex, located near the Si mid-gap [24], highly degrades solar cell performance. In addition, much higher temperatures are required for the B-diffusion process compared to the P-diffusion using $POCl_3$ precursors due to the low diffusion coefficient of B into Si substrates [25]. Therefore, the lower fabrication throughput and higher energy consumption are recognized as a drawback of TOPCon technology compared with conventional PERC. Some breakthrough novel technology will be required to prevail over passivating-contact c-Si solar cells manufactured by high-throughput processes and lower energy consumption with a low-temperature route.

A recent study proposed the dopant-free asymmetric heterocontact (DASH) concept and demonstrated high-efficiency c-Si solar cells of over 20% [26]. This type of solar cell possesses transition metal oxide with a high work function, such as MoO_3 [27], WO_3 [28], and V_2O_5 [29], instead of a B-diffused layer. The upward band bending of the Si surface is induced by contacting such high work function materials on an n-type c-Si surface, creating an inversion layer with a large amount of hole (minority carrier) accumulations at the Si surface. However, the sharp reduction of electrons by repelling from the Si surface allows us to obtain hole-selective contact [30]. On the other hand, low work function materials such as LiF_x [31], TiO_x [32], and MgO_x [33] contacting on an n-type Si surface create an accumulation layer with a large number of electrons (majority carrier), but the sharp decrease in a hole concentration at the Si surface, enabling electron-selective contact. Therefore, since the inversion layer plays a role in the p^+ emitter of n-type c-Si solar cells without impurity diffusion into the Si surface, the impurity-rerated defect states are not formed. Moreover, this DASH technology does not require the high-temperature process [26].

In addition, an inversion layer can be created using an oxide layer like AlO_x or Al-doped SiO_2 possessing extremely high fixed charge density (Q_f) on the order of 10^{12} cm^{-2} [34, 35]. For instance, Al-doped ultrathin SiO_2 has a negative Q_f, inducing hole accumulation and creating an inversion layer at the surface of n-type c-Si. This Al-doped ultrathin SiO_2 layer on n-type c-Si demonstrated excellent surface passivation quality with a saturation current density (J_0) as low as 25 fA cm^{-2} corresponding to an effective surface recombination velocity (S_{eff}) of 2.7 cm s^{-1} and

contact resistivity (ρ_c) of ~200 mΩ cm^2 [36]. Furthermore, the inversion layer induced by Al_2O_3 showed an excellent lateral hole conductivity on n-type c-Si, which effectively acts as an emitter layer and demonstrated more than 20% efficient n-type c-Si solar cells [37, 38]. However, in this previous research, since atomic layer deposition (ALD) was adapted to form Al_2O_3, high vacuum condition is required, and energy consumption and the maintenance cost of flammable gases like trimethyl aluminum (TMA) will be much higher [39]. As an alternative, atmospheric pressure chemical vapor deposition (APCVD) is a high-throughput industrially comparable deposition process [40]. However, the relatively high temperature of ~400 °C and >10 nm thick Al_2O_3 layer is necessary to obtain an excellent surface passivation quality [40], which cannot be used for carrier-selective passivating contacts due to such a thick dielectric layer.

A novel wet chemical technology that might be a breakthrough has emerged. E. Schmid *et al*. presented a cost-effective negative fixed charge passivation method, the so-called "Wet AlO_x" process, in 2018 [41]. This process requires two wet chemical processes: formation of ultrathin SiO_x dipping cleaned Si wafers in hot sulfuric peroxide mixture followed by dipping in aqueous solution dissolved Al salts ($Na[Al13_3O_4(OH)_{24}(H_2O)_{12}](NO_3)_8$, $AlCl_3$, or $Al(NO_3)_3$). Through these wet chemical processes, the layer structure with one monolayer Al adsorbed on wet-chemically formed SiO_x was realized with a high negative surface charge of up to ~1.4×10^{12} cm^{-2}. The self-saturation of Al adsorption results in monolayer deposition of AlO_x. In addition, they demonstrated cell efficiency comparable to conventional silicon nitride (SiN_x) passivated samples on n-type c-Si with a higher tolerance to many metal impurities. Although such an ultrathin negative fixed charge layer has a considerable potential to realize a hole-selective passivating contact, a wet chemically grown ultrathin negative fixed charged oxide layer has not demonstrated the device operation.

Therefore, this Ph.D. research demonstrated an outstanding surface passivation quality despite an ultrathin oxide layer of ~1 nm thickness with excellent hole-selectivity by a novel, simple wet chemical process, and the device operation was successfully confirmed with an induced inversion layer acting as a p^+ emitter of n-type c-Si solar cells [42, 43]. I named this novel solar cell architecture "Al-induced charged oxide inversion layer (Al-COIL) solar cells." It allows simultaneous p^+ emitter formation and surface passivation in a simple low-temperature wet chemical process. However, one of the drawbacks is that this process cannot form a relatively thick layer for an antireflective coating (ARC). When this layer is used as a front surface of solar cells, some layers with good optical properties, such as the SiN_x layer, must be deposited, or an ultralow reflection structure, such as black Si [44], formed to obtain higher solar cell performance. However, due to plasma damage to the ultrathin layer, such an ultrathin layer is unlikely to deposit ARC by conventional plasma-enhanced chemical vapor deposition (PECVD) [45]. Hence, the ARC has to be gently deposited by other alternatives. As shown in Figure 1.2, a comparison of

process flows for PERC, TOPCon, SHJ, and interdigitated back contact (IBC) [46] with Al-COIL, Al-COIL has a massive advantage with much fewer processes compared to any other industrialized process flows. However, it is noted that this Al-COIL process flow is provisional. In this work, since I focused on the study of $Al(NO_3)_3$ treatment process, metal electrodes were formed by physical vapor deposition (PVD) as a fundamental research step. Hence, it is necessary to develop a rear-side surface passivation and screen printing (SP) process for the mass production of Al-COIL solar cells in the future.

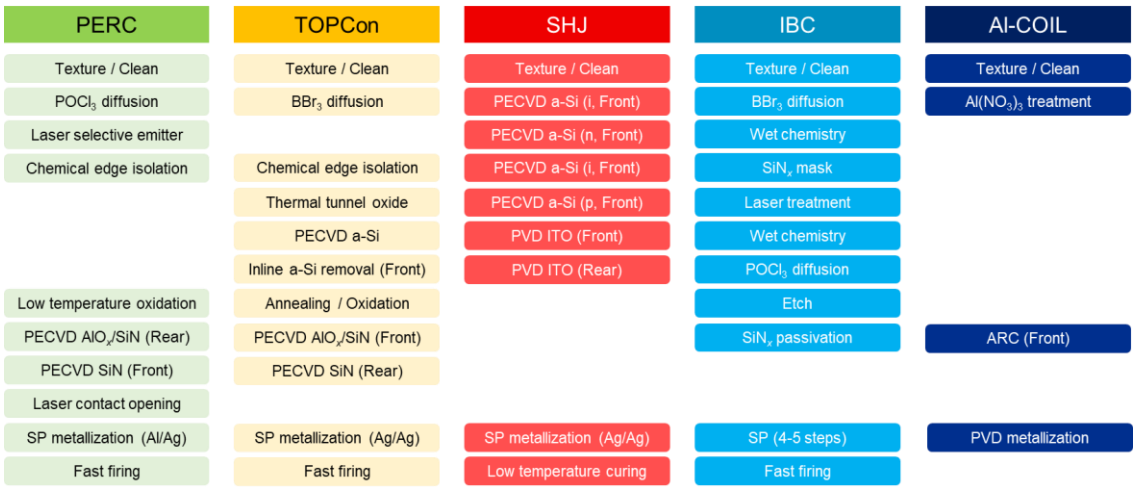

Fig. 1.2 Process flows for PERC, TOPCon, SHJ, IBC, and Al-COIL.

1.3 Potential of Al-doped SiO_x material

Firstly, since Al, Si, and O are highly abundant elements on earth, and the top three elements on Clarke number: 49.20% for O, 25.67% for Si, and 7.50% for Al, respectively [47], choosing Al-doped SiO_x is a sustainable option. Secondly, a sufficient Al concentration of ~6×10^{14} cm^{-2} is contained in one monolayer AlO_x [48]. Suppose 100% of Al atoms have negative charges on them ; in that case, an impeccable surface passivation quality will be expected from the calculation of S_{eff} as a function of $Q_{f,}$ as shown in Figure 1.3. The calculation was performed using a simplified Shockley–Read–Hall (SRH) equation for a single defect energy level under the assumption of sufficiently high negative Q_f [49] assuming the electron capture cross section (σ_n) of 1.8×10^{-14} cm^2 [40] and interface state density per area (N_{it}) of ~1.0×10^{12} cm^{-2} [40] for resistivity of 2.5 Ω cm and Δn of 1×10^{15} cm^{-3} condition. Even though the layer is one monolayer with only 6.7% negatively charged Al, the calculated S_{eff} will be the same value obtained from PECVD a-

Si/SiO_x/SiN_x stacks, which are reported as the most excellent surface passivation for c-Si surface as S_{eff} of 0.1 cm s^{-1} [50]. Furthermore, since four coordinated aluminum oxides (AlO_4) adjacent to the SiO_2 structure stabilize in the four coordinated SiO_2 structures [48], creating a negative fixed charge, the field effect passivation from Al-doped SiO_x material is the highly expected approach.

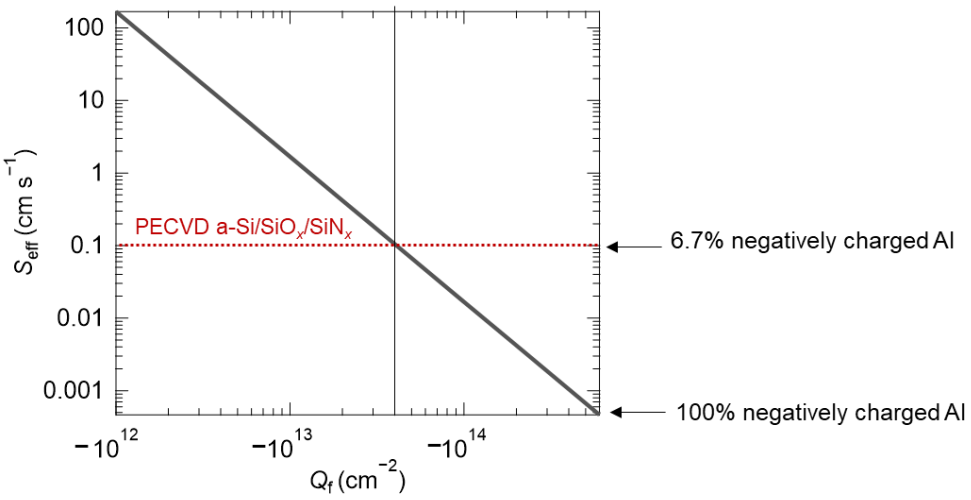

Fig. 1.3 Relationship between effective surface recombination velocity (S_{eff}) and fixed charge density (Q_f) in Al-doped SiO_x/Si structure.

1.4 Outline of this work

This doctoral dissertation accesses the cost-effective and high-efficiency novel Si-based solar cells, realizing an excellent surface passivation quality and hole-selective contact by an ultrathin Al-doped SiO_x, which can form using a simple wet chemical treatment. Its structure is divided as follows. Chapter 2 reviews the principle of carrier recombination in c-Si and its surface passivation with carrier-selective contacts. Chapter 3 explains the characterization techniques this work used. Chapter 4 demonstrated excellent surface passivation quality and the hole-selective contact by a simple wet chemical process. Moreover, several approaches, such as spectroscopic, electrical, and microscopic methods, revealed the mechanism of the hole-selective passivating contact. Chapter 5 demonstrated the operation of a solar cell device with Al-COIL architecture, the p-type inversion layer acting as a p^+ emitter. Chapter 6 investigated and discussed the effectiveness of a pyramidal-textured Si surface and an anti-reflection coating to increase cell efficiency.

References

[1] IPCC 6thAssessment Report, Climate Change 2022: Mitigation of Climate Change

[2] Fourth National Climate Assessment Volume II: Impacts, Risks, and Adaptation in the United States (USGCRP, 2018).

[3] H. Murakami, E. Levin, T. L. Delworth, R. Gudgel, and P.-C. Hsu, "Dominant effect of relative tropical Atlantic warming on major hurricane occurrence," Science **362**, 794 (2018).

[4] 2021 The impact of disasters and crises on agriculture and food security (Food and Agriculture Organization of the United Nations, 2021).

[5] NREL. NSRDB: National Solar Radiation Database: https://nsrdb.nrel.gov/data-sets/international-data

[6] D. M. Chapin, C. S. Fuller, and G. L. Pearson, "A new silicon p-n junction photocell for converting solar radiation into electrical power," J. Appl. Phys. **25**, 676 (1954).

[7] Photovoltaics report (2023): https://www.ise.fraunhofer.de/en/publications/studies/photovoltaics-report.html

[8] International Technology Roadmap for Photovoltaic (ITRPV) 2022 Results 14th edition (2023).

[9] Emissions Gap Report 2022: The Closing Window (UNEP, 2022).

[10] A. W. Blakers, A. Wang, A. M. Milne, J. Zhao, and M. A Green, "22.8% efficient silicon solar cell," Appl. Phys. Lett. **55**, 1363 (1989).

[11] J. Schmidt, R. Peibst, and R. Brendel, "Surface passivation of crystalline silicon solar cells: Present and future," Sol. Energy Mater. Sol. Cells **187**, 39 (2018).

[12] A. Richter, Ma. Hermle, and S. W. Glunz, "Reassessment of the limiting efficiency for crystalline silicon solar cells," IEEE J. Photovolt. **3**, 1184 (2013).

[13] F. Feldmann, M. Bivour, C. Reichel, M. Hermle, and S. W. Glunz, "Passivated rear contacts for high-efficiency n-type Si solar cells providing high interface passivation quality and excellent transport characteristics," Sol. Energy Mater. Sol. Cells **120**, 270 (2014).

[14] M. Taguchi, K. Kawamoto, S. Tsuge, T. Baba, H. Sakata, M. Morizane, K. Uchihashi, N. Nakamura, S. Kiyama, and O. Oota, "HIT™ cells high-efficiency crystalline Si cells with novel structure," Prog. Photovolt. Res. Appl. **8**, 503 (2000).

[15] J. Melskens, B. W. H. van de Loo, B. Macco, L. E. Black, S. Smit, and W. M. M. (Erwin) Kessels, "Passivating contacts for crystalline silicon solar cells: From concepts and materials to prospects," IEEE J. Photovolt. **8**, 373 (2018).

[16] Z. C. Holman, A. Descoeudres, L. Barraud, F. Z. Fernandez, J. P. Seif, S. D. Wolf, and C. Ballif, "Current losses at the front of silicon heterojunction solar cells," IEEE J. Photovolt. **2**, 2156 (2012).

[17] A. Richter, J. Benick, F. Feldmann, A. Fell, B. Steinhauser, J.-I. Polzin, N. Tucher, J. N. Murthy, M. Hermle, and S. W. Glunz, "Both sides contacted silicon solar cells: Options for approaching 26% efficiency," In: Proceedings of the 36th European PV Solar Energy Conference and Exhibition, Marseille, France, 9–13 (2019).

[18] H. Lin, M. Yang, X. Ru, G. Wang, S. Yin, F. Peng, C. Hong, M. Qu, J. Lu, L. Fang, C. Han, P. Procel, O. Isabella, P. Gao, Z. Li, and Xi. Xu, "Silicon heterojunction solar cells with up to 26.81% efficiency achieved by electrically optimized nanocrystalline-silicon hole contact layers," Nat. Energy **8**, 789 (2023).

[19] E. Bellini, "Jolywood claims 26.7% efficiency for n-type TOPCon solar cell," April 12, 2023: https://www.pv-magazine.com/2023/04/12/jolywood-claims-26-7-efficiency-for-n-type-topcon-solar-cell/

[20] M. Fischer, ITRPV 14th edition, March 2023, key findings & report presentation (2023).

[21] A. Richter, J. Benick, F. Feldmann, A. Fell, M. Hermle, and S. W. Glunz, "n-Type Si solar cells with passivating electron contact: Identifying sources for efficiency limitations by wafer thickness and resistivity variation," Sol. Energy Mater. Sol. Cells **173**, 96 (2017).

[22] M. A. Kessler, T. Ohrdes, B. Wolpensinger, R. Bock, and N.-P. Harder, "Characterisation and implications of the boron rich layer resulting from open-tube liquid source BBR_3 boron diffusion processes," In: Proceedings of the 34th IEEE Photovoltaic Specialists Conference, Philadelphia, Pennsylvania, USA, pp. 001556–001561 (2009).

[23] P. J. Cousins, and J. E. Cotter, "The influence of diffusion-induced dislocations on high efficiency silicon solar cells," IEEE Trans. Electron Devices **53**, 457 (2006).

[24] J. Schmidt, and A. Cuevas, "Electronic properties of light-induced recombination centers in boron-doped Czochralski silicon," J. Appl. Phys. **86**, 3175 (1999).

[25] R. B. Fair, "Concentration profiles of diffused dopants in silicon," In: Impurity doping processes in silicon, North Holland, Amsterdam, 315–442 (1981).

[26] J. Bullock, Y. Wan, Z. Xu, S. Essig, M. Hettick, H. Wang, W. Ji, M. Boccard, A. Cuevas, C. Ballif, and A. Javey, "Stable dopant-free asymmetric heterocontact silicon solar cells with efficiencies above 20%," ACS Energy Lett. **3**, 508 (2018).

[27] J. Bullock, D. Yan, A. Cuevas, Y. Wan, and C. Samundsett, "n- and p-type silicon solar cells with molybdenum oxide hole contacts," Energy Procedia **77**, 446 (2015).

[28] H. Ali, S. Koul, G. Gregory, J. Bullock, A. Javey, A. Kushima, and K. O. Davis, "Thermal stability of hole-selective tungsten oxide: In situ transmission electron microscopy study," Sci. Rep. **8**, 12651 (2018).

[29] X. Yang, H. Xu, W. Liu, Q. Bi, L. Xu, J. Kang, M. N. Hedhili, B. Sun, X. Zhang, and S. D. Wolf, "Atomic layer deposition of vanadium oxide as hole-selective contact for crystalline silicon solar cells," Adv. Electron. Mater. **6**, 2000467 (2020).

[30] T. Sun, R. Wang, R. Liu, C. Wu, Y. Zhong, Y. Liu, Y. Wang, Y. Han, Z. Xia, Y. Zou, T. Song, N. Koch, S. Duhm, and B. Sun, "Investigation of MoO_x/n-Si strong inversion layer interfaces via dopant-free heterocontact," Phys. Status Solidi RRL **11**, 1700107 (2017).

[31] S. Wan, G. Zhang, J. Niederhausen, D. Wu, Q. Wang, B. Sun, T. Song, and S. Duhm, "Schottky contact formation by an insulator: Lithium fluoride on silicon," Appl. Phys. Lett. **118**, 241601 (2021).

[32] X. Yang, P. Zheng, and Q. Bi, K. Weber, "Silicon heterojunction solar cells with electron selective TiO_x contact," Sol. Energy Mater. Sol. Cells **150**, 32 (2016).

[33] J. Yu, M. Liao, D. Yan, Y. Wan, H. Lin, Z. Wang, P. Gao, Y. Zeng, B. Yan, and J. Ye, "Activating and optimizing evaporation-processed magnesium oxide passivating contact for silicon solar cells," Nano Energy **62**, 181 (2019).

[34] B. Hoex, J. J. H. Gielis, M. C. M. van de Sanden, and W. M. M. Kessels, "On the surface passivation mechanism by the negative-charge-dielectric Al_2O_3," J. Appl. Phys. **104**, 113703 (2008).

[35] D. König, D. Hiller, S. Gutsch, M. Zacharias, and S. Smith, "Modulation doping of silicon using aluminium-induced acceptor states in silicon dioxide," Sci. Rep. **7**, 46703 (2017).

[36] D. Hiller, P. Honicke, and D. König, "Material combination of tunnel-SiO_2 with a (sub-)monolayer of ALD-AlO_x on silicon offering a highly passivating hole selective contact," Sol. Energy Mater. Sol. Cells **215**, 110654 (2020).

[37] D. Choi and K. Seo, "Field-induced radial junction for dopant-free crystalline silicon microwire solar cells with an efficiency of over 20%," Adv. Energy Mater. **11**, 2003707 (2021).

[38] N. Kim, D. Choi, H. Kim, H.-D. Um, and K. Seo, "Silicon microwire arrays with nanoscale spacing for radial junction c-Si solar cells with an efficiency of 20.5%," ACS Nano **15**, 14756 (2021).

[39] B. Hoex, "Precursors for enabling higher-efficiency silicon wafer solar cells," Photovoltaics International **27**, 11 (2015).

[40] L. E. Black, "New perspectives on surface passivation: Understanding the Si–Al_2O_3 interface," Ph.D. thesis, Australian National University (2015).

[41] E. Schmid, S. Schmitt, T. Boescke, E. Wefringhaus, F. Buchholz, C. Peter, R. Marczak, A. Ramakrishnan, M. Mateescu, and P. Kunze, "WetAlO_x: A Novel, Cost Effective, Negative Charge Passivation Method for Crystalline Silicon Solar Cells", In: Proceedings of the 35th European Photovoltaic Solar Energy Conference and Exhibition, Brussels, Belgium, 591–596 (2018).

[42] H. Nakajima, H. T. C. Tu, and K. Ohdaira, "Hole-selective ultrathin Al-doped SiO_x passivation layer formed by immersing in aluminum nitrate aqueous solution," Phys. Status Solidi RRL **16**, 2200052 (2022).

[43] H. Nakajima, H. T. C. Tu, and K. Ohdaira, "Ultrathin Al-doped SiO_x passivating hole-selective contacts formed by a simple wet process," Jpn. J. Appl. Phys. **62**, SK1040 (2023).

[44] X. Liu, P. R. Coxon, M. Peters, B. Hoex, J. M. Cole, and D. J. Fray, "Black silicon: fabrication methods, properties and solar energy applications," Energy Environ. Sci. **7**, 3223 (2014).

[45] B. Mojrová, H. Chu, C. Peter, P. Preis, J. Lossen, V. D. Mihailetchi, and R. Kopecek, "A comparison study of boron emitter passivation by silicon oxide and a PECVD silicon nitride stack," Energy Procedia **124**, 288 (2017).

[46] R. Kopecek, F. Buchholz, V. D. Mihailetchi, J. Libal, J. Lossen, N. Chen, H. Chu, C. Peter, T. Timofte, A. Halm, Y. Guo, X. Qu, X. Wu, J. Gao, and P. Dong, "Interdigitated back contact technology as final evolution for industrial crystalline single-junction silicon solar cell," Solar **3**, 1 (2023).

[47] F. W. Clarke, The data of geochemistry, Bulletin 770, U.S. Government Printing Office, Washington, D.C. (1924).

[48] D. Hiller, J. Göttlicher, R. Steininger, T. Huthwelker, J. Julin, F. Munnik, M. Wahl, W. Bock, B. Schoenaers, A. Stesmans, and D. König, "Structural properties of Al−O monolayers in SiO_2 on silicon and the maximization of their negative fixed charge density," ACS Appl. Mater. Interfaces **10**, 30495 (2018).

[49] K. R. McIntosh and L. E. Black, "On effective surface recombination parameters," J. Appl. Phys. **116**, 014503 (2014).

[50] R. S. Bonilla, C. Reichel, M. Hermle, and P. R. Wilshaw, "Extremely low surface recombination in 1 Ω cm n-type monocrystalline silicon," Phys. Status Solidi RRL **11**, 1600307 (2017).

CHAPTER 2

SURFACE RECOMBINATION THEORY AND PASSIVATING CONTACTS

Surface recombination is one of the crucial events in Si-based devices. Nowadays, since the bulk property has been exceptionally high and the wafer is becoming thinner, the surface is much more critical for the device's performance. Also, pyramidal textured and nano-structured Si surfaces are used to boost photocurrent density, but surface recombination will be a much more crucial problem due to the increase of surface defect density derived from the larger surface area. However, if the surface is well passivated by induction of Si band bending, the carriers can be effectively separated, causing carrier-selective contact. This might be a breakthrough if a simple process achieves it. Hence, it is essential to understand the surface recombination theory and construct the mitigative methods.

In this chapter, to provide a theoretical background for the c-Si solar cells with carrier-selective contact, the recombination theory in the bulk and surface and the surface passivation method are reviewed. In particular, the description is focused on the carrier-selective contacts. Several types of carrier-selective contacts are reviewed to understand this research finding of hole-selective contact by a charged oxide. A simplified case of the surface recombination model, proposed by McIntosh and Black, followed for this work, is described. This chapter also introduces a method for determining the Q_f and the interface state density values for ultrathin dielectric layers through the combination of measurable values of surface potential and the surface recombination model.

2.1 Carrier recombination in crystalline silicon

2.1.1 Carrier recombination in bulk

When a semiconductor absorbs light with a more significant energy than the material's band gap energy, it generates excited carriers. This process is called generation. However, the energy must be released as photons or phonons to return the system to thermal equilibrium by combining with the excited electrons and holes. These recombination processes can be measured as carrier lifetime (τ), the time it takes for the carriers to recombine. τ can be described as

$$\tau = \frac{\Delta n}{U}. \tag{2.1}$$

Where Δn is the excess carrier density, and U is the recombination rate per volume. The recombination process takes place in the bulk and surface.

Radiative recombination

The radiative recombination directly occurs by releasing excess energy as a photon with an energy corresponding to the close value of band gap energy, and the radiative recombination rate can be described as

$$U_{\mathrm{rad}} = B_{\mathrm{rad}}(np - n_{\mathrm{i}}^2). \tag{2.2}$$

Where B_{rad} is the radiative recombination coefficient, n is the electron density, p is the hole density, and n_{i} is the intrinsic carrier density. The B_{rad} value of Si is known as 9.5×10^{-15} cm^3 s^{-1} at room temperature [1]. The value is considerably lower than the direct transition material, such as GaAs, due to the indirect transition material of Si. Therefore, since the contribution of the radiative recombination of the Si material is low compared with other types of recombination, it can be negligible.

Auger recombination

Auger recombination is also known as intrinsic recombination. The recombination process is involved in a three-carrier interaction. The recombination occurs by a relaxation due to the energy transfer of one excited electron (or hole) to the neighbor excited electron (or hole) to excite them

higher state. The Auger recombination rate can be described as

$$U_{\mathrm{Aug}} = C_{\mathrm{n}}\left(n^2p - n_{\mathrm{i}}^2 n_0\right) + C_{\mathrm{p}}\left(np^2 - p_0 n_{\mathrm{i}}^2\right) \approx C_{\mathrm{n}}n^2p + C_{\mathrm{p}}np^2. \tag{2.3}$$

Where C_{n} and C_{p} are the Auger coefficients for electron and hole. The Auger lifetime of p-type material can be simplified as

$$\tau_{\mathrm{Aug,li}} = \frac{1}{C_{\mathrm{p}}N_{\mathrm{A}}^2} \quad and \quad \tau_{\mathrm{Aug,hi}} = \frac{1}{(C_{\mathrm{n}} + C_{\mathrm{p}})\Delta n^2}\,. \tag{2.4}$$

These are Auger lifetimes at low and high injection levels, respectively. From these equations, Auger lifetime at a high injection level or heavy doping is crucial to the Si solar cells. Therefore, the doping concentration in the emitter must be optimized so as not to decrease the Auger lifetime. However, in the actual case, the Auger lifetime is lower than the generated value from Eq. (2.4) due to the columbic interaction of charge carriers. One of the correct models was proposed by Kerr and Cuevas [2]. The model created by fitting the experimental data set is given by

$$\tau_{\mathrm{Aug}} = \frac{\Delta n}{np(1.8\times10^{-24}\,n_0^{0.65} + 6\times10^{-25}\,p_0^{0.65} + 3\times10^{-27}\,\Delta n^{0.8})}\,. \tag{2.5}$$

The more accurate parametrization was proposed by Richter *et al*., which is consistent with the theory of Coulomb-enhanced Auger recombination and accounts for Coulomb-enhanced radiative recombination [3].

Shockley-Read Hall (SRH) recombination

The Schockley-Read Hall recombination is the recombination via a defect state in the band gap of the material. The recombination process was first investigated by Schockley, Read, and Hall [4, 5]. Therefore, the recombination process is called Schockley-Read-Hall (SRH) recombination. The SRH recombination is known as extrinsic recombination due to the recombination coming from extrinsic factors such as extended defects: Dislocations or stacking faults and intrinsic or extrinsic point defects, causing the discrete energy levels in the band gap.

Firstly, an electron in the conduction band relaxes to the defect level and afterward relaxes to the valence band, annihilating a hole. The defect state near the mid-gap of the material drastically increases the recombination rate because of the similar probability for the capturing of electrons from a conduction band and holes from the valence band, which is referred to as the recombination

center. The recombination rate based on the SRH model with a single defect level is given by

$$U_{\mathrm{SRH}} = \frac{np - n_i^2}{\tau_{p0}(n + n_1) + \tau_{n0}(p + p_1)}, \tag{2.6}$$

$$n_1 = n_{\mathrm{i}} \exp\left(\frac{E_{\mathrm{t}} - E_{\mathrm{i}}}{k_{\mathrm{B}}T}\right), \quad p_1 = n_{\mathrm{i}} \exp\left\{\frac{-(E_{\mathrm{t}} - E_{\mathrm{i}})}{k_{\mathrm{B}}T}\right\}, \tag{2.7}$$

$$\tau_{n0} = \frac{1}{N_{\mathrm{t}}\sigma_{\mathrm{n}}\nu_{\mathrm{th}}}, \quad \tau_{p0} = \frac{1}{N_{\mathrm{t}}\sigma_{\mathrm{p}}\nu_{\mathrm{th}}}. \tag{2.8}$$

Where n_1 and p_1 are the statistical values of the equilibrium electron and hole density when the fermi level is consistent with the defect energy level ($E_F = E_t$). τ_{n0} and τ_{p0} are the capture time constants for the electron and hole. The SRH recombination lifetime (τ_{SRH}) can be expressed as

$$\tau_{\mathrm{SRH}} = \frac{\tau_{\mathrm{n0}}(p_0 + p_1 + \Delta n) + \tau_{\mathrm{p0}}(n_0 + n_1 + \Delta n)}{n_0 + p_0 + \Delta n}. \tag{2.9}$$

Where σ_n and σ_p are the capture cross section for electron and hole, respectively, and ν_{th} is the carrier thermal velocity. At the low injection level, the τ_{SRH} is independent of the Δn and can be simplified as, for p-type,

$$\tau_{\mathrm{SRH}} = \tau_{\mathrm{n0}}, \tag{2.10}$$

for n-type,

$$\tau_{\mathrm{SRH}} = \tau_{\mathrm{p0}}. \tag{2.11}$$

At the high injection level, since the Δn is considerably higher than n_0, n_1, p_0, and p_1, τ_{SRH} is also independent of the Δn and can be simplified as

$$\tau_{\mathrm{SRH}} = \tau_{\mathrm{n0}} + \tau_{\mathrm{p0}}. \tag{2.12}$$

2.1.2 Carrier recombination at the surface

The carrier recombination at the surface is different from bulk as follows: the active defect levels at the surface are continuously distributed over the entire band gap. As an extended SRH formalism, the surface recombination rate (U_s) [6, 7] is described as

$$U_S = \left(n_s p_s - n_i^2\right)\nu_{th} \int_{E_V}^{E_C} \frac{D_{it}(E)}{\frac{n_s + n_1(E)}{\sigma_p(E)} + \frac{p_s + p_1(E)}{\sigma_n(E)}}\, dE. \tag{2.13}$$

Where n_s and p_s are the electron and hole densities at the surface, and $D_{it}(E)$ is the interface state density per energy interval. By using U_s, the surface recombination velocity (SRV) can be described as

$$S = \frac{U_S}{\Delta n_s}. \tag{2.14}$$

Where Δn_s is an excess carrier density at the surface, hence, the recombination lifetime at the surface can be defined as an inverse SRV. The Eq. (2.13) is generally simplified by assuming a single defect level with the interface state per unit area (N_{it}) as

$$U_S = \frac{n_s p_s - n_i^2}{\frac{n_s + n_1}{S_{p0}} + \frac{p_s + p_1}{S_{n0}}}, \tag{2.15}$$

$$S_{n0} = \sigma_n N_{it} \nu_{th} \text{ and } S_{p0} = \sigma_p N_{it} \nu_{th}. \tag{2.16}$$

Where S_{n0} and S_{p0} are the SRVs of electron and hole, respectively. The simplified SRH equation, proposed by McIntosh and Black [8], was applied to this research. In the simplification to the n-type Si, the following situations are restricted: $n_s >> n_1$, $(n_s + n_1)/S_{p0} >> (p_s + p_1)/S_{n0}$, which means the defect is not very close to the band edges. The situation of $p_s n_s >> n_i^2$ is also imposed, which is valid in all situations but deficient injection level. Hence, under these assumptions, the SRH equation can be simplified as

$$U_S = S_{p0}\, p_S. \tag{2.17}$$

The equilibrium minority carrier density at the distance of *d*: the edge of the energy band, unaffected by changes in the surface dielectric layer, is negligible. Hence, the carrier density at the distance of *d* can be described as

$$n_{\mathrm{d}} = N_{\mathrm{dop}} + \Delta n_{\mathrm{d}}. \tag{2.18}$$

Where N_{dop} is the doping density in bulk, and Δn_{d} is the excess carrier density at the distance of *d*. Since the minority carrier is generated as an excess carrier, the Δn_{d} can be replaced with a minority carrier density at *d* (n_{d}),

$$n_{\mathrm{d}} = N_{\mathrm{dop}} + n_{\mathrm{d}}\,. \tag{2.19}$$

Therefore, by using Eq. (2.14) and (2.17), the effective SRV can be described as

$$S_{\mathrm{eff}} = S_{\mathrm{p0}}\,\frac{p_{\mathrm{s}}}{p_{\mathrm{d}}}. \tag{2.20}$$

Thus, under the negligible band bending condition, p_{s} should be equal to $n_{d,}$ and S_{eff} is equal to S_{p0}. When a positive charge is applied, $p_{\mathrm{s}} < p_{\mathrm{d}}$, leading to $S_{\mathrm{eff}} < S_{\mathrm{p0}}$. Vice versa, when a negative charge is applied, $p_{\mathrm{s}} > p_{\mathrm{d}}$, leading to $S_{\mathrm{eff}} > S_{\mathrm{p0}}$.

The relationship between the carrier densities, band bending, and surface charge [6] in Eq. (2.21).

$$p_{\mathrm{s}} - p_{\mathrm{d}} + n_{\mathrm{s}} - n_{\mathrm{d}} + (N_{\mathrm{A}} - N_{\mathrm{D}})\frac{\Psi_{\mathrm{s}}}{V_{\mathrm{T}}} = \frac{Q^2}{2q\varepsilon_{\mathrm{Si}}V_{\mathrm{T}}} \tag{2.21}$$

Where Ψ_{s} is the surface potential with respect to $\Psi_{\mathrm{d}} = 0$, $\varepsilon_{\mathrm{Si}}$ is the permittivity of Si, and Q is the charge in the material induced by the dielectric layer and the interface. The quasi-Fermi levels between the surface and the position at a distance of *d* are assumed flat in Eq. (2.21).
The carrier densities can be described using the surface potential. When assuming Boltzmann statics and the flat quasi-Fermi levels, surface carrier densities can be described as

$$n_{\mathrm{s}} = n_{\mathrm{d}} \exp\left(\frac{\Psi_{\mathrm{s}}}{V_{\mathrm{T}}}\right), \tag{2.22}$$

$$p_s = p_d \exp\left(-\frac{\Psi_s}{V_T}\right). \tag{2.23}$$

Therefore, the relationship between surface carrier densities of surface and the distance of d can be described as,

$$p_s n_s = p_d n_d. \tag{2.24}$$

For the exceptional cases below, S_{eff} can be derived as follows,

(1) In the case of negligibly small Q_f ($\Psi_s \sim 0$),

$$n_s = n_d\,, \tag{2.25}$$

$$S_{eff} = S_{p0}\,. \tag{2.26}$$

(2) In the case of sufficiently small Q_f, form Eq. (2.21) and (2.23), since n-type material, this equation requires n_s, $n_d >> p_s$, p_d, simplifying Eq. (2.21) to give

$$\exp\left(\frac{\Psi_s}{V_T}\right) - 1 - \frac{N_D}{n_d}\frac{\Psi_s}{V_T} = \frac{Q^2}{2q\varepsilon_{Si}V_T n_d}\,. \tag{2.27}$$

In low injection level, when $p_d \sim N_A$, it can be further simplified by introducing a partial Maclaurin series for carrier densities,

$$\sum_{k=2}^{\infty} \frac{\left(\frac{\Psi_s}{V_T}\right)^k}{k!} - 1 + \frac{\Psi_s}{V_T} = \frac{Q^2}{2q\varepsilon_{Si}V_T N_A}\,, \tag{2.28}$$

$$\frac{\Psi_s}{V_T} = \frac{Q}{\sqrt{qV_T\varepsilon_{Si}N_A}}\,, \tag{2.29}$$

$$n_s = n_d \exp\left(\frac{Q}{\sqrt{k_B T\varepsilon_{Si}N_A}}\right) \text{ and } p_s = p_d \exp\left(-\frac{Q}{\sqrt{k_B T\varepsilon_{Si}N_A}}\right), \tag{2.30}$$

$$S_{\mathrm{eff}} = S_{\mathrm{p0}} \exp\left(-\frac{Q}{\sqrt{k_{\mathrm{B}} T \varepsilon_{\mathrm{Si}} N_{\mathrm{D}}}}\right). \tag{2.31}$$

(3) In the case of sufficiently positive Q_{f}, carrier densities of Eq. (2.21) equals n_{s} ($n_{\mathrm{s}} >> n_{\mathrm{d}}$, p_{s}, p_{d}), therefore,

$$n_{\mathrm{s}} = \frac{Q^2}{2 k_{\mathrm{B}} T \varepsilon_{\mathrm{Si}}}, \tag{2.32}$$

$$S_{\mathrm{eff}} = S_{\mathrm{p0}} n_{\mathrm{d}} \frac{2 k_{\mathrm{B}} T \varepsilon_{\mathrm{Si}}}{Q^2}. \tag{2.33}$$

(4) In the case of sufficiently negative Q_{f}, carrier densities of Eq. (2.21) equals p_{s} ($p_{\mathrm{s}} >> n_{\mathrm{s}}$, n_{d}, p_{d}), therefore,

$$p_{\mathrm{s}} = \frac{Q^2}{2 k_{\mathrm{B}} T \varepsilon_{\mathrm{Si}}}, \tag{2.34}$$

$$S_{\mathrm{eff}} = S_{\mathrm{n0}} n_{\mathrm{d}} \frac{2 k_{\mathrm{B}} T \varepsilon_{\mathrm{Si}}}{Q^2}. \tag{2.35}$$

By substituting the Eq. (2.16),

$$S_{\mathrm{eff}} = \sigma_{\mathrm{n}} N_{\mathrm{it}} \nu_{\mathrm{th}} n_{\mathrm{d}} \frac{2 k_{\mathrm{B}} T \varepsilon_{\mathrm{Si}}}{Q^2}. \tag{2.36}$$

Therefore, N_{it} can be described as

$$N_{\mathrm{it}} = \frac{S_{\mathrm{eff}}\, Q^2}{2 k_{\mathrm{B}} T \varepsilon_{\mathrm{Si}} \sigma_{\mathrm{n}} \nu_{\mathrm{th}} p_{\mathrm{d}}}. \tag{2.37}$$

Thus, if Q and S_{eff} are obtained, N_{it} can be determined using Eq. (2.37) since the other parameters are known values.

This study used a highly negatively charged oxide layer on the n-type c-Si substrate. Hence, Eq. (2.37) was adequate for the Al-doped SiO_x/n-type Si substrate, and the equation was used to determine the N_{it} value with analyzed S_{eff} from carrier lifetime measurement. The σ_n was referred from the reported value in the literature [9–11]. The σ_n of the interface trap between a dielectric layer of SiO_2 or Al_2O_3 and Si have a similar value of ~10^{-14} cm^2 at the mid-gap of Si. There is no significant difference among these different processed samples, which has been reported in several literatures [9–11]. Hence, in this study, the value of 1.8×10^{-14} cm^2 for Al_2O_3/p-type c-Si [11] was applied to determine N_{it}. Therefore, S_{eff} and Q must be experimentally obtained to access the N_{it} value. The SRV (S) can be described by introducing effective minority carrier lifetime (τ_{eff}) as below.

$$\frac{1}{\tau_{\mathrm{eff}}}=\frac{1}{\tau_{\mathrm{rad}}}+\frac{1}{\tau_{\mathrm{Auger}}}+\frac{1}{\tau_{\mathrm{SRH}}}+\frac{1}{\tau_{\mathrm{surf}}}, \tag{2.38}$$

$$\frac{1}{\tau_{\mathrm{bulk}}}=\frac{1}{\tau_{\mathrm{rad}}}+\frac{1}{\tau_{\mathrm{Auger}}}+\frac{1}{\tau_{\mathrm{SRH}}}, \tag{2.39}$$

$$\frac{1}{\tau_{\mathrm{surf}}}=\frac{2S}{W}, \tag{2.40}$$

$$\frac{1}{\tau_{\mathrm{eff}}}=\frac{1}{\tau_{\mathrm{bulk}}}+\frac{2S}{W}. \tag{2.41}$$

Where τ_{bulk} is the bulk lifetime, and W is the thickness of the substrate. For the n-type semiconductor, the value of $S_{p0}\Delta p_s$ can be defined as the recombination rate per unit area (cm^{-2} s^{-1}), and it can be described as a form of the diffusion equation for the Δn from surface to bulk of material when the carrier generation evenly occurs.

$$S_{\mathrm{p0}}\Delta p(0)=D_{\mathrm{p}}\frac{d\Delta p(x)}{dx}\Big|_{x=0} \tag{2.42}$$

Where D_p is the diffusion coefficient for hole. The τ_{bulk} has been modeled [2] as,
for n-type,

$$\frac{1}{\tau_{\mathrm{bulk}}}=(\Delta p+N_{\mathrm{D}})\left(1.8\times10^{-24}\,{N_{\mathrm{D}}}^{0.65}+3.0\times10^{-27}\,\Delta p^{0.8}+9.5\times10^{-15}\right), \tag{2.43}$$

and for p-type,

$$\frac{1}{\tau_{\text{bulk}}} = (\Delta n + N_{\text{A}})\left(6.0 \times 10^{-25}\, {N_{\text{A}}}^{0.65} + 3.0 \times 10^{-27}\, \Delta n^{0.8} + 9.5 \times 10^{-15}\right). \quad (2.44)$$

Hence, the τ_{bulk} of the used Si substrates in this study can be estimated to be 12.6 ms with a resistivity of 2.5 Ω cm for n-type Si substrate at the Δn of 1×10^{15} cm^{-3} using Eq. (2.43). For the determination of Q value, from the Eqs. (2.23) and (2.34), Q is proportional to the root of exponential Ψ_{s} as described,

$$Q = \sqrt{2k_{\text{B}}T\varepsilon_{\text{Si}}p_{\text{d}} \exp\left(-\frac{\Psi_{\text{s}}}{V_{\text{T}}}\right)}. \quad (2.45)$$

The surface potential corresponds to surface band bending, which can be analyzed from capacitance–voltage (*C–V*). The evaluation technique is described in the next Chapter.

2.2 Carrier-selective passivating contact

2.2.1 Surface passivation

Since the surface recombination centers are distributed in the entire band gap of the material, the surface recombination significantly affects the solar cell performance, especially in open-circuit voltage (V_{oc}). To achieve high-efficiency solar cells, the surface recombination must be mitigated by surface passivation. In general, there are two types of surface passivation schemes. One is "chemical passivation," which is the termination of the active surface defects such as Si dangling bonds to form Si-H and Si-O bonds by hydrogen treatment and oxidation of the Si surface, respectively, resulting in the reduction of interface states. Another type of surface passivation is "field-effect passivation, " which is the carrier population controlled by the electric fields near the surface, originating from the charged ions or fixed charges in a surface layer. This electric field increases the concentration of one type of carrier and decreases another type of carrier at the surface, causing significantly different concentrations between these two types of carriers. This significant difference in the two types of carrier concentration at the surface allows the reduction of surface recombination even though there are defect states at the interface. For instance, the

positively charged silicon nitride (SiN_y) is commonly used as a surface passivation layer due to its excellent surface passivation quality originating from both chemical and field-effect passivation. However, the layer must be locally etched, usually performing fire-through with screen-printed Ag electrode to contact metal electrode. Hence, the front surfaces are locally contacted with metal electrodes in the conventional c-Si solar cell with Al-BSF, PERC, and TOPCon structures. The SRV at the metal contacted area is extremely large (>10^5 cm s^{-1}), and J_0 will be unacceptably high as ~2000 fA cm^{-2} when using 2 Ω cm c-Si covered with only 1% of the metal electrode [12]. Thus, carrier-selective passivating contacts would realize excellent surface passivation with a high conductivity without direct contact with metal electrodes. It would be a breakthrough technology to access a practical limit of solar cell performance. So far, SHJ solar cells have achieved the highest conversion efficiency (η) of 26.81% [13], with carrier-selective passivating contacts on both sides for p- and n-type contacts.

2.2.2 Theory of carrier-selective contacts

Here, the theory of carrier-selective contacts is explained by referring [14]. In a semiconductor material, the two types of carriers (electrons and holes) are simultaneously affected by two forces. One is an electric force, and the other is a generalized force related to the gradient of the carrier densities.

In the case of assuming only electric field (E) exists in the system, the charge current of particle k ($J_{f,k}$, electron is k = e or hole is k = h) is given by

$$j_{\mathrm{f,k}} = q n_{\mathrm{k}} \mu_{\mathrm{k}} E \,, \tag{2.46}$$

$$q n_{\mathrm{k}} \mu_{\mathrm{k}} E = \sigma_{\mathrm{k}} E \,, \tag{2.47}$$

$$\sigma_{\mathrm{k}} E = -\frac{\sigma_{\mathrm{k}}}{z_{\mathrm{k}} q} \mathrm{grad}(z_{\mathrm{k}} q \varphi) \,. \tag{2.48}$$

Where q is the elementary charge, n_k is the charge carrier density, μ_k is the mobility of the charge carrier, φ is the electric potential, and $z_k q$ is the charge.

In the case of assuming only a concentration gradient of charge carriers k exists without an electric field, their charge current is given by Fick's law.

$$j_{\mathrm{d,k}} = z_{\mathrm{k}} q(-D_{\mathrm{k}} \mathrm{grad}\, n_{\mathrm{k}}) \tag{2.49}$$

$$z_{\mathrm{k}} q(-D_{\mathrm{k}} \mathrm{grad}\, n_{\mathrm{k}}) = -z_{\mathrm{k}} q\, n_{\mathrm{k}} D_{\mathrm{k}} \frac{\mathrm{grad}\, n_{\mathrm{k}}}{n_{\mathrm{k}}} \tag{2.50}$$

Take into consideration of Einstein's relation of

$$D_{\mathrm{k}} = \frac{\mu_{\mathrm{k}} k_{\mathrm{B}} T}{q}, \tag{2.51}$$

hence,

$$-z_{\mathrm{k}} q\, n_{\mathrm{k}} D_{\mathrm{k}} \frac{\mathrm{grad}\, n_{\mathrm{k}}}{n_{\mathrm{k}}} = -\frac{z_{\mathrm{k}} \sigma_{\mathrm{k}} k_{\mathrm{B}} T}{q} \frac{\mathrm{grad}\, n_{\mathrm{k}}}{n_{\mathrm{k}}} \tag{2.52}$$

is given. By applying the chemical potential of charge carriers k with a standard value of the chemical potential ($\Phi_{\mathrm{chem,k,0}}$), their charge current is given by

$$j_{\mathrm{d,k}} = -\frac{\sigma_{\mathrm{k}}}{z_{\mathrm{k}} q} \mathrm{grad}\, \Phi_{\mathrm{chem,k}}\,. \tag{2.53}$$

In the actual case, the electrical force and chemical force are present simultaneously, and the total current must be considered as an electrochemical potential of charge carriers (η_{k}). Hence, the resulting force can be described as

$$-\mathrm{grad}\,(\Phi_{\mathrm{chem,k}} + z_{\mathrm{k}} q \varphi) = -\mathrm{grad}\, \eta_{\mathrm{k}}\,. \tag{2.54}$$

The electrochemical potential means a quasi-Fermi energy of electron (E_{Fn}) and a quasi-Fermi energy of hole (E_{Fp}), which describes the occupation of states in the conduction band or the valence band. Hence, they can be described as

$$\eta_{\mathrm{e}} = E_{\mathrm{Fn}} \text{ and } \eta_{\mathrm{h}} = -E_{\mathrm{Fp}}\,, \tag{2.55}$$

z_{e} of −1 is for the charge current of electrons in all cases. Therefore, the charge current of electrons is given by

$$j_e = \frac{\sigma_e}{q}\text{grad}\,\eta_e = \frac{\sigma_e}{q}\text{grad}\,E_{Fn}\,. \tag{2.56}$$

z_e of 1 is for the charge current of holes in all cases. Therefore, the charge current of holes is given by

$$j_h = -\frac{\sigma_h}{q}\text{grad}\,\eta_h = \frac{\sigma_h}{q}\text{grad}\,E_{Fp}. \tag{2.57}$$

Eqs. (2.56) and (2.57) describe the only actual charge currents of electrons and holes in semiconductors in a steady state. In the c-Si solar cells with carrier-selective passivating contact layers for n-type and p-type, the V_{oc} is defined as an energy difference between E_{Fn} and E_{Fp}. Therefore, to obtain high V_{oc}, the energy drop must be mitigated. As described in Eqs. (2.56) and (2.57), the energy drop can be mitigated by increasing conductivity and reducing one type of carrier concentration for each carrier type.

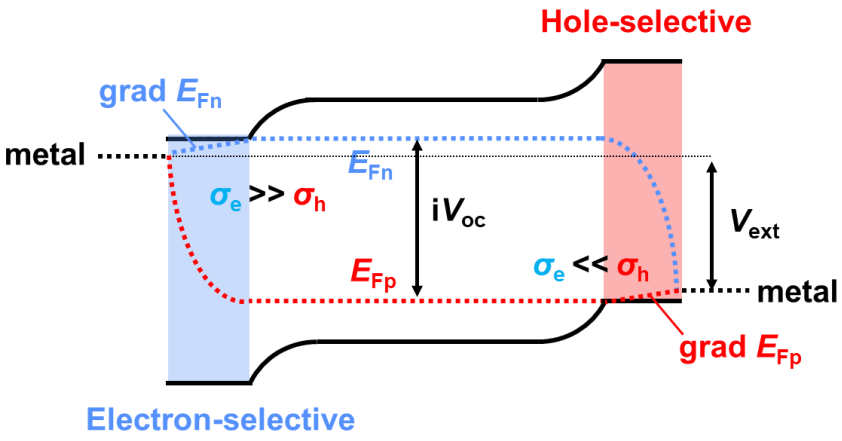

Fig. 2.1 Band diagram of the c-Si solar cell with carrier-selective contacts under open-circuit conditions.

2.2.3 Carrier selectivity

Here, the definition of carrier selectivity is explained by referring to [12]. As described above, the carrier-selective contacts enable one polarity of charge carriers to pass to the metal electrode through the carrier-selective layers and to block the other polarity of carriers. Hence, the carrier selectivity is related to the resistance to each charge carrier. The resistance for minority carriers can be described as

$$\rho_{\mathrm{m}} = \frac{V}{qR(V)}. \tag{2.58}$$

Where $R(V)$ is the recombination rate, V is the internal quasi-Fermi level splitting at the contact. The resistance for the majority carriers can be described as

$$\rho_{\mathrm{M}} = \rho_{\mathrm{c}}. \tag{2.59}$$

Where ρ_{c} is the contact resistivity. Thus, the ratio of the resistance is given by

$$\frac{\rho_{\mathrm{m}}}{\rho_{\mathrm{M}}} = \frac{V}{qR(V)\rho_{\mathrm{c}}} = S(V)\, g(V). \tag{2.60}$$

$S(V)$ is the selectivity of contact, which is given by

$$S(V) = \frac{V_{\mathrm{th}}}{\rho_{\mathrm{c}}\left[\dfrac{qR(V)}{\exp\left(\dfrac{V}{V_{\mathrm{th}}}\right) - 1}\right]}. \tag{2.61}$$

Where V_{th} is the thermal voltage. $g(V)$ is the voltage-dependent factor, which is given by

$$g(V) = \frac{V}{V_{\mathrm{th}}\left[\exp\left(\dfrac{V}{V_{\mathrm{th}}}\right) - 1\right]}. \tag{2.62}$$

The selectivity factor is defined as a logarithmically scaled selectivity as follows.

$$S_{10}(V) = \log_{10}[S(V)] \tag{2.63}$$

As described below, the recombination rate of the contact can be expressed as an ideal Shockley diode equation.

$$R(V) = \frac{J_0}{q}\left[\exp\left(\frac{V}{V_{\mathrm{th}}} - 1\right)\right] \tag{2.64}$$

Where J_0 is the emitter saturation current density as a recombination current density parameter. The ideality factor is one even if Auger recombination dominates due to a highly doped surface region in low injection. The ρ_c is often independent of voltage. Therefore, selectivity can be expressed as

$$S = \frac{V_{\mathrm{th}}}{\rho_{\mathrm{c}} J_0}. \tag{2.65}$$

Hence, the selectivity of the S_{10} value can be described as

$$S_{10} = \log_{10}\left(\frac{V_{\mathrm{th}}}{\rho_{\mathrm{c}} J_0}\right), \tag{2.66}$$

for the electron-selective contact,

$$S_{10,\mathrm{e}} = \log_{10}\left(\frac{V_{\mathrm{th}}}{\rho_{\mathrm{c,e}} J_{0,\mathrm{e}}}\right), \tag{2.67}$$

for the hole-selective contact,

$$S_{10,\mathrm{h}} = \log_{10}\left(\frac{V_{\mathrm{th}}}{\rho_{\mathrm{c,h}} J_{0,\mathrm{h}}}\right). \tag{2.68}$$

2.2.4 Passivating contact materials and structures

Therefore, to obtain excellent carrier selectivity, conductivity for only one polarity type must be increased for one side. The band alignments between Si and the carrier-selective materials should be carefully considered. Hence, the band offsets and work functions of the materials with c-Si are engineered to achieve excellent carrier selectivity. The band offsets and work functions depend on the material itself, but the composition and structure of each material affect their properties. Figure 2.2 shows the band diagrams of Si surfaces with several types of carrier-selective contacts for the n-type c-Si under open-circuit conditions. Type 1 indicates that hole-selective contact as a p^+ doping layer is introduced by a boron (B) diffusion layer on the Si surface. Type 2 indicates that an external potential source, such as a deposited layer with negative fixed charges, modifies the hole-selective contacts. For instance, the highly negatively charged Al_2O_3 layer demonstrated a lower sheet resistance and a possibility of usage as a p^+ emitter for the n-type c-Si solar cells [15]. Type 3 indicates the hole-selective contacts formed by a heterojunction with a wide-bandgap material, realizing a suitable Fermi level alignment with c-Si and blocking electrons by the large conduction band edge. Type 4 indicates the hole-selective contact by the surface band bending induced by a heavily doped p-type semiconductor such as B-doped amorphous Si (p-a-Si). This type of structure is conventionally used for SHJ solar cells. Type 5 indicates the hole-selective contact by increased hole concentration at the c-Si surface induced by the work function difference between materials such as MoO_3, V_2O_5, and WO_3 [16]. Type 6 indicates electron-selective contact by increased electron concentration at the c-Si surface induced by the high phosphorus (P)-doped poly c-Si and an insertion of the tunnel SiO_2 layer, which has a large valence band offset. This type of carrier-selective contact includes TOPCon.

As described above, many types of carrier-selective contact structures exist, but in this research, the external charge-induced carrier-selective contact (type 2) was used. Because it does not require the dopants and the diffusion process using high-temperature annealing in a specific gas atmosphere such as $POCl_3$ and BBr_3. In addition, as described in Eq. (2.34), surface hole density is proportional to squared surface charge. Hence, increasing the surface charge density can significantly increase hole selectivity. Additionally, as described in Eq. (2.35), since the S_{eff} is inversely proportional to the surface charge density, the surface passivation quality can be significantly improved. Importantly, as described in Eq. (2.35), the surface charge density significantly affects S_{eff} compared with the N_{it}. Hence, the field-effect passivation would be a relatively significant solution compared with a chemical passivation to reduce S_{eff}. The reported carrier-selective contacts of the J_0 and ρ_c are plotted in Figure 2.3 with S_{10} values [17–29]. There has been developed a lot of carrier-selective contacts but the example of the external charge-induced carrier-selective contact is few.

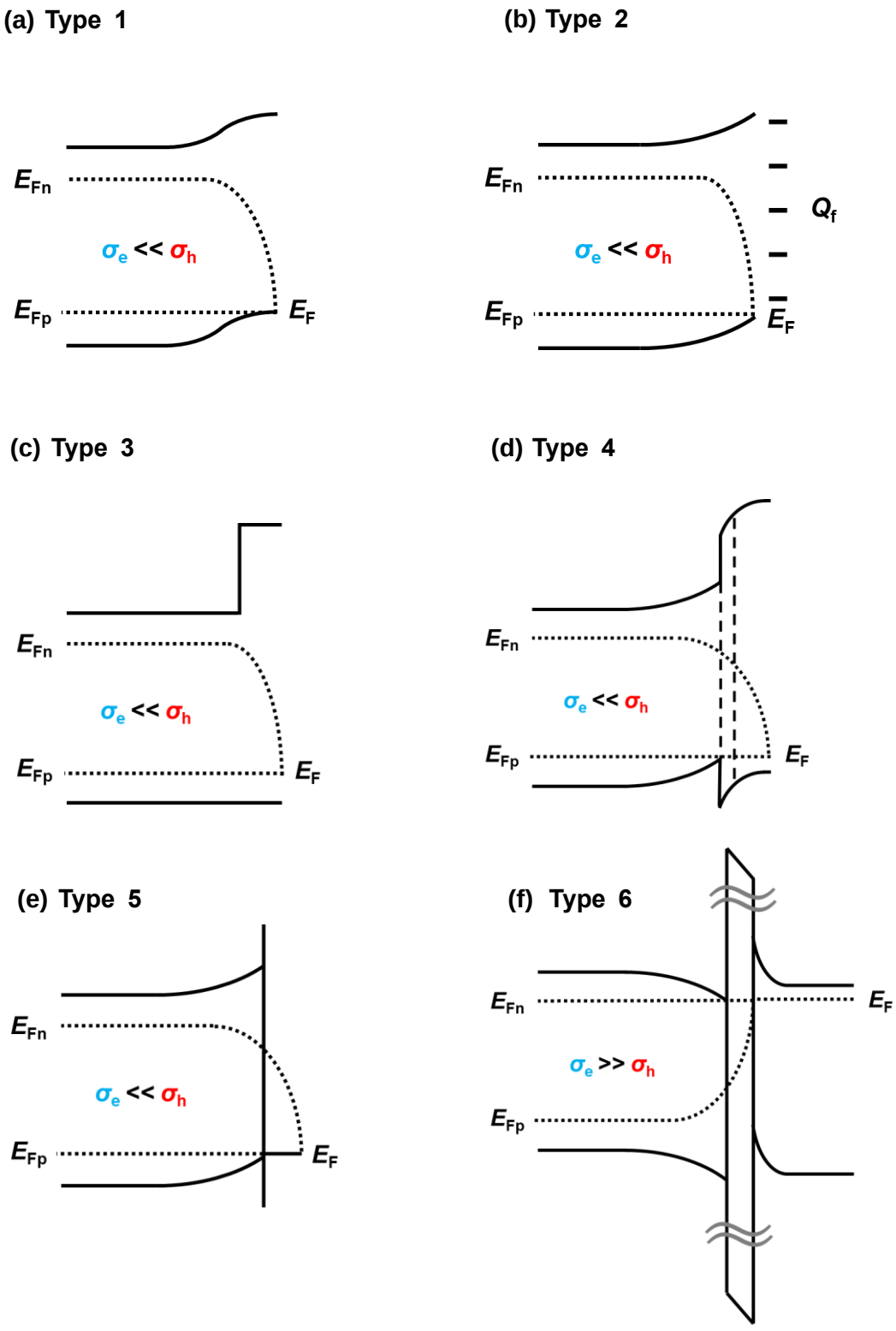

Fig. 2.2 Band diagrams of the c-Si solar cell with several types of carrier-selective contacts under open-circuit conditions.

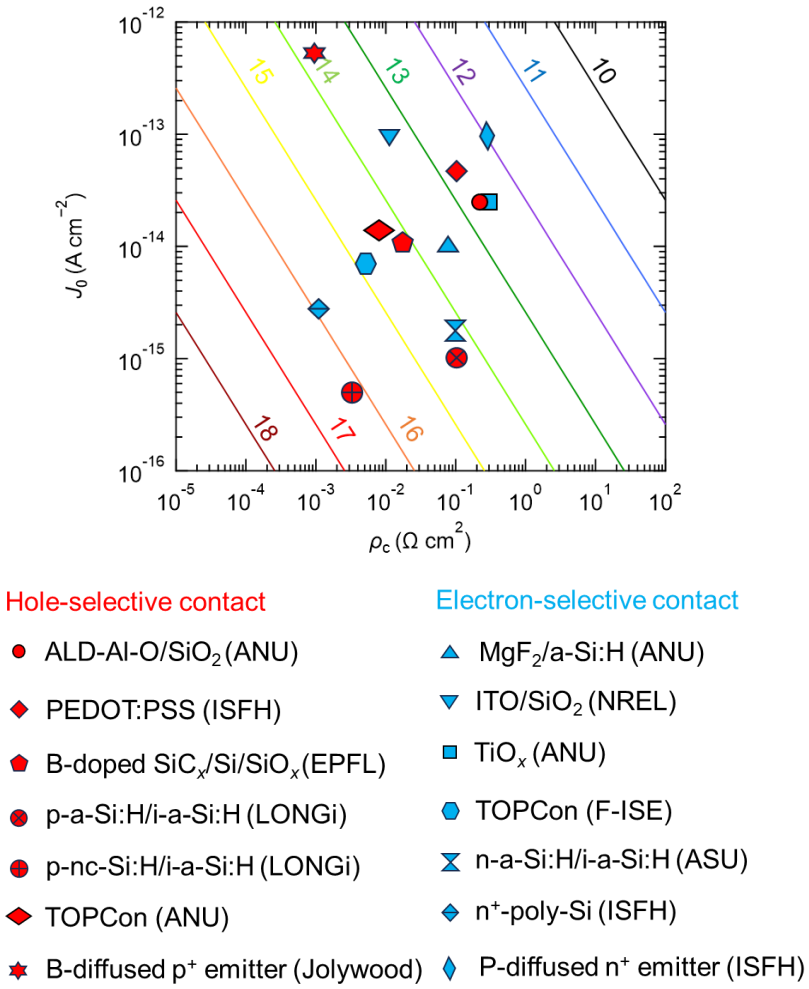

Fig. 2.3 Carrier selectivity for the reported carrier-selective contacts.

2.3 Summary

Since surface recombination significantly affects the solar cell performance, the surface recombination must be mitigated by surface passivation. One of the critical solutions to access the theoretical limit of c-Si solar cells is carrier-selective passivating contacts. The carrier population control enables the reduction of surface recombination and the increase of conductivity for one type of carrier. There are many types and materials of carrier-selective passivating contacts, but the surface charge-induced type is highly expected to be the best choice because of the significant effect on surface recombination according to the simplified SRH formalism.

References

[1] T. Trupke, M. A. Green, P. Wurfel, P. P. Altermatt, A. Wang, J. Zhao, and R. Corkish, "Temperature dependence of the radiative recombination coefficient of intrinsic crystalline silicon," J. Appl. Phys. **94**, 4930 (2003).

[2] M. J. Kerr and A. Cuevas, "General parameterization of Auger recombination in crystalline silicon," J. Appl. Phys. **91**, 2473 (2002).

[3] A. Richter, S. W. Glunz, F. Werner, J. Schmidt, and A. Cuevas, "Improved quantitative description of Auger recombination in crystalline silicon," Phys. Rev. B **86**, 165202, (2012).

[4] W. Shockley and W. T. Read Jr., "Statistics of the recombinations of holes and electrons," Phys. Rev. **87**, 835 (1952).

[5] R. Hall, "Electron-Hole Recombination in Germanium," Phys. Rev. **87**, 387 (1952).

[6] A. S. Grove and D. J. Fitzgerald, "Surface effects on p-n junctions: Characteristics of surface space-charge regions under non-equilibrium conditions," Solid. State. Electron. **9**, 783 (1966).

[7] D. J. Fitzgerald and A. S. Grove, "Surface recombination in semiconductors," IEEE Trans. Electron Devices **15**, 426 (1968).

[8] K. R. McIntosh and L. E. Black, "On effective surface recombination parameters," J. Appl. Phys. **116**, 014503 (2014).

[9] P. Saint-Cast, E. Billot, P. Olwal, S. Kühnhold, A. Richter, M. Hofmann, J. Rentsch, and R. Preu, "Surface passivation of highly and lowly doped p-type silicon surfaces with PECVD Al_2O_3 for industrially applicable solar cell concepts," In: Proceedings of the 26th European PV Solar Energy Conference and Exhibition, Hamburg, Germany, pp. 1125–1128 (2011).

[10] A.G. Aberle, S.W. Glunz, A.W. Stephens, and M.A. Green, "High efficiency silicon solar cells: Si/SiO_2 interface parameters and their impact on device performance," Prog. Photovolt. **2**, 265 (1994).

[11] L. E. Black, "New perspectives on surface passivation: Understanding the $Si–Al_2O_3$ interface," Ph.D. thesis, Australian National University (2015).

[12] J. Schmidt, R. Peibst, and R. Brendel, "Surface passivation of crystalline silicon solar cells: Present and future," Sol. Energy Matter. Sol. Cells **187**, 39 (2018).

[13] H. Lin, M. Yang, X. Ru, G. Wang, S. Yin, F. Peng, C. Hong, M. Qu, J. Lu, L. Fang, C. Han, P. Procel, O. Isabella, P. Gao, Z. Li, and Xi. Xu, "Silicon heterojunction solar cells with up to 26.81% efficiency achieved by electrically optimized nanocrystalline-silicon hole contact layers," Nat. Energy **8**, 789 (2023).

[14] U. Wurfel, A. Cuevas, and P. Wurfel, "Charge carrier separation in solar cells," IEEE J. Photovolt. **5**, 461 (2014).

[15] D. Choi and K. Seo, "Field-induced radial junction for dopant-free crystalline silicon microwire solar cells with an efficiency of over 20%," Adv. Energy Mater. **11**, 2003707 (2021).

[16] L. G. Gerling, S. Mahato, C. Voz, R. Alcubilla, and J. Puigdollers, "Characterization of transition metal oxide/silicon heterojunctions for solar cell applications," Appl. Sci. **5**, 695, (2015).

[17] D. Hiller, P. Hönicke, and D. König, "Material combination of tunnel-SiO_2 with a (sub-)monolayer of ALD-AlO_x on silicon offering a highly passivating hole selective contact," Sol. Energy Mater. Sol. Cells **215**, 110654 (2020).

[18] R. Gogolin, D. Zielke, W. Lövenich, R. Sauer, and J. Schmidt, "Silicon Heterojunction Solar Cells Combining an a-Si:H (n) Electron-collector with a PEDOT:PSS Hole-collector," Energy Procedia **92**, 638 (2016).

[19] G. Nogay, J. Stuckelberger, P. Wyss, E. Rucavado, C. Allebéb, T. Koida, M. Morales-Masisa, M. Despeisse, F.-J. Haug, P. Löper, and C. Ballif, "Interplay of annealing temperature and doping in hole selective rear contacts based on silicon-rich silicon-carbide thin films," Sol. Energy Mater. Sol. Cells **173**, 18 (2017).

[20] H. Lin, M. Yang, X. Ru, G. Wang, S. Yin, F. Peng, C. Hong, M. Qu, J. Lu, L. Fang, C. Han, P. Procel, O. Isabella, P. Gao, Z. Li, and Xi. Xu, "Silicon heterojunction solar cells with up to 26.81% efficiency achieved by electrically optimized nanocrystalline-silicon hole contact layers," Nat. Energy **8**, 789 (2023).

[21] J. Bao, C. Chen, L. Ma, C. Huang, X. Zhang, Z. Wang, C. Chen, S. Zhan, R. Liu, Z. Qiao, Z. Du, Z. Liu, and J. Chen, "Towards 24% efficiency for industrial n-type bifacial passivating-contact solar cells with homogeneous emitter," In: Proceedings of the 37th European Photovoltaic Solar Energy Conference and Exhibition, online, pp. 160–164 (2020).

[22] D. Yan, A. Cuevas, Y. Wan, and J. Bullock, "Passivating contacts for silicon solar cells based on boron-diffused recrystallized amorphous silicon and thin dielectric interlayers," Sol. Energy Mater. Sol. Cells **152**, 73 (2016).

[23] Y. Wan, C. Samundsett, J. Bullock, T. Allen, M. Hettick, D. Yan, P. Zheng, X. Zhang, J. Cui, J. McKeon, A. Javey, and A. Cuevas, "Magnesium fluoride electron-selective contacts for crystalline silicon solar cells," ACS Appl. Mater. Interfaces **8**, 14671 (2016).

[24] D. L. Young, W. Nemeth, S. Grover, A. Norman, B. G. Lee, and P. Stradins, "Carrier-selective, passivated contacts for high efficiency silicon solar cells based on transparent conducting oxides," Energy Procedia **55**, 733 (2014).

[25] X. Yang, P. Zheng, Q. Bi, and K. Weber, "Silicon heterojunction solar cells with electron selective TiO_x contact," Sol. Energy Mater. Sol. Cells **150**, 32 (2016).

[26] S. W. Glunz, F. Feldmann, A. Richter, M. Bivour, C. Reichel, H. Steinkemper, J. Benick, and M. Hermle, "The irresistible charm of a simple current flow pattern–25% with a solar cell featuring a full-area back contact," In: Proceedings of the 31st European Photovoltaic Solar Energy Conference and Exhibition, Hamburg, Germany, pp. 259–263 (2015).

[27] S. Y. Herasimenka, W. J. Dauksher, and S. G. Bowden, ">750 mV open circuit voltage measured on 50 µm thick silicon heterojunction solar cell," Appl. Phys. Lett. **103**, 053511 (2013).

[28] M. Rienäcker, M. Bossmeyer, A. Merkle, U. Römer, F. Haase, J. Krügener, R. Brendel, and R. Peibst, "Junction resistivity of carrier-selective polysilicon on oxide junctions and its impact on solar cell performance," IEEE J. Photovolt. **7**, 11 (2017).

[29] R. Brendel and R. Peibst, "Contact selectivity and efficiency in crystalline silicon photovoltaics," IEEE J. Photovolt. **6**, 1413-1420 (2016).

CHAPTER 3

CHARACTERIZATION TECHNIQUES

3.1 Carrier lifetime measurements

The carrier lifetime can be determined by measuring the photoconductance of the semiconductor. The photoconductance can be analyzed by measuring the eddy current generated in an inductively coupled coil or the reflectance of microwaves. Hence, the quasi-steady state photoconductance (QSSPC) method and the microwave photoconductivity decay (μ-PCD) method have been widely used for Si-based devices.

3.1.1 Quasi-steady state photoconductance (QSSPC)

The quasi-steady state photoconductance (QSSPC) method was first proposed by Sinton and Cuevas [1], which has been widely used to evaluate the carrier lifetime of c-Si solar cells. This technique can obtain the Δn by analyzing the conductivity of the light-illuminated sample through an inductively coupled coil. This method allows us to obtain injection-dependent carrier lifetimes because the excitation intensity gradually decays over time using a Xenon flash lamp. The short wavelength light must be cut using a long pass filter as a homogeneous generation must occur in the entire wafer. The gradual decay of the Δn over time can be described as

$$\frac{d\Delta n(t)}{dt} = G(t) - U(t)\,. \tag{3.1}$$

Where $G(t)$ is the generation rate at the time of t, and $U(t)$ is the recombination rate at the time of t. By substituting the relationship between the recombination rate and the effective lifetime described as

$$U = \frac{\Delta n}{\tau_{\text{eff}}}. \tag{3.2}$$

The effective lifetime as a generalized analysis [2] can be determined by

$$\tau_{\text{eff}} = \frac{\Delta n}{G(t) - \frac{d\Delta n(t)}{dt}}. \tag{3.3}$$

The generation rate (G) can be analyzed by the photocurrent of a reference solar cell, which is mounted in the equipment near the sample on the sample stage. In addition, the sample's optical property must be considered an optical factor (*OF*). It is a ratio of optical properties between a sample and a reference cell. In this study, the *OF*s were determined by the calculated photon current densities from the absorbance spectra. For the flat Si substrates, the *OF* should be 0.7, but the wafer with surface roughness or ARC must apply suitable *OF* values for each case. The generation rate at the time of t can be described as

$$G(t) = OF\,\frac{I_{\text{ref}}(t)}{qW_{\text{ref}}}. \tag{3.4}$$

Where $I_{\text{ref}}(t)$ is the photocurrent of a reference solar cell at the time of t, and W_{ref} is the wafer thickness of the reference cell. The injection level can be determined from the equation below.

$$\Delta n(t) = \frac{\Delta\sigma(t)}{q(\mu_{\text{n}} + \mu_{\text{p}})W} \tag{3.5}$$

Where $\Delta\sigma$ is the measured excess conductivity in the sample, μ_{n} and μ_{p} are the electron and hole mobilities, and W is the wafer thickness.

At last, the effective lifetime can be calculated using Eq. (3.3). In addition, implied open-circuit

voltage (iV_{oc}) can be determined at each illumination intensity using the equation below.

$$iV_{oc} = \frac{k_B T}{q} \ln\left[\frac{(N_{dop} + \Delta n)\Delta n}{{n_i}^2}\right] \tag{3.6}$$

Where k_B is the Boltzmann constant, T is the absolute temperature, N_{dop} is the doping concentration, and n_i is the intrinsic carrier density. Moreover, the J_0 can be derived from the below equation of the Kane and Swanson method [3] using the auger-corrected effective minority carrier lifetime (τ_{corr}) over the high injection level.

$$\frac{1}{\tau_{eff}} = \frac{1}{\tau_{bulk}} + \frac{2J_0(N_{dop} + \Delta n)}{q{n_i}^2 W}. \tag{3.7}$$

At high injection levels, since the bulk lifetime dominates the Auger lifetime, the equation can be described as

$$\frac{1}{\tau_{eff}} = \frac{1}{\tau_{Auger}} + \frac{2J_0(N_{dop} + \Delta n)}{q{n_i}^2 W}. \tag{3.8}$$

Hence, J_0 can be derived from the slope in the relation between τ_{corr} and injection level. The schematic illustration of the lifetime tester equipment is illustrated in Figure 3.1. In this work, Sinton lifetime tester WCT-120 was used for τ_{eff} and iV_{oc} analysis.

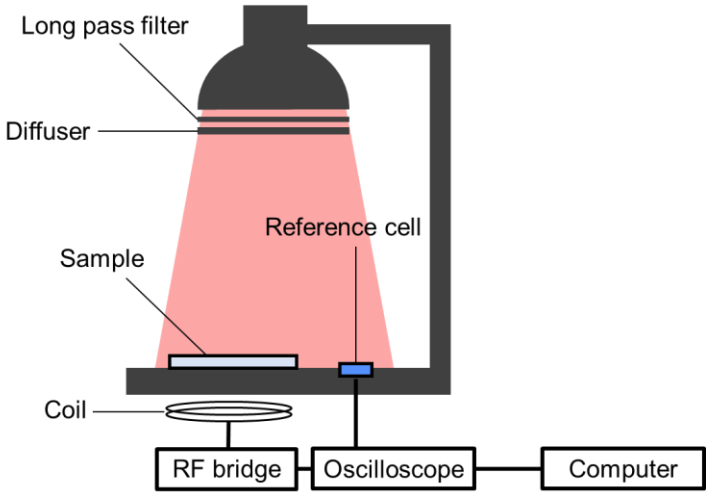

Fig. 3.1 Schematic illustration of setup for the QSSPC measurements.

3.1.2 Microwave photoconductivity decay (μ-PCD)

The microwave photoconductivity decay (μ-PCD) utilizes pulsed laser (~200 ns) light for the excitation of carriers in the substrate. The photoconductivity is indirectly analyzed by detecting microwave reflection. The excited carriers increase the conductivity of the material, and the photoconductivity increases microwave reflection. Hence, by detecting the decay of the microwave reflection over time, an effective minority carrier lifetime (τ_{eff}) can be derived from the decay of excess carriers [4]. In general, the carrier lifetime can be defined as the time constant at 1/e of the maximum microwave intensity just after being irradiated by the pulsed laser light. In this experiment, a wavelength of 904 nm was used for the excitation by pulsed laser light. Since the system is applied pulsed laser excitation, the μ-PCD method cannot measure Δn dependence on the τ_{eff}. Since the usual areal photon density is 5×10^{13} cm^{-2}, assuming a homogeneous generation in the entire substrate with a thickness of 280 μm, the instant Δn would be 1.2×10^{15} cm^{-3}. Hence, this method has a transient feature: the generation rate (G) equals zero. Therefore, Eq. (3.3) can be described as

$$\tau_{\text{eff}} = \frac{\Delta n}{-\frac{d\Delta n(t)}{dt}}. \tag{3.9}$$

The deferential Δn has a solution of $\Delta n = A \exp(-t/\tau_{eff})$. The τ_{eff} can be derived from the fitting of the single exponential curves. Additionally, the unique important feature of this method is measurable τ_{eff} mappings. The excitation area is ~1 mm^2, and the movable sample stage allows us to obtain τ_{eff} mappings. The τ_{eff} mapping can display the distribution within the sample area, allowing us to evaluate the evenness of surface passivation quality of semiconductor materials. This research used Kobelco Research Institute, Inc., LTA-1510EP to acquire τ_{eff} mappings by μ-PCD method. In this equipment, the wavelength of 349 nm is also mounted with variable laser light intensity in the range of 5×10^{12} –1.1×10^{15} cm^{-2}. This research used this option to acquire the pulsed laser light intensity dependence on the τ_{eff}. However, since the Si material has a large absorption coefficient of light with a wavelength of 349 nm (~1×10^6 cm^{-1}), such a short wavelength of light is absorbed in the surface of Si substrates. Thus, homogeneous generation cannot be realized, but the bulk quality of the material is exceptionally high enough compared to the surface. This method can also evaluate the surface passivation quality. However, the carrier generation almost occurred in the space charge region. The minority carrier density is relatively higher than the long wavelength laser excitation, which might result in lower τ_{eff}. Moreover, steady-state light can be illuminated during the measurement as a bias light in this system. In this

research, the transient lifetime was also evaluated under the bias light illumination, varying the bias light intensity in the range of 0.025–1.2 suns. In general, if the band bending exists at the surface of the material, the band bending is reduced by the light illumination due to the increase of Δn in the space charge region. If the surface passivation is dominated by field-effect passivation, the surface passivation quality would be gradually decreased with increasing the steady-state light. Hence, this research utilizes this method to elucidate the surface passivation scheme.

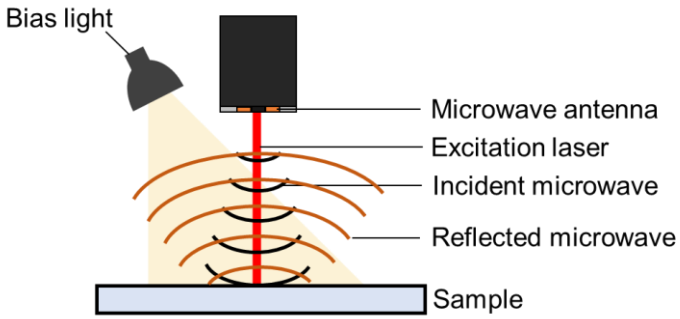

Fig. 3.2 Schematic illustration of setup for the μ-PCD measurements.

3.2 X-ray photoelectron spectroscopy (XPS)

Principle

X-ray photoelectron spectroscopy provides information about the chemical bond states, the atomic composition at the surface of materials, and the thickness of the ultrathin layer on the substrates. When the X-ray hits the surface of materials, the generated photoelectrons are emitted from the surface with kinetic energies corresponding to each material and chemical bond states. The relation between the kinetic energy and the binding energy of the chemical bond states is described as

$$E_k = hv - E_b - \Phi. \tag{3.10}$$

Where E_k is the kinetic energy of photoelectrons, hv is the X-ray energy, E_b is the binding energy of the chemical bond states, and Φ is the spectrometer work function. Since the hv and Φ are known values, if E_k is measured, E_b can be determined. In the XPS measurement, E_k and the intensity are acquired simultaneously. Concretely, the intensity is defined as the detected number of photoelectrons with each E_k. Hence, XPS measurement acquires the spectrum as a function of the binding energy. The intensity peaks are shifted to higher or lower binding energy. The

chemical shift allows us to know the information about the chemical bond states. For instance, in the case of the SiO_2/Si interface, the SiO_2 thin layer does not entirely consist of "SiO_2". Usually, SiO_2 consists of four chemical bond states such as Si^{1+}, Si^{2+}, Si^{3+}, and Si^{4+}(SiO_2). With increasing the amount of bonded oxygen, the silicon oxide peak can be observed at the higher binding energy. According to the literature [5], the relative binding energies to the Si^0 (the bulk of Si) for each chemical bond state are 0.95, 1.75, 2.48, and 3.90 eV, respectively. The components of Si^{1+}, Si^{2+}, and Si^{3+} are known as sub-oxides, which are lower-quality SiO_2. Therefore, the film quality can be evaluated by analyzing the sub-oxides and SiO_2 components. Thus, high-resolution analysis is essential to evaluate such chemical shifts. This work used Al Kα (hv = 1486.6 eV) as an X-ray source to generate photoelectrons. For the detection of photoelectrons, they were collected from a normal angle; in other words, detected photoelectrons perpendicularly emitted from the surface by setting a take-off angle of 90°. The reason for detectable photoelectrons from less than ~10 nm depth is due to the decay of photoelectrons by the inelastic scattering in the surface of materials. Hence, the XPS measurement allows us to do very surface-sensitive analysis and has a massive advantage for the ultrathin layer, like an Al-doped SiO_x layer formed in this study. The hemispherical analyzer enables us to obtain high-resolution binding energies. However, during the measurement on the insulator surface, the charge-up occurs at the X-ray irradiated surface, leading to an unexpected shift to the higher binding energy. Therefore, the peaks must be calibrated to evaluate the chemical shifts accurately. In general, all acquired peaks are calibrated by the acquired C 1s peak positions. However, in this research, the chemical shift concerning the Si^0 is not crucial. Hence, the peaks of Si^0 were fixed to the reference value of 99.2 eV [6]. The schematics of the XPS system (Shimadzu Corporation, Kratos AXIS-ULTRA DLD) used in this study are shown in Figure 3.3.

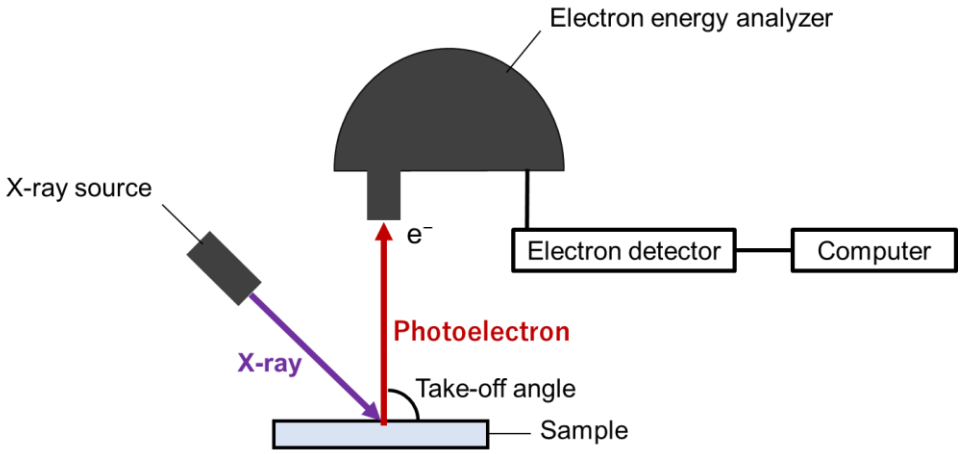

Fig. 3.3 Schematic illustration of XPS measurements.

Evaluation of the surface atomic concentration

The surface atomic composition can also be obtained by XPS analysis. In this study, I acquired all core-level spectra of each atom, Si 2*p*, O 1*s*, and Al 2*p*. To evaluate the atomic concentration of the layer, the areas of peak fitted intensities for each atom are applied to the equation below [7],

$$X_{\mathrm{i}} = \frac{\left(\frac{I_{\mathrm{i}}}{RSF_{\mathrm{i}}}\right)}{\sum_{\mathrm{j=1}}^{\mathrm{n}}\left(\frac{I_{\mathrm{j}}}{RSF_{\mathrm{j}}}\right)}. \tag{3.11}$$

Where I_{i} is the area of intensity for the specific atom, RSF_{i} is the relative sensitivity factor for the specific atom, I_{j} is the area of intensity for each atom, and RSF_{j} is the relative sensitivity factor for each atom. The *RSF* of 0.283 for Si 2*p* [8], 0.711 for O 1*s* [8], and 0.193 for Al 2*p* [8] were applied to evaluate the surface atomic concentration of oxidized Al and oxidized Si. Each area of intensity can be derived from the peak-fitted spectra by subtracting the background using the Shirley–Proctor–Sherwood method [9, 10] and peak fitting using the Voigt function.

Evaluation of the SiO_x thickness

The SiO_x thickness can be evaluated from the area of intensity for Si^0 (I_{Si}) and the sum of the area of intensity for the components of $I_{\mathrm{SiO_2}}$ using the equation below [5],

$$d = l_{\mathrm{SiO_2}} \ln\left(\frac{I_{\mathrm{SiO_2}}}{I_{\mathrm{Si}}}\frac{n_{\mathrm{Si}}\sigma_{\mathrm{Si}}l_{\mathrm{Si}}}{n_{\mathrm{SiO_2}}\sigma_{\mathrm{SiO_2}}l_{\mathrm{SiO_2}}}\right). \tag{3.12}$$

Where σ_{Si} and $\sigma_{\mathrm{SiO_2}}$ are the photoionization cross sections, n_{Si} and $n_{\mathrm{SiO_2}}$ are the density of Si atoms, l_{Si} and $l_{\mathrm{SiO_2}}$ are the escape depths for Si and SiO_2, respectively. n_{Si} of 5.00×10^{22} cm^{-3}, $n_{\mathrm{SiO_2}}$ of 2.28×10^{22} cm^{-3}, l_{Si} of 2.7 nm [11], $l_{\mathrm{SiO_2}}$ of 3.7 nm [11], and the ratio of the photoionization ($\sigma_{\mathrm{SiO_2}}/\sigma_{\mathrm{Si}}$) of 1.1 [12] were used in this research.

3.3 Current–voltage (*I–V*) measurement

Current and voltage measurement (*I–V*) is the method to characterize the relationship of current and voltage, which are applied between the top and bottom metal electrodes on the device structure, such as solar cells, and the more fundamental structure of metal oxide semiconductor (MOS). While sweeping the bias voltage, the current is measured. In this study, I used a precision semiconductor parameter analyzer (Hewlett-Packard Company, 4156 A) mounted with a kelvin type four-terminal connection system and acquired dark *I–V* characteristics for MOS structure. The current densities were calculated by the measured current values divided by the top electrode area.

Tunneling current density

Then, the calculated dark current density on the MOS structure is defined as a tunneling current density in this work. When the negative bias voltage is applied on top of the electrode, the n-type Si band is bent upward, and an inversion layer is created. Hence, the hole current is dominant as a tunneling current through the oxide layer at the inversion condition. On the other hand, when a positive bias voltage is applied on top of the electrode, the n-type Si band is bent downward, and the electrons are accumulated at the Si surface. Thus, the electron current dominates as a tunneling current through the oxide layer at the accumulation condition. As considered in this theorem, the tunneling current density should be evaluated for the hole tunneling current density under applying the negative bias voltage. Hence, in this study, I acquired a current density at the inversion condition to evaluate the hole tunneling current density. The depiction of the MOS structure and the band structures at each voltage-applied condition is depicted in Figure 3.4. In this configuration, a similar work function material should be selected as a top electrode to the electron affinity of n-type Si to avoid creating a Schottky diode by the work function difference. Thus, in this work, Al was used for the top electrode with a work function of 4.28 eV [13].

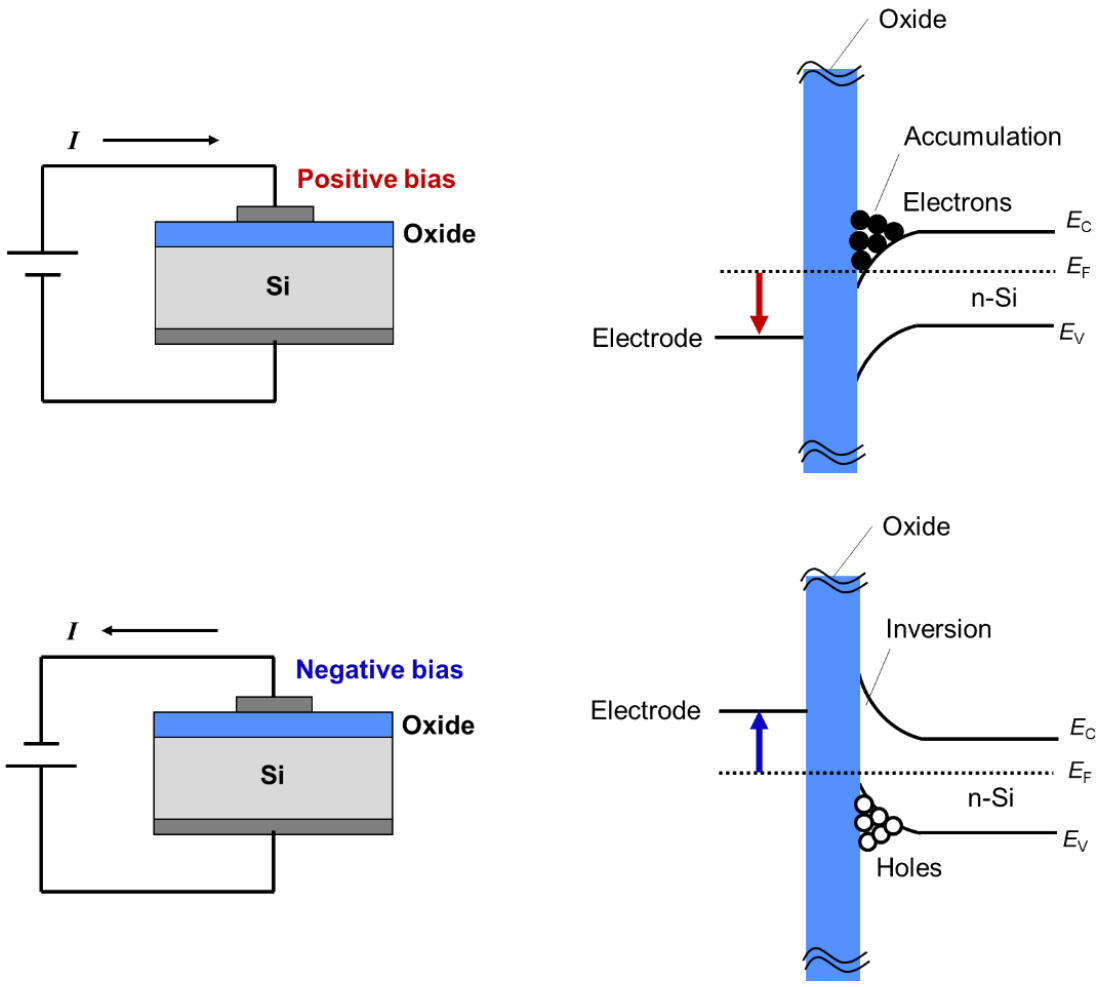

Fig. 3.4 Depiction of the MOS and band structures when positive and negative bias are applied.

Characteristics of solar cell performance

I–V measurements can also evaluate the solar cell performance. The device structure must be fabricated with a finger or grid electrode and the bottom electrode on a Si substrate with a p-n junction. The test is performed by measuring the *I–V* characteristics under 1 sun illumination. The measurement must undergo a short-circuit condition (at zero bias), open-circuit condition (at zero current), and between these bias conditions to determine the short-circuit current density (J_{sc}), V_{oc}, and maximum power point (P_{max}) to derive fill factor (FF), and η. The typical photo *J–V* curve is shown in Figure 3.5 with J_{sc}, V_{oc}, and maximum power point (P_{max}).

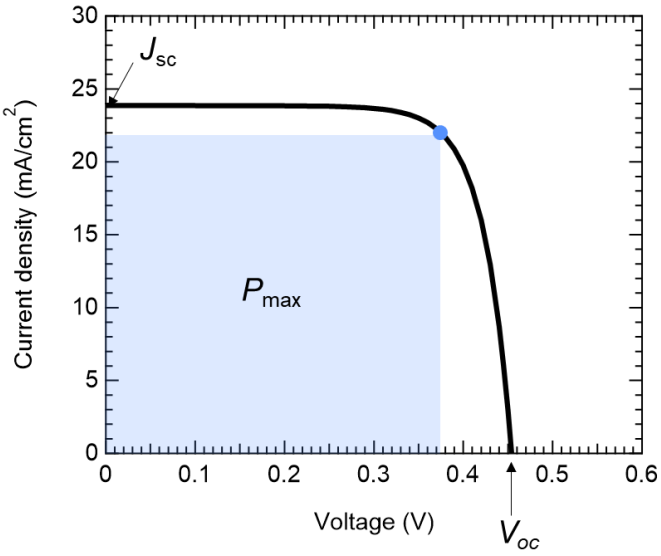

Fig. 3.5 Typical photo *J–V* curve with J_{sc}, V_{oc}, and P_{max}.

Also, the formula to evaluate the FF and the η are described as

$$FF = \frac{P_{\max}}{J_{\mathrm{sc}}\, V_{\mathrm{oc}}}, \tag{3.13}$$

$$\eta = \frac{P_{\max}}{P_{\mathrm{input}}} = \frac{J_{\mathrm{sc}}\, V_{\mathrm{oc}}\, \mathrm{FF}}{P_{\mathrm{input}}}. \tag{3.14}$$

Contact resistivity (Cox and Strack analysis) [14]

The total resistance (R_{total}) can be described as the sum of the spreading resistance (R_{spread}), the contact resistance (R_c), and the residual resistance due to a substrate or the contact resistance of the back side contact (R_0).

$$R_{\text{total}} = R_{\text{spread}} + R_{\text{c}} + R_0 \tag{3.15}$$

By using ρ_c, R_c can be described as

$$R_{\text{c}} = \frac{\rho_{\text{c}}}{\frac{1}{4}\pi d^2} = \frac{\rho_{\text{c}}}{A}. \tag{3.16}$$

Where d is the diameter of the circular electrode, and A is the area of the electrode. Hence, the ρ_c can be derived from the slope of the ($R_{total} - R_{spread}$) as a function of the inverse area of the electrode.

$$R_{\text{total}} - R_{\text{spread}} = \frac{\rho_{\text{c}}}{A} + R_0 \tag{3.17}$$

The R_{spread} is determined from the below equation.

$$R_{\text{spread}} = \frac{\rho}{2d} B \tag{3.18}$$

$$B \approx \frac{2}{\pi} \arctan\left(\frac{4t}{d}\right) \tag{3.19}$$

Where B is the geometrical factor, which corrects for the finite thickness of the substrate, ρ is the substrate resistivity, and t is the substrate thickness. This analysis is known as the Cox and Strack method, and the Cox and Strack equation is given by

$$R_{\text{total}} = \frac{\rho}{\pi d} \arctan\left(\frac{4t}{d}\right) + \frac{\rho_{\text{c}}}{A} + R_0. \tag{3.20}$$

Hence, using this equation, the ρ_c can be analyzed from the measured *I–V* data for several sizes of electrodes. This study used 13 circular electrodes ranging from 0.28 to 32.15 mm^2.

3.4 Capacitance–voltage (*C–V*) measurement

The capacitance and voltage (*C–V*) measurement [15] acquires capacitance while sweeping the voltage applied to the MOS structure. This technique widely analyzes interface properties such as D_{it}, Q_f, d_{ox}, and ε_{ox}. The applied voltage contains an AC component, and 1 MHz was applied for this study to avoid responding to the minority carriers. To obtain the Q_f value, the flat band voltage (V_{FB}) was estimated from the flat band capacitance (C_{FB}). By using Debye length (L_D), the C_{FB} is described as

$$\frac{1}{C_{FB}} = \frac{1}{C_{ox}} + \frac{L_D}{\varepsilon_{Si}}. \tag{3.21}$$

Where C_{ox} is the oxide capacitance, the C_{ox} can be measured at an accumulation condition. The L_D is given by

$$L_D = \sqrt{\frac{\varepsilon_{Si} k_B T}{q^2 N_A}}. \tag{3.22}$$

Then, the V_{FB} was derived from the measured *C–V* curves at the voltage corresponding to the calculated C_{FB}. The Q_f value can be calculated using the equation below.

$$Q_f = \frac{C_{ox}}{qA}(\Delta\Phi_{ms} - V_{FB}) \tag{3.23}$$

$$C_{ox} = \frac{A\ \varepsilon_r\ \varepsilon_0}{d} \tag{3.24}$$

Where $\Delta\Phi_{ms}$ is the work function difference between metal and Si, A is the electrode area, and ε_r is the relative permittivity of the insulator.

Mott-Schottky plot [16]

The built-in potential (V_{bi}) of the semiconductor can be analyzed by Mott-Schottky plot analysis. The Mott-Schottky plot is the plot of inverse squared capacitance ($1/C^2$) concerning the applied voltages. The plots are extrapolated from 0 V to the interception of the horizontal axis.

Considering the relation between the $1/C^2$ and the voltage described below, the V_{bi} can be derived from the interception of the voltage axis,

$$\frac{1}{C^2} = \frac{2}{\varepsilon\varepsilon_0 A^2 q N_{dop}}\left(V - V_{bi} - \frac{k_B T}{q}\right). \tag{3.25}$$

Where ε is the relative permittivity of the material, ε_0 is the permittivity of vacuum, respectively. When $1/C^2 = 0$, the V_{bi} can be derived as

$$V_{bi} = V - \frac{k_B T}{q}. \tag{3.26}$$

Hence, V_{bi} can be obtained using the Mott-Schottky plot and some known parameters: k_B, T, and q.

3.5 Four-point probe technique

Four-point probe technique determines the sheet resistance (R_{sheet}) of the material. As shown in the schematics of the four-point probe technique in Figure 3.6, during the measurement, while a small current passes through the two outer probes, voltage is measured between the other two inner probes. Hence, the sheet resistance can be obtained from the measured voltage and the flow current. In addition, resistivity (ρ) can be described as

$$\rho = R_{sheet}\, d\,, \tag{3.27}$$

where d (cm) is the film thickness. This method can avoid the lead and contact resistance from the measurement because the probes are separated for measuring voltage and flowing current, resulting in a more precise measurement of the R_{sheet}. This research used a four-point probe technique (Mitsubishi Chemical Analytech Co., Ltd., Loresta-AX MCP-T370) in the dark and 1 sun illumination conditions.

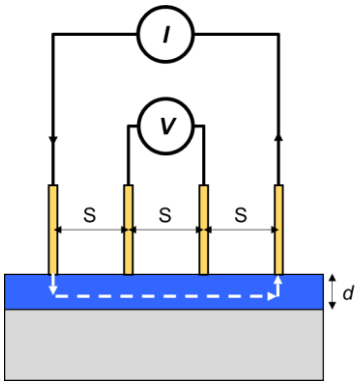

Fig. 3.6 Schematics of the principle for the four-point probe technique.

In this study, to investigate the illumination effect on the R_{sheet}, the measurements were also performed under 1 sun illumination. The experimental setup is illustrated in Figure 3.7. The samples are illuminated from the front side, and the probes are placed on the rear side of the samples to avoid the shading of probes. Considering the bulk lifetime is >10 ms, it is >10 times longer carrier diffusion length of ~0.36 cm compared with the substrate thickness of 280 μm. Hence, generated holes at the front surface can also reach the rear surface before the recombination. The diffusion length (L) can be described as $\sqrt{D\tau}$. Where D is the diffusion coefficient of carriers and τ is the carrier lifetime in the bulk. In this case, D is the diffusion coefficient for holes of 12.9 $cm^2\ s^{-1}$ [15]. Therefore, this method is available to obtain R_{sheet} under 1 sun illumination.

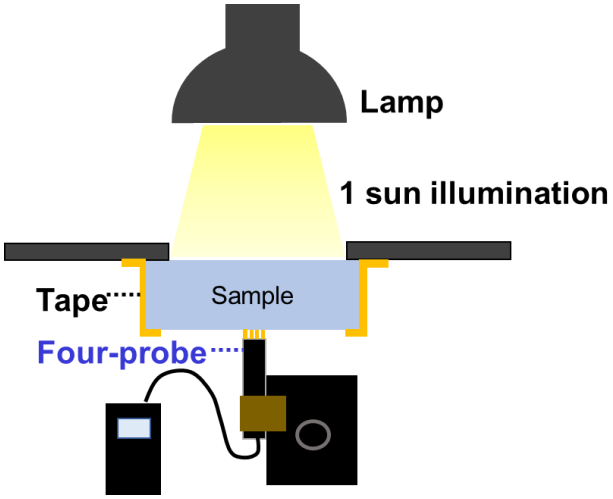

Fig. 3.7 Schematic illustration of setup for the sheet resistance measurement under 1 sun illumination.

3.6 Fourier transform infrared spectroscopy (FTIR)

Infrared (IR) spectroscopy gives us information about the interaction between IR light and materials. In general, IR absorption spectroscopy is applied since each chemical bond absorbs light with specific frequencies, which is involved in their nature and the chemical environment surrounding them. Therefore, IR spectroscopy allows us to investigate the chemical composition of materials. Using an interferometer, it is simultaneously measurable for all the wavelengths in an IR spectrum. Hence, the system does not require a monochromator. In this study, FTIR measurements were performed to estimate the atomic density of the interfacial SiO_x layer. The atomic density of the SiO_x can be determined by observing the wavenumber of longitudinal optical (LO) and transversal optical (TO) phonons modes [17]. The frequencies of the TO and LO modes are described as

$$\nu_{\mathrm{TO}} = \frac{1}{2\pi}\sqrt{2[\alpha \sin^2(\theta/2) + \beta \cos^2(\theta/2)]/m}\,, \tag{3.28}$$

$$\nu_{\mathrm{LO}} = \frac{1}{2\pi}\sqrt{2\{\alpha \sin^2(\theta/2) + \beta \cos^2(\theta/2) + Z^2\rho/[\varepsilon_\infty(2m+M)]\}/m}\,. \tag{3.29}$$

Where ν_{LO} and ν_{TO} are the frequency of LO and TO modes, α and β are the central and noncentral force constants, θ is the Si–O–Si bridging bond angle, m and M are the atomic masses of O and Si atoms, respectively, ε_∞ is the permittivity at the infinite frequency of the oxide film, Z is the electrical charge related to the movement of O atoms. Hence, SiO_x atomic densities (ρ) were calculated from the equations below,

$$\nu_{\mathrm{LO}}{}^2 - \nu_{\mathrm{TO}}{}^2 = \frac{2Z^2}{[\varepsilon_\infty(2m+M)]m}\,\rho = C\rho\,. \tag{3.30}$$

For the estimation of C, the reported value of 1.71×10^{-17} cm from bulk SiO_2 [18, 19] was used in this study. However, the objective of this study is an ultrathin SiO_x layer with a thickness of ~1 nm, which causes difficulty in observing off-plane vibration by the standard setup of vertical incident light. Thus, to detect the longitudinal optical (LO) phonon vibrational mode of SiO_x, the measurements were performed at an oblique incident light setting of 74° by using a variable angular holder, which can be detected LO mode by p-polarized light due to the Berreman effect [20].

3.7 UV-vis-NIR spectrometry

UV-vis-NIR spectroscopy analyzes the material's optical properties, such as reflectance, transmittance, and absorbance. These optical properties are acquired with varying the wavelength of the incident light. Since the light can scatter at the surface of samples, the integrating sphere is equipped with a highly reflective coating to detect all the scattering light. The relation among the reflectance (R), transmittance (T), and absorbance (A) is described as

$$A = 1 - (R + T)\,, \tag{3.31}$$

and the absorption coefficient (α) can be determined by

$$\frac{I}{I_0} = \frac{T}{1 - R} = e^{-\alpha t}. \tag{3.32}$$

Where t is the thickness of samples.

3.8 Scanning electron microscopy (SEM)

Scanning electron microscopy (SEM) can observe surface and cross-sectional structures of materials on a micrometer scale to a nanometer scale. In the microscope system, the emitted electrons are accelerated by applying high anode bias (0.5–30 kV). Then, the accelerated electrons are condensed into a narrow beam using the magnetic lens, which is focused on the samples. The impinged electron beam at the sample surface can scatter back, emit secondary electrons (SE), or generate X-rays. Generally, the surface structure is observed by collecting SE due to the generation of SE only at the proximity of the surface, which originated from losing their energy at the surface by collisions. The image can be obtained by scanning the beam and collecting electrons at each position. The above-all processes occur in a vacuum chamber with a pressure of $<10^{-3}$ Pa. In this study, SEM (Hitachi, TM3030Plus) was used to observe the surface structure of a pyramidal textured Si surface.

3.9 Transmission electron microscopy (TEM)

Transmission electron microscopy (TEM) observes the surface and cross-sectional structures of materials on a nanometer scale. The accelerated and focused electron beam is transmitted through the sample and detected. By detecting the intensity of transmitted electrons, it observes a spatial distribution of the transmittance of electrons. The structures and composition of the materials differ in electron transmittance, providing an image by acquiring transmitted electrons at each position. Since the electron must be transmitted, the sample must be thin enough to be less than 100 nm. The acceleration voltage is generally 100 kV, and the TEM measurement is performed under high vacuum conditions of $<10^{-4}$ Pa.

3.10 Energy dispersive X-ray spectroscopy (EDS)

Energy dispersive X-ray spectroscopy (EDS) analyses the elements' composition of the samples. The energy of the generated X-ray is inherent to each atom. Hence, detecting the energy and the intensity gives us information about the element species and their compositions. By impinging accelerated electrons to the samples, secondary electrons are emitted from the core level of the sample. Then, outer shell electrons are transferred to the vacancy of the inner shell to be stable, and the excess energy corresponding to the transition energy is emitted as an X-ray. In this study, X-rays of Si Kα, O Kα, and Al Kα were detected. The emitted secondary electron comes out from the K-shell, and the electron transfer occurs from L to K-shells; then, the emitted X-ray is referred to as Kα. In general, the EDS system is mounted in SEM and TEM systems. Hence, the X-ray intensity mapping for each atom can be obtained, referred to as EDS mapping.

3.11 Scanning probe microscopy (SPM)

Atomic force microscopy (AFM)

Scanning probe microscopy observes the surface structure of samples by scanning a physical probe. One of the surface imaging modes of atomic force microscopy (AFM) can produce surface images at the atomic level. While scanning a cantilever over a sample surface, the laser light is irradiated on the cantilever, and the reflected light is detected to obtain information about the surface structure. While probing and contacting the surface with a sharp tip on the edge of the cantilever, bending of the cantilever causes the change in the amount of the reflected laser light detected by a photodiode, which provides a spatial image with information of surface structure

due to tracing of the height of cantilever. The piezoelectric element is mounted for precise scanning and oscillates cantilever at its eigenfrequency.

Kelvin probe force microscopy (KPFM)

Kelvin probe force microscopy (KPFM) is the contact potential difference (CPD) measurement between the tip of the cantilever and the sample surface. The CPD corresponds to a work function difference between the two materials. Since this is the scanning probe method, it provides a surface potential mapping on the sample. When the two materials are contacted, Fermi levels are placed at the same level. Hence, it generates contact potential (V_{cpd}). However, when the contact potential is nullified by applying an external voltage, the Fermi level of the sample returns to its original position. The applied external bias is known as backing potential (V_{b}). This means the V_{b} equals V_{cpd}, as shown in Figure 3.8. Hence, the relation between CPD and work function for tip and sample can be described as

$$V_{\mathrm{b}} = V_{\mathrm{CPD}} = \frac{\Phi_{\mathrm{tip}} - \Phi_{\mathrm{sample}}}{q}. \tag{3.33}$$

Hence, the work function of the sample can be estimated by measured V_{cpd} and the known work function of the tip.

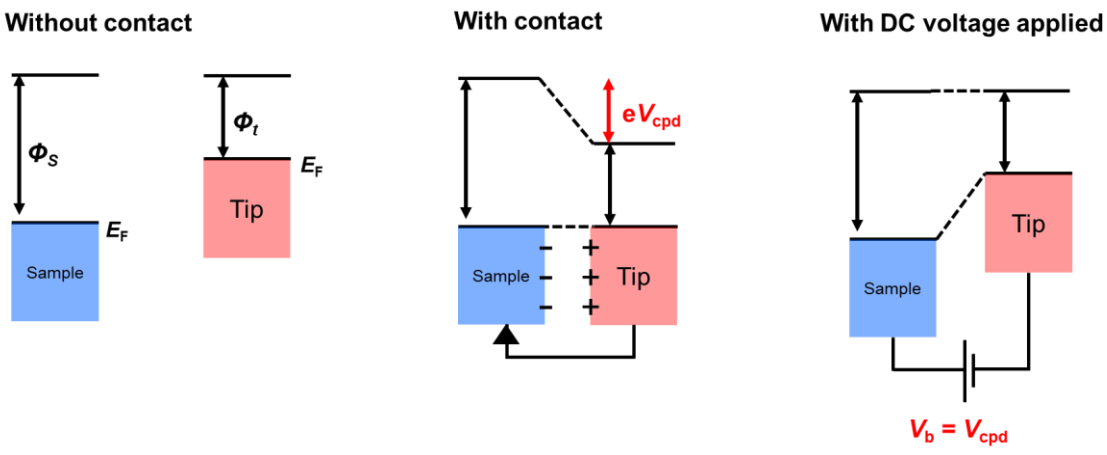

Fig. 3.8 Schematics of the principle for the KPFM measurement.

References

[1] R. A. Sinton, A. Cuevas, and M. Stuckings, "Quasi-steady-state photoconductance, a new method for solar cell material and device characterization," In: Proceedings of 25th IEEE Photovoltaic Specialists Conference, p. 457 (1996).

[2] H. Nagel, C. Berge, and A. G. Aberle, "Generalized analysis of quasi-steady-state and quasi-transient measurements of carrier lifetimes in semiconductors," J. Appl. Phys. **86**, 6218 (1999).

[3] D. Kane and R. Swanson, "Measurement of the emitter saturation current by a contactless photoconductivity decay method," In: Proceedings of the 18th IEEE Photovoltaic Specialist Conf., IEEE, Las Vegas, NV, pp. 578–583 (1985).

[4] M. Kunst and G. Beck, "The study of charge carrier kinetics in semiconductors by microwave conductivity measurements," J. Appl. Phys. **60**, 3558, (1986).

[5] F. J. Himpsel, F. R. McFeely, A. Taleb-Ibrahimi, J. A. Yarmoff, and G. Hollinger, "Microscopic structure of the SiO_2/Si interface," Phys. Rev. B **38**, 6084 (1988).

[6] M. Cardona and L. Ley, Photoemission In Solids I, Topics In Applied Physics, Springer, Berlin, Heidelberg (1978).

[7] S. Tanuma and T. Kimura, "Quantitative Auger and X-ray photoelectron analysis of Au-Cu alloys with three kinds of relative sensitivity factors," J. Surf. Anal. **10**, 163 (2003).

[8] C. D. Wagner, L. E. Davis, M. V. Zeller, J. A. Taylor, R. H. Raymond, and L. H. Gale, "Empirical atomic sensitivity factors for quantitative analysis by electron spectroscopy for chemical analysis," Surf. Interface Anal. **3**, 211 (1981).

[9] D. A. Shirley, "High-resolution x-ray photoemission spectrum of the valence bands of gold," Phys. Rev. B **5**, 4709 (1972).

[10] A. Proctor and P. M. A. Sherwood, "Data analysis techniques in x-ray photoelectron spectroscopy," Anal. Chem. **54**, 13 (1982).

[11] J. M. Hill, D. G. Royce, C. S. Fadley, L. F. Wagner, and F. J. Grunthaner, "Properties of oxidized silicon as determined by angular-dependent X-ray photoelectron spectroscopy," Chem. Phys. Lett. **44**, 225 (1976).

[12] M. F. Hochella Jr. and A. H. Carim, "A reassessment of electron escape depths in silicon and thermally grown silicon dioxide thin films," Surf. Sci. Lett. **197**, L260 (1988).

[13] J. Hölzl and F. K. Schulte, “Work Functions of Metals” in Solid Surface Physics, Springer-Verlag, Berlin (1979).

[14] R. H. Cox and H. Strack, “Ohmic contacts for GaAs devices,” Solid-State Electron. **10**, 1213 (1967).

[15] S. M. Sze and Kwok K. Ng, Physics of Semiconductor Devices, 3rd edition (John Wiley & Sons, 2007).

[16] K. Gelderman, L. Lee, and S. W Donne, “Flat-band potential of a semiconductor: Using the Mott–Schottky equation,” J. Chem. Educ. **84**, 685 (2007).

[17] A. Lehmann, L. Schumann, and K. Hübner, “Optical phonons in amorphous silicon oxides Ⅰ. Calculation of the density of states and interpretation of LO－TO splittings of amorphous SiO_2,” Phys. Status Solidi B **117**, 689 (1983).

[18] Asuha, T. Kobayashi, M. Takahashi, H. Iwasa, and H. Kobayashi, “Spectroscopic and electrical properties of ultrathin SiO_2 layers formed with nitric acid,” Surf. Sci. **547**, 275 (2003).

[19] C. Martinet and R. A. B. Devine, “Analysis of the vibrational mode spectra of amorphous SiO_2 films,” J. Appl. Phys. **77**, 4343 (1995).

[20] D. W. Berreman, “Infrared absorption at longitudinal optic frequency in cubic crystal films,” Phys. Rev. **130**, 2193 (1963).

CHAPTER 4

HOLE-SELECTIVE CONTACT BY AN ULTRATHIN Al-DOPED SILICON OXIDE

To accomplish high η of Si solar cells, the device requires interlayers with not only surface passivation but also sufficient carrier tunnel probability. In particular, SiO_2 layers have a high advantage for the front-side passivation layer because of their extremely high optical properties with low parasitic absorption attributed to their high bandgap properties. However, the carrier tunneling through SiO_2 decreases exponentially with increasing layer thickness [1]. In contrast, to achieve high surface passivation quality, the SiO_2 layer has to be thickened by a high-temperature annealing process, such as thermal oxidation, followed by forming gas annealing (FGA) to terminate active defects by hydrogens [2,3]. Therefore, the device performance will be limited due to the trade-off between the carrier tunneling probability and the surface passivation quality. Thus, this chapter overcomes this problem by impurity-doped SiO_x. The film properties of thickness and composition were investigated. In addition, surface passivation quality and hole selectivity. Moreover, Q_f and interface state density were estimated by an analyzed surface potential and simplified extended SRH formalism. The hole-selective passivating contact mechanism is proposed by considering the important finding of the light-induced activation effect.

4.1 Impurity doped SiO_x for carrier-selective contacts

Impurity doping into the SiO_2 layer will be one of the expected solutions. Recently, D. König *et al*. reported that ultrathin Al–O/SiO_2 stacks show high hole selectivity induced by negative fixed charges originating from Al-induced acceptor states occupied with electrons, which are formed in the SiO_2 layer [4]. According to their proposed model, a hole-selective passivating contact — selective hole tunneling through the SiO_2 layer with an excellent surface passivation — can be realized by hole tunneling via the Al-induced acceptor states and effective carrier separation due to upward band bending of Si surface induced by the negative fixed charges existing in the SiO_2 layer.

In addition, if the SiO_2 layer has sufficient negative fixed charges, p-type inversion layers are formed on the n-type Si substrates. Such modulation doping emerged as a technology of providing free carriers at the surface of a semiconductor by doping materials adjacent to the semiconductor without direct doping of impurities in Si, which can eliminate dopant-associated defect states [5,6]. The modulation doping technology was first implemented for GaAs/AlAs in the 1970s [7]. In recent years, Si modulation doping has emerged by using $Al_xGa_{1-x}N$ as a dielectric layer [8], and the SiO_2 layer was used for the modulation doping of III-V semiconductors [4]. The density functional theory (DFT) calculation revealed that Al [4], Sc, and Ga could be candidates for impurities for modulation doping in SiO_2 [9]. These impurities in SiO_2 form the modulation acceptor states and the energies of acceptor levels relative to vacuum levels are 5.36, 5.51, and 5.39, respectively. Since the modulation acceptor states exist in the band gap of SiO_2 and below the Si valence-band edge, the relaxations of electrons from Si readily occur by transition into the modulation acceptor states without thermal activation, delivering a large number of holes to the Si surface at very low temperatures, which cannot be realized by the conventional doping process.

4.2 Concept of aluminum nitrate oxidation treatment

Although the ultrathin Al–O/SiO_2 stacks showed an excellent hole-selective passivating contact property, the ultrathin Al–O/SiO_2 stacks were formed by rapid thermal oxidation (RTO) or plasma-enhanced chemical vapor deposition (PECVD) for the SiO_2 formation, followed by the formation of monolayer or multilayer Al–O by using atomic layer deposition (ALD). In addition, high-temperature annealing at 1000 °C is required to activate the surface passivation [4]. These processes lead to degraded throughput of solar cell manufacturing. On the other hand, ultrathin SiO_x layers can be simply formed by acid aqueous solutions such as $HClO_4$ [10], HNO_3 [11, 12],

HCl + H_2O_2 [12], H_2SO_4 + H_2O_2 [12]. In addition, ozonated water [13], and direct current anodization process can also form ultrathin SiO_x layers [2]. Though these processes can be performed at low temperatures and are thus cost-effective cell production, these SiO_x layers themselves have inferior surface passivation quality and after all require further reformation such as thickening to ~5 nm by thermal oxidation, high-temperature annealing at 1100 °C, and FGA to increase surface passivation quality [2, 3]. Indeed, the lowest SRV of 42 cm s^{-1} at a Δn of 10^{15} cm^{-3} has been reported, in which SiO_x was formed using HNO_3 oxidation followed by high-temperature thermal treatment [2]. However, ultrathin SiO_x layers themselves with both good surface passivation quality and carrier-selective contact have not yet been reported by realizing only using a low-temperature process. Therefore, this research investigated a simple wet chemical method realizing a hole-selective passivating contact by ultrathin SiO_x layers with impurity doping.

If the wet chemical solution contains Al and the processing Si surface is terminated by the OH group, the Al atoms are favorably adsorbed on the Si surface as a formation of Si-O-$Al(OH)_3$ (final state) due to highly reactive combinations between Si-OH and $Al(OH)_4$ (initial state), decreasing potential energy and stabilizing [14]. The enthalpy change (ΔH) from the initial state to the final state of −0.91 eV suggests that the final state is stabilized [14]. Al is generally considered a metal contaminant, creating a shallow energy state in the Si band gap; however, this Al adsorption mechanism is effectively used to form an Al-doped SiO_x layer for this research aim. Hence, in this experiment, Al precursors are intentionally added into the process solution. Moreover, in order to form SiO_x layers, an oxidant is required in the process solution. As mentioned above, HNO_3 can oxidize the Si surface and form ultrathin SiO_x layers. However, in such a strong acid, Al is not expected to adsorb on the Si substrate because metal contaminants, including Al, exist as metal ions (cation), and they are repelled from the Si surface due to positive zeta potential, dissolving into the acid solution. Therefore, one of the suitable Al precursors is aluminum nitrate ($Al(NO_3)_3$) because the material has a moderate pH of 5−6 with an oxidant generated from nitrate (NO_3^-). Assumed by the proposed oxidation model by Asuha *et al*. [15] and M. Takahashi *et al*. [16], the nitrate ions are decomposed into O^- ions at the surfaces with SiO_2 pore structures and the O^- ions diffuse into SiO_2 layers by electric field enhanced by the adsorbed NO_3^-, oxidizing Si surfaces by the diffused O^- ions. Hence, the method can be simplified by using $Al(NO_3)_3$ aqueous solution: just Si substrates are immersed into $Al(NO_3)_3$ aqueous solution, forming simultaneously Al−O and Si−O in a low-temperature as an ultrathin Al-doped SiO_x layer. The remarkable feature is that this process is a simple wet chemical low-temperature method, expecting high throughput and high-efficiency c-Si solar cells.

4.3 Film properties of Al-doped SiO_x

4.3.1 Sample fabrication

In this research, double-side-polished 280 μm thick float-zone (FZ) n-type Si (100) substrates with a resistivity of 2.5 Ω cm (TOPSIL PV-FZ™) were used. The Si substrates were cleaved into 20×20 mm-sized test sample pieces, followed by Radio Corporation of America (RCA) cleaning [17]. After 1% diluted hydrofluoric acid (HF) treatment for 1 min and rinse in deionized water (DIW) (resistivity of 18.2 MΩ cm) for 1 min, the hydrophobic Si substrates were immersed in $Al(NO_3)_3$ aqueous solution with an $Al(NO_3)_3 \cdot 9H_2O$ molar concentration of 0.25 mol L^{-1} for 5 to 30 min, as depicted in Figure 4.1. The hot $Al(NO_3)_3$ aqueous solution was prepared in advance by dissolving $Al(NO_3)_3 \cdot 9H_2O$ (17.8 g, special grade, Junsei Chemical Co., Ltd.) in DIW (190 mL) in a Pyrex glass beaker (Corning Pyrex 600 mL) and heating to a boiling temperature (~95 °C) on a hot plate (AS ONE Corporation, CHPS-170DF). During the heating process, the beaker was capped to avoid the evaporation of the solution. The solutions were not intentionally stirred during the process; however, drastically generated bubbles could be confirmed at the boiling temperature. After the $Al(NO_3)_3$ treatment, processed Si substrates were rinsed in DIW for 1 min and completely dried by N_2 blow.

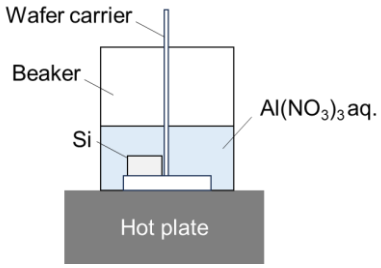

Fig. 4.1 Schematics of the appearance for $Al(NO_3)_3$ oxidation treatment.

4.3.2 Sample evaluation

XPS (Shimadzu Corporation, Kratos AXIS-ULTRA DLD) measurement acquired Si 2*p*, Al 2*p*, and O 1*s* core-level spectra, in which monochromatized Al Kα radiation ($h\nu$ = 1486.6 eV) was used for X-ray source. The generated photoelectrons were collected in the surface-normal direction. The pass energy of photoelectrons was set to 20 eV. To calibrate all spectra, measured Si $2p_{3/2}$ peaks were fixed to a binding energy of 99.2 eV [18]. The Al 2*p* and O 1*s* spectra were also calibrated using these shifted binding energies of each sample. The backgrounds of photoelectrons were subtracted using the Shirley–Proctor–Sherwood method [19, 20], and the

experimental spectra were peak fitted using Voigt functions. The fraction of Lorentzian contributions and full width at half maximum (FWHM) of the peaks were not fixed to a particular value, and all peaks were optimized until the dissociations between experimental spectra and fitted curves were minimized using XPSPEAK 4.1 software. In this study, Si^0 $2p_{3/2}$, Si^0 $2p_{1/2}$, and Si^{4+} (SiO_2) peaks were taken into account for the Si 2*p* peak fitting. Si^0 $2p_{1/2}$ area intensity was fixed to the half of Si^0 $2p_{3/2}$ peak area intensity, and the splitting energy between Si^0 $2p_{3/2}$ and Si^0 $2p_{1/2}$ was set to 0.6 eV [18]. Each SiO_x thickness was calculated using area intensity, atomic density, photoionization cross-section [21], and the escape depths for Si and SiO_2 [22], respectively. For quantitative analysis of the oxide, surface atomic concentrations of oxidized Al and Si were calculated using atomic sensitivity factors of 0.283 for Si 2*p*, 0.711 for O 1*s*, and 0.193 for Al 2*p* [23]. The deconvolution of Si 2*p* core-level spectra was performed after fixing the chemical shift for the suboxide components (Si^{1+}, Si^{2+}, Si^{3+}) and the FWHM ratio of each component concerning the Si^0. 0.95 [21], 1.75 [21], and 2.48 eV [21] were set as each chemical shift and 1.57 [21], 2.07 [21], and 2.36 [21] as each FWHM ratio, respectively. In addition to that, Si 2*p* and Al 2*p* core-level spectra were acquired with varying the take-off angle (TOA) of photoelectrons in the range of 10 to 90° to investigate by using the surface sensitive conditions. To confirm the Al-doping distribution semi-quantitatively, the oxidized Al and Si peak intensity ratio was evaluated with respect to the varied TOA. FTIR measurements were conducted to analyze the atomic density of the interfacial SiO_x layers. The cross-sectional structure and the composition of the interface were evaluated using TEM-EDS.

4.3.3 Chemical bond states

Figure 4.2 shows the Si 2*p* and Al 2*p* core-level XPS spectra for samples treated in boiled $Al(NO_3)_3$ aqueous solution with a molar concentration of 0.25 mol L^{-1} for various treatment times in the range of 5 to 30 min. The measurement observed bulk-Si and SiO_2-derived Si 2*p* peaks at the binding energies of 99.2 and 102.5 eV, respectively. The SiO_x intensities slightly increase with the passing of treatment time. The binding energies of Al oxide can be assigned to be generally larger than those of metal Al of 72.5–73.0 eV due to creating bonds with high electronegativity element of O. [18, 24–26] For instance, the reported values are listed as follows: 75.8–76.6 eV[24] for amorphous and crystalline Al oxide, 74.7 eV[25] for γ-Al_2O_3, and 73.9 eV[26] for α- Al_2O_3. Therefore, the observed peaks ~74–76 eV can be assigned as the Al–O bond states. No peak at ~73 eV indicates the films do not contain metallic Al–Al states.

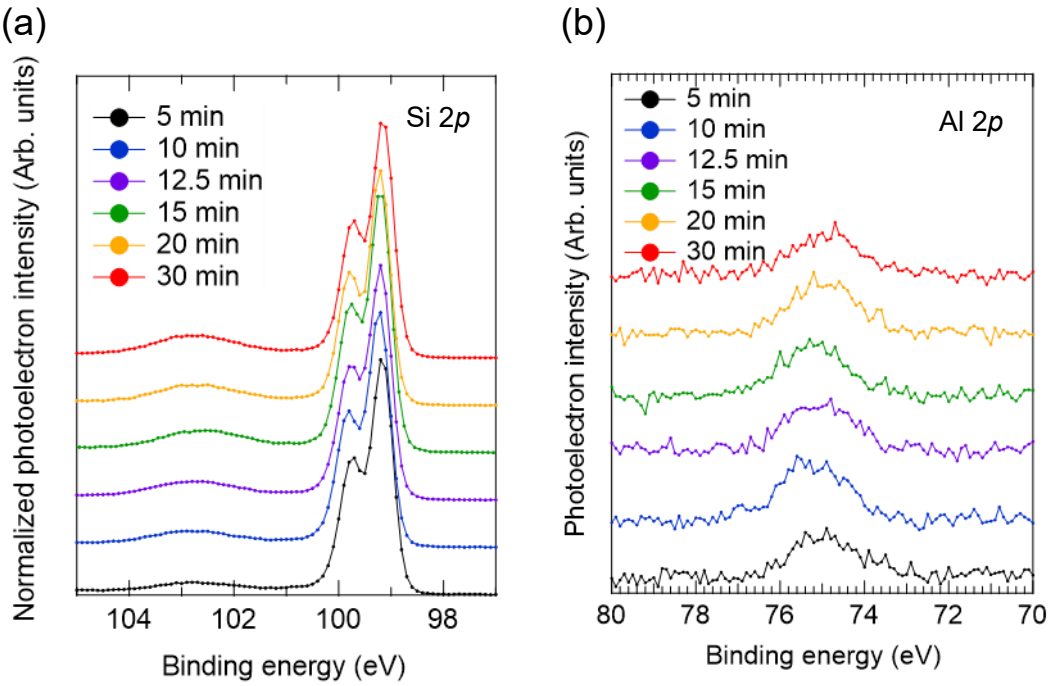

Fig. 4.2 (a) Si 2*p* and (b) Al 2*p* core-level X-ray photoelectron spectroscopy (XPS) spectra for samples treated in boiled $Al(NO_3)_3$ aqueous solution with a molar concentration of 0.25 mol L^{-1} for various treatment times in the range of 5 to 30 min.

4.3.4 Atomic concentration and thickness

Figure 4.3 displays the computed atomic concentrations of oxidized Al and Si and the SiO_x thickness on samples treated in boiled $Al(NO_3)_3$ aqueous solution with a molar concentration of 0.25 mol L^{-1} for various treatment times in the range of 5 to 30 min. Although Si oxide peaks gradually increase from 8.0 to 10.7 at.% with passing the $Al(NO_3)_3$-treatment time, the atomic concentrations of all Al–O peaks are saturated in a range of 0.7–1.2 at.%. The estimated SiO_x thickness gradually increased from ~0.7 to ~1.2 nm. These results indicate that the growth of Al oxides is finished in the initial stage, whereas only Si oxides can grow further. As mentioned in 4.2, nitrate ions are decomposed into O^- ions at the SiO_2 surfaces and diffuse into SiO_2 layers, and the migrated O^- ions oxidize Si at the interface. Considering this O^- diffusion oxidation model and the growth rate difference between Al oxide and Si oxide, the fact implies that the Al-doped SiO_x layers consist of $AlO_y/SiO_x/Si$ stack structures.

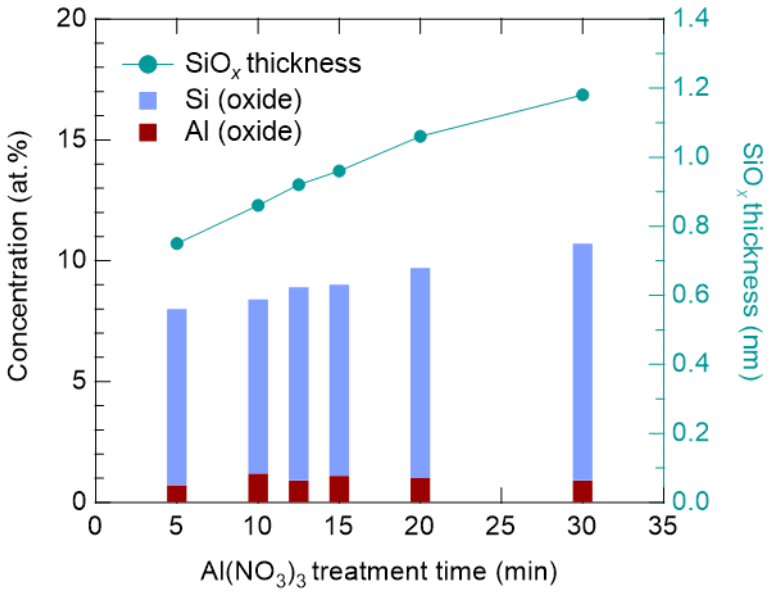

Fig. 4.3 Computed atomic concentrations of oxidized Al and Si, and the SiO_x thickness on samples treated in boiled $Al(NO_3)_3$ aqueous solution with a molar concentration of 0.25 mol L^{-1} as a function of $Al(NO_3)_3$ treatment time.

4.3.5 Composition of sub-oxide and SiO_2 component

Figure 4.4 illustrates the composition of sub-oxide (Si^{1+}, Si^{2+}, Si^{3+}) and SiO_2 (Si^{4+}) components obtained from deconvoluted Si 2*p* spectra on samples treated in boiled $Al(NO_3)_3$ aqueous solution with a molar concentration of 0.25 mol L^{-1} for various treatment times in the range of 5 to 30 min. The Si^{4+} component increases; on the other hand, the Si^{1+} component decreases with increasing $Al(NO_3)_3$-treatment time from 5 to 30 min. D. Hiller *et al*. proposed that the tetrahedral structure of O-coordinated Al oxide is generated because the adjacent SiO_2 imprints its tetrahedral near-order and bond length into the Al–O MLs. [27] Considering this experimental fact, more tetrahedral structures of O-coordinated Al oxide favorably form with increasing $Al(NO_3)_3$-treatment time.

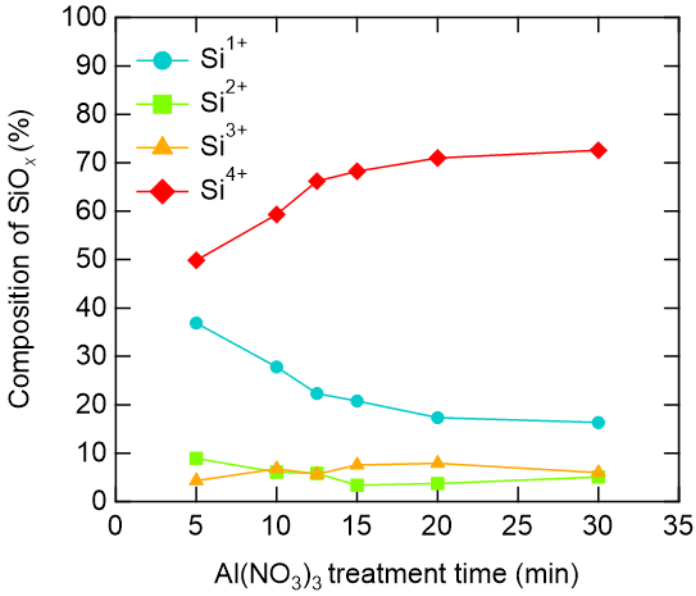

Fig. 4.4 Composition of sub-oxide (Si^{1+}, Si^{2+}, Si^{3+}) and SiO_2 (Si^{4+}) components on samples treated in boiled $Al(NO_3)_3$ aqueous solution with molar concentration of 0.25 mol L^{-1} as a function of $Al(NO_3)_3$ treatment time.

4.3.6 Al composition evaluated by surface sensitive condition

Figure 4.5 shows the Si 2*p* and Al 2*p* core-level XPS spectra for samples treated in boiled $Al(NO_3)_3$ aqueous solution with molar concentration of 0.25 mol L^{-1} for 12.5 min acquiring with varying the TOA of photoelectron in the range of 10 to 90° to investigate in the surface sensitive conditions. As shown in Si 2*p* and Al 2*p* spectra, peak intensities gradually decrease with decreasing TOA. To compare those spectra, using each atomic concentration of oxidized Al (X_{AlOx}) and Si (X_{SiOx}), each oxidized Al atomic concentration ratio (r_{AlOx}), as described below, was estimated.

$$r_{AlOx} = \frac{X_{AlOx}}{X_{SiOx} + X_{AlOx}} \tag{4.1}$$

Figure 4.6 describes the Al composition in the oxide layer as a function of TOA. Al composition observed at TOA of 30° was minimal but linearly increased from 30 to 10°. Since surface sensitive condition (small number of TOA) observes higher Al composition compared to interface sensitive

condition (large number of TOA), Al oxides possibly exist at the surface of the SiO_x layer. More surface-sensitive TOA conditions might show higher Al composition, but less than 10° of TOA was not able to be set due to the limitation of the XPS setting. Hence, this result also indicates that the ultrathin Al-doped SiO_x consists of a bi-layer of AlO_y/SiO_x on a Si substrate.

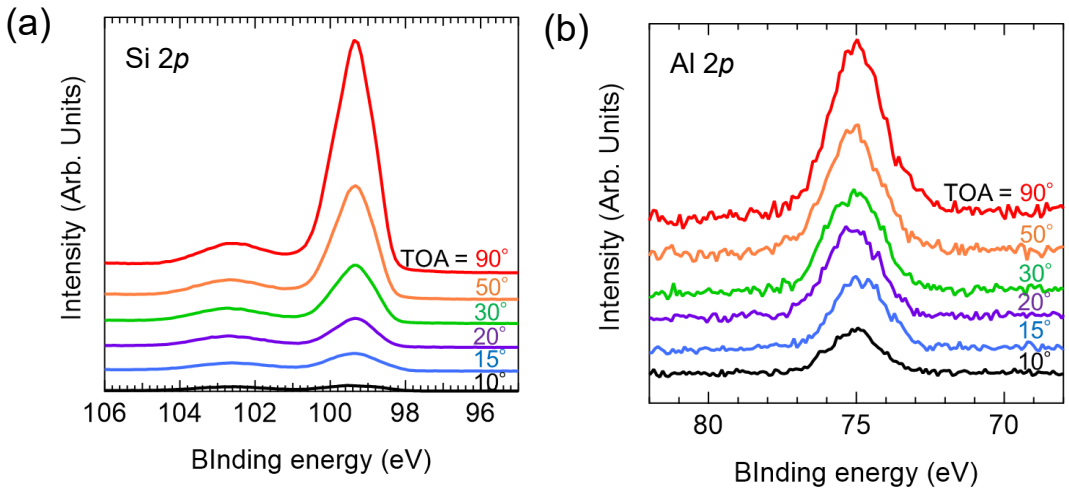

Fig. 4.5 **(a)** Si 2*p* and **(b)** Al 2*p* core-level XPS spectra acquired with varying the TOA of photoelectron in the range of 10 to 90°.

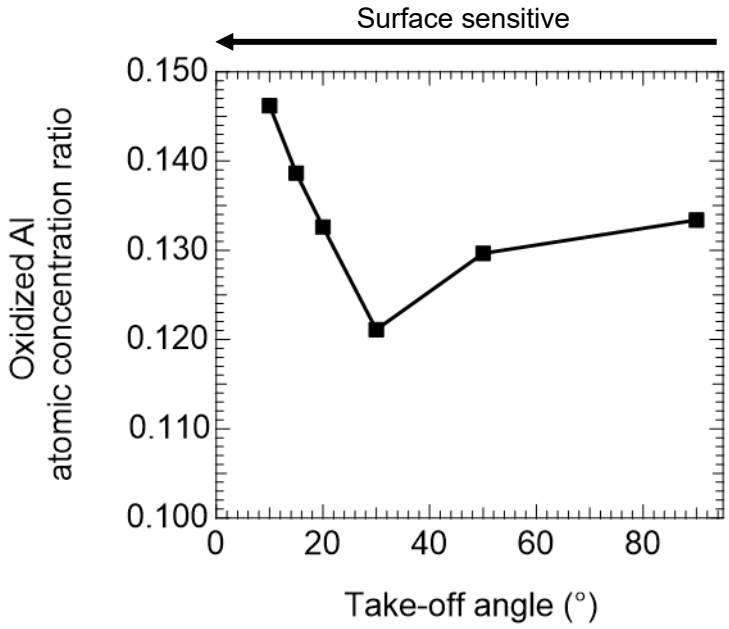

Fig. 4.6 Oxidized Al atomic concentration ratio as a function of TOA.

4.3.7 Atomic density of interfacial SiO_x

To deduce the atomic density of the interfacial SiO_x layer, FTIR measurements were performed on $Al(NO_3)_3$-treated samples. For such an ultrathin layer, the off-plane vibration cannot be detected by a standard setup of vertical incident light. In order to detect the longitudinal optical (LO) phonon vibrational mode of SiO_x, the measurements were performed at an oblique incident light setting of 74° by using a variable angular holder, which can be detected in LO mode by p-polarized light due to the Berreman effect [28]. Figure 4.7 displays FTIR spectra of samples treated in boiled $Al(NO_3)_3$ aqueous solution with a molar concentration of 0.25 mol L^{-1} for various treatment times. The transversal optical (TO) phonon modes were detected and confirmed no significant shift in the wavenumber range of 1029–1032 cm^{-1}. On the other hand, significant shifts of LO modes were confirmed and the LO peaks were shifted to the higher wavenumber from 1071 to 1207 cm^{-1} with increasing $Al(NO_3)_3$ treatment time. From the wavenumber of LO and TO phonons modes, SiO_x atomic densities (ρ) were calculated from the equation [29] below.

$$\nu_{LO}^2 - \nu_{TO}^2 = C\rho \tag{4.2}$$

Where C is a constant, and ν_{LO} and ν_{TO} are the frequency of LO and TO modes, respectively. As the value of C, the reported value of 1.71×10^{-17} cm from bulk SiO_2 [29, 30] was used. Figure 4.8 represents the deduced SiO_x atomic densities as a function of $Al(NO_3)_3$ treatment time. This result indicates that atomic density increases from 1.79×10^{22} to 2.24×10^{22} cm^{-3} with increasing $Al(NO_3)_3$ treatment time from 5 to 30 min. Hence, this atomic density increase agrees with the SiO_2 composition increase with increasing treatment time, as described in Figure 4.4. The Al-doped SiO_x layer can be of higher quality, which is denser and has a lower concentration of sub-oxides.

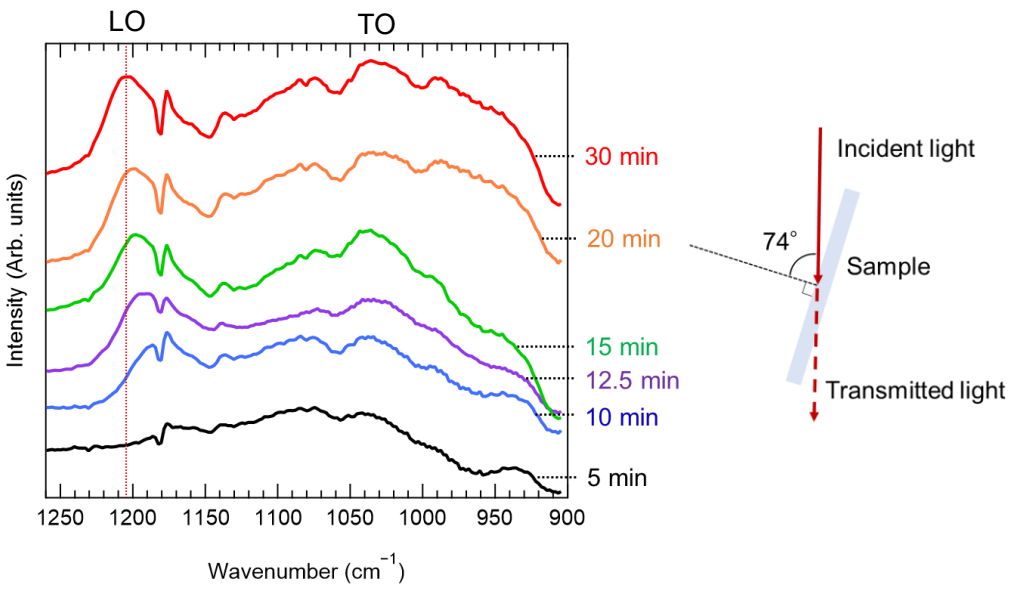

Fig. 4.7 FTIR spectra of samples treated in boiled $Al(NO_3)_3$ (aq.) with a molar concentration of 0.25 mol L^{-1} for various treatment times.

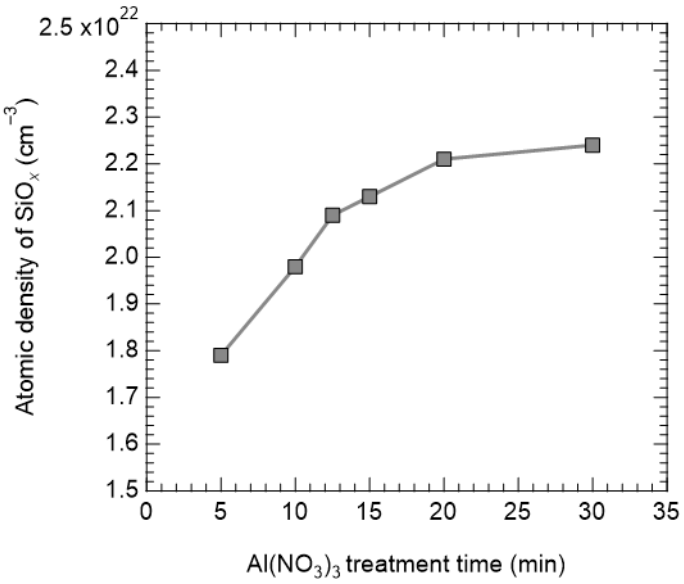

Fig. 4.8 Deduced SiO_x atomic density of Al-doped SiO_x formed in boiled $Al(NO_3)_3$ (aq.) with a molar concentration of 0.25 mol L^{-1} for various treatment times.

4.3.8 Cross-sectional structure

Figure 4.9 illustrates the cross-sectional TEM image of the Al-doped SiO_x/Si interface for samples treated in boiled $Al(NO_3)_3$ aqueous solution with a molar concentration of 0.25 mol L^{-1} for 12.5 min, and Figure 4.10 shows EDS mapping concerning the depth: (a) O Kα, (b) Si Kα (c) Al Kα, respectively. The thickness of the layer was determined to be 0.93 nm, and it is also recognizable from the detected TEM-EDS O Kα signals, as shown in Figure 4.10 (b). The thickness is estimated to be close to 0.92 nm from XPS results. The important thing here is that a microscopic analysis also revealed that the Al-doped SiO_x layer can be recognized as an ultrathin layer. Moreover, Al Kα detection was also performed to confirm the Al depth distribution, but the Al Kα signal was a noise level, as shown in Figure 4.10 (c).

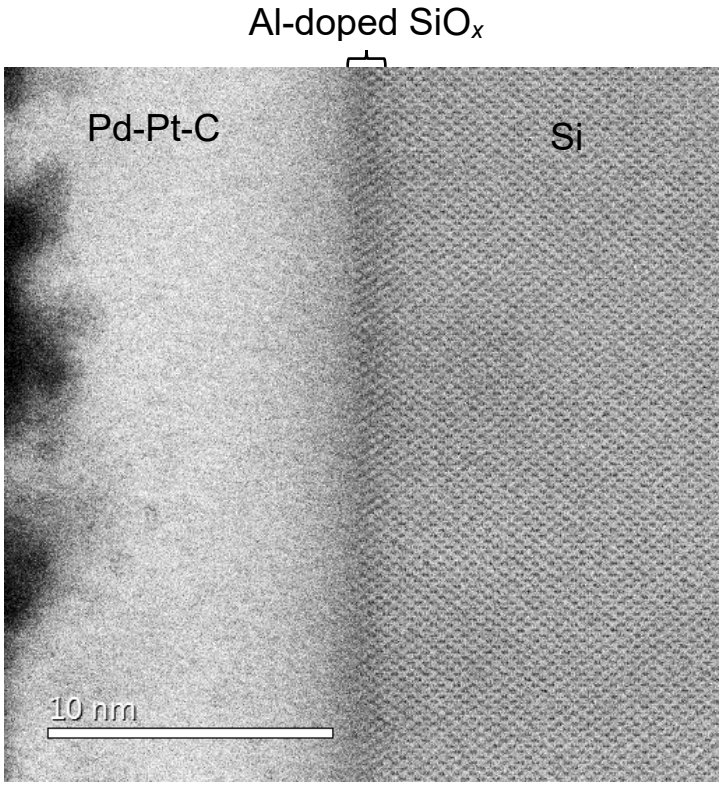

Fig. 4.9 Cross-sectional TEM image of Al-doped SiO_x/Si interface for samples treated in boiled $Al(NO_3)_3$ aqueous solution with a molar concentration of 0.25 mol L^{-1} for 12.5 min.

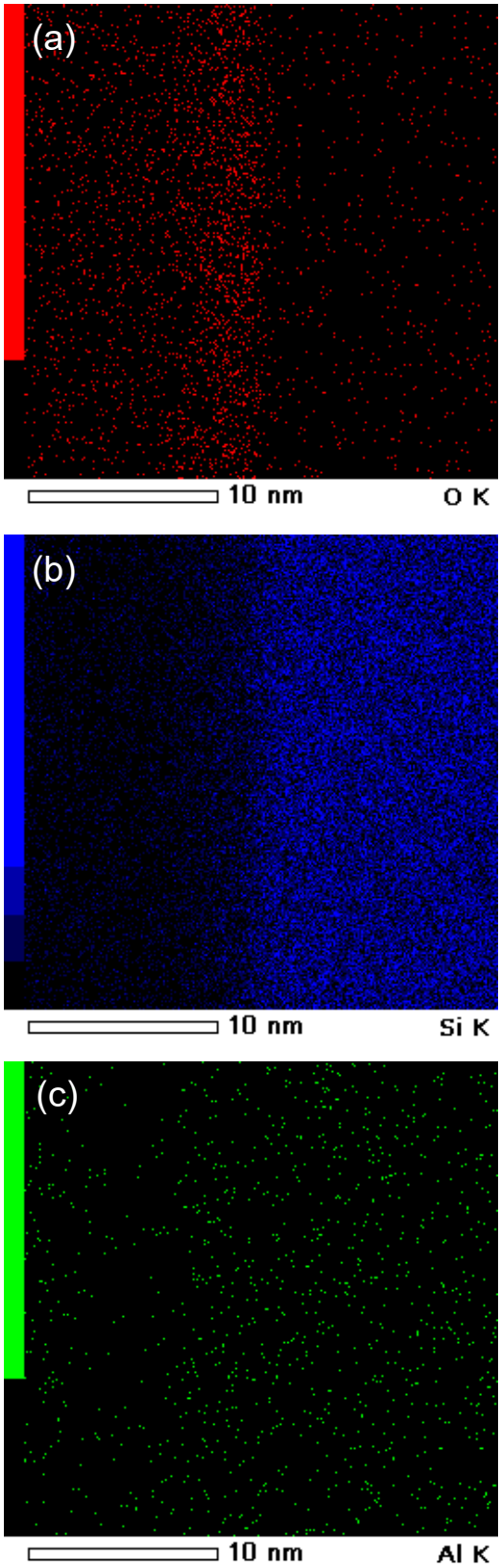

Fig. 4.10 Cross-sectional TEM-EDS mapping of Al-doped SiO_x/Si interface in the same viewpoint of the Cross-sectional TEM-image shown in Fig. 4.9: **(a)** O Kα, **(b)** Si Kα **(c)** Al Kα.

4.4 Surface passivation quality by Al-doped SiO_x

4.4.1 Sample fabrication

Double-side-polished 280 μm thick FZ n-type Si (100) with a resistivity of 2.5 Ω cm (TOPSIL PV-FZ™) were used in this study. The Si substrates were cleaved into 50×50 and 22×22 mm-sized test sample pieces, followed by RCA cleaning [17]. After 1% diluted HF treatment for 1 min and rinse in DIW (resistivity of 18.2 MΩ cm) for 1 min, the hydrophobic Si substrates were immersed in $Al(NO_3)_3$ aqueous solution with $Al(NO_3)_3 \cdot 9H_2O$ molar concentration of 0.15, 0.25, or 0.50 mol L^{-1} for 3 to 30 min. The hot $Al(NO_3)_3$ aqueous solution was prepared in advance by dissolving $Al(NO_3)_3 \cdot 9H_2O$ (10.7, 17.8, or 35.6 g, special grade, Junsei Chemical Co., Ltd.) in DIW (190 mL) in a Pyrex glass beaker (Corning Pyrex 600 mL) and heating to a boiling temperature (~95 °C) on a hot plate (AS ONE Corporation, CHPS-170DF). During the heating process, the beaker was capped to avoid the evaporation of the solution. The solutions were not intentionally stirred during the process; however, drastically generated bubbles could be confirmed at the boiling temperature. After the $Al(NO_3)_3$ treatment, processed Si substrates were rinsed in DIW for 1 min and completely dried by N_2 blow. In addition, the process temperature and duration of the $Al(NO_3)_3$ treatment were also varied from room temperature to boiling temperature with an $Al(NO_3)_3 \cdot 9H_2O$ molar concentration of 0.15 mol L^{-1} for 10 to 90 min.

4.4.2 Sample evaluation

τ_{eff} measurements were performed using microwave photoconductivity decay (μ-PCD) [31] (Kobelco Research Institute, Inc., LTA-1510EP). The τ_{eff} mapping data were acquired within the area of 20×20 mm^2 in 22×22 mm^2 sized samples with a 0.5 mm pitch. A pulsed laser with a wavelength of 904 nm and an areal photon density of 5×10^{13} cm^{-2} was used for the carrier excitation. In addition, τ_{eff} and iV_{oc} as a function of Δn were analyzed using QSSPC [32] (Sinton Instruments, WCT-120) for 50×50 mm^2 sized samples treated under one of the best conditions. The relationship between τ_{eff} and S_{eff} was used for finding $S_{eff\,max}$ values, which are described as [33]

$$\tau_{eff}^{-1} = \tau_{bulk}^{-1} + 2S_{eff}W^{-1}, \tag{4.3}$$

where τ_{bulk} and W represent the minority carrier lifetime in bulk c-Si and the thickness of Si substrates, respectively. In this study, assumed $\tau_{bulk} = \infty$, due to the exceptionally high τ_{bulk} of the

Si substrates, $S_{eff,\,max}$ is thus defined as

$$\tau_{eff}^{-1} = 2S_{eff,max}\,W^{-1} \tag{4.4}$$

and $S_{eff,max}$ was calculated using τ_{eff} at $\Delta n = 1\times10^{15}$ cm^{-3}, and W = 280 μm for wafer thickness. J_0 value was also analyzed by the Kane and Swanson method [34] using the auger-corrected effective minority carrier lifetime (τ_{corr}) over the Δn range of 1×10^{15} to 9×10^{15} cm^{-3}.

4.4.3 Surface passivation quality

Figure 4.11 represents the τ_{eff} and the corresponding maximum effective surface recombination velocity ($S_{eff,\,max}$) as a function of $Al(NO_3)_3$ treatment time for the various $Al(NO_3)_3$ molar concentrations. $S_{eff,\,max}$ decreases to <26 cm s^{-1} and rapidly decreases with increasing $Al(NO_3)_3$ molar concentration from 0.15 to 0.50 mol L^{-1}. The treatment time acquiring the minimum $S_{eff,\,max}$ value can be reduced from 17.5 to 10 min by the higher concentration of the $Al(NO_3)_3$ aqueous solution. However, further longer treatment causes gradual degradation of surface passivation quality, as shown in $S_{eff,\,max}$ increase. One of the τ_{eff} mapping data is depicted in Figure 4.12. Except for the lower center region, the areal homogeneity of the τ_{eff} is good. Those τ_{eff} were acquired using the typical excitation condition of 904 nm excitation laser light with areal density of 5.0×10^{13} cm^{-2}.

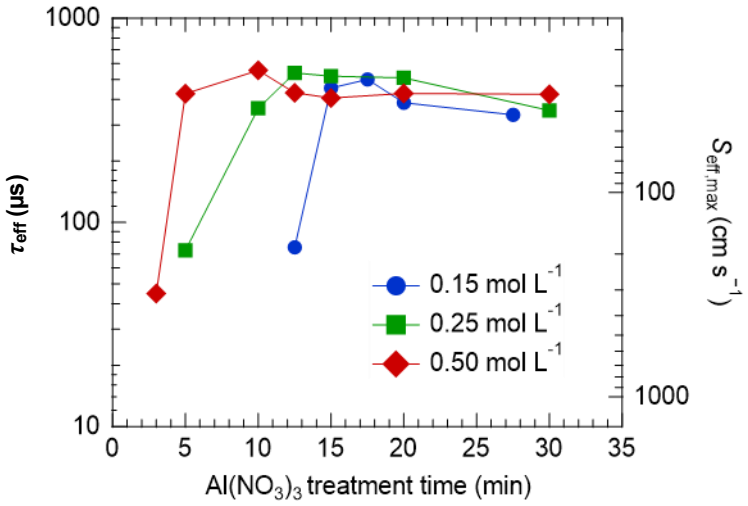

Fig. 4.11 τ_{eff} and the corresponding $S_{eff,\,max}$ as a function of $Al(NO_3)_3$ treatment time for the various $Al(NO_3)_3$ molar concentrations.

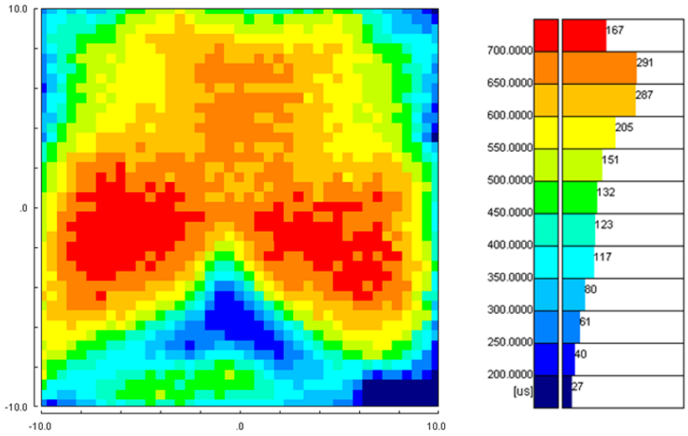

Fig. 4.12 τ_{eff} mapping of the sample treated in boiled 0.25 mol L^{-1} $Al(NO_3)_3$ (aq.) for 12.5 min.

Figure 4.13 displays τ_{eff} and the corresponding $S_{eff,\,max}$ as a function of $Al(NO_3)_3$ treatment time for the $Al(NO_3)_3$ molar concentrations 0.15 mol L^{-1} at various treatment temperatures from room temperature to boiling temperature. As shown in the figure, τ_{eff} significantly increases with increasing process temperature in a short treatment time. In addition to that, each temperature condition has maximum τ_{eff} values and further longer treatment degrades the surface passivation quality. Moreover, the maximum surface passivation quality can be obtained by increasing the process temperature relatively quickly. Besides τ_{eff} of 502 μs was achieved in a relatively short time (17.5 min) at boiling temperature, it took a longer time (240 min) to obtain a τ_{eff} of 271 μs at room temperature. The possible reason for the existence of the maximum τ_{eff} value is discussed below. Considering the induction of negative Q_f originated from AlO_4 structures formed by trapping the excited electrons into Al-induced acceptor states in the Al-doped SiO_x layer, more adjacent to stoichiometric SiO_2 stabilizes to create this AlO_4 structure. As shown in XPS and FTIR results, the SiO_2 component is increased with increasing $Al(NO_3)_3$ oxidation treatment time. However, excess treatment time make the further oxide grow at the interface, which suppresses the electron tunneling through the oxide and trapping into the Al-induced acceptor states. Hence, excess oxide growth inhibits the negative Q_f induction, causing the τ_{eff} degradation.

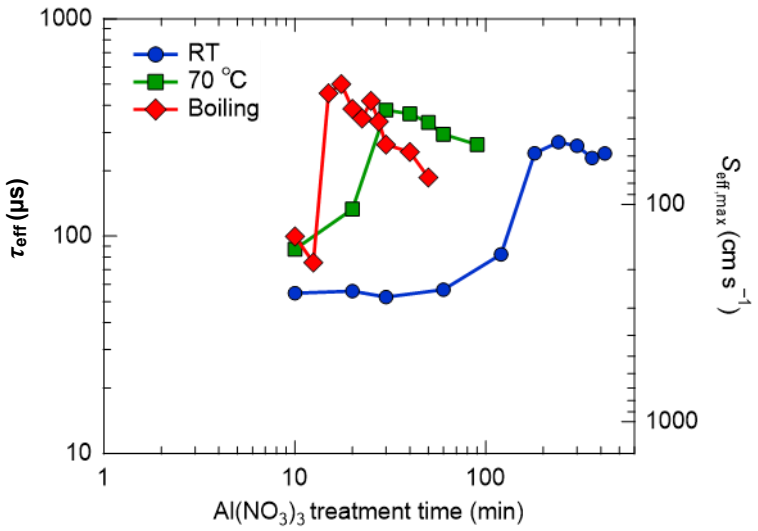

Fig. 4.13 τ_{eff} and the corresponding $S_{eff,\,max}$ as a function of $Al(NO_3)_3$ treatment time for the $Al(NO_3)_3$ molar concentrations of 0.15 mol L^{-1}at various treatment temperatures.

For one of the best $Al(NO_3)_3$-treatment conditions, a molar concentration of 0.25 mol L^{-1} for 12.5 min, QSSPC measurement was performed and confirmed a high τ_{eff} of 886 μs at $\Delta n = 1\times10^{15}$ cm^{-3}, as shown in Figure 4.14. In particular, since the low Δn region ~10^{14} cm^{-3} shows high surface passivation quality as τ_{eff} of >1 ms, the field effect might be related to such good surface passivation, which can induce the band bending of the Si surface. The corresponding $S_{eff,\,max}$ was estimated to be <16 cm s^{-1}, and an iV_{oc} = 670 mV at 1 sun illumination and J_0 = 65 fA cm^{-2} were analyzed, as shown in Figure 4.15 and Figure 4.16, respectively.

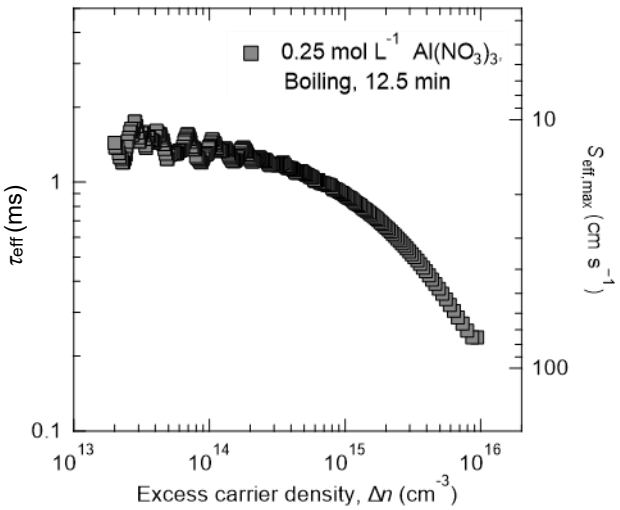

Fig. 4.14 Δn dependence on τ_{eff} and $S_{eff,\,max}$ of the sample treated in boiled 0.25 mol L^{-1} $Al(NO_3)_3$ (aq.) for 12.5 min.

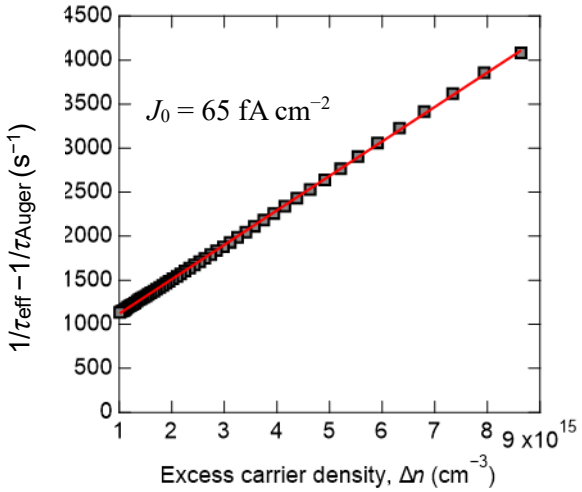

Fig. 4.15 Δn dependence on Auger-corrected inverse effective lifetimes of the sample treated in boiled 0.25 mol L^{-1} $Al(NO_3)_3$ (aq.) for 12.5 min.

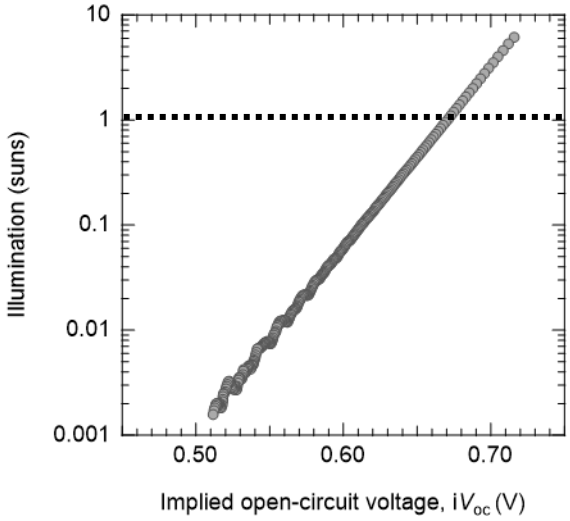

Fig. 4.16 Light intensity dependence on iV_{oc} of the sample treated in boiled 0.25 mol L^{-1} $Al(NO_3)_3$ (aq.) for 12.5 min.

4.5 Electrical properties of Al-doped SiO_x/Si interface

4.5.1 Tunneling current density

Double-side-polished 280 μm thick FZ n-type Si (100) substrates with a resistivity of 2.5 Ω cm (TOPSIL PV-FZ™) were cleaved into 20×20 mm-sized test sample pieces, followed by performing RCA cleaning [17]. After 1% diluted HF treatment for 1 min and rinse in DIW (resistivity of 18.2 MΩ cm) for 1 min, the hydrophobic Si substrates were immersed in $Al(NO_3)_3$ aqueous solution with $Al(NO_3)_3 \cdot 9H_2O$ molar concentration of 0.25 mol L^{-1} for 5 to 30 min. The hot $Al(NO_3)_3$ aqueous solution was prepared in advance by dissolving $Al(NO_3)_3 \cdot 9H_2O$ (17.8 g, special grade, Junsei Chemical Co., Ltd.) in DIW (190 mL) in a Pyrex glass beaker (Corning Pyrex 600 mL) and heating to a boiling temperature (~95 °C) on a hot plate (AS ONE Corporation, CHPS-170DF). During the heating process, the beaker was capped to avoid the evaporation of the solution. The solutions were not intentionally stirred during the process; however, drastically generated bubbles could be confirmed at the boiling temperature. After the $Al(NO_3)_3$ treatment, processed Si substrates were rinsed in DIW for 1 min and completely dried by N_2 blow. After the layer formation, Al circular electrodes were deposited on the $Al(NO_3)_3$-treated samples through a mask by thermal evaporation in a vacuum chamber at a pressure of 9×10^{-4} Pa. Their areas were estimated to be 0.0028 cm^2 on average by observing the deposited electrodes using differential interference contrast microscopy (Olympus Corporation, BX51), as shown in Figure 4.17 (a). The deposited sides were covered with polyimide films, and the samples were immersed in 1% diluted HF solution for 1 min to remove the oxide layer on the rear side of the samples. After the DIW rinse, Al films were deposited on the rear sides of the HF-treated surfaces, which were scratched with a diamond pencil to form good ohmic contacts between Al electrodes and Si substrates. After peeling off the polyimide films, *J–V* characteristics were evaluated using a precision semiconductor parameter analyzer (Hewlett-Packard Company, 4156 A) mounted with a kelvin-type four-terminal connection system. The *J–V* characteristics evaluated tunneling current density for the metal–oxide–semiconductor (MOS) structure, as depicted in Figure 4.17 (b).

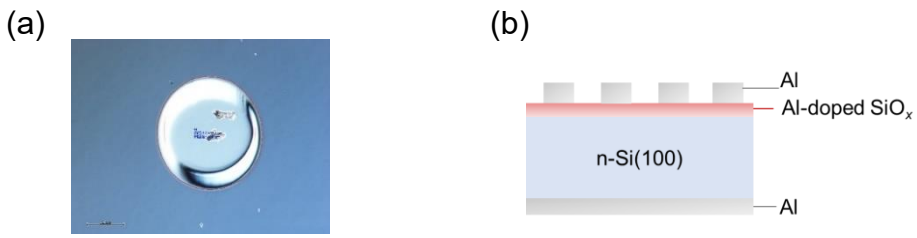

Fig. 4.17 **(a)** Deposited and used Al circular electrode and **(b)** metal–oxide–semiconductor (MOS) structure of Al circular electrode/Al-doped SiO_x/n-Si(100)/Al.

Figure 4.18 displays the *J–V* characteristics of MOS structures formed using the samples treated in boiled 0.25 mol L^{-1} $Al(NO_3)_3$ aqueous solution for various treatment times. A significant increase in leakage current density can be seen with the increasing treatment time when the negative voltage is applied despite an extremely low voltage, especially in the samples treated for 10 min or further treatment time. This result implies that hole tunneling current density increases with increasing $Al(NO_3)_3$ treatment time, originating from upward band bending of the Si surface induced by negative fixed charges existing in the Al-doped SiO_x layer, accumulating large amounts of holes in the space charge region as mirrored charges of the negative Q_f. In addition, the formation of Al-induced acceptor states in the oxide layer might be increased with increasing $Al(NO_3)_3$ treatment time, which might be related to the hole tunneling through the oxide layer. Assuming the model that has been proposed, hole tunneling occurs via the Al-induced acceptor states; the increase of tunneling current density is also attributed to the increase of the Al-induced acceptor states with increasing the $Al(NO_3)_3$ treatment time. In such a circumstance, even though the extremely low negative voltage is applied, the leakage current density is significantly increased by the accumulated large number of holes at the Si surface. Therefore, the 5 min $Al(NO_3)_3$-treated sample still shows low leakage current density due to the insufficient upward band bending and formation of Al-induced acceptor states. The crucial evidence for the existence of negative fixed charges in the oxide layer is demonstrated later in Section 4.5.4.

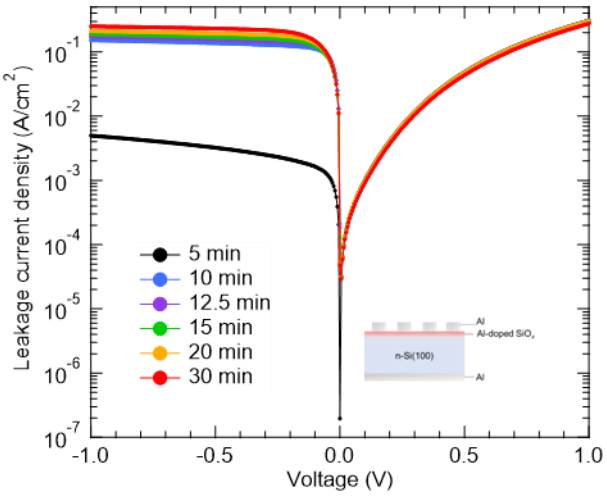

Fig. 4.18 *J–V* characteristics of MOS structures formed using the samples treated in boiled 0.25 mol L^{-1} $Al(NO_3)_3$ aqueous solution for various treatment times.

Figure 4.19 shows the leakage current density of the MOS samples at various applied negative voltages concerning the $Al(NO_3)_3$-treatment time. The leakage current density at voltages of <0.1 V enlarges despite increasing SiO_x thickness. This result implies that the Al-doped SiO_x layers

can realize both good surface passivation quality and sufficient hole tunneling and overcome the problem of the conventional SiO_x layers. More AlO_4 structure is created in the SiO_2 structure by the longer $Al(NO_3)_3$-treatment time due to the structurally stable tetrahedral compounds. As described in Figure 4.4, since the SiO_2 (Si^{4+}) component is gradually increased with increasing $Al(NO_3)_3$-treatment time, the incorporated Al is possibly more stable as a formation of AlO_4 structure, resulting in more formation of Al-induced acceptor states and the induction of upward band bending of Si surface. In contrast, the AlO_4 structure is hardly generated in the SiO_x, with many suboxides formed by the shorter $Al(NO_3)_3$-treatment time due to the structurally unstable compounds. Considering that the trap-assisted tunneling current proportionally enlarges with increasing the density of trap states and the depth of the level in the trap [35], the increased factors might overcompensate the growing barrier thickness with increasing $Al(NO_3)_3$-treatment time, realizing an increase in a hole tunneling. Moreover, according to Figure 4.18, a current density of ~40 mA cm^{-2} at a maximum power point for typical high-efficiency c-Si solar cells leads to a voltage drop of −0.02 V for the samples with Al-doped SiO_x formed by $Al(NO_3)_3$ treatment. This voltage drop is much less than the reported value of 0.06 V for the samples with Al-doped SiO_x formed by ALD and rapid thermal oxidation (RTO) in the literature [4].

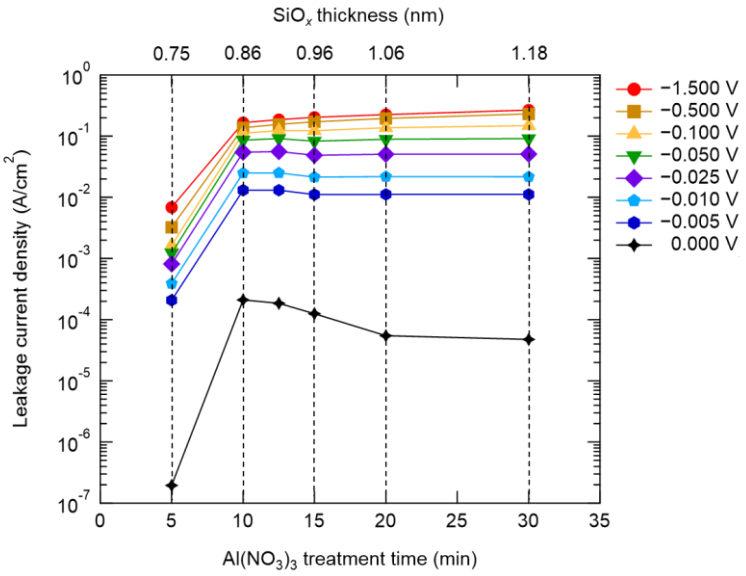

Fig. 4.19 Leakage current density of MOS samples with Al-doped SiO_x formed in boiled 0.25 mol L^{-1} $Al(NO_3)_3$ (aq.) at various applied negative voltages concerning the $Al(NO_3)_3$-treatment time.

4.5.2 Contact resistivity

For the evaluation of ρ_c, palladium (Pd) circular electrodes with various sizes (diameter of 0.3–3.2 mm) were deposited on the surface of $Al(NO_3)_3$-treated p-type Si(100) substrates through a mask by thermal evaporation in a vacuum chamber at a pressure of 9×10^{-4} Pa. For the rear side of the samples, the surface was treated with a cotton swab dipped in 5% diluted HF aqueous solution in advance until the hydrophobic surface was visually confirmed. The full-area Al electrodes were thermally evaporated on the rear surfaces, which were scratched in advance to obtain a good ohmic contact. The Pd circular electrodes (Cox and Strack pattern) and metal–oxide–semiconductor (MOS) structure of Pd circular electrode/Al-doped SiO_x/p-Si(100)/Al are shown in Figure 4.20.

Current–voltage (*I–V*) measurements were performed for each-sized electrode using a precision semiconductor parameter analyzer (Hewlett–Packard Company, 4156 A) mounted with a kelvin-type 4-terminal connection system in the dark at RT. *I–V* characteristics were measured when the negative bias was applied to the Pd top electrode to acquire the hole tunneling current at the hole accumulation condition for the p-type Si substrates. By the Cox and Strack method [36], R_{total} for each electrode was calculated under negative voltages from ~1 to ~15 mV, corresponding to a current density of ~40 mA cm^{-2} at a typical maximum power point of c-Si solar cells [37]. R_{spread} was calculated using the equation proposed in the literature [36], and each $R_{total} - R_{spread}$ was plotted concerning the inverse values of electrode areas. ρ_c was estimated by extracting the slope obtained from the linearly fitted curve.

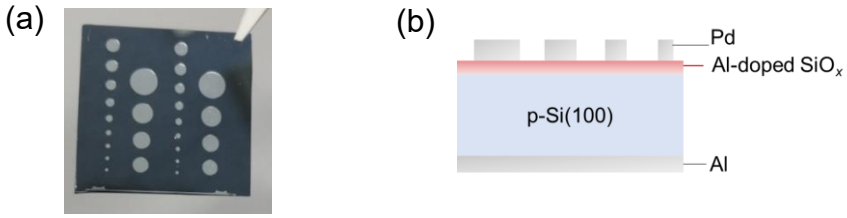

Fig. 4.20 **(a)** Deposited and used Pd circular electrodes (Cox and Strack pattern) and **(b)** metal–oxide–semiconductor (MOS) structure of Pd circular electrodes/Al-doped SiO_x/p-Si(100)/Al referred to the structure in the literature [37].

Figure 4.21 (a) displays dark *I–V* curves obtained for circular electrodes of various sizes and Figure 4.21 (b) describes the R_{total}, calculated from Figure 4.21 (a), subtracted by R_{spread} ($R_{total} - R_{spread}$) as a function of inverse electrode areas. The fitted curve in Figure 4.21 (b) shows good linearity and the ρ_c was calculated to be 20 mΩ cm^2 from the slope of the fitted curve. The

estimated value is one order lower magnitude compared with those of the ALD Al–O (1 ALD cycle)/thermal-SiO_2 stacks reported in the literature [37]

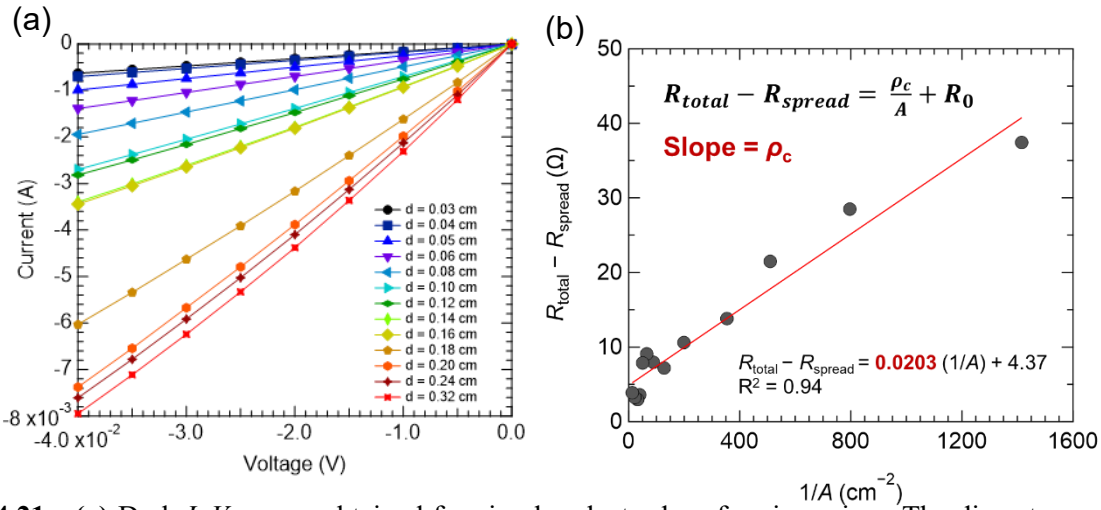

Fig. 4.21 **(a)** Dark *I–V* curves obtained for circular electrodes of various sizes. The diameters of the electrodes (*d*) are shown in the inset. **(b)** R_{total} subtracted by R_{spread} ($R_{total} - R_{spread}$) as a function of inverse electrode areas.

4.5.3 Sheet resistance

The sheet resistance (R_{sheet}) of Al-doped SiO_x/n-Si(100) was measured using the four-point probe method (Mitsubishi Chemical Analytech Co., Ltd., Loresta-AX MCP-T370) in the dark condition. As a reference, the sheet resistance of non-doped SiO_x/n-Si(100) and HF-treated n-Si(100) were also evaluated. The non-doped SiO_x with a thickness of ~1 nm was formed by immersing a Si substrate into 70 wt.% concentrated nitric acid aqueous solution at room temperature for 10 min. Besides, R_{sheet} was not able to be measured for the non-doped SiO_x surface because the resistances are higher than the limitation of the order of 10^7 Ω sq^{-1}; Al-doped SiO_x allowed measuring the R_{sheet} and 5.85×10^5 Ω sq^{-1} was obtained on average of 18 measurement points in 30×25 mm sized sample. This result, therefore, implies that holes are accumulated at the surface of Si, reducing the R_{sheet} to a measurable level. However, considering the application for the solar cell, the value is considerably huge as an emitter layer on the n-type c-Si solar cells. However, under the light illumination condition, R_{sheet} was drastically reduced, two orders of magnitude lower than those in the dark condition. In this experiment, the sample surface was illuminated at 1 sun intensity. The Measurement setup of the R_{sheet} is displayed in Figure 4.22. Since the Al-doped SiO_x layer is formed by a dipping process, the layer is formed on both sides of the sample. To avoid the shadow of the four-point probe, the measurements were performed on the rear side of the sample, whereas the 1 sun was illuminated on the front side of the sample. This measurement can come into effect

because of the sufficiently high bulk lifetime of the used Si substrate (τ_{bulk} >10 ms), which means a longer diffusion length of hole in c-Si (~0.36 cm) compared to the thickness of the used Si substrate (0.028 cm), leading to the sufficient hole accumulations at the surface of the rear side as well. Eventually, an R_{sheet} of 4.86×10^3 Ω sq^{-1} was obtained under the 1 sun illumination. This drastic reduction of R_{sheet} might be attributed to increasing the concentration of accumulated holes at the Si surface due to further strong upward band bending induced by enhancement of trapping excited electrons at the Al-induced acceptor states, existing in combination with Q_f enlargement. This result suggests that the inversion layer induced by an ultrathin Al-doped SiO_x can possibly be used as a p^+ emitter for the n-type c-Si solar cells under light illumination. As a reference, a non-doped ultrathin SiO_x layer with a thickness of ~1 nm was formed by immersing a Si substrate into HNO_3 aqueous solution for 10 min at RT. The sheet resistances in the dark and 1 sun illumination condition were not able to be measurable because of the high resistance over the measurement limitation of >10^7 Ω sq^{-1}. Hence, Al-doped SiO_x demonstrated huge advantage with more conductive layer less than two order magnitude of R_{sheet} compared to the non-doped SiO_x surface. The sheet resistances of Al-doped SiO_x/n-Si(100) in the dark and under light illumination are shown in Table 4.1.

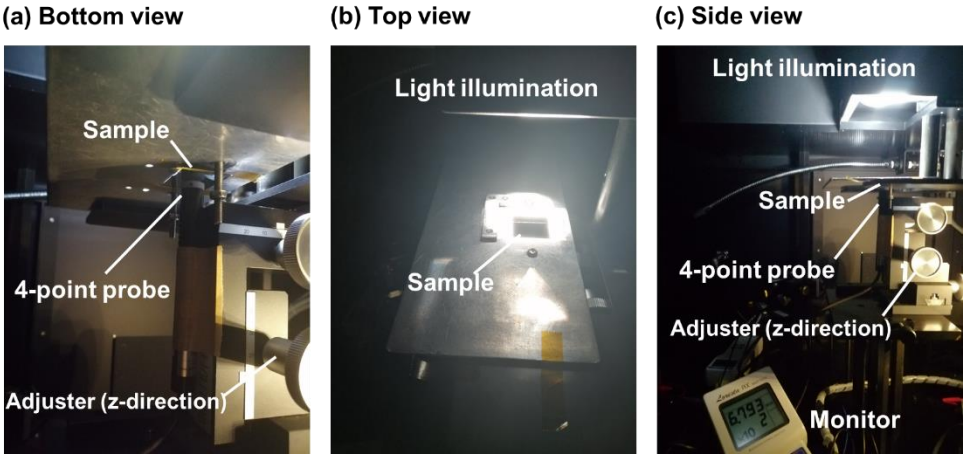

Fig. 4.22 Measurement setup of the R_{sheet} under light illumination.

Table 4.1 Sheet resistances of Al-doped and non-doped SiO_x/n-Si(100) in the dark and under 1 sun illumination.

Measurement condition	Al-doped SiO_x/n-Si(100)	Non-doped SiO_x/n-Si(100)
Dark	5.85×10^5 Ω sq^{-1}	>10^7 Ω sq^{-1}
Light illumination (1 sun)	4.86×10^3 Ω sq^{-1}	>10^7 Ω sq^{-1}

4.5.4 Determination of Fixed charge density and Interface state density

In general, to estimate Q_f and N_{it}, capacitance–voltage (C–V) measurement is conducted and calculated from the obtained capacitance of oxide (C_{ox}) [38], but such an ultrathin layer hardly evaluates these values due to the high leakage current, causing the lack of accuracy of measuring C_{ox} comes from an insufficient carrier accumulation at the interface of dielectric layer and semiconductor. Thus, one of the promising solutions to analyze without such a lack of accuracy is the estimation from V_{bi} generated by an ultrathin layer. As described in the literature [39], surface hole density (p_s) is exponentially proportional to the $V_{bi,}$ and Q_f is proportional to the squared p_s. Assuming the dielectric layer with a sufficient negative Q_f, the relationship among p_s, V_{bi}, and Q_f is described as,

$$Q_f = -\sqrt{2k_B T \varepsilon_{si} p_d \exp(\frac{V_{bi}}{V_T})}, \tag{4.5}$$

$$p_s = p_d \exp\left(\frac{V_{bi}}{V_T}\right), \tag{4.6}$$

where p_d is the concentration of holes at a depth of the flat band region and V_T is the thermal voltage, respectively. Hence, Q_f can be easily estimated from the measured and analyzed V_{bi} value. In addition, N_{it} is proportional to S_{eff} and can be described as follows.

$$N_{it} = \frac{S_{eff}}{\sigma_n \nu_n \left(N_{dop} + \Delta n\right)\left(\frac{2k_B T \varepsilon_{Si}}{Q_f^2}\right)} \tag{4.7}$$

Where σ_n is the electron capture cross section, and ν_n is the velocity of the electron, respectively. Hence, N_{it} can also be estimated from the analyzed S_{eff} value from measured τ_{eff}.

For the determination of Q_f and N_{it}, the oxide on the rear side of the $Al(NO_3)_3$-treated sample was removed with a cotton swab dipped in 5% diluted HF aqueous solution in advance until the hydrophobic surface was visually confirmed. The full-area Al electrodes were thermally evaporated on the rear surfaces, which were scratched in advance to obtain a good ohmic contact. Subsequently, a C–V measurement was performed to obtain depletion capacitance in the negative voltage region using a mercury (Hg) probe. The V_{bi} was evaluated by Mott-Schottky plot analysis [40], linearly fitted capacitance in the voltage range of −2.5 to 0 V.

Figure 4.23 depicts the Mott-Schottky plot for n-type Si(111) samples with Al-doped SiO_x

formed in boiled 0.25 mol L^{-1} $Al(NO_3)_3$ aqueous solution for 12.5 min. V_{bi} was extracted to be 0.870 V from the interception of the extrapolated fitted line concerning the voltage. The large V_{bi} of Al-doped SiO_x/n-Si means that strong upward band bending is induced at the surface of n-Si. This is crucial evidence for the existence of a large number of negative charges in the Al-doped SiO_x layer, and Q_f was calculated to be -3.21×10^{12} cm^{-2}. Furthermore, assumed σ_n is 1.8×10^{-14} cm^2, determined for Al_2O_3/Si in the literature [41], the N_{it} was estimated to be 1.43×10^{12} cm^{-2} using $S_{eff,\,max}$ of 23.3 cm s^{-1}, which was analyzed from measured τ_{eff} of Al-doped SiO_x/n-Si(111). This N_{it} value is very close to the N_{it} of 1.03×10^{12} cm^2 for HNO_3 grown SiO_x, ~4.03 × 10^{12} cm^2 for HCl grown SiO_x, and ~2.73×10^{12} cm^2 for H_2SO_4 + H_2O_2 grown SiO_x [12]. Hence, the surface passivation mechanism originated from chemical passivation and field-effect passivation. However, in general, since the wet chemical oxide shows very low τ_{eff} of ~5 μs, more than two orders of magnitude lower than Al-doped SiO_x, the field effect passivation is the main scheme for this surface passivation mechanism. The determined Q_f and N_{it} are summarized in Table 4.2.

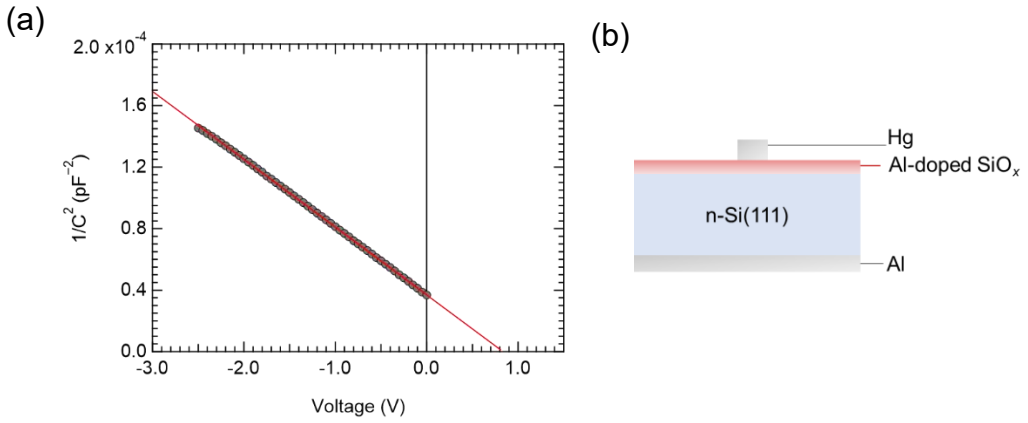

Fig. 4.23 **(a)** Mott-Schottky plot for the samples of n-type Si(111) with Al-doped SiO_x formed in boiled 0.25 mol L^{-1} $Al(NO_3)_3$ (aq.) for 12.5 min. **(b)** Metal–oxide–semiconductor (MOS) structure of Hg probe/Al-doped SiO_x/n-Si(111)/Al.

Table 4.2 Determined Q_f and N_{it}

Sample structure	Q_f (cm^{-2})	N_{it} (cm^{-2})
Al-doped SiO_x/n-Si(111)	-3.21×10^{12} cm^{-2}	1.43×10^{12} cm^{-2}

Using PC1D simulation software, the estimated Q_f values were confirmed to determine whether they were reasonable. Assuming an estimated Q_f value of -3.21×10^{12} cm^{-2} on the n-type Si substrate with a N_{dop} of 2×10^{15} cm^{-3} and a thickness of 200 μm, the p_s, surface electron density

(n_s) and V_{bi} were calculated to 3.974×10^{19} cm^{-2}, 2.516 cm^{-2}, and 0.887 V, respectively. Hence, the simulated V_{bi} agrees well with the measured value of 0.870 V. The simulated carrier densities and energy bands are shown in Figures 4.24 and 4.25. These simulated results show that the c-Si surface is strongly inverted over the depth of ~250 nm in the short-circuit and under the dark condition.

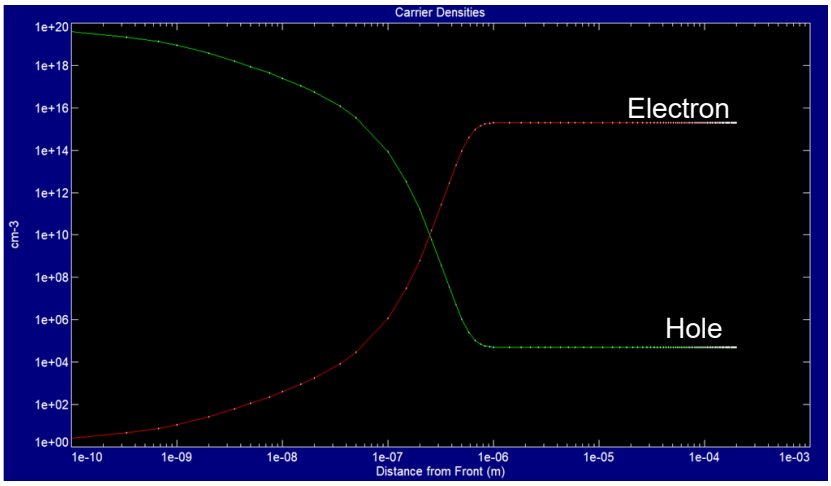

Fig. 4.24 Depth profile of carrier densities for the negatively charged n-type c-Si surface.

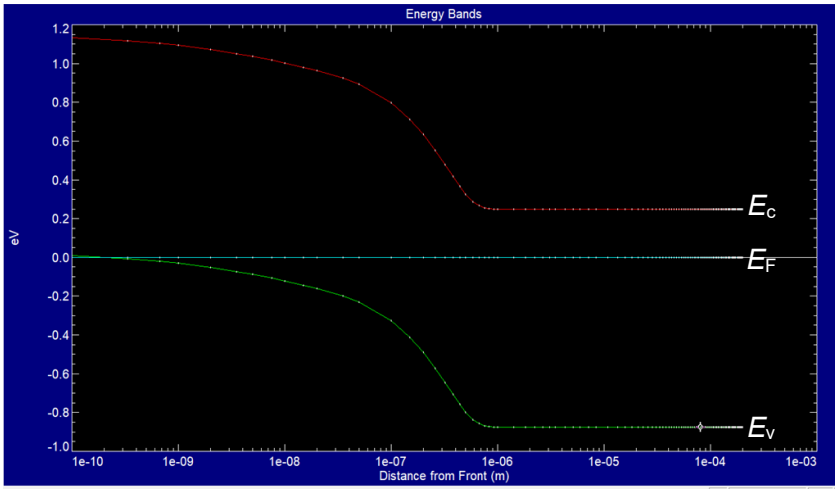

Fig. 4.25 Depth profile of energy bands for the negatively charged n-type c-Si surface.

4.6 Carrier selectivity of Al-doped SiO_x

Here, the selectivity (S_{10}) [42] was estimated to be 13.3 by using the equation below with two analyzed values of J_0 = 65 fA cm^{-2} and ρ_c = 20 mΩ cm^2,

$$S_{10} = \log_{10}\left(\frac{V_{th}}{J_0\rho_c}\right), \tag{4.8}$$

where V_{th} represents thermal voltage. In addition, assuming the optimum contact fraction f_{max} = 1, the maximum efficiency (η_{max}) can be calculated using S_{10} obtained in the equation below [42],

$$\eta_{max}(S_{10}) = [(2.452\,S_{10} - 4.240)^{-19.52} + (29.21)^{-19.52}]^{-\frac{1}{19.52}}. \tag{4.9}$$

Since the η_{max} can be calculated to 27.7% with S_{10} of 13.3, this carrier-selective contact has a high potential because of a comparable passivating contact with other technology that has been reported [37, 43–52]. Note that since Ag electrode degraded surface passivation as described in Chapter 5, but the J_0 was analyzed for a no Ag deposited sample and the ρ_c was analyzed using p-Si as a substrate and Pd as a contact electrode, the analyzed J_0 and ρ_c are not the practical value due to the different sample structure from the real Al-COIL device structure (Ag/Al-doped SiO_x/n-Si). To compare other carrier-selective passivating contacts, the relationship among J_0, ρ_c, and S_{10} with various carrier-selective passivating contacts are displayed in Figure 4.26. The red star represents the carrier selectivity of Al-doped SiO_x analyzed in this study. It can be recognized that the S_{10} value is comparable to other technology, but it must be further improved to achieve high-efficiency c-Si solar cells close to the theoretical limit.

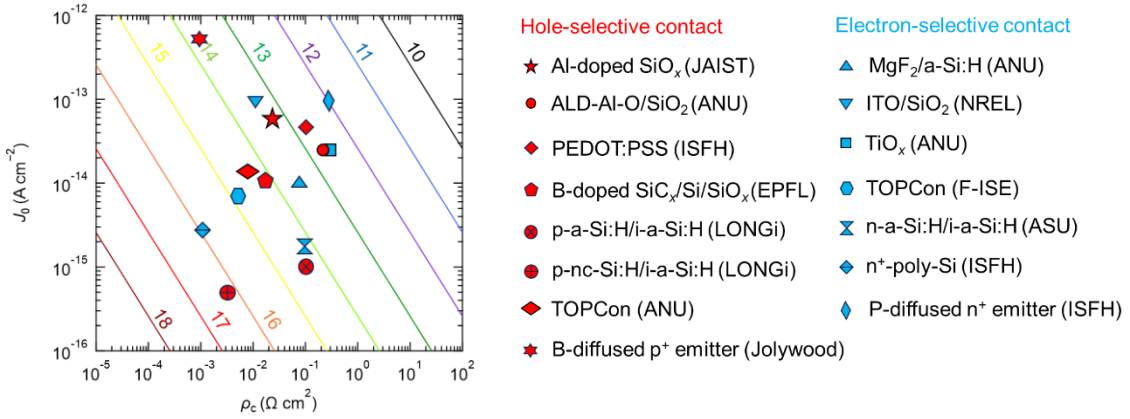

Fig. 4.26 J_0, ρ_c, and S_{10} for various passivating contacts. Each solid line shows S_{10} values from 10 to 18.

4.7 Effect of surface orientation

4.7.1 Surface passivation on Si(100) and Si(111)

Figure 4.27 shows τ_{eff} and the corresponding $S_{eff,\,max}$ as a function of $Al(NO_3)_3$ treatment time for the various $Al(NO_3)_3$ molar concentrations from 0.15 to 0.50 mol L^{-1} for Si(100) and Si(111) substrates. It can be seen τ_{eff} improvement for Si(111) substrates relatively in a short time, especially in a low $Al(NO_3)_3$ concentration condition, shows a significant difference in the process time by reaching the maximum τ_{eff}. However, both orientation shows a significant increase in τ_{eff} for a short process time with increasing the $Al(NO_3)_3$ molar concentration; it is presumably due to the fast oxidation. For all concentration conditions, Si(100) enabled higher surface passivation. For instance, at the condition of 0.50 mol L^{-1}, 10 min treated (100)-oriented sample shows a relatively high τ_{eff} of 556 µs but 5 min treated (111)-oriented sample shows a lower τ_{eff} of 423 µs. Besides, Si(111) showed a partially high τ_{eff} region can be observed for 7.5 min in 0.15 mol L^{-1}, as shown in Figure 4.28. Furthermore, the highest maximum τ_{eff} was 933 µs. Since such a short process time allows us to obtain excellent τ_{eff} and a higher concentration process did not show such a high maximum τ_{eff}, Si(111) might have a narrow process window. The lower concentration and longer treatment time will be a promising solution for obtaining a higher surface passivation for the Si(111) surface. As observed in Figure 4.11, further $Al(NO_3)_3$ treatment caused the τ_{eff} degradation for all conditions and both orientated substrates. This might have originated from a lack of electron trapping in the Al-induced acceptor states due to the thickened SiO_x formed by the more prolonged treatment suppressing the electron tunneling through the SiO_x layer from Si to the acceptor states, resulting in low induction of the negative fixed charges and the suppression of the upward band bending of Si surface. In particular, this significant degradation for Si(111) was confirmed at the relatively high condition of 0.50 mol L^{-1}. H. Angermann *et al.* reported that Si(111) shows lower N_{it} compared with Si(100) in wet-chemical passivation schemes such as SiO_2 formed by RCA or hot water. They proposed that a faster oxidation rate for Si(100) leads to higher N_{it}, originating from lower stability of H-terminated Si(100) surfaces against reoxidation in air. In addition, the electronegativity difference between the two bonded substituents such as H, OH, and F and the Si occurs a stronger polarization of the Si back bond in Si(100), leading to a heavy attack of oxidants [56]. However, in the case of $Al(NO_3)_3$ oxidation, the oxidation reaction on Si(111) seems faster than on Si(100). If so, there is a discrepancy in the oxidation rate, but the relatively low surface passivation on Si(111) can be explained by this degradation model.

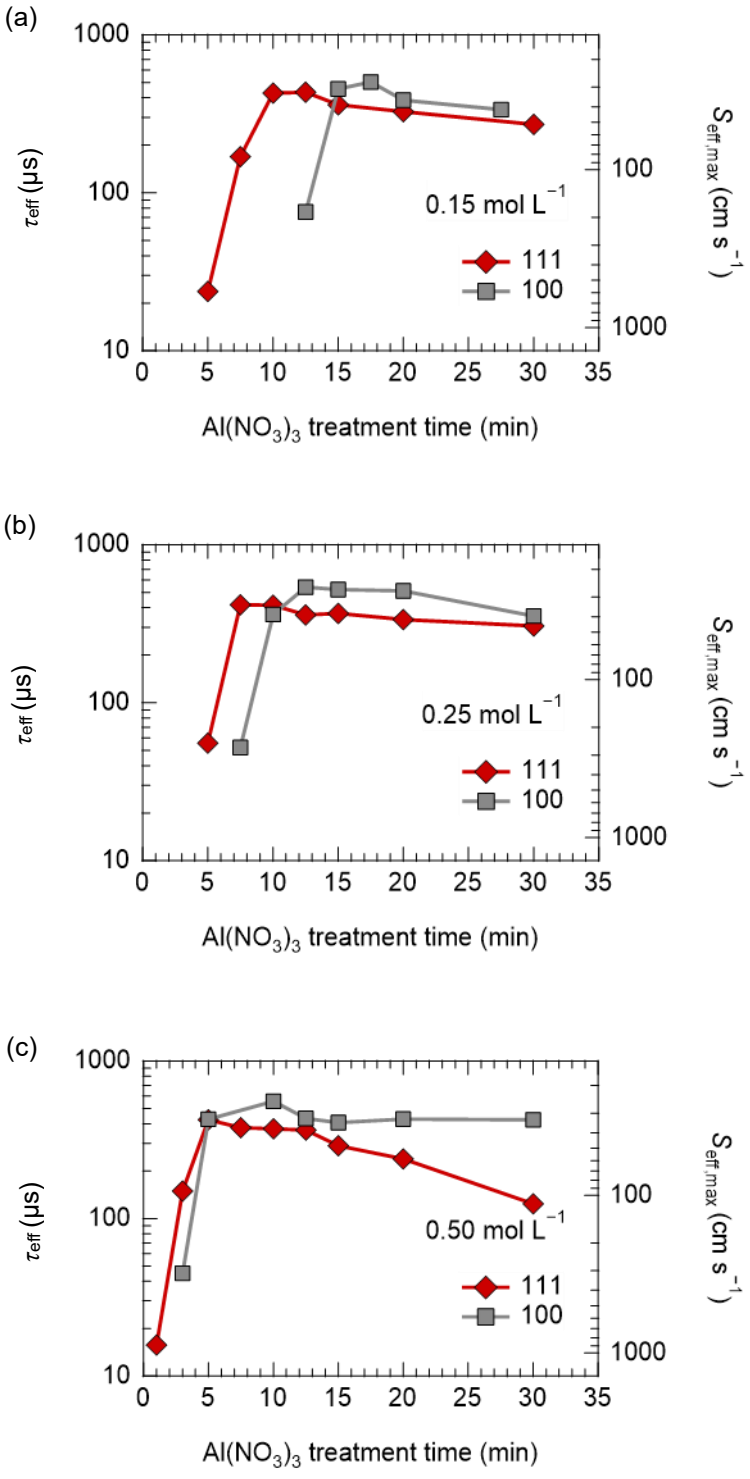

Fig. 4.27 τ_{eff} and $S_{eff,max}$ as a function of $Al(NO_3)_3$ treatment time for the various $Al(NO_3)_3$ molar concentrations: **(a)** 0.15, **(b)** 0.25, **(c)** 0.50 mol L^{-1} for Si(100) and Si(111) substrates.

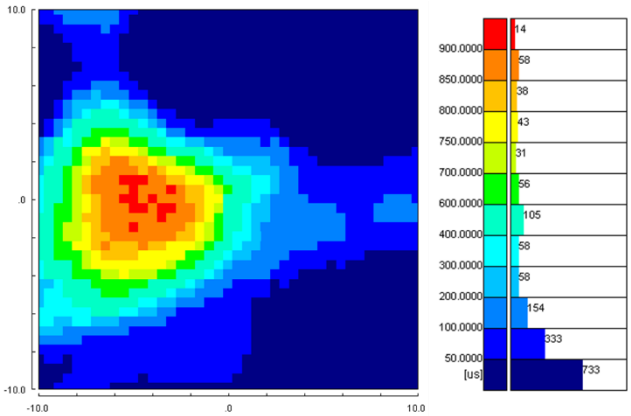

Fig. 4.28 τ_{eff} mapping of $Al(NO_3)_3$-treated Si(111) for 7.5 min in 0.15 mol L^{-1} $Al(NO_3)_3$ (aq.).

4.7.2 Chemical bond states on Si(100) and Si(111)

Figure 4.29 illustrates the Si 2*p* and Al 2*p* core-level XPS spectra for Si(111) and (100) samples treated in boiled $Al(NO_3)_3$ aqueous solution with a molar concentration of 0.25 mol L^{-1} for various treatment times in the range of 2.5 to 30 min. The observed peak around 102.5–103 eV and ~75 eV can be assigned to SiO_2 (Si^{4+}) and Al–O, respectively.

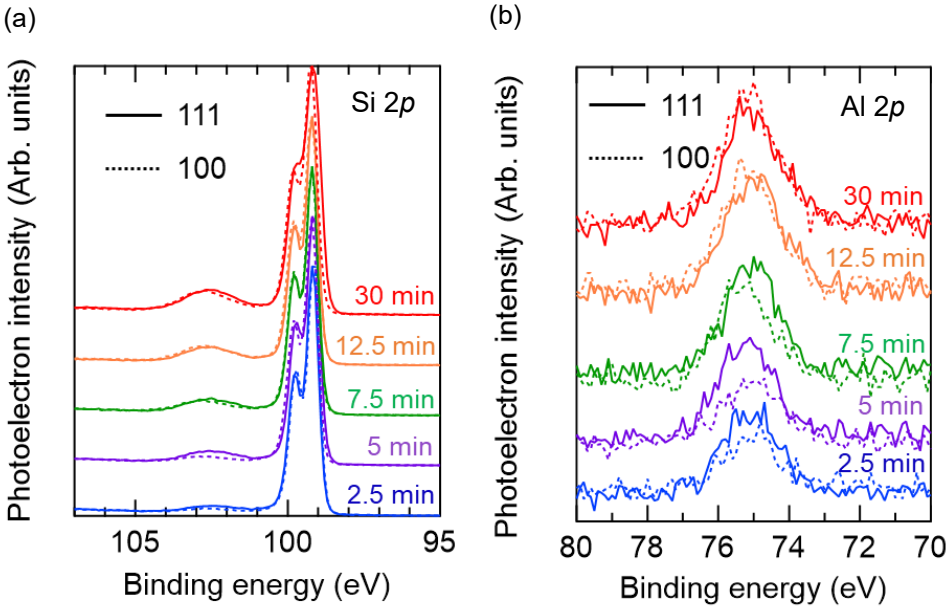

Fig. 4.29 **(a)** Si 2*p* and **(b)** Al 2*p* core-level XPS spectra for Si(111) and (100) samples treated in boiled $Al(NO_3)_3$ (aq.) with a molar concentration of 0.25 mol L^{-1} for various treatment times.

Their peaks were fitted with the Voigt function, and the evaluated SiO_2 composition, SiO_x thickness, and oxidized Al atomic concentration as a function of $Al(NO_3)_3$ treatment time are shown in Figure 4.30 (a), (b), and (c), respectively. As expected, the SiO_x on Si(111) was thicker than that on Si(100) and formed in a short treatment time. Hence, Si(111) has a higher growth rate in the initial oxidation reaction. Depending on the higher growth rate, SiO_2 composition is also higher value from the initial oxidation reaction. However, the thickness and the SiO_2 composition for both orientations are almost the same at 30 min treatment time. Similarly, the oxidized Al atomic concentration of Si(111) is higher than that of Si(100) in a short process time of 5 min. After that, the atomic concentration slightly fluctuated between 1.2–1.4 at.% and saturated at ~1.2 at.% for both orientations. Hence, Al oxides are formed in the initial reaction stage, especially on the Si(111) surface. Considering the fast oxide growth rate of Si(111), the faster oxidation rate causes higher N_{it} on Si(111). One possible reason for the higher oxidation rate is that the terminated OH on the Si(111) has a higher density of electrons due to the larger number of Si back bonds, providing electrons from three back bond Si to one terminated OH. Hence, a nucleophilic Si-OH is highly reacting with Al precursor as a Lewis acid, and negatively charged Al oxides might assist the O^- diffusion to the Si surface by the repulsion force between AlO_4^- and O^-, causing faster formation of Al oxides and SiO_x.

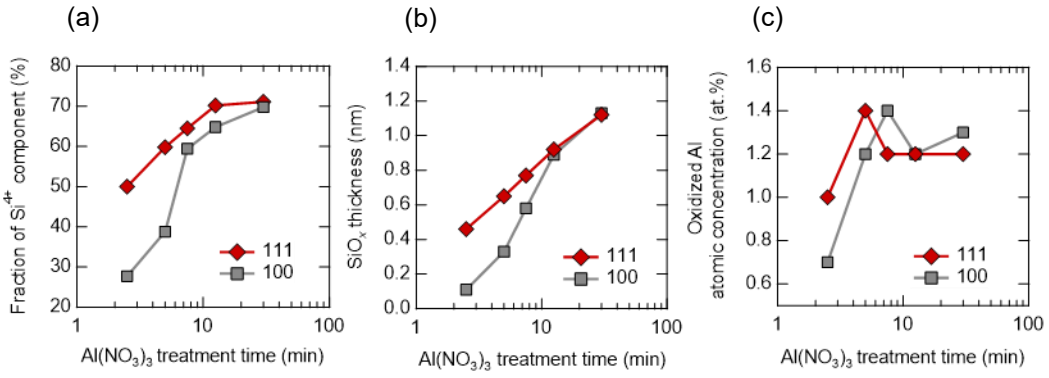

Fig. 4.30 (a) SiO_2 composition, **(b)** SiO_x thickness, and **(c)** oxidized Al atomic concentration as a function of $Al(NO_3)_3$ treatment time for Si(111) and (100) samples with Al-doped SiO_x formed in boiled $Al(NO_3)_3$ (aq.) with a molar concentration of 0.25 mol L^{-1} for various treatment times.

4.7.3 Electrical properties on Si(100) and Si(111)

Tunneling current density

Figure 4.31 represents *J–V* characteristics of MOS structures on Si(111) and Si(100) formed using the samples treated in boiled 0.25 mol L^{-1} $Al(NO_3)_3$ aqueous solution for various treatment times from 2.5 to 30 min in the applied voltage range of −1 to 0 V. The sample fabrication and evaluation were performed using the same procedure and method as described in 4.5.1. For all the treatment time conditions, Si(111) samples show higher leakage current density, meaning higher tunneling current density through the Al-doped SiO_x on Si(111) substrates. In addition, the significant difference was confirmed at the short treatment time, especially in 2.5 min, four orders of magnitude higher than that of Si(100) substrate. Furthermore, the leakage current density was gradually increased with increasing treatment time, while the 30-minute treated sample shows an order decrease in the leakage current density due to the weakened upward band bending, resulting in a reduction in the hole selectivity. This result shows the same tendency with the amount of SiO_2 component and SiO_x thickness except for 30 min treated samples. The higher leakage current density on Si(111) is highly related to the higher SiO_2 content and larger SiO_x thickness. Moreover, as shown in Figure 4.30 (b), in a short treatment time until 10 min, τ_{eff} of Si(111) showed higher values. Hence, these results imply that Si(111) shows faster induction of hole selectivity because of the faster oxide growth rate.

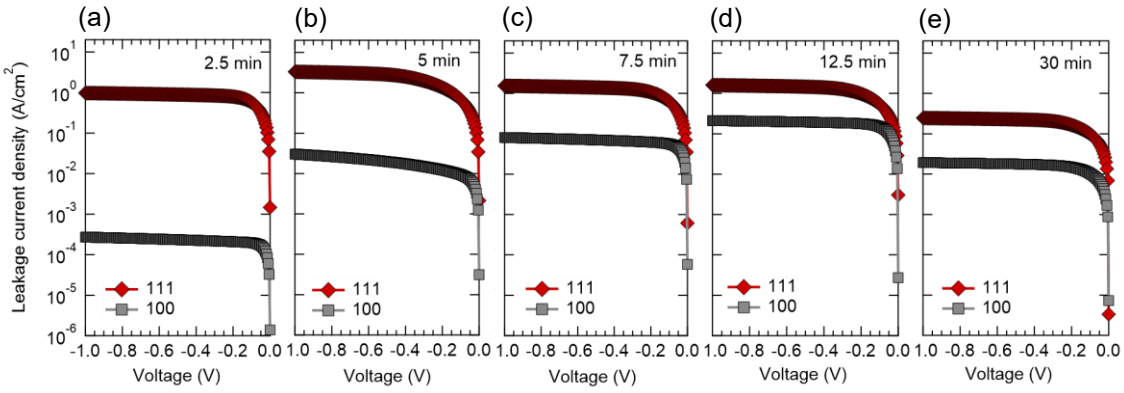

Fig. 4.31 *J–V* characteristics of Al circular electrode/Al-doped SiO_x/n-Si/Al MOS structures on Si(111) and Si(100) formed using the samples treated in in boiled 0.25 mol L^{-1} $Al(NO_3)_3$ aqueous solution for various treatment times: **(a)** 2.5 min, **(b)** 5min, **(c)** 7.5 min, **(d)** 12.5 min, and **(e)** 30 min.

Sheet resistance on Si(100) and Si(111)

Figure 4.32 describes an R_{sheet} of Al-doped SiO_x/n-Si(100) or (111) under the dark or 1 sun illumination. Si(111) shows one order of magnitude lower R_{sheet} compared to Si(100) in the dark condition. Moreover, 1 sun illumination realized a further two orders of magnitude decrease in R_{sheet}, obtaining 317 Ω sq^{-1} on average. Since solar cell device operates under 1 sun illumination as a standard condition and the conventional c-Si solar cell has a pyramidal textured Si surface with (111)-oriented facet, the result under the 1 sun illumination condition demonstrated practical values as a comparable R_{sheet}, even though it is still one order higher than that of 50–85 Ω sq^{-1} for the conventionally formed B-diffused p^+ emitter surfaces [47]. Regarding tunneling current density and sheet resistance, the Si(111) surface has a higher potential for hole-selective contacts. In addition, as described above, since the pyramidal textured Si surface consists of (111)-facets, it will be favorably implemented for this type of hole-selective contact.

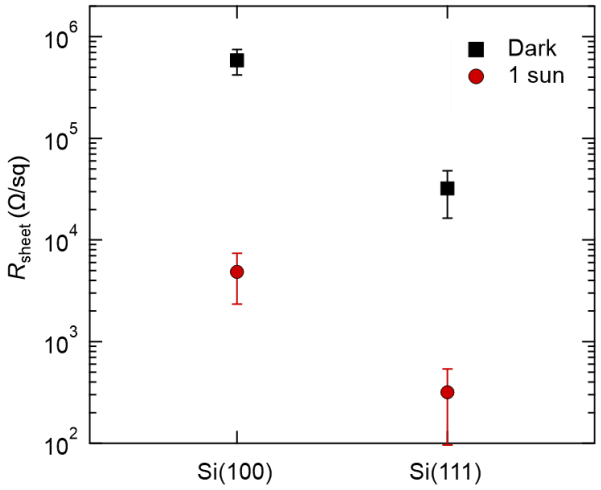

Fig. 4.32 R_{sheet} of Al-doped SiO_x/n-Si(100) or (111) in the dark or under 1 sun illumination.

4.7.4 Effect of light illumination

Influence on sheet resistance

To investigate the influence of light illumination on the sheet resistance, R_{sheet} values were acquired under the monochromatized light with a wavelength of 550 nm and various areal photon densities in the range of 5×10^{12} –1×10^{14} cm^{-2}. Figure 3.33 (a) shows a measuring sample under light illumination with a wavelength of 550 nm and an areal photon density of 1×10^{14} cm^{-2}. Figure 4.33 (b) shows R_{sheet} values of Al-doped SiO_x/n-Si(111) measured under the monochromatized light illumination with a wavelength of 550 nm as a function of areal photon density. As a result, R_{sheet}s were slightly decreased with increasing light intensity. Since the obtained data plots can be linearly fitted with a good correlation coefficient of 0.996, R_{sheet} positively correlates to light illumination intensity.

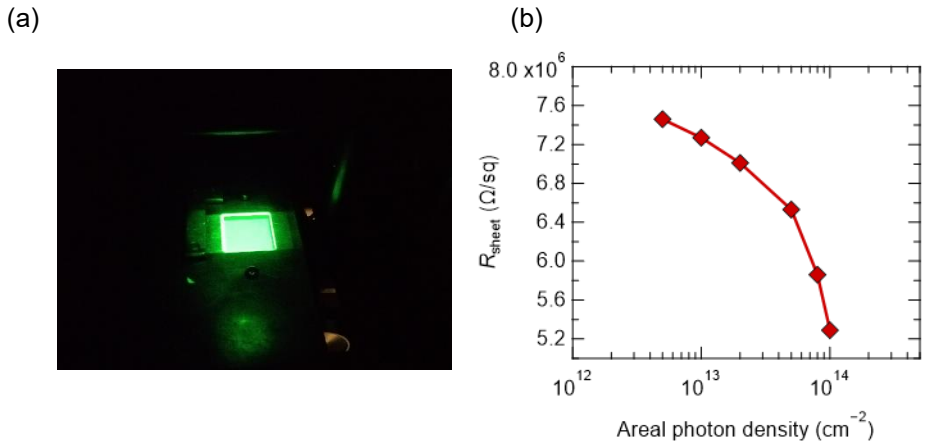

Fig. 4.33 **(a)** Measuring sample under the light illumination with a wavelength of 550 nm and an areal photon density of 1×10^{14} cm^{-2}. **(b)** R_{sheet} of Al-doped SiO_x/n-Si(111) measured under the monochromatized light illumination with a wavelength of 550 nm as a function of areal photon density.

Influence on surface passivation

Figure 4.34 (a) shows τ_{eff} of $Al(NO_3)_3$-treated n-Si(111) in boiled 0.25 mol L^{-1} $Al(NO_3)_3$ aqueous solution for 12.5 min as a function of areal photon density for an excitation pulsed laser light with a wavelength of 349 nm. The τ_{eff} were acquired using μ-PCD. As described in the figure, τ_{eff} was significantly increased with increasing areal photon density, and this effect cannot be observed for the non-doped SiO_x/n-Si structure. This increase might be attributed to the enhancement of the negative Q_f induced by electron trapping in the Al-induced acceptor states due to the instantly generated excess carriers during the illumination of the pulsed laser light, increasing the upward band bending and enhancement of field-effect passivation.

In addition, the τ_{eff} measurement under the steady state light illumination was performed. Figure 4.34 (b) shows τ_{eff} of $Al(NO_3)_3$-treated Si(111) in boiled 0.25 mol L^{-1} $Al(NO_3)_3$ (aq.) for 12.5 min as a function of the intensity of steady-state light. A pulsed laser light with a wavelength of 904 nm was used to generate excess carriers. Generally, although τ_{eff} decreases under the steady state light illumination due to reducing the band bending, resulting in the degradation of field-effect passivation. However, in this Al-doped SiO_x/n-Si case, a drastic increase of τ_{eff} was confirmed under the illumination with a low-intensity steady state light below 0.7 suns. This increase might also originate from the enhancement of the negative Q_f by the steady-state light illumination, resulting in the upward band bending increase and enhancement of field-effect passivation.

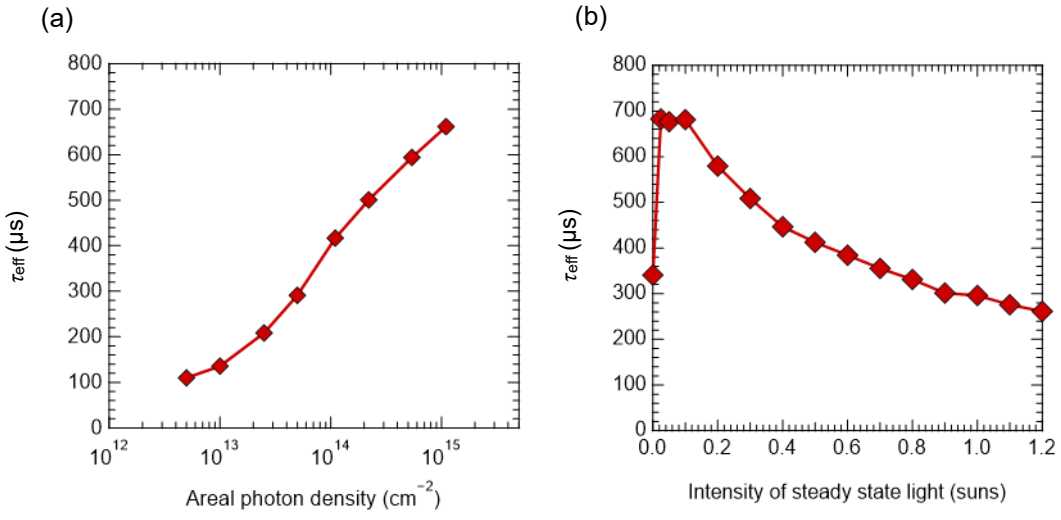

Fig. 4.34 **(a)** τ_{eff} as a function of areal photon density for an excision pulsed laser light with a wavelength of 349 nm. **(b)** τ_{eff} as a function of the intensity of steady-state light measured using an excision pulsed laser light with an areal photon density of 1×10^{13} cm^{-2} and wavelength of 904 nm. Both measurements were conducted for the same sample.

Moreover, Δn dependency of τ_{eff} was investigated before and after light illumination. Figure 4.35 illustrates τ_{eff} as a function of Δn acquired using QSSPC before and after the illumination of laser light with a wavelength of 349 nm and an areal photon density of 1.1×10^{15} cm^{-2}, mounted in a μ-PCD system. The laser light was illuminated on the $Al(NO_3)_3$-treated Si(111) sample in the area of 44×44 mm with a 1 mm pitch. As clearly seen in Figure 4.35, after the laser light illumination, τ_{eff} was significantly increased, especially in the low injection level of 10^{14} cm^{-3}. This result implies that activation is necessary to obtain high surface passivation, which can be realized by light illumination. Unoccupied Al-induced acceptor states capture the laser-excited electrons from the Si side, leading to highly negative Q_f and field-effect passivation. The significant increase at the low injection level suggests that the surface passivation comes from the field effect induced by the occupied Al-induced acceptor states.

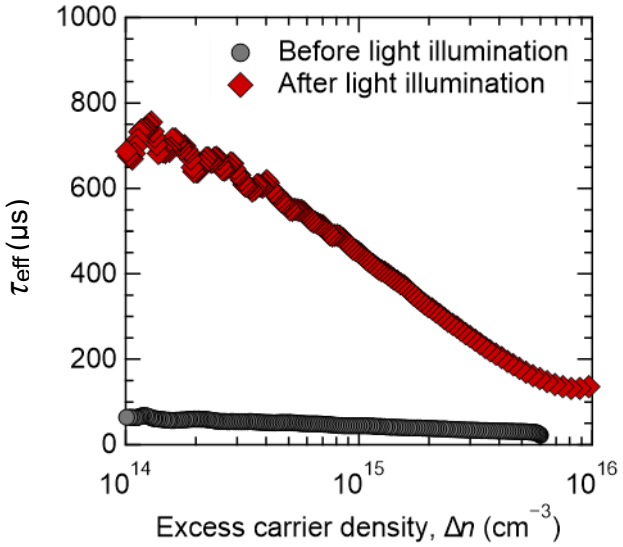

Fig. 4.35 τ_{eff} as a function of excess carrier density (Δn) acquired using QSSPC before and after the laser light illumination with a wavelength of 349 nm and an areal photon density of 1.1×10^{15} cm^{-2}.

4.8 Model of hole-selective passivating contact

Figure 4.36 (a) shows a model for the induction of negative Q_f in the Al-doped SiO_x layer on the Si substrate after or under light illumination. As demonstrated in this experiment, light illumination highly influences the surface passivation and hole tunneling properties. The negative fixed charges are generated due to the captured excited electron in the Al-induced acceptor states existing in the Al-doped SiO_x layer, occurring upward band bending of the Si surface and creating an inversion layer as a hole accumulation layer. Suppose the electrode is deposited on the Al-doped SiO_x layer. In that case, the generated holes selectively tunnel through the oxide layer because the minority (electron) barrier is quite high while the majority (hole) barrier is significantly reduced by the creation of Al-induced acceptor states located below the valence band edge of Si [4]. Hence, electrons are repelled from the surface due to the strong upward band bending induced by the field effect and the high minority barrier, while holes are selectively tunneling through via the Al-induced acceptor states, possibly occurring trap-assisted tunneling; therefore, electrons and holes are effectively separated by the field-effect at the surface of Si. This model for the hole-selective passivating contact is schematically described in Figure 4.36 (b). In this configuration, the inversion layer possibly acts as a p^+ emitter of the n-type c-Si solar cells. Chapter 5 demonstrated this model as a novel device architecture fabricated by a simple wet chemical process.

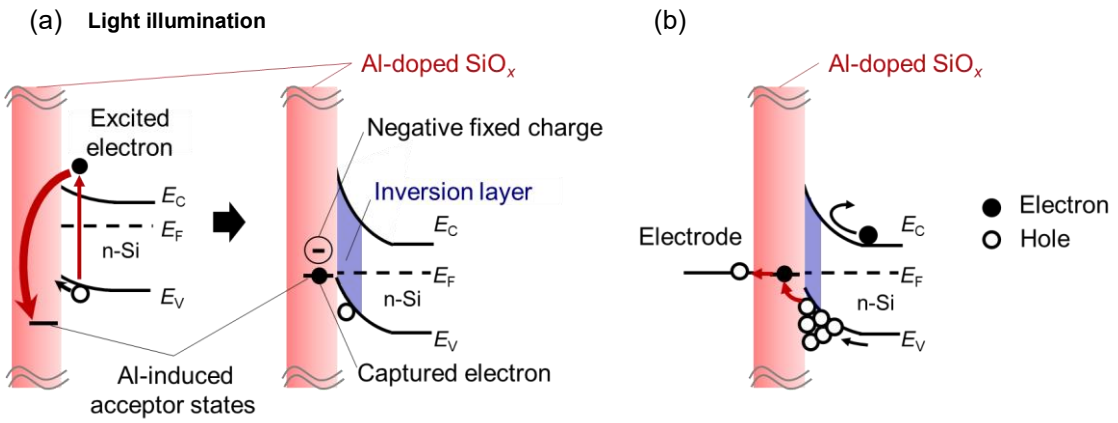

Fig. 4.36 **(a)** Model for the induction of negative Q_f in the Al-doped SiO_x layer on Si substrate after or under light illumination. **(b)** Model for the hole-selective passivating contact of the Al-doped SiO_x layer on Si substrate.

4.9 Summary

This chapter developed an ultrathin Al-doped SiO_x on c-Si substrates by a simple wet chemical process using $Al(NO_3)_3$ aqueous solution. The excellent hole-selective passivating contact properties (S_{eff} of <16 cm s^{-1}, iV_{oc}=670 mV, S_{10}=13.3) were confirmed despite the ~1 nm thick ultrathin layer. The ultrathin layer consists of a bilayer of AlO_y/SiO_x with an Al concentration of ~1 at.%. The *C–V* measurement and simplified extended SRH formalism revealed the ultrathin layer has highly negative charges. The Q_f value was estimated to be -3.2×10^{12} cm^{-2}, contributing excellent hole selectivity by induction of strong upward band bending. Since the estimated N_{it} value was almost the same level as any other wet chemical oxide, the charge-induced field effect is dominant. Si(111) surface also showed excellent surface passivation, greater hole tunneling property, and lower sheet resistance. Interestingly, after the light illumination, the surface passivation quality was significantly increased, and sheet resistance was also significantly improved under 1 sun illumination. The light-illuminated activation effect assists in elucidating the mechanism for the hole-selective passivating contact in the ultrathin Al-doped SiO_x. The increased negative charges might originate from the captured excited electrons in the trap state formed in the ultrathin layer.

References

[1] M. Lenzlinger and E. H. Snow, "Fowler-Nordheim tunneling into thermally grown SiO_2," J. Appl. Phys. **40**, 278 (1969).

[2] N. E. Grant and K. R. McIntosh, "Passivation of a (100) silicon surface by silicon dioxide grown in nitric acid," IEEE Electron Device Lett. **30**, 922 (2009).

[3] T. Matsumoto, H. Nakajima, D. Irishika, T. Nonaka, K. Imamura, and H. Kobayashi, "Ultrathin SiO_2 layer formed by the nitric acid oxidation of Si (NAOS) method to improve the thermal-SiO_2/Si interface for crystalline Si solar cells," Appl. Surf. Sci. **395**, 56 (2017).

[4] D. König, D. Hiller, S. Gutsch, M. Zacharias, and S. Smith, "Modulation doping of silicon using aluminium-induced acceptor states in silicon dioxide," Sci. Rep. **7**, 46703 (2017).

[5] D. König, S. Gutsch, H. Gnaser, M. Wahl, M. Kopnarski, J. Göttlicher, R. Steininger, M. Zacharias, and D. Hiller, "Location and electronic nature of phosphorus in the Si nanocrystal–SiO_2 system," Sci. Rep. **5**, 09702 (2015).

[6] R. N. Pereira, A. J. Almeida, A. R. Stegner, M. S. Brandt, and H. Wiggers, "Exchange-coupled donor dimers in nanocrystal quantum dots," Phys. Rev. Lett. **108**, 126806 (2012).

[7] R. Dingle, H. L. Störmer, A. C. Gossard, and W. Wiegmann, "Electron mobilities in modulation-doped semiconductor heterojunction superlattices," Appl. Phys. Lett. **33**, 665 (1978).

[8] D. König and J. Rudd, "Formation of Si or Ge nanodots in Si_3N_4 with in-situ donor modulation doping of adjacent barrier material," AIP Adv. **3**, 012109 (2013).

[9] D. König, D. Hiller, and S. Smith, "SiO_2 modulation doping for Si: Acceptor candidates," Phys. Rev. Appl. **10**, 054034 (2018).

[10] M. Nishiyama, T. Mizokuro, K. Yoneda, and H. Kobayashi, "Oxidation of silicon by perchloric acid," Appl. Surf. Sci. **133**, 287 (1998).

[11] H. Kobayashi, Asuha, O. Maida, M. Takahashi, and H. Iwasa, "Nitric acid oxidation of Si to form ultrathin silicon dioxide layers with a low leakage current density," J. Appl. Phys. **94**, 7328 (2003).

[12] Y. Yamashita, K. Namba, Y. Nakato, Y. Nishioka, and H. Kobayashi, "Spectroscopic observation of interface states of ultrathin silicon oxide," J. Appl. Phys. **79**, 7051 (1996).

[13] F. D. Smedt, C. Vinckier, I. Cornelissen, S. D. Gendt, and M. Heyns, "A detailed study on the growth of thin oxide layers on silicon using ozonated solutions," J. Electrochem. Soc. **147**, 1124 (2000).

[14] H. Morinaga, T. Hoshino, Y. Omura, M. Kitagawa, and M. Aoki, "Mechanism of Metal Hydroxide Adsorption onto Si Surfaces in Alkali Solutions and Its Prevention," In: Extended Abstracts of Electrochemical Society 196th meeting, Hawaii, Vol.99-2, Abstract No. 1077 (1999.10). / Electrochemical Society Proceeding Series PV99-36, Pennington, NJ (2000).

[15] Asuha, S.-S. Im, M. Tanaka, S. Imai, M. Takahashi, and H. Kobayashi, "Formation of 10–30 nm SiO_2/Si structure with a uniform thickness at ~120 °C by nitric acid oxidation method," Surf. Sci. **600**, 2523 (2006).

[16] M. Takahashi, S.-S. Im, M. Madani, and H. Kobayashi, "Nitric acid oxidation of 3C-SiC to fabricate MOS diodes with a low leakage current density," J. Electrochem. Soc. **155**, H47 (2008).

[17] W. Kern and D. A. Puotinen, "Cleaning solution based on hydrogen peroxide for use in silicon semiconductor technology," RCA Rev. **31**, 187 (1970).

[18] M. Cardona and L. Ley, Photoemission In Solids I, Topics In Applied Physics, Springer, Berlin, Heidelberg (1978).

[19] D. A. Shirley, "High-resolution x-ray photoemission spectrum of the valence bands of gold," Phys. Rev. B **5**, 4709 (1972).

[20] A. Proctor and P. M. A. Sherwood, "Data analysis techniques in x-ray photoelectron spectroscopy," Anal. Chem. **54**, 13 (1982).

[21] F. J. Himpsel, F. R. McFeely, A. Taleb-Ibrahimi, J. A. Yarmoff, and G. Hollinger, "Microscopic structure of the SiO_2/Si interface," Phys. Rev. B **38**, 6084 (1988).

[22] S. Tanuma, C. J. Powell, and D. R. Penn, "Calculations of electron inelastic mean free paths. V. Data for 14 organic compounds over the 50–2000 eV range," Surf. Interface Anal. **21**, 165 (1994).

[23] C. D. Wagner, L. E. Davis, M. V. Zeller, J. A. Taylor, R. H. Raymond, and L. H. Gale, "Empirical atomic sensitivity factors for quantitative analysis by electron spectroscopy for chemical analysis," Surf. Interface Anal. **3**, 211 (1981).

[24] R. M. Henry, B. W. Walker, and P. C. Stair, "A blue colored surface observed during high temperature oxidation of aluminum (111)," Solid State Commun. **42**, 23 (1982).

[25] Y.-C. Jung, H. Miura, K. Ohtani, and M. Ishida, "High-quality silicon/insulator heteroepitaxial structures formed by molecular beam epitaxy using Al_2O_3 and Si," J. Cryst. Growth **196**, 88 (1999).

[26] C. D. Wagner, Practical Surface Analysis, vol. 1, Auger and X-ray Photoelectron Spectroscopy. John Wiley & Sons, Chichester (1990).

[27] D. Hiller, J. Göttlicher, R. Steininger, T. Huthwelker, J. Julin, F. Munnik, M. Wahl, W. Bock, B. Schoenaers, A. Stesmans, and D. König, "Structural properties of Al−O monolayers in SiO_2 on silicon and the maximization of their negative fixed charge density," ACS Appl. Mater. Interfaces **10**, 30495 (2018).

[28] D. W. Berreman, "Infrared absorption at longitudinal optic frequency in cubic crystal films," Phys. Rev. **130**, 2193 (1963).

[29] Asuha, T. Kobayashi, M. Takahashi, H. Iwasa, and H. Kobayashi, "Spectroscopic and electrical properties of ultrathin SiO_2 layers formed with nitric acid," Surf. Sci. **547**, 275 (2003).

[30] C. Martinet and R. A. B. Devine, "Analysis of the vibrational mode spectra of amorphous SiO_2 films," J. Appl. Phys. **77**, 4343 (1995).

[31] S. Deb and B. R. Nag, "Measurement of lifetime of carriers in semiconductors through microwave reflection," J. Appl. Phys. **33**, 1604 (1962).

[32] R. A. Sinton and A. Cuevas, "Contactless determination of current–voltage characteristics and minority-carrier lifetimes in semiconductors from quasi-steady-state photoconductance data," Appl. Phys. Lett. **69**, 2510 (1996).

[33] A. B. Sproul, "Dimensionless solution of the equation describing the effect of surface recombination on carrier decay in semiconductors," J. Appl. Phys. **76**, 2851 (1994).

[34] D. Kane and R. Swanson, "Measurement of the emitter saturation current by a contactless photoconductivity decay method," In: Proceedings of the 18th IEEE Photovoltaic Specialist Conf., IEEE, Las Vegas, NV, pp. 578–583 (1985).

[35] K. A. Nasyrov, S. S. Shaimeev, and V. A. Gritsenko, "Trap-assisted tunneling hole injection in SiO_2: Experiment and theory," J. Exp. Theor. Phys. **109**, 786 (2009).

[36] R. H. Cox and H. Strack, "Ohmic contacts for GaAs devices," Solid-State Electron. **10**, 1213 (1967).

[37] D. Hiller, P. Hönicke, and D. König, "Material combination of tunnel-SiO_2 with a (sub-)monolayer of ALD-AlO_x on silicon offering a highly passivating hole selective contact," Sol. Energy Mater. Sol. Cells **215**, 110654 (2020).

[38] E. H. Nicollian, and J. R. Brews, MOS (Metal Oxide Semiconductor) Physics and Technology. New York: John Wiley & Sons (1982).

[39] K. R. McIntosh, and L. E. Black, "On effective surface recombination parameters," J. Appl. Phys. **116**, 014503 (2014).

[40] K. Gelderman, L. Lee, and S. W Donne, "Flat-band potential of a semiconductor: Using the Mott–Schottky equation," J. Chem. Educ. **84**, 685 (2007).

[41] L. E. Black, "New perspectives on surface passivation: Understanding the Si–Al_2O_3 interface," Ph.D. thesis, Australian National University (2015).

[42] R. Brendel, M. Rienaecker, and R. Peibst, "A quantitative measure for the carrier selectivity of contacts to solar cells," In: Proceedings of the 32nd European Photovoltaic Solar Energy Conference and Exhibition, Munich, pp. 447–451 (2016).

[43] H. Nakajima, H. T. C. Tu, and K. Ohdaira, "Ultrathin Al-doped SiO_x passivating hole-selective contacts formed by a simple wet process," Jpn. J. Appl. Phys. **62**, SK1040 (2023).

[44] R. Gogolin, D. Zielke, W. Lövenich, R. Sauer, and J. Schmidt, Energy Procedia **92**, 638 (2016).

[45] G. Nogay, J. Stuckelberger, P. Wyss, E. Rucavado, C. Allebéb, T. Koida, M. Morales-Masisa, M. Despeisse, F.-J. Haug, P. Löper, and C. Ballif, "Interplay of annealing temperature and doping in hole selective rear contacts based on silicon-rich silicon-carbide thin films," Sol. Energy Mater. Sol. Cells **173**, 18 (2017).

[46] H. Lin, M. Yang, X. Ru, G. Wang, S. Yin, F. Peng, C. Hong, M. Qu, J. Lu, L. Fang, C. Han, P. Procel, O. Isabella, P. Gao, Z. Li, and Xi. Xu, "Silicon heterojunction solar cells with up to 26.81% efficiency achieved by electrically optimized nanocrystalline-silicon hole contact layers," Nat. Energy **8**, 789 (2023).

[47] J. Bao, C. Chen, L. Ma, C. Huang, X. Zhang, Z. Wang, C. Chen, S. Zhan, R. Liu, Z. Qiao, Z. Du, Z. Liu, and J. Chen, "Towards 24% efficiency for industrial n-type bifacial passivating-contact solar cells with homogeneous emitter," In: Proceedings of the 37th European Photovoltaic Solar Energy Conference and Exhibition, online, pp. 160–164 (2020).

[48] D. Yan, A. Cuevas, Y. Wan, and J. Bullock, "Passivating contacts for silicon solar cells based on boron-diffused recrystallized amorphous silicon and thin dielectric interlayers," Sol. Energy Mater. Sol. Cells **152**, 73 (2016).

[49] Y. Wan, C. Samundsett, J. Bullock, T. Allen, M. Hettick, D. Yan, P. Zheng, X. Zhang, J. Cui, J. McKeon, A. Javey, and A. Cuevas, "Magnesium fluoride electron-selective contacts for crystalline silicon solar cells," ACS Appl. Mater. Interfaces **8**, 14671 (2016).

[50] D. L. Young, W. Nemeth, S. Grover, A. Norman, B. G. Lee, and P. Stradins, "Carrier-selective, passivated contacts for high efficiency silicon solar cells based on transparent conducting oxides," Energy Procedia **55**, 733 (2014).

[51] X. Yang, P. Zheng, Q. Bi, and K. Weber, "Silicon heterojunction solar cells with electron selective TiO_x contact," Sol. Energy Mater. Sol. Cells **150**, 32 (2016).

[52] S. W. Glunz, F. Feldmann, A. Richter, M. Bivour, C. Reichel, H. Steinkemper, J. Benick, and M. Hermle, "The irresistible charm of a simple current flow pattern–25% with a solar cell featuring a full-area back contact," In: Proceedings of the 31st European Photovoltaic Solar Energy Conference and Exhibition, Hamburg, pp. 259–263 (2015).

[53] S. Y. Herasimenka, W. J. Dauksher, and S. G. Bowden, ">750 mV open circuit voltage measured on 50 μm thick silicon heterojunction solar cell," Appl. Phys. Lett. **103**, 053511 (2013).

[54] M. Rienäcker, M. Bossmeyer, A. Merkle, U. Römer, F. Haase, J. Krügener, R. Brendel, and R. Peibst, "Junction resistivity of carrier-selective polysilicon on oxide junctions and its impact on solar cell performance," IEEE J. Photovolt. **7**, 11 (2017).

[55] R. Brendel and R. Peibst, "Contact selectivity and efficiency in crystalline silicon photovoltaics," IEEE J. Photovolt. **6**, 1413-1420 (2016).

[56] H. Angermann, W. Henrion, A. Röseler, and M. Rebien, "Wet-chemical passivation of Si(111)- and Si(100)-substrates," Mater. Sci. Eng. B **73**, 178 (2000).

CHAPTER 5

AL-INDUCED CHARGED OXIDE INVERSION LAYER SOLAR CELLS

The wet chemically grown ultrathin Al-doped SiO_x provides surface passivation and hole-selective contact at the same time. The negatively charged oxide induces an inversion layer in the n-type c-Si surface, which originates from electron trapping in the Al-induced acceptor states existing in the oxide as a formation of AlO_4 structure. Surprisingly, since the excited electron activates the hole selectivity in the Al-doped SiO_x layer, the hole-selective passivating contact properties are initiated under light illumination. In contrast, the surface passivation and the electrical properties are inferior under dark conditions, as described in Chapter 4. Fortunately, since solar cells certainly operate under light illumination, the light-activated ultrathin Al-doped SiO_x is expected to be able to be used under the practical 1 sun illumination condition. Hence, expectedly, the light-induced hole-selectivity allows us to realize that the wet chemically grown Al-doped SiO_x acts as a p^+ emitter for the n-type c-Si solar cells.

In this chapter, the concept of the novel Si-based solar cells is proposed, with an inversion layer induced by the ultrathin Al-doped SiO_x. I named it Al-induced charged oxide inversion layer (Al-COIL) solar cells, and the first fabricated Al-COIL solar cell was demonstrated following a simple process and structure. This demonstration allows us to confirm the device's operation and elucidate the mechanism, as shown in the last chapter.

5.1 Concept of Al-COIL architecture

The Al-COIL architecture conceptualizes to realize excellent surface passivation and carrier selective contact using an ultrathin dielectric layer formed by a simple wet chemical process. The recent study demonstrated excellent surface passivation of S_{eff} <20 cm s^{-1} by a wet chemically processed ultrathin SiO_x layer treated by rigorous cleaning processes and using superacidic (bis(trifluoromethane)sulfonimide crystals) solutions under inert conditions. In contrast, the $Al(NO_3)_3$ treatment also provides an excellent surface passivation of $S_{eff, max}$ <16 cm s^{-1} by Al-COIL architecture, and it can be recognized as a more industrially feasible process considering a wet chemically grown ultrathin oxide layer with a thickness of ~1 nm formed by a simple wet process using a relatively low-cost and safer chemical under atmospheric pressure conditions. In addition, the surface passivation of the superacidic treated-ultrathin SiO_x is mainly attributed to the reduction of the N_{it} and minor contribution of the negative Q_f of the order of 10^{10} cm^{-2} [1]. Hence, this surface passivation layer does not expect the hole-selective contact because the surface hole density induced by a Q_f of -4.5×10^{10} cm^{-2} [1] can be calculated to 2.65×10^{6} cm^{-3} from PC1D simulation, which cannot invert the Si surface. Therefore, to enable hole-selective passivating contact through ultrathin SiO_x formed by a simple wet chemical process, only Al-COIL is the promising solution, which can invert the n-type Si surface. Such an excellent ultrathin passivation layer enables sufficient carrier tunneling without degrading surface passivation quality, rather than hole-selective carrier tunneling due to the hole accumulation at the Si surface as the negatively charged oxide layer induces the mirrored charges.

The fabrication process flow, the device structure, and the principle of the device operation are shown in Figure 5.1. The Al-COIL solar cells are expected to reduce the processing steps with a cost-effective, simple wet chemical process. In addition, since impurities such as B or Al are not diffused into the Si surface, surface recombination can be mitigated from the recombination center generated by the impurities. The following leading cell structure of TOPCon requires more processing steps, and the cell efficiency is limited by Auger recombination in the front boron emitter [2]. For the SHJ structure, the solar cell performance is limited by parasitic absorption in the front a-Si passivation layer [3]. Thus, the inversion layer induced by a negatively charged ultrathin SiO_x layer can not only reduce the processing steps but also achieve higher efficiency due to avoiding the Auger recombination and parasitic absorption loss in the emitter. However, one of the biggest problems would be a difficulty to obtain an enough lateral conductivity through the inversion layer.

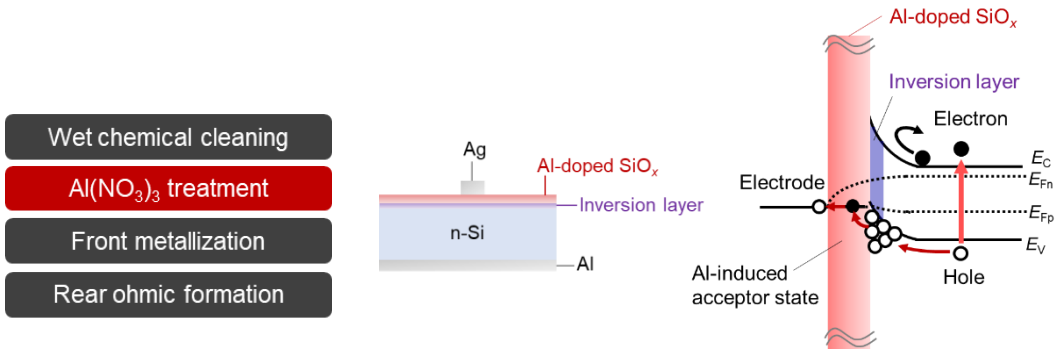

Fig. 5.1 Fabrication process flow, the device structure, and the principle of the device operation.

The negative charge density must be sufficiently high to obtain conductive enough to be comparable to the B-diffused emitter. In the previous study, fixed charges in various oxide layers have been investigated for the induction of an inversion layer in the Si surface [4, 5, 6]. However, this approach also finds it challenging to provide sufficiently high charge densities in the dielectric layer, mitigating lateral resistive losses. Although, for a p-type base, a very high positive charge density of 1.1×10^{13} cm^{-2} has been realized by silicon nitride (SiN_x) [7], the charge density was not high enough to introduce a sufficient lateral conductivity compared with conventional P-diffused emitters. M. Yu *et al*. reported that the simulation revealed a positive charge density of 4×10^{13} cm^{-2} can provide a sheet resistance of the inversion layer as low as ~180 Ω sq^{-1} [8], which is close to that of 130 Ω sq^{-1} for a P-diffused emitter [9]. Therefore, such a highly charged ultrathin oxide layer must be formed to accomplish carrier-selective contact with a comparable level of lateral conductivity on the front surface of other types of solar cells, such as PERC, TOPCon, and SHJ. As shown in Figure 1.3, only 6.7% charged Al in the Al-O monolayer induces such a high charge density of -4×10^{13} cm^{-2} and very low S_{eff} of 0.1 cm s^{-1} simultaneously. Moreover, PC1D simulation suggests that the negative Q_f shows a comparable sheet resistance of 119 Ω sq^{-1} to a B-diffused emitter [9]. The R_{sheet} was calculated from the simulated hole density and hole mobility concerning the depth using the equation below.

$$R_{\text{sheet}} = \frac{1}{q \int_0^z \mu(z)\, p(z)\, dz} \tag{5.1}$$

Where μ is hole mobility, p is hole density, and z is depth from the surface. The calculated R_{sheet} concerning the Q_f is shown in Figure 5.2.

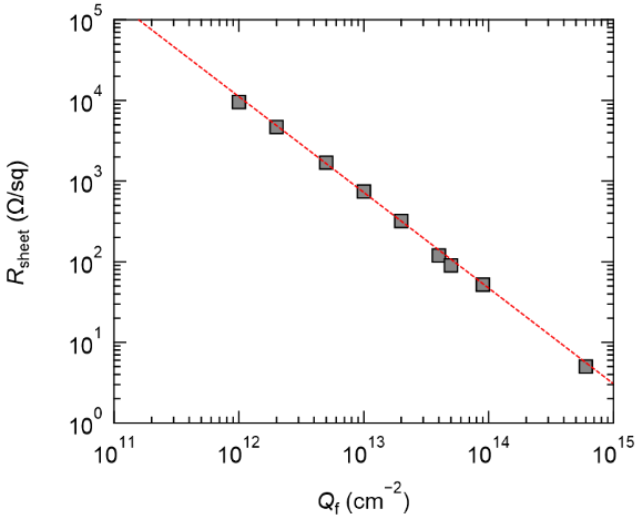

Fig. 5.2 R_{sheet} concerning the Q_f calculated from PC1D simulation.

Hence, since R_{sheet} reduces inversely proportional to the Q_f^2, improving Q_f is the most effective approach to increase the lateral conductivity. However, considering achieving a 317 Ω sq^{-1} value under 1 sun illumination, Q_f might be enhanced to ~ -2×10^{13} cm^{-2}, as following this relationship between R_{sheet} and Q_f. Therefore, the concept of this novel simple device will possibly be realized as a high-efficiency, cost-effective c-Si solar cell.

5.2 Simulation for Al-COIL solar cells

The *J–V* characteristics and power densities were simulated using PC1D software. The device structure with surface charge-induced emitter, which is assumed to be an Al-COIL and B-diffused emitter, and these input parameters for PC1D simulation are shown in Figures 5.3 and 5.4, respectively. For the surface charge, the front surface charge density was set to -3×10^{13} cm^{-2}, and for the B-diffused emitter, the typical B-doping concentration was set to 1×10^{19} cm^{-3} [10] with a depth factor of 1.135 μm which can be set a sheet resistance as 95 Ω sq^{-1} [10]. The simulations were performed under the steady state condition of 1 sun illumination (steady state intensity of 0.1 W cm^{-2} with an AM 1.5 Global spectrum). In this simulation, the internal series resistance is assumed to be sufficiently low (1×10^{-6} Ω cm^2). In addition, it is not considered an optical loss attributed to the front reflectance but considered internal light diffusive reflection from the rear

surface. Figure 5.5 demonstrated excellent *J–V* characteristics even without a B-diffused emitter. As shown in Table 5.1 of the simulated solar cell performance, η was calculated to be 27.21%. Since the calculated η is very close to the theoretical limit of SHJ solar cells (27.5%) [11], it can be recognized the surface charge-induced emitter device is expected to realize high-efficiency c-Si solar cells. Figure 5.6 shows a PC1D simulated band energy diagram of the front surface at a maximum power point. As shown in the diagram, the generated large quasi-fermi level splitting of 0.676 eV indicates that the negative charges from the surface induce an inversion layer as a p^+ emitter of n-type c-Si solar cells. The *J–V* characteristics for the conventional B-diffused device and the simulated solar cell performance are shown in Figure 5.7 and Table 5.2, respectively. Compared with the two types of solar cells, the surface-charged-induced device can be superior to the conventional B-diffused device. Hence, these simulation results demonstrated that the surface charge, in principle, induces a p^+ emitter for the high-efficiency c-Si solar cell. Note that PC1D simulation neglects the effect of sheet resistance. Hence, the simulated results display values when the sheet resistance is ideal.

DEVICE
Device area: 1 cm^2
No surface texturing
Front surface charge: -3×10^{13} cm^{-2}
Rear surface neutral
No Exterior Front Reflectance
No Exterior Rear Reflectance
Internal optical reflectance enabled
Front surface optically rough
Rear surface optically rough
Emitter contact enabled
Base contact enabled
No internal shunt elements
REGION 1
Thickness: 200 µm
Material modified from program defaults
Carrier mobilities from internal model
Dielectric constant: 11.9
Band gap: 1.124 eV
Intrinsic conc. at 300 K: 1×10^{10} cm^{-3}
Refractive index: 3.58
Absorption coeff. from internal model
No free carrier absorption
N-type background doping: 5×10^{15} cm^{-3}
No front diffusion
No rear diffusion
Bulk recombination: $\tau_n = \tau_p = 1\times10^{100}$ µs
No Front-surface recombination
No Rear-surface recombination
EXCITATION
Excitation mode: Steady State
Temperature: 300 K
Base circuit: Zero
Collector circuit: Zero
Primary light source enabled
Steady state intensity: 0.1 W cm^{-2}
Spectrum from am15g.spc
Secondary light source disabled

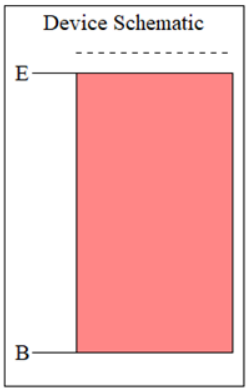

Fig. 5.3 Device structure and input parameters for PC1D simulation to obtain ideal *J–V* characteristics of the device with the surface charge-induced emitter.

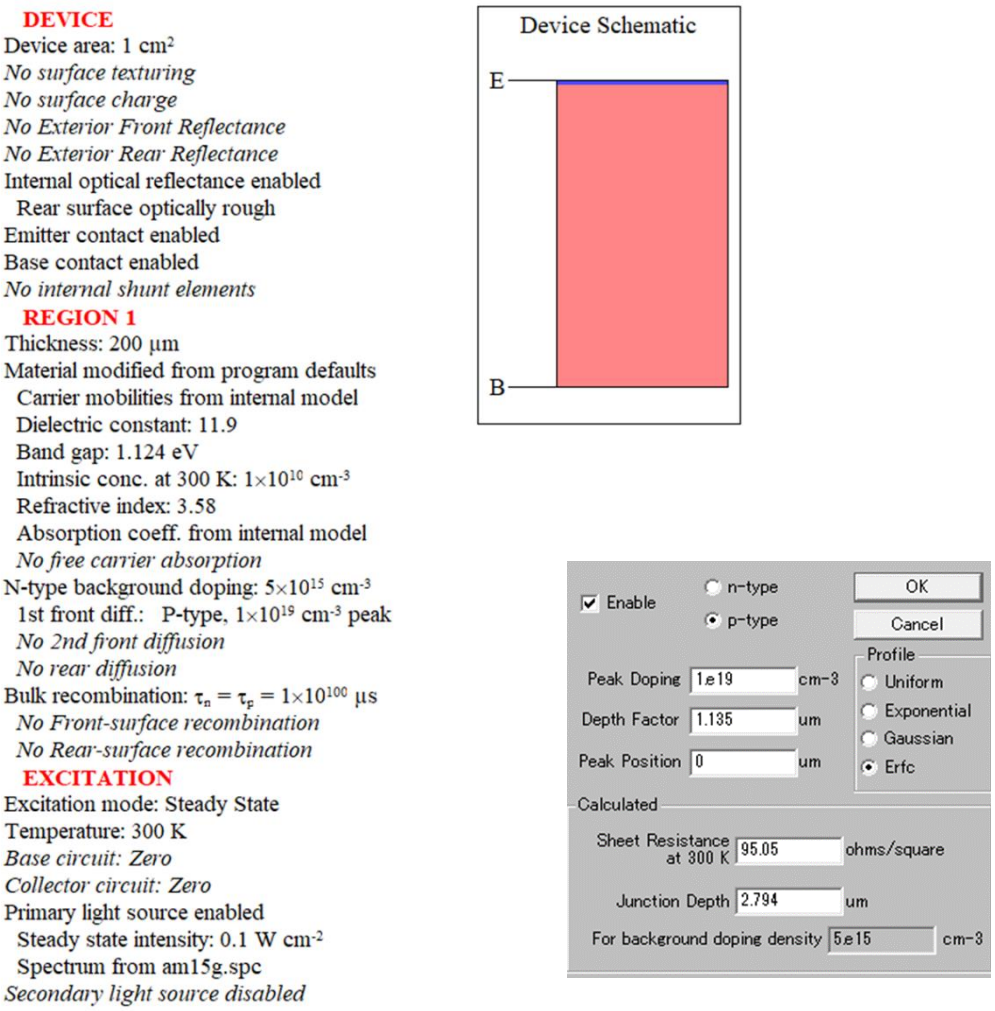

Fig. 5.4 Device structure and input parameters for PC1D simulation to obtain ideal *J–V* characteristics of the device with B-diffused emitter.

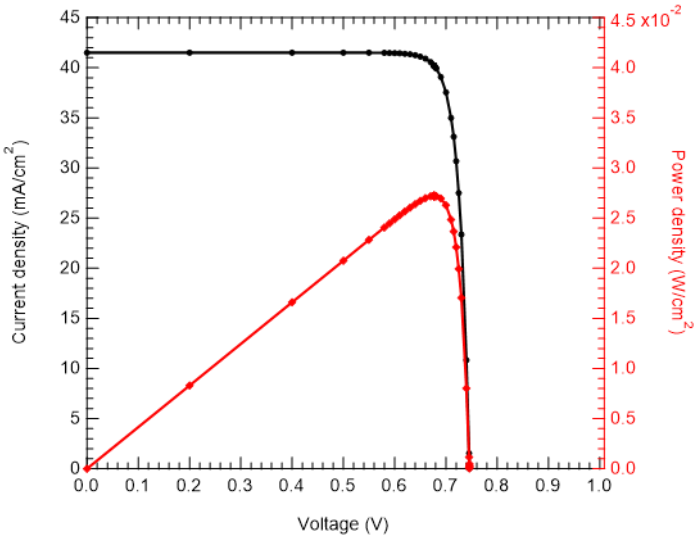

Fig. 5.5 PC1D simulated *J–V* curve and power density for surface charge-induced emitter.

Table 5.1 PC1D simulated solar cell performance for surface charge-induced emitter.

J_{sc} (mA cm^{-2})	V_{oc} (mV)	FF (%)	η (%)
41.50	0.746	87.91	27.21

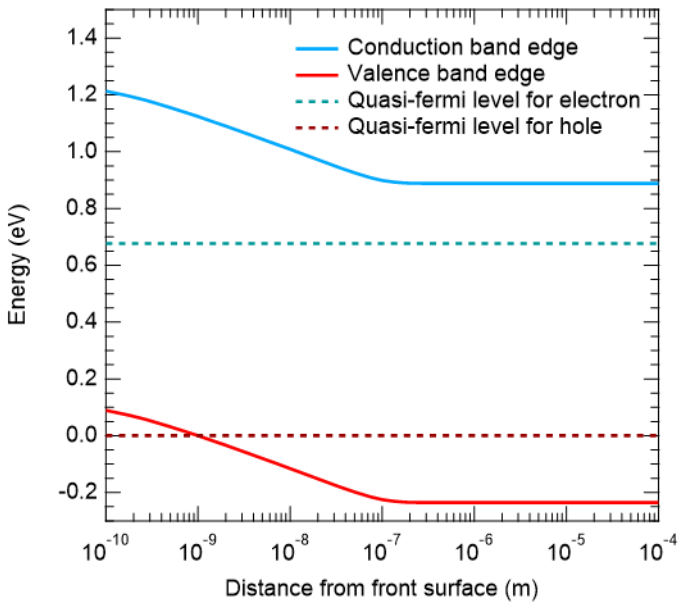

Fig. 5.6 Band energy diagram of the front surface at the maximum power point for surface charge-induced emitter.

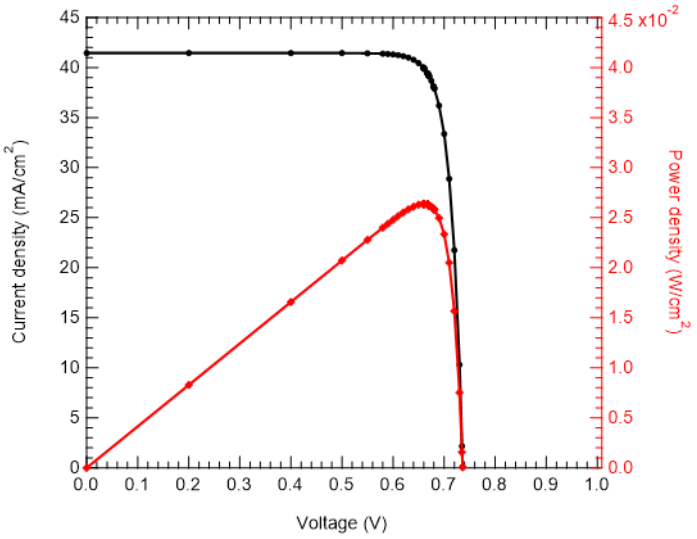

Fig. 5.7 PC1D simulated *J–V* curve and power density for B-diffused emitter.

Table 5.2 PC1D simulated solar cell performance for B-diffused emitter.

J_{sc} (mA cm^{-2})	V_{oc} (mV)	FF (%)	η (%)
41.45	0.736	86.43	26.37

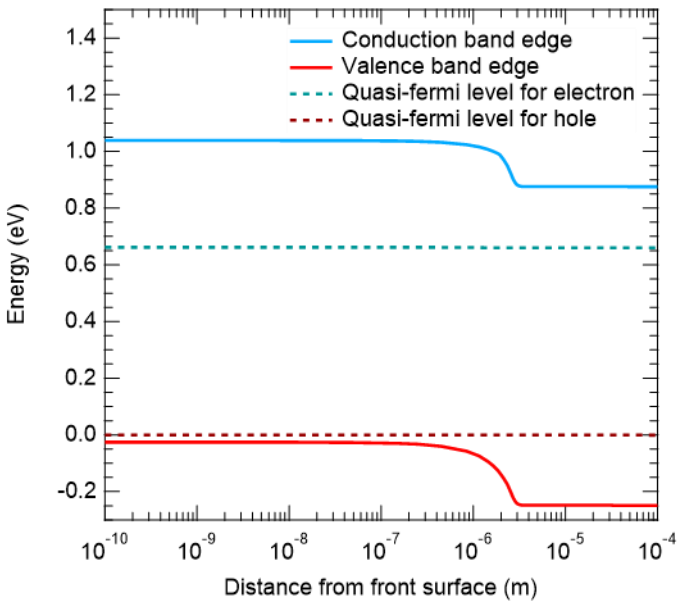

Fig. 5.8 Band energy diagram of the front surface at maximum power point for B-diffused emitter.

Moreover, Figure. 5.9 shows the simulated V_{oc} as a function of S for the device structure with surface charge-induced emitter and B-diffused emitter. Significant V_{oc} reduction was confirmed in the device structure with B-diffused emitter in the range of $S > 10^2$ cm s^{-1} order. In comparison, such a significant reduction cannot appear by the order of 10^6 cm s^{-1} for the device structure with surface charge-induced emitter. This is considered to be attributed to the significant difference in the surface carrier densities between electrons and holes, which comes from the strong surface band bending shown in the band diagram of Figure 5.6. As shown in Figure 5.10, the surface electron density of the surface-charged device is considerably low at 10^{10} cm^{-2} orders compared to 10^{13} cm^{-2} orders for the B-diffused device, resulting in high tolerance to the surface carrier recombination in the surface-charged device structure. In other words, surface charged device structure allows us to obtain high-efficiency solar cell performance even though there are large amounts of interface states as high as ~10^{13} cm^{-2}, which cannot be realized by B-diffused emitter without reducing N_{it} as low as ~10^{10} cm^{-2} or further deposition of negatively charged dielectric layers.

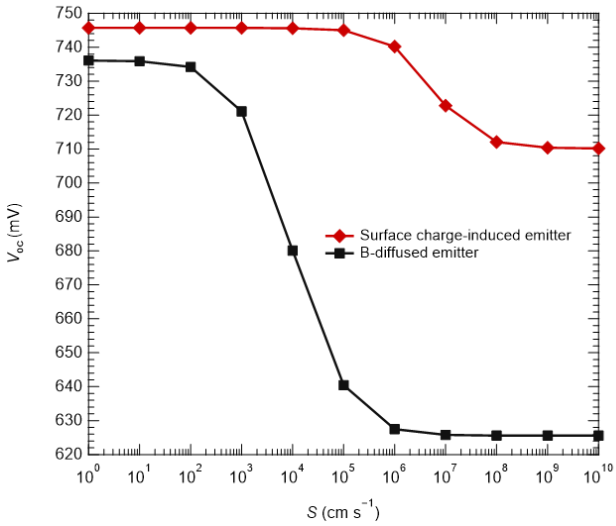

Fig. 5.9 V_{oc} as a function of S for surface charge-induced emitter and B-diffused emitter.

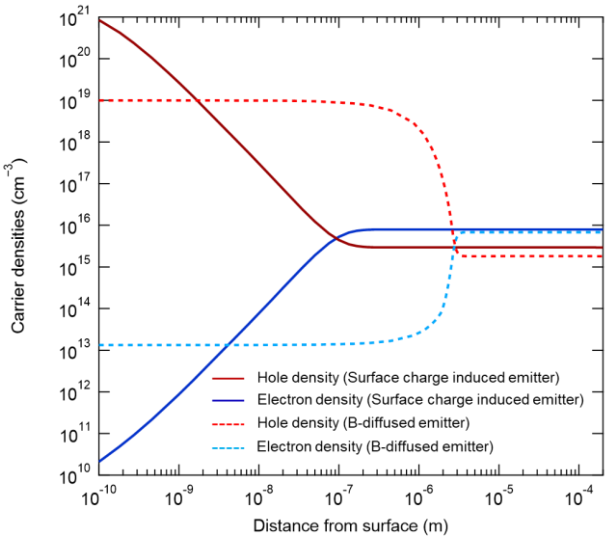

Fig. 5.10 Carrier densities for the devices with a surface charge-induced emitter or a B-diffused emitter.

In addition, the free carrier absorption can be mitigated by the surface charge-induced emitter, obtaining slightly higher J_{sc} values. Free carrier absorption loss was calculated to be 0.035 mA cm^{-2} for the B-diffused emitter and 0.003 mA cm^{-2} for the charged-induced emitter, respectively. The free carrier absorption (α_{FC}) was calculated using Green's model [12], as expressed below.

$$\alpha_{FC} = 2.6 \times 10^{-27}\, n\lambda^3 + 2.7 \times 10^{-24}\, p\lambda^2 \tag{5.2}$$

Where n is the electron density, p is the hole density, and λ is the wavelength. Parasitic absorption can also be mitigated because SiO_2 has no absorption ($\alpha = 0$) over the wide wavelength of 210 to 2000 nm [13], and the thickness is negligibly thin.

Furthermore, the surface charge-induced emitter shows large Auger lifetimes (τ_{Auger}) in the wide region of the Si substrate due to shallow modulation doping. It suggests that Auger recombination can be mitigated by a surface charge-induced emitter except for a very narrow region of less than 2 nm. The calculated depth profile of τ_{Auger} is shown in Figure 5.11. For the calculation, simulated hole densities and the following equations [14] were used:

$$R = C\, n\, p^2, \tag{5.3}$$

$$\tau_{Auger} = \frac{n}{R} = \frac{1}{Cp^2}. \tag{5.4}$$

Where R is the recombination rate, and C is the Auger coefficient. For the value of C, 1.2×10^{-31} cm^6 s^{-1} was used for p-type Si [15].

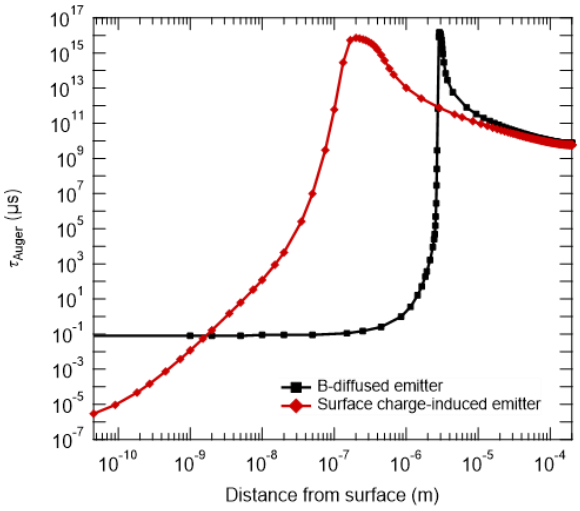

Fig. 5.11 Depth profile of τ_{Auger} for the devices with a surface charge-induced emitter or a B-diffused emitter.

To summarize, the concept for the Al-COIL solar cell using surface charge-induced emitter can realize high-throughput, low-cost p^+ emitter formation by a simple wet chemical process, excellent ultrathin surface passivation with high tolerance to the interface states, reduction of free carrier absorption loss, and no parasitic absorption using high band gap material of SiO_2.

5.3 Fabrication and evaluation of Al-COIL solar cells

5.3.1 Sample fabrication

The samples were fabricated on the double-side-polished FZ n-type Si (100) with a resistivity of 2.5 Ω cm and a thickness of 280 μm (TOPSIL PV-FZ™). The Si substrate was cleaved into 20×20 mm-sized pieces, followed by RCA cleaning [16]. After 1% diluted hydrofluoric acid (HF) treatment for 1 min and rinse in deionized water (DIW) (resistivity of 18.2 MΩ cm) for 1 min, the hydrophobic Si substrates were immersed in $Al(NO_3)_3$ aqueous solution with an $Al(NO_3)_3 \cdot 9H_2O$ molar concentration of 0.25 mol L^{-1} for 12.5 min. The hot $Al(NO_3)_3$ aqueous solution was prepared in advance by dissolving $Al(NO_3)_3 \cdot 9H_2O$ (17.8 g, special grade, Junsei Chemical Co., Ltd.) in DIW (190 mL) in a Pyrex glass beaker (Corning Pyrex 600 mL) and heating to a boiling temperature (~95 °C) on a hot plate (AS ONE Corporation, CHPS-170DF). During the heating process, the beaker was capped to avoid the evaporation of the solution. The solutions were not intentionally stirred during the process; however, drastically generated bubbles could be confirmed at the boiling temperature. After the $Al(NO_3)_3$ treatment, the processed Si substrates were rinsed in DIW for 1 min and completely dried by N_2 blow. Subsequently, the Ag finger electrode was deposited on the $Al(NO_3)_3$-treated samples through a mask by thermal evaporation in a vacuum chamber at a pressure of 9×10^{-4} Pa. For the rear side of the samples, the surface was treated with a cotton swab dipped in 5% diluted HF aqueous solution in advance until the hydrophobic surface was visually confirmed. The full-area Al electrodes were thermally evaporated on the rear surfaces, which were scratched in advance to obtain an excellent ohmic contact. The fabrication process flow and the fabricated solar cell structure are shown in Figure 5.12.

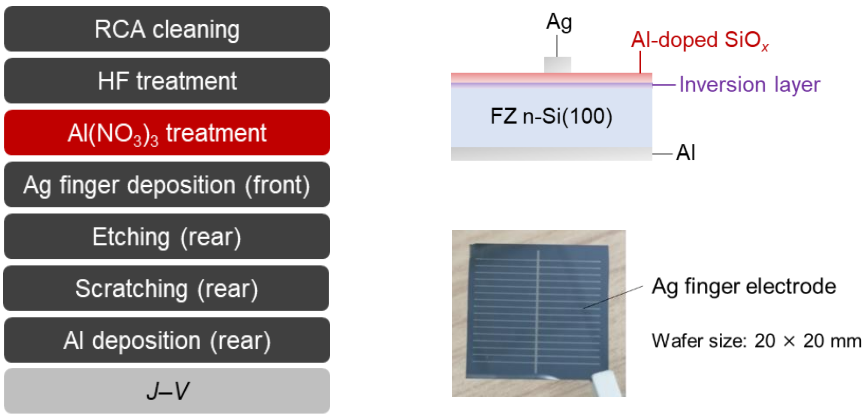

Fig. 5.12 Al-COIL solar cell fabrication process flow and the fabricated solar cell structure.

5.3.2 Sample evaluation

The current density–voltage (*J–V*) curves were acquired in the dark and under 1 sun illumination (AM 1.5 G). The light intensity was calibrated with a Si reference cell (Bunkoukeiki Co., Ltd., BS-500BK Si photodiode detector) to an irradiance of 0.1 W cm^{-2} at RT. The J_{sc} was calculated with an active area of 3.67 cm^2 after subtracting the estimated area of Ag front electrodes of 0.33 cm^2. During the measurement, one probe was placed on the Ag finger electrode, and the other was placed on the Cu plate, which was contacted on the Al electrode of the rear side of the test cell to collect the holes and electrons, respectively. The appearance of the setting and the photo *J–V* measurement is shown in Figure 5.13.

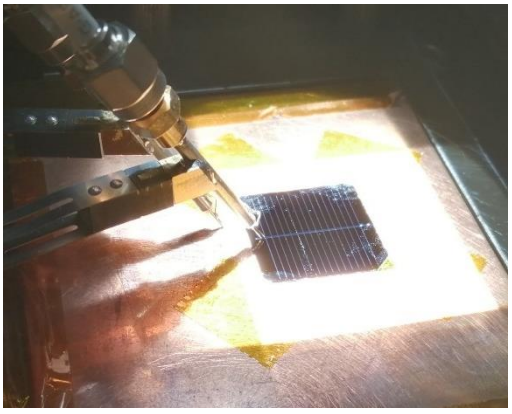

Fig. 5.13 Appearance of the setting and the photo *J–V* measurement under 1 sun illumination.

For the discussion, photo *J–V* curves for the Q_f dependency as front surface charges were simulated using PC1D software, assuming the enormous front SRV of 1×10^{10} cm s^{-1} and without front surface recombination. The other set of parameters is shown in the appendix. Additionally, τ_{eff} mapping measurement was performed after the one-side deposition of the Ag finger electrode on the symmetrical structure of n-Si(100) with an Al-doped SiO_x layer.

The τ_{eff} mapping data were acquired within the area of 20×20 mm^2 with a 0.5 mm pitch. A pulsed laser with a wavelength of 904 nm and an areal photon density of 5×10^{13} cm^{-2} was used for the carrier excitation. The laser was illuminated on the rear side (without an Ag finger electrode) to excite carriers evenly in the bulk of Si within the illuminated area.

5.3.3 J–V characteristics of Al-COIL solar cells

Figure 5.14 shows the *J–V* characteristics of a device with Al-doped SiO_x, an Al-COIL solar cell, and a device without Al-doped SiO_x acquired in the dark (dotted lines) and under 1 sun illumination (solid lines). As shown in Table 5.3 of the solar cell performance, a relatively high η of 3.35% was acquired for the device with an Al-COIL structure. Although the η is quite low as a c-Si solar cell, a simple wet chemical process realizes the c-Si solar cells with a relatively high V_{oc} of 0.454 V compared to the device without an Al-doped SiO_x layer. Therefore, this result demonstrated the device operation and the charge-induced inversion layer acts as a p^+ emitter formed by a simple wet chemical process. The low FF of 50.8% might be mainly attributed to the series resistance, especially in a high sheet resistance of the front surface, but not from shunt resistance because of no shunting occurrence in the dark *J–V* curve.

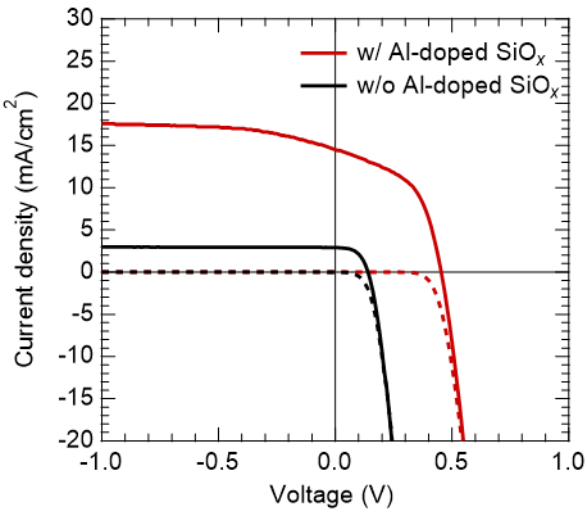

Fig. 5.14 *J–V* characteristics of the devices w/ Al-doped SiO_x (Al-COIL solar cell) and w/o Al-doped SiO_x acquired in the dark (dotted lines) and under 1 sun illumination (solid lines).

Table 5.3 Fabricated solar cell performance with or without Al-COIL structure.

	J_{sc} (mA cm^{-2})	V_{oc} (V)	FF	η (%)
w/ Al-doped SiO_x (Al-COIL)	14.5	0.454	0.508	3.35
w/o Al-doped SiO_x	2.9	0.140	0.528	0.21

As described in Chapter 4, however, Al-doped SiO_x/n-Si(100) showed a high implied V_{oc} of 0.670 V, while the measured V_{oc} of 0.454 V was relatively low. This might be mainly due to high recombination at the rear surface receiving scratching and direct deposition of the Al electrode. In addition, PC1D simulation shows that if the rear-SRV is as high as 1×10^{10} cm s^{-1}, the simulated V_{oc} would be 0.587 V. Since this is still higher than the measured V_{oc} of 0.454 V, further carrier recombination might also occur at the front emitter surface. Figure 5.15 shows PC1D simulated photo J–V characteristics for the devices with surface charge-induced emitters assuming various Q_f values in the range of -8.8×10^{10} – -1.0×10^{13} cm^{-2}, enormous front-SRV of 1×10^{10} cm s^{-1}, and emitter resistance of 5 Ω cm^2 for each device. As shown in the figure, not only V_{oc} but also J_{sc} are significantly diminished with decreasing Q_f values. Considering that the reduction of J_{sc} is not observed without surface recombination, shown in Figure 5.16, the J_{sc} reduction might originate from carrier recombination at the emitter surface due to increased minority carrier density in the low Q_f, as described in Figure 5.17.

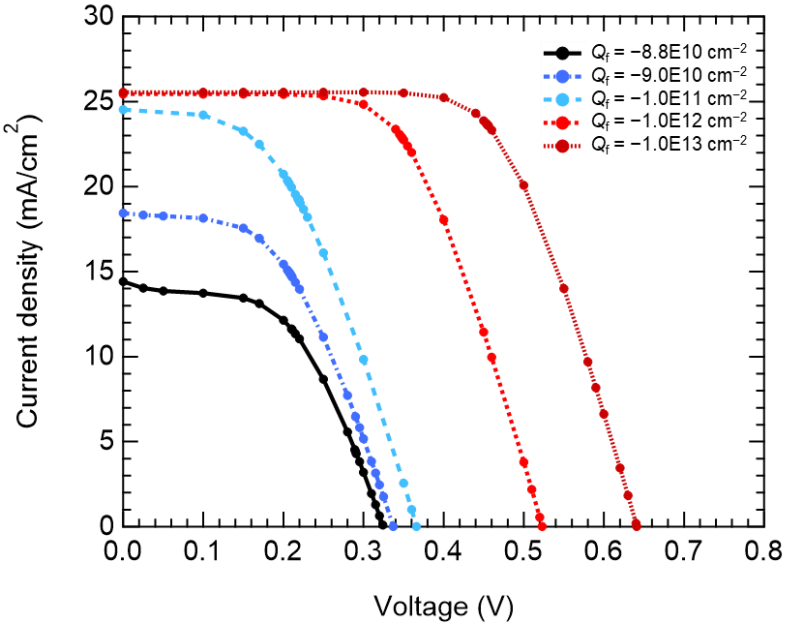

Fig. 5.15 PC1D simulated photo J–V characteristics for the devices with surface charge-induced emitters assuming various Q_f values with a front S of 1×10^{10} cm s^{-1}.

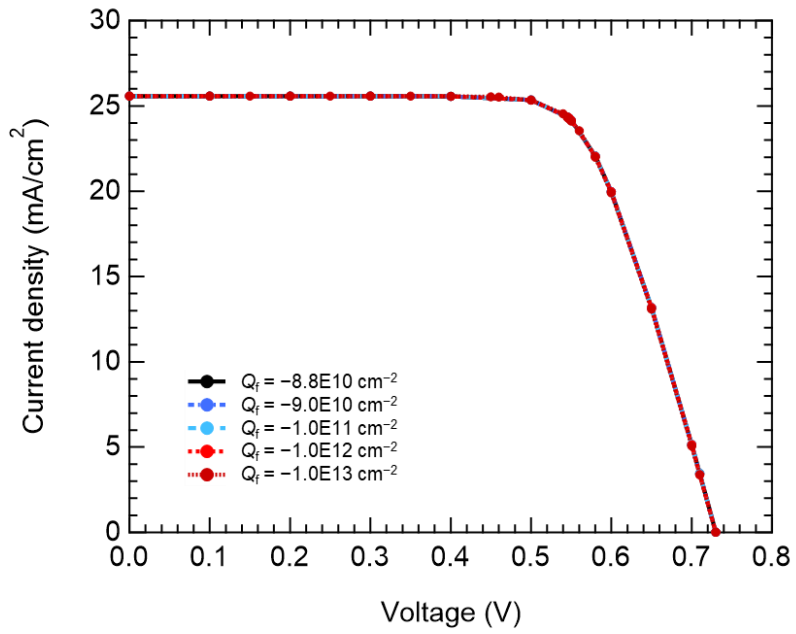

Fig. 5.16 PC1D simulated photo *J–V* characteristics for the devices with surface charge-induced emitters assuming various Q_f values without front-surface recombination.

.

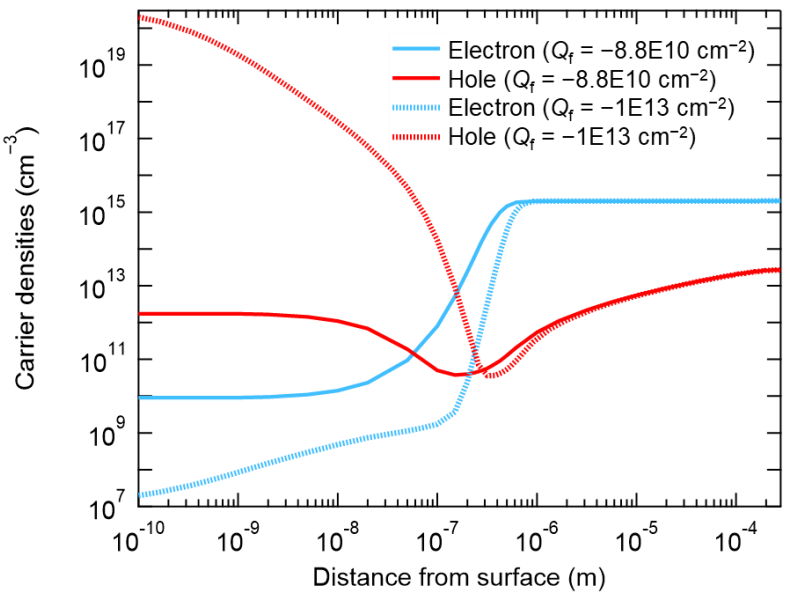

Fig. 5.17 PC1D simulated carrier densities of devices with surface charge-induced emitters assuming low and high Q_f values.

The possible reason for the degradation is the reduction of the V_{bi} under the Ag finger electrode because Ag has a low work function: 4.26 eV for a polycrystalline phase and 4.52–4.74 eV for a crystalline phase [17], concerning the electron affinity of n-type c-Si (4.05 eV). Figure 5.18 shows τ_{eff} mapping measured after Ag finger deposition on the front side. The τ_{eff} mapping measurement was performed from the rear side to avoid the suppression of the excess carrier generation and microwave reflection by the deposited Ag electrode. As seen in the τ_{eff} mapping, a significant reduction of τ_{eff} has occurred at the deposited position. Hence, the deposited Ag electrode might increase minority carrier (electron) density due to decreased band bending, which deteriorates the surface passivation quality. Previous studies also showed that the metallization massively reduced τ_{eff} of ALD-Al_2O_3/SiO_2/n-Si by Pd, Ni, and Al [18]. Although there is a contradiction to this work, Ag did not show such degradation in the previous study [18]. However, higher work function materials such as Pt, Ir, and Au should be applied to maintain the high V_{bi}. Favorably, relatively low-cost transition metal oxides such as MoO_3, WO_3, and V_2O_5 (work function ~7 eV [19]) might be used underneath the Ag electrodes.

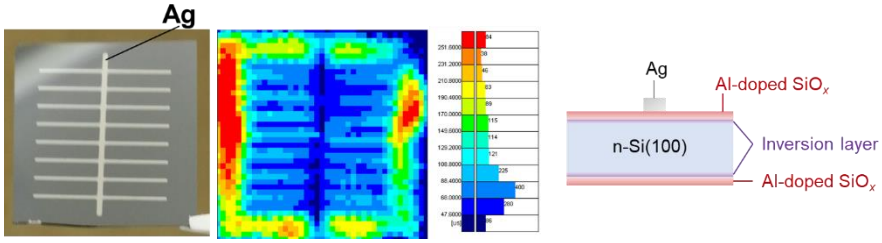

Fig. 5.18 τ_{eff} mapping for Ag finger electrode deposited Al-doped SiO_x/n-Si/ Al-doped SiO_x/ structure and the schematic of the sample structure.

5.4 Summary

Al-COIL solar cells using surface charge-induced emitter realize high-throughput, low-cost p^+ emitter formation by a simple wet chemical process. The PC1D simulation showed a high-efficiency c-Si solar cell performance with a high tolerance to the interface states, a reduction of free carrier absorption, and Auger recombination in the wide region of the Si substrate. The first fabricated test cell demonstrated a device operation with an η of 3.35% and a relatively high V_{oc} of 0.454 V, which implies that the induced inversion layer acts as a p^+ emitter of an n-type c-Si solar cell. However, a considerable divergence between V_{oc} and iV_{oc} was confirmed. In addition, J_{sc} also diverged from the theoretical J_{sc} of ~26 mA cm^{-2}. It might be mainly due to a combination

of Q_f degradation and high recombination at the rear and front surfaces. PC1D simulation revealed that V_{oc} and J_{sc} are significantly diminished with decreasing Q_f values if the enormous front-SRV is exceptionally high. The Q_f reduction might have occurred under the Ag electrode due to fermi-level pinning. The promising solution is inserting a buffer layer between Ag and Al-doped SiO_x to mitigate the degradation; also, sheet resistance must be decreased by increasing Q_f values in the oxide layer.

References

[1] N. E. Grant, S. L. Pain, J. T. White, M. Walker, I. Prokes, and J. D. Murphy, "Enhanced surface passivation of subnanometer silicon dioxide films by superacidic treatments," ACS Appl. Energy Mater. **5**, 1542 (2022).

[2] J.-I. Polzin, F. Feldmann, B. Steinhauser, M. Hermle, and S. Glunz, "Realization of TOPCon using industrial scale PECVD equipment," AIP Conf. Proc. **1999**, 040018 (2018).

[3] J. Haschke, O. Dupré, M. Boccard, and C. Ballif, "Silicon heterojunction solar cells: Recent technological development and practical aspects - from lab to industry," Sol. Energy Mater. Sol. Cells **187**, 140 (2018).

[4] P. Van Halen, R. P. Mertens, R. J. Van Overstraeten, R. E. Thomas, and J. Van Meerbergen, "New TiO_x-MIS and SiO_2-MIS Silicon Solar Cells," IEEE Trans. Electron Devices **25**, 507 (1978).

[5] R. E. Thomas, R. B. North, and C. E. Norman, "Low cost - high efficiency MIS/inversion layer solar cells," IEEE Electron Device Lett. **1**, 79 (1980).

[6] F. Werner, Y. Larionova, D. Zielke, T. Ohrdes, and J. Schmidt, "Aluminum-oxide-based inversion layer solar cells on n-type crystalline silicon: Fundamental properties and efficiency potential," J. Appl. Phys. **115**, 073702 (2014).

[7] K. Jager, and R. Hezel, "Optical stability of silicon nitride MIS inversion layer solar cells," IEEE Trans. Electron Devices **32**, 1824 (1985).

[8] M. Yu, Y. Shi, J. Deru, I. Al-Dhahir, S. McNab, D. Chen, M. Voss, E.-T. Hwu, A. Ciesla, B. Hallam, P. Hamer, P. P. Altermatt, P. Wilshaw, and R. S. Bonilla, "Assessing the potential of inversion layer solar cells based on highly charged dielectric nanolayers," Phys. Status Solidi RRL **15**, 2100129 (2021).

[9] International Technology Roadmap for Photovoltaic (ITRPV) 2022 Results 14th edition (2023).

[10] J. Bao, C. Chen, L. Ma, C. Huang, X. Zhang, Z. Wang, C. Chen, S. Zhan, R. Liu, Z. Qiao, Z. Du, Z. Liu, and J. Chen, "Towards 24% efficiency for industrial n-type bifacial passivating-contact solar cells with homogeneous emitter," In: Proceedings of the 37th European PV Solar Energy Conference and Exhibition, Online, 160–163 (2020).

[11] J. Schmidt, R. Peibst, and R. Brendel, "Surface passivation of crystalline silicon solar cells: Present and future," Sol. Energy Mater. Sol. Cells **187**, 39 (2018).

[12] M. A. Green, Silicon Solar Cells: Advanced Principles & Practice (University of New South Wales, Sydney, Australia 1995).

[13] E. D. Palik, Handbook of Optical Constants of Solids I (Academic Press, 1985).

[14] A. Goetzberger, J. Knobloch, and B. Voß, Crystalline Silicon Solar Cells (John Wiley & Sons, 1998).

[15] J. D. Beck and R. Conradt, "Auger recombination in Si," Solid State Commun. **13**, 93 (1973).

[16] W. Kern and D. A. Puotinen, "Cleaning solution based on hydrogen peroxide for use in silicon semiconductor technology," RCA Rev. **31**, 187 (1970).

[17] A. W. Dweydari and C. H. B. Mee, "Work function measurements on (100) and (110) surfaces of silver," Phys status solidi (a) **27**, 223 (1975).

[18] D. Hiller, P. Hönicke, and D. König, "Material combination of tunnel-SiO_2 with a (sub-)monolayer of ALD-AlO_x on silicon offering a highly passivating hole selective contact," Sol. Energy Mater. Sol. Cells **215**, 110654 (2020).

[19] M. T. Greiner, L. Chai, M. G. Helander, W.-M. Tang, and Z.-H. Lu, "Transition metal oxide work functions: The influence of cation oxidation state and oxygen vacancies," Adv. Funct. Mater. **22**, 4557 (2012).

CHAPTER 6

ANTI-REFLECTIVE STRUCTURES AND LAYERS ON AL-COIL ARCHITECTURE

In the first test cell, it was discovered that the surface charge-induced inversion layer acted as a p^+ emitter for an n-type c-Si solar cell. However, the solar cell performance was significantly lower than that of commercial c-Si solar cells. The front surface of the conventional c-Si solar cell has pyramidal textured Si structures to increase light-trapping, boosting photocurrent density. Moreover, to increase photocurrent density further, an ARC, such as the SiN_y layer with an adequate refractive index, is deposited on the pyramidal textured Si surface. According to the optical simulation, a photocurrent density of 14.75 mA cm^{-2} will be increased by applying optically optimized SiN_y and pyramidal textured Si substrate. Since this increment is almost double for the first test cell, implementing such anti-reflective structures and layers will be a promising solution to improve the performance of Al-COIL solar cells. In addition, an increased carrier generation rate might enhance Q_f in the Al-doped SiO_x layer for Al-COIL solar cells, leading to further hole-selective passivating contact properties. Hence, anti-reflective structures and layers possibly also increase V_{oc} and FF.

In this chapter, the effectiveness of the anti-reflective structures and layers on Al-COIL architecture is elucidated to access high-efficiency c-Si solar cells, from the fabrication of pyramidal textured Si surfaces to the evaluation of the solar cell performance, including the study of SiN_y/Al-doped SiO_x stacks for testing the surface passivation quality and optical property.

6.1 Strategy of improvement for Al-COIL solar cell performance

6.1.1 Enhancement of photocurrent density

A pyramidal textured structure is conventionally formed on the c-Si surface to enhance photocurrent density due to increased light-trapping in the c-Si substrate. Since the reflected light from the textured Si surface is reduced by increasing the chances of reflected light bouncing return to the surface, rather than out to the air, increasing light trapping. Table 6.1 shows the photon current of the incident (J_{inc}), reflected (J_R), absorbed in film (J_A), and absorbed in the substrate (J_G) under 1 sun illumination, simulated by OPAL 2 simulator [1]. PECVD-SiN_y (n = 1.99) was used as an ARC, and the Si substrate thickness was set to 200 μm. Lambertian limit [2] was considered to be a light-trapping model. The simulation shows optimized ARC on the pyramidal textured Si substrate, which realizes J_G = 43.64 mA cm^{-2}. In contrast, planar Si substrate without ARC shows 28.89 mA cm^{-2}. Therefore, the combination of ARC and pyramidal texture increases carrier generation significantly, and implementing this on the Al-COIL structure can lead to a 1.51 times enhancement of photocurrent density. The anti-reflective effect of pyramidal texture and ARC on the Si substrate is depicted in Figure 6.1.

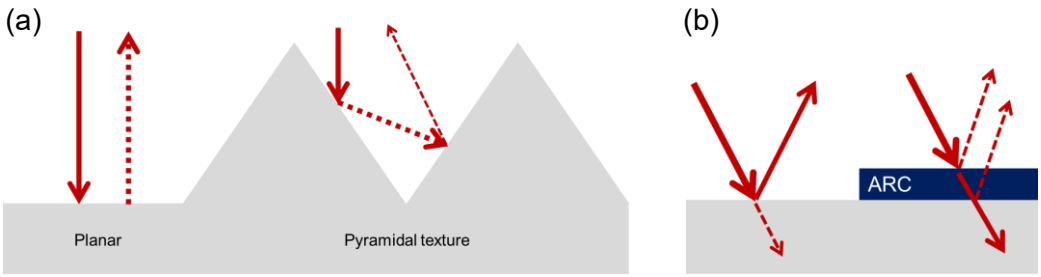

Fig. 6.1 Anti-reflective effect by **(a)** pyramidal textured Si surface and **(b)** anti-reflective coating (ARC) on Si substrate.

Table 6.1 Photon current density (J_G) simulated by OPAL 2.

	J_{inc} (mA cm^{-2})	J_R (mA cm^{-2})	J_A (mA cm^{-2})	J_G (mA cm^{-2})
w/o ARC planar sub.	44.54 (100%)	15.65 (35.1%)	0.00 (0.0%)	28.89 (64.9%)
w/o ARC texture sub.	44.54 (100%)	4.28 (9.6%)	0.04 (0.1%)	40.22 (90.3%)
w/ ARC planar sub.	44.54 (100%)	4.47 (10.0%)	0.00 (0.0%)	40.07 (90.0%)
w/ ARC texture sub.	44.54 (100%)	0.83 (1.9%)	0.07 (0.2%)	43.64 (98.0%)

6.1.2 Enhancement of surface passivation quality

As described earlier, the enhancement of carrier generation up to 1.51 times will be theoretically realized compared to the planar Si surface by implementing the pyramidal textured surface with ARC. As expressed in the equation below [3], in the sufficiently high negative charge condition, the S_{eff} will be decreased with increasing surface hole density (p_{s}). Since p_{s} is proportional to squared Q_{f}, the S_{eff} will be dramatically decreased by the Q_{f} enhancement.

$$S_{\mathrm{eff}} = \frac{S_{n0} n_{\mathrm{d}}}{p_{\mathrm{s}}} \tag{6.1}$$

$$p_{\mathrm{s}} = \frac{{Q_{\mathrm{f}}}^2}{2 k_{\mathrm{B}} T \varepsilon_{\mathrm{Si}}} \tag{6.2}$$

Where S_{n0} is the SRV of the electron, and n_{d} is the sum of N_{dop} and Δn.

At the same time, the increased excited electrons expectedly trapped in the Al-induced acceptor states of the Al-doped SiO_x layer, which leads to a higher negative Q_{f} value with increasing excess carriers at the surface that might be in the inversion layer and the generated carrier at the outermost surface might dominantly affect the carrier trapping. Thus, the depth profile of the generation rate (G) was simulated by the OPAL 2 simulator. As shown in Figure 6.2 (a), the pyramidal texture and pyramidal texture with ARC show higher G values of 2.31×10^{14} and 3.05×10^{14} $\mathrm{cm^{-2}\ s^{-1}}$, respectively. Figure 6.2 (b) shows the ratio of the G values concerning the G value of the planar Si substrate. 1.4 times higher generation occurs at the outermost surface of pyramidal textured Si substrate even without ARC. Hence, a pyramidal textured surface is expected to induce more Q_{f} value. Assuming 1.4 times increment of Δn, the Q_{f} value enhances 1.4 times if the excess carriers are entirely trapped in the Al-induced acceptor states. Additionally, the steeper angle of the high aspect ratio of pyramidal texture with a steeper angle of 80° shows higher G values. It is 1.65 times higher than that of the planar surface. This significant enhancement of G values is attributed to the excellent light-trapping by a pyramidal texture with a pillar-like structure with a high aspect ratio, which can realize ultra-low reflection of only 0.2% in the whole wavelength range of 300 to 1200 nm, as shown in Figure 6.3. Therefore, in this type of solar cell, light absorption is significant for not only J_{sc} but also V_{oc}.

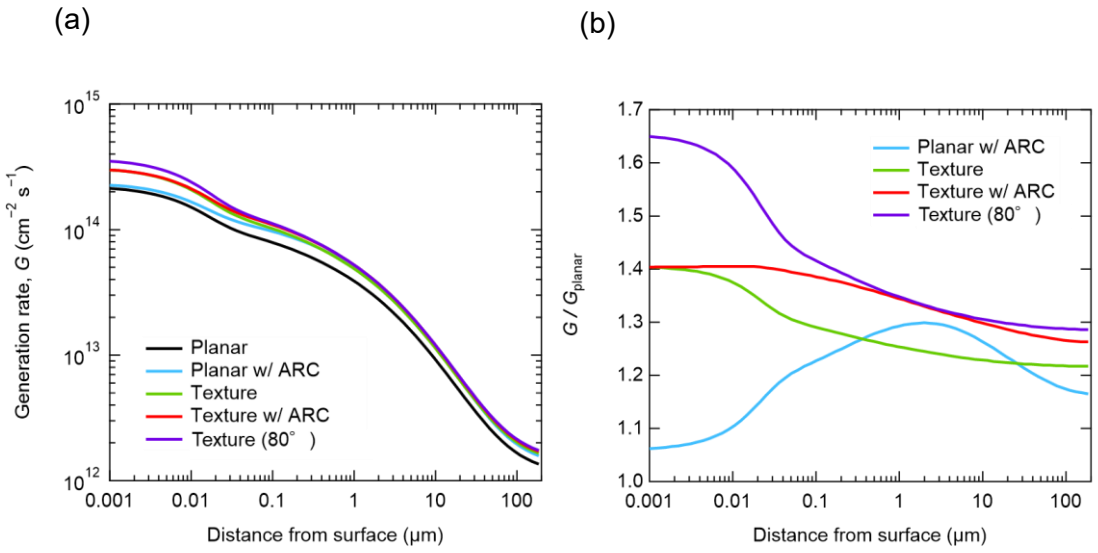

Fig. 6.2 (a) Depth profile of the generation rate (G) for the Si substrates with planar or pyramidal texture surface w/ or w/o ARC, including a pyramidal texture with a base angle of 80°. **(b)** The ratio of the G values concerning the G value of planar Si substrate.

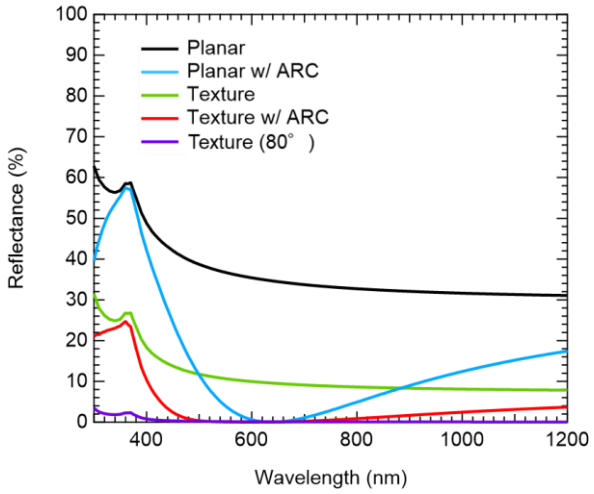

Fig. 6.3 Reflectance spectra for the Si substrates with planar or pyramidal texture surface w/ or w/o ARC, including a pyramidal texture with a base angle of 80°.

As in the following equations [3], S_{eff} will be squared decreased with increasing Q value. Hence, in the case of ARC-coated pyramidal textured Si substrate, the S_{eff} and the surface saturation current density ($J_{0\mathrm{S}}$) will be reduced to 1.96 times lower than the planar Si surface.

$$S_{\mathrm{eff}} = \frac{2k_{\mathrm{B}}T\varepsilon_{\mathrm{Si}}S_{\mathrm{n0}}n_{\mathrm{d}}}{Q^2} \tag{6.3}$$

$$J_{0\mathrm{S}} = q\, n_{\mathrm{i}}^2 \frac{2k_{\mathrm{B}}T\varepsilon_{\mathrm{Si}}S_{\mathrm{n0}}}{Q^2} \tag{6.4}$$

$$S_{\mathrm{n0}} = \nu_{\mathrm{thn}}N_{\mathrm{it}}\sigma_{\mathrm{n}} \tag{6.5}$$

Where T is the absolute temperature, ν_{thn} is the thermal velocity of the electron, N_{it} is the interface state density per area, and σ_{n} is the capture cross-section of the electron, respectively.

However, the pyramidal textured Si surface has a 1.73 times larger surface area than the planar surface. Therefore, the increment of the surface area should be considered to influence the N_{it} value. If the N_{it} value is proportionally increased with increasing the surface area, S_{eff} and $J_{0\mathrm{S}}$ will be reduced ~1.13 times lower than that of the planar Si substrate.

In addition, as shown in Figure 6.2, since R_{sheet} reduces inversely proportional to the Q_{f}^2, R_{sheet} possibly reduces ~50% by 1.4 times increment of the carrier generation. Therefore, J_{sc}, V_{oc}, and FF are expected to be improved using pyramidal texture with ARC by this light-trapping approach. However, the front emitter surface should be sufficiently low R_{sheet}, as low as less than 100 Ω sq^{-1}. To enable such a low level of R_{sheet}, a negative Q_{f} of ~6×10^{13} cm^{-2} might will be needed, corresponding to a very high p_{s} of ~1×10^{22} cm^{-3}.

6.2 Effectiveness of pyramidal textured Si surfaces

The pyramidal textured Si surface typically has a sub-micrometer-sized pyramidal structure with a base angle of 54.74°, as shown in Figure 6.4. The structure consists of several crystal orientations: (100) for the top and bottom, (111) for the slope, and (110) for the ridgeline. Since most of the surface contains (111)-facet, c-Si solar cell performance should have a high-quality hole-selective passivating contact on a (111) surface. In general, however, the pyramidal textured Si makes a tiny structure at the top and the bottom of the valley, which causes insufficient surface cleaning due to increased surface tension of the cleaning solution [4] and degradation of the following surface passivation. Hence, to improve the passivation quality on pyramidal textured Si, it would be crucial to reduce the surface tension.

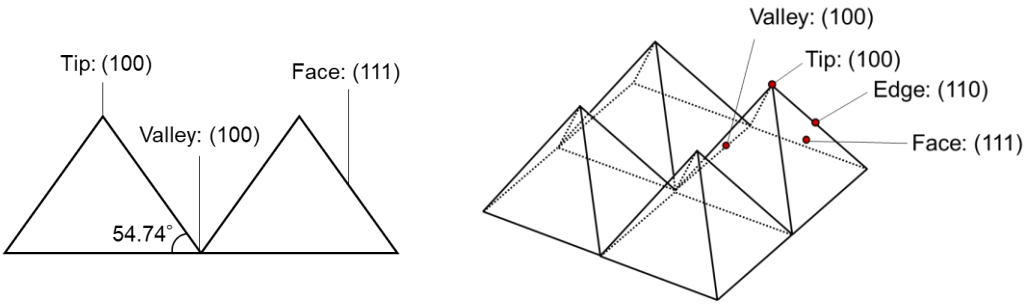

Fig. 6.4 Structure of pyramidal textured Si surface.

However, the field-effect passivation effectively mitigates the surface recombination by the highly negative charges despite the large surface area on nano-sized structures due to the increase of hole density and the reduction of electron density. The previous study showed that black-Si (b-Si) surface can be effectively passivated by a highly negatively charged ALD-Al_2O_3 and demonstrated more than 22% high-efficiency b-Si solar cells [5, 6]. They mentioned the excellent passivation mechanism is attributed to the enhancement of the effective Q_f values by the larger effective surface area. Since the surface charges affect the sub-hundred-nanometer region to generate mirror charges, the opposite face surface charge is affected due to the distance of the sub-hundred nanometer between both sides. The dependence of the distance from the opposite side was simulated using PC1D simulation to investigate the effect of the opposite surface of the negative charges. Figure 6.5 shows the depth profile of carrier densities with highly negative Q_f of 1×10^{13} cm^{-2} for both surfaces. As shown in the Figure, hole density gradually increases, but electron density significantly decreases with closing the faced-surface distance. In contrast, the distance sufficiently far away from each surface does not affect carrier density in the Si substrate. The high Q_f in the oxide generates positive charge carriers in the space charge region as mirrored charges. If the space charge region was compressed by reducing the face-to-face distance of Si

surfaces, the space charges are increased when the surface Q_f is moderate. Hence, the simulation implies that a nano-sized structure with sufficiently high negative Q_f enhances hole density and reduces minority carriers in the Si surface. This enhancement originated from the space charge region compression effect [7,8]. The schematics of the face-to-face structures with nano-sized or micrometer-sized distances between both sides with negative charges are shown in Figure 6.6. In the case of a nano-sized structure, induced mirror charges exist in bulk Si. On the other hand, in the case of a micrometer-sized structure, the mirrored charges only exist at the surface of Si. The nano-sized structure induces an inversion layer in the whole Si structure, as shown in Figures 6.5 and 6.6. Hence, the nano-sized pyramidal textured Si surface with highly negative charges expectedly enhances the hole-selective passivating contact. However, the typical alkaline texturing process is unavailable for fabricating such a nano-sized structure. As the first stage, I focused on the effectiveness of conventionally available pyramidal texture formed by alkaline texturization for the Al-COIL solar cells.

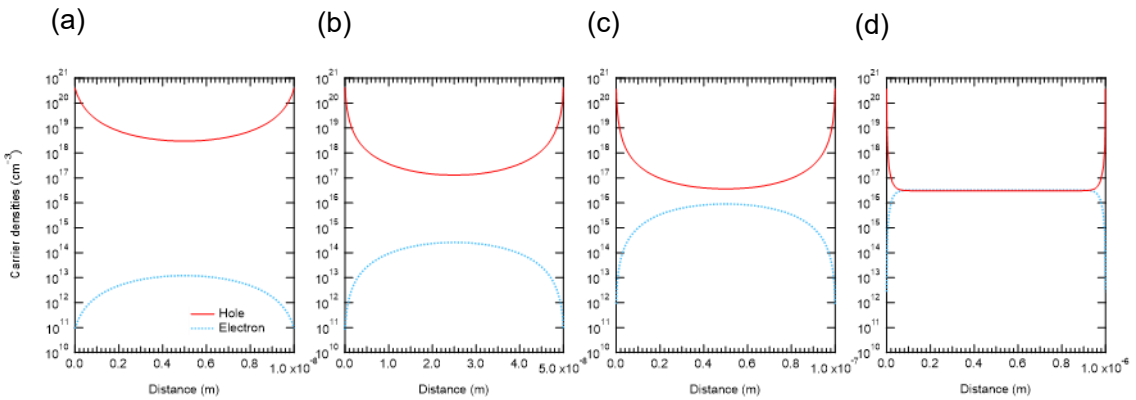

Fig. 6.5 Depth profile of carrier densities of face-to-face structure with distances of **(a)** 10 nm, **(b)** 50 nm, **(c)** 100 nm, and **(d)** 1 μm between both sides with highly negative Q_f of 1×10^{13} cm^{-2}.

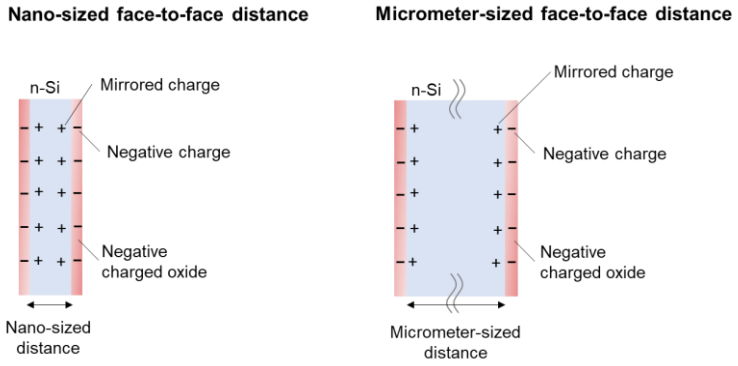

Fig. 6.6 Schematics of the face-to-face structures with nano-sized or micrometer-sized distance between both sides with negative charges.

6.3 Sample fabrication

6.3.1 Texturing process

Double-side-polished 280 μm thick FZ n-type Si (100) with a resistivity of 2.5 Ω cm (TOPSIL PV-FZ™) was used. The Si substrate was cleaved into 50 × 50 mm-sized pieces and cleaned by ultrasonication with acetone (Electrical grade, Kanto Chemical Co., Inc.) followed by ultrasonication with ethanol (Electrical grade, Kanto Chemical Co., Inc.). The cleaned samples were immersed into an alkaline solution at 80 °C for 15 min with a magnetic stirrer agitating (600 rpm) to form pyramidal textures on Si substrates. The 80 °C alkaline solution was prepared in advance by dissolving 85% potassium hydroxide (KOH) (9 g, Nacalai Tesque Inc.) into DIW (440 mL) with an addition of TP101 (1.35 g, Hayashi pure chemical Ind., Ltd.) as a micro-masking agent.

6.3.2 Cleaning and surface passivation

After the texturing process, the samples were rinsed with DIW for >2 min. After the treatment of 5% diluted hydrofluoric acid (DHF) containing 60% methanol for 2 min and rinse in DIW for 1 min, the textured Si substrates were cleaned by RCA cleaning. Between SC-1 and SC-2, and after the SC-2 cleaning, the methanol-added DHF treatment was performed for 2 min. After rinsed with DIW for 1 min followed by ethanol for 1 min, $Al(NO_3)_3$ treatment was performed in $Al(NO_3)_3$ aqueous solution with $Al(NO_3)_3 \cdot 9H_2O$ molar concentration of 0.25 mol L^{-1} for 12.5 min. The hot $Al(NO_3)_3$ aqueous solution was prepared in advance by dissolving $Al(NO_3)_3 \cdot 9H_2O$ (28.1 g, special grade, Junsei Chemical Co., Ltd.) and added polyethylene glycol (PEG) (3 mL, molecular weight of 200, extra pure reagent, Junsei Chemical Co., Ltd.) as a surfactant in DIW (300 mL) in a Pyrex glass beaker (SCI 1000 mL) and heated to a boiling temperature (~95 °C) on a hot plate (AS ONE Corporation, CHPS-170DF). During the heating process, the beaker was capped to avoid the evaporation of the solution. The solutions were not intentionally stirred during the process; however, drastically generated bubbles could be confirmed at the boiling temperature. After the $Al(NO_3)_3$ treatment, processed Si substrates were rinsed in DIW for 1 min, followed by ethanol for 1 min, and entirely dried by N_2 blow.

The sample fabrication process flow, the sample structure, and the appearance of the $Al(NO_3)_3$ treatment are shown in Figures 6.7 and 6.8, respectively.

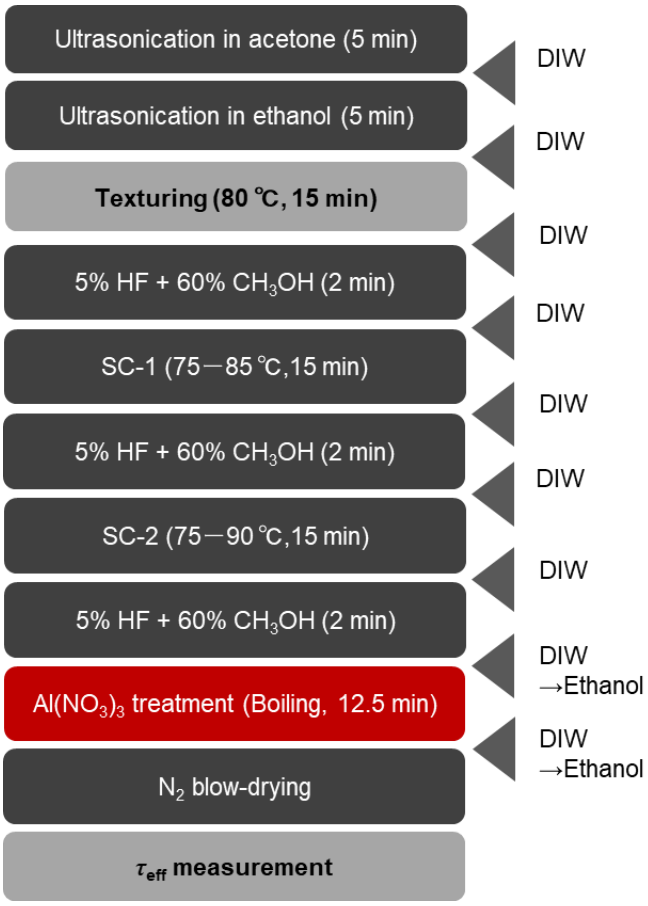

Fig. 6.7 Sample fabrication process flow

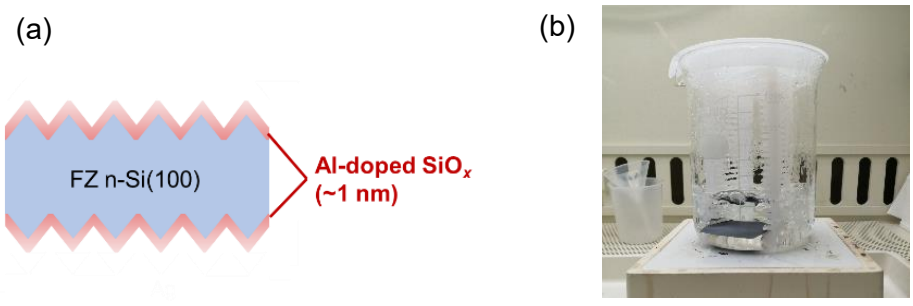

Fig. 6.8 **(a)** Sample structure and **(b)** appearance of $Al(NO_3)_3$ treatment.

6.4 Sample evaluation

The τ_{eff} measurements were performed using μ-PCD (Kobelco Research Institute, Inc., LTA-1510EP). The τ_{eff} mapping data were acquired within the 44×44 mm^2 area in 50×50 mm^2 sized samples with a 1 mm pitch. A pulsed laser with a wavelength of 904 nm and an areal photon density of 5 × 10^{13} cm^{-2} was used for the carrier excitation. Additionally, τ_{eff} and iV_{oc} as a function of Δn were analyzed using QSSPC (Sinton Instruments, WCT-120). For the analysis, the estimated value of 1.05 was used as an optical factor (f_{opt}). Using the following relationship, the f_{opt} was calculated from photon current density (J_G) of 40.03 mA cm^{-2} generated from measured reflectance and transmittance spectra. The reflectance and transmittance spectra were acquired using a UV-vis-NIR spectrophotometer (Shimadzu, UV-3150).

$$A(\lambda) = 1 - R(\lambda) - T(\lambda) \tag{6.6}$$

$$J_G = q \int_{\lambda_{300}}^{\lambda_{1200}} F_{ph}(\lambda)\, A(\lambda)\, d\lambda \tag{6.7}$$

$$f_{opt} = \frac{J_G\ (\mathrm{mA\ cm^{-2}})}{38\ (\mathrm{mA\ cm^{-2}})} \tag{6.8}$$

Here, $A(\lambda)$, $R(\lambda)$, $T(\lambda)$, and $F_{ph}(\lambda)$ are absorbance, reflectance, transmittance, and photon flux at each wavelength. J_G is photon current density, and q is elemental charge. 38 mA cm^{-2} means the photocurrent density of a standard cell, which is mounted in the Sinton lifetime tester, and the 38 mA cm^{-2} corresponds to f_{opt} = 1. The $S_{eff,\,max}$ was calculated using Eq. (4.3). Since the $S_{eff,\,max}$ calculation requires wafer thickness, it is measured using a micrometer at the 9 points of samples after τ_{eff} measurements. The measurements estimated 269 μm as an average thickness. The measured thicknesses are shown in Figure 5.9. In addition, the J_0 value was also analyzed by the Kane and Swanson method using the auger-corrected effective minority carrier lifetime (τ_{corr}) over the Δn range of 1×10^{15} to 9×10^{15} cm^{-3}.

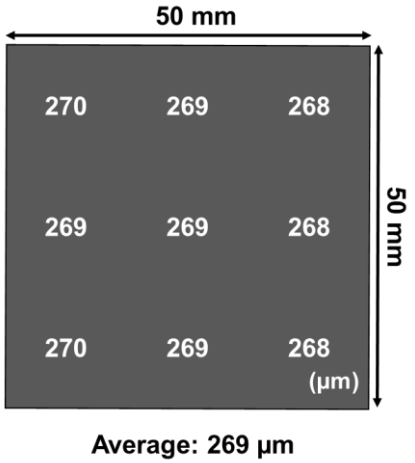

Fig. 6.9 Measured wafer thickness of a fabricated pyramidal textured Si surface.

The surface morphology was observed by SEM (Hitachi, TM3030Plus) and AFM mode, mounted in SPM (Bruker, Dimension Icon). Additionally, the surface potential was measured by a kelvin probe force microscope (KPFM) mounted in the SPM system. Pt-Ir coated Sb highly doped Si (Bruker, SCM-PIT) was used for the tip of the probe. The sample was placed on the sample stage with an Ag paste on the corner of the sample to form an electrical contact between the sample and the sample stage.

6.5 Surface morphology

Figure 6.10 shows the SEM image of the fabricated pyramidal textured Si surface. The ~2 µm sized pyramidal textures were randomly formed on the Si surface, and less than 1 µm sized pyramidal texture also existed on the Si substrate. The planar surface was transformed entirely into pyramidal structures, and the shape of the tip, valley, edge, and face structures was seen. Most structures consist of (111)-facets at the face structures. AFM measurement revealed the depth of pyramidal texture is ~1 µm, as shown in Figure 6.11. The estimated base angle was a lower value of 49.8°compared with a theoretical value of 54.74°.

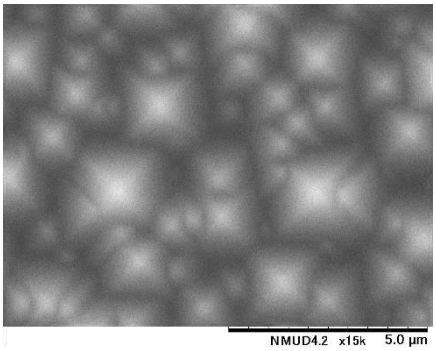

Fig. 6.10 SEM image of the fabricated pyramidal textured Si surface.

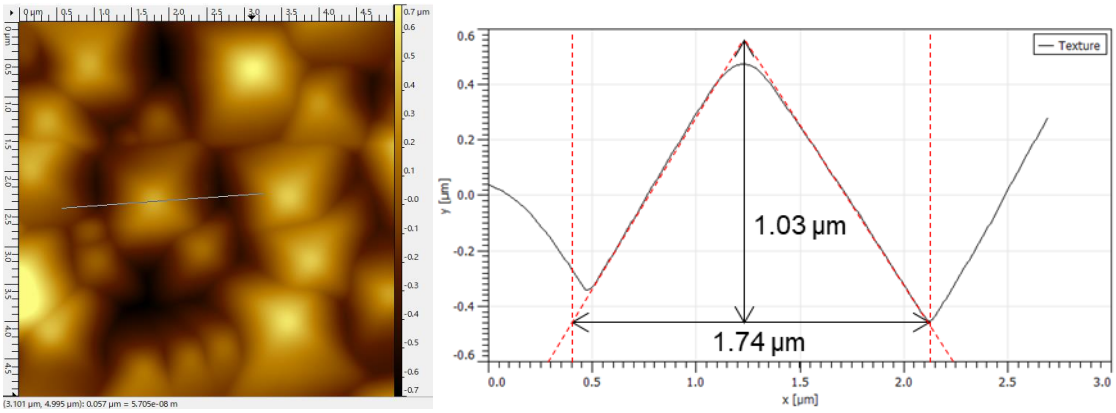

Fig. 6.11 AFM image and the depth profile of the fabricated pyramidal textured Si surface.

6.6 Estimation of photon current density

Figure 6.12 shows (a) the reflectance (R), (b) transmittance (T) spectra, and Figure 6.13 shows the calculated absorbance (A) spectra for the fabricated pyramidal textured Si substrate and mirror polished Si substrate as a reference. The pyramidal textured Si surface significantly decreased reflectance below 10% in the wide wavelength range of 500–1070 nm. In addition, the transmittance also reduced in the wavelength range of ~950–1200 nm. The calculated absorbance spectra estimated the J_G to be 40.03 mA cm^{-2} for pyramidal texture and 26.00 mA cm^{-2} for planar using eq. (5.6)–(5.8), respectively. Hence, the J_G gain from the pyramidal textured Si substrate was estimated to be 14.03 mA cm^{-2}. The calculated J_G and f_{opt} are summarized in Table 6.2.

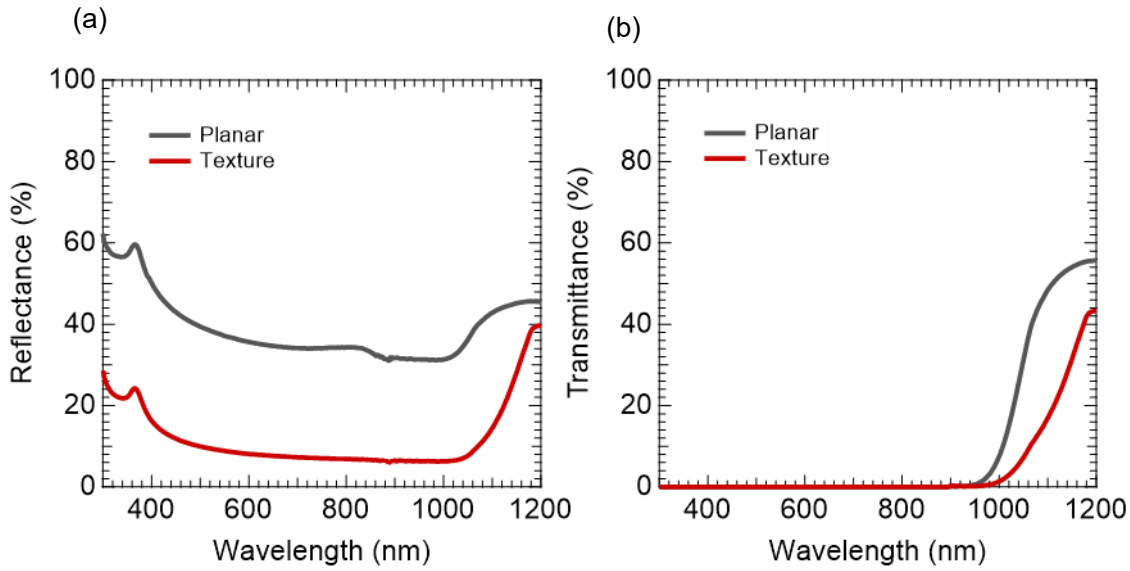

Fig. 6.12 **(a)** Reflectance and **(b)** transmittance spectra for the fabricated pyramidal textured and mirror polished Si substrate.

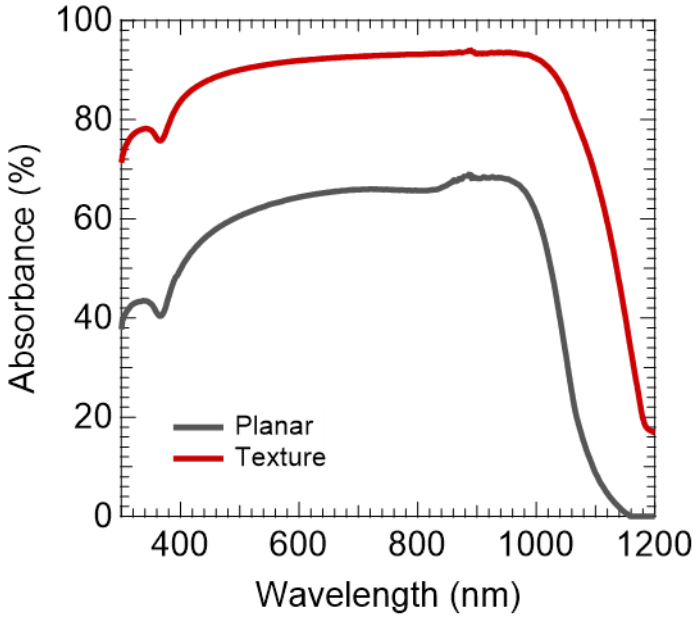

Fig. 6.13 Calculated absorbance spectra for the fabricated pyramidal textured and mirror-polished Si substrate.

Table 6.2 Estimated photon current density (J_G) and optical factor (f_{opt}).

Substrate	J_G (mA cm^{-2})	f_{opt}
Planar	26.00	0.69
Pyramidal texture	40.03	1.05

6.7 Surface passivation quality

Figure 6.14 shows time-related τ_{eff} mappings for the passivated pyramidal textured Si substrate stored in ambient air. The high τ_{eff} could not be obtained after the passivation and decreased after 10 min. However, after 6 h stored in the ambient air, the τ_{eff} was dramatically increased to 491 µs, on average. This time-related τ_{eff} increase might be attributed to the lack of surface oxidation. If the formed interfacial SiO_x is too thin, the Q_f value will be decreased due to the low concentration of AlO_4 structure. Thus, the interfacial Si will oxidize while stored in ambient air, resulting in higher surface passivation quality with a negative Q_f value. For this sample fabrication, methanol rinse was not performed before the $Al(NO_3)_3$ treatment, and PEG was not added to the $Al(NO_3)_3$ aqueous solution. The pyramidal texture has very fine structures, especially in the part of the valley. Therefore, it might be challenging to passivate such a fine structure due to low wettability on the surface [9].

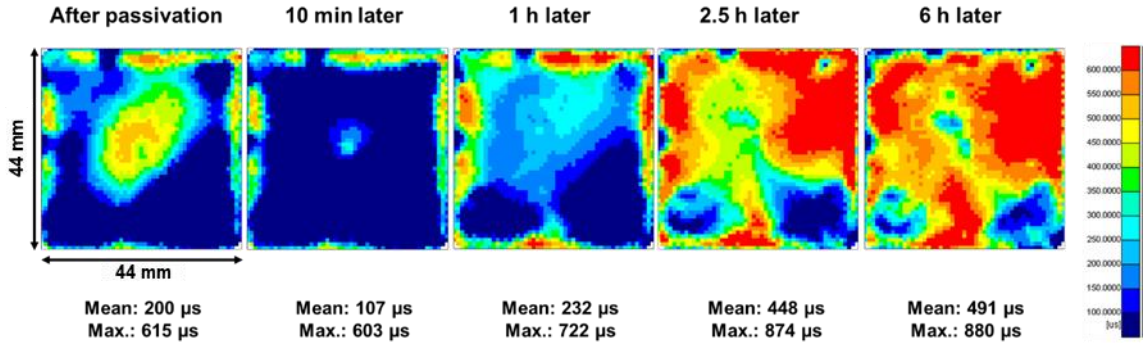

Fig. 6.14 Time-related τ_{eff} mappings acquired by µ-PCD for the passivated pyramidal textured Si substrate stored in ambient air.

To enhance the wettability and oxidation reaction on the pyramidal textured structure, one of the promising solutions was performing an ethanol rinse before the $Al(NO_3)_3$ treatment to remove the residue of HF chemicals altogether. Moreover, adding a surfactant into $Al(NO_3)_3$ aqueous solution was another solution. Therefore, the ethanol rinse was performed before the passivation and $Al(NO_3)_3$ treatment with PEG as a surfactant. Figure 6.15 shows τ_{eff} mappings acquired by µ-PCD for (a) just after the surface passivation and (b) after 6 hours. As a result, good surface passivation quality was observed just after the passivation. On average, τ_{eff} of 400 µs and 474 µs, and 698 µs and 692 µs were obtained as maximum τ_{eff}, respectively. As described in Chapter 4, the $Al(NO_3)_3$-treated mirror polished n-type Si(111) showed a τ_{eff} of 360 µs. If compared just after

the passivated sample, passivated pyramidal textured Si shows slightly higher τ_{eff}. However, time-related changes were confirmed in the τ_{eff}. After 6 h storage in ambient air, the low τ_{eff} region became higher τ_{eff}. On the other hand, the high τ_{eff} region became slightly lower τ_{eff}.

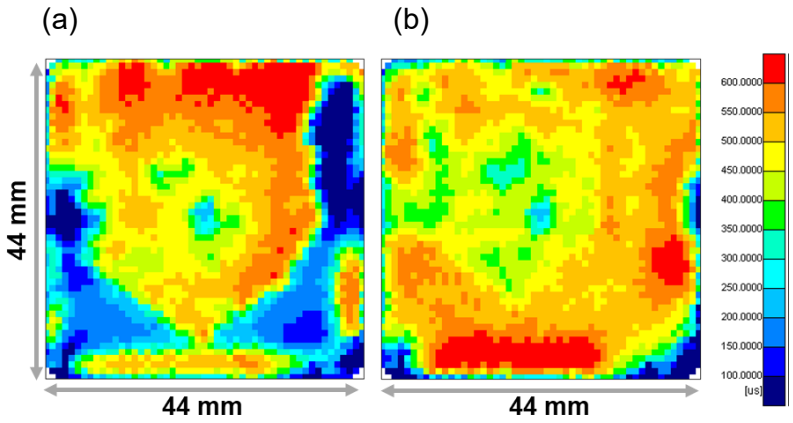

Fig. 6.15 τ_{eff} mappings acquired by μ-PCD for **(a)** just after the surface passivation and **(b)** after 6 hours of storage in ambient air.

Figure 6.16 shows τ_{eff} and $S_{eff,\,max}$ of the pyramidal textured Si substrate treated in boiled 0.25 mol L^{-1} $Al(NO_3)_3$ (aq.) for 12.5 min as a function of Δn for just after the surface passivation and after 6 hours storage in ambient air. Considering the low Δn region of ~10^{14} cm^{-3} shows high surface passivation quality as τ_{eff} of >1 ms, the field effect might have dominantly originated from surface passivation. The high τ_{eff} of 935 and 1012 μs were confirmed at Δn =1×10^{15} cm^{-3}, and the corresponding $S_{eff,\,max}$ were estimated to be 14.4 and 13.3 cm s^{-1}, respectively. The iV_{oc} were estimated to be 680 and 682 mV at 1 sun illumination, and J_0 were analyzed as 68 and 59 fA cm^{-2}, respectively. The fitted Auger-corrected inverse effective lifetimes and iV_{oc} as a function of light intensity are shown in Figures 6.17 and 6.18, respectively.

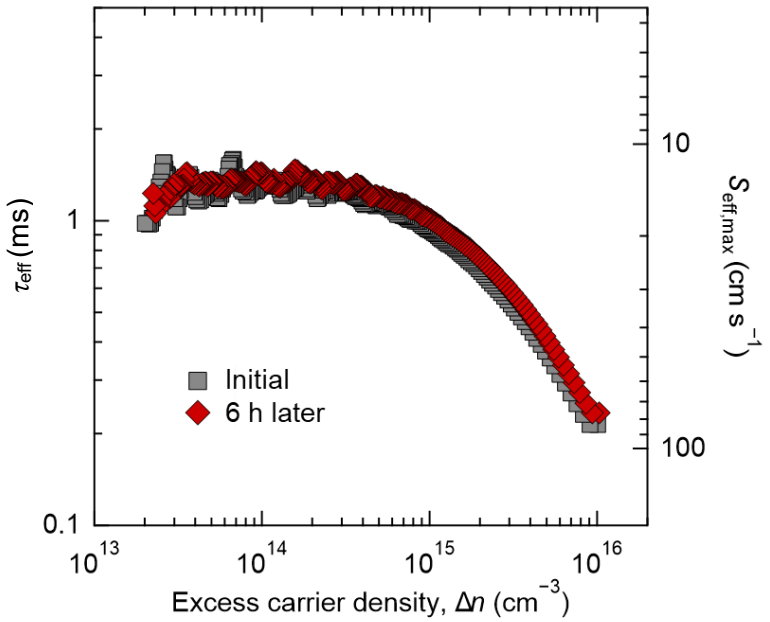

Fig. 6.16 τ_{eff} and $S_{eff,\,max}$ of the pyramidal textured Si substrate treated in boiled 0.25 mol L^{-1} $Al(NO_3)_3$ (aq.) for 12.5 min as a function of Δn for just after the surface passivation and after 6 hours storage in ambient air.

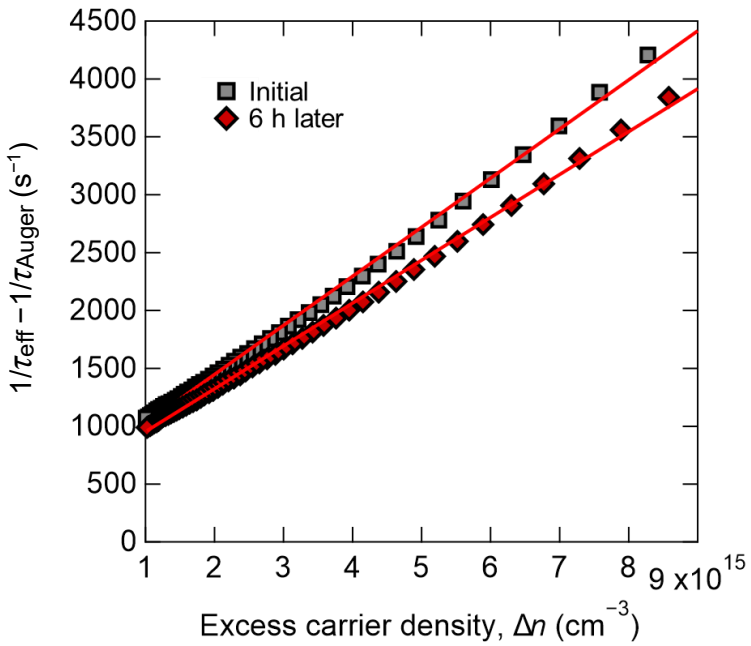

Fig. 6.17 Fitted Auger-corrected inverse effective lifetimes of the pyramidal textured Si substrate treated in boiled 0.25 mol L^{-1} $Al(NO_3)_3$ (aq.) for 12.5 min as a function of Δn for just after the surface passivation and after 6 hours storage in ambient air.

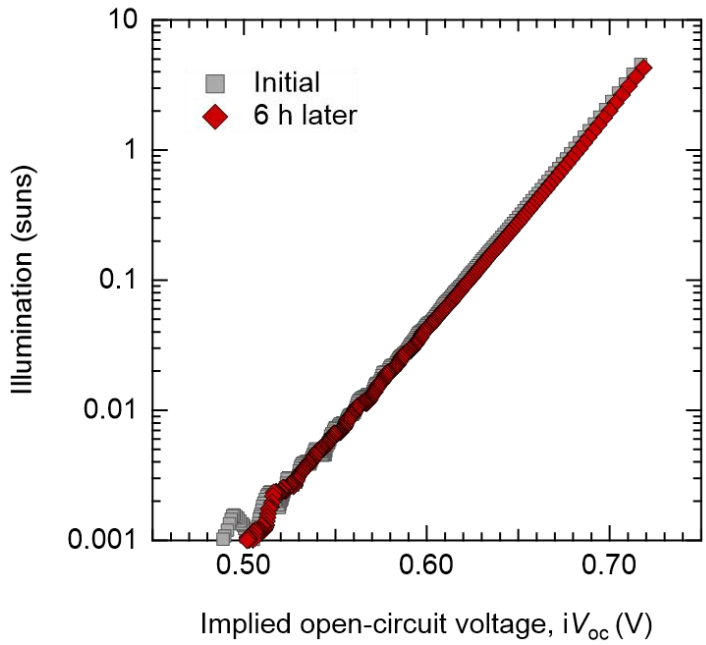

Fig. 6.18 iV_{oc} of the pyramidal textured Si substrate treated in boiled 0.25 mol L^{-1} $Al(NO_3)_3$ (aq.) for 12.5 min as a function of light intensity for just after the surface passivation and after 6 hours storage in ambient air.

For pyramidal textured Si substrate, it is difficult to evenly passivate Si surface with a large area of 50×50 mm^2 at a laboratory level. It might be due to unevenness of the process temperature during the $Al(NO_3)_3$ treatment because the heating process was performed using a hot plate, which can only heat from the bottom of a beaker. Therefore, 15×15 mm^2 sized relatively small Si pieces are evaluated to compare the surface passivation quality of the planar and pyramidal textured Si substrates. Figure 6.19 shows the τ_{eff} mappings acquired by μ-PCD for an $Al(NO_3)_3$-treated pyramidal textured Si substrate and a planar Si (111) substrate. These pieces are proceeded through the same process (cleaning and surface passivation). The pyramidal texture showed a significant increase in τ_{eff} up to 688 μs on average compared with a planar substrate of 387 μs. The 1.77 times higher τ_{eff} might have originated from the increased carrier generation. The estimated absorbances of the 904 nm light are 93.4% for a textured surface and 68.1% for a planar surface, respectively. Hence, the pyramidal textured Si substrate can absorb a 1.37 times higher photon concentration. If the increased excess carriers can be trapped in the Al-induced acceptor states, τ_{eff} will be increased 1.88 times because τ_{eff} is proportional to Q_f^2 in sufficiently high negative charged conditions. Since this enlargement is close to the τ_{eff} increment, the τ_{eff} increment mainly originated from an increase in light-trapping. However, considering D_{it} increase by the surface area of pyramidal texture, another effect must be regarded to explain this τ_{eff} increment.

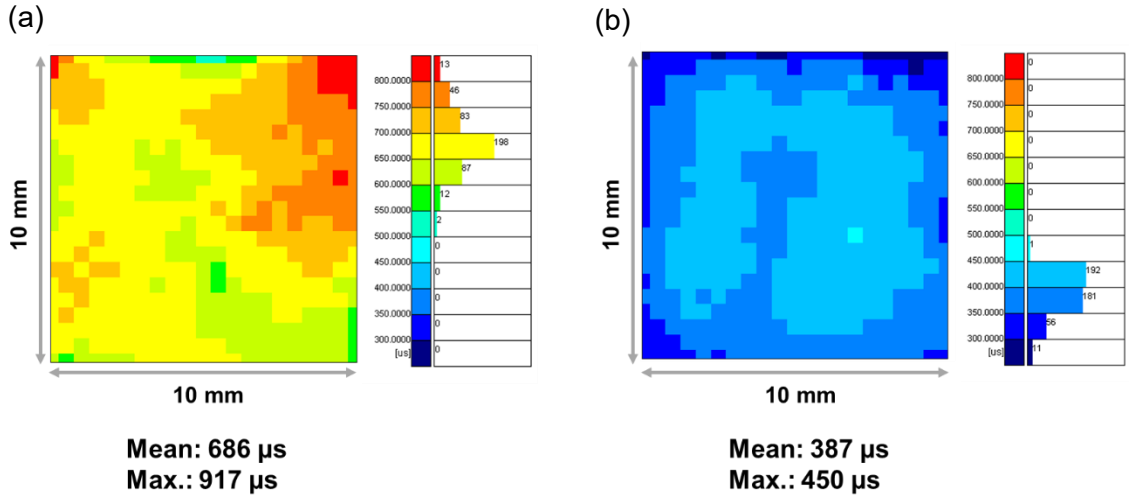

Fig. 6.19 τ_{eff} mappings acquired by µ-PCD for the $Al(NO_3)_3$-treated **(a)** pyramidal textured and **(b)** planar Si substrate.

6.8 Surface potential

The surface potential of Al-COIL on a pyramidal textured Si surface was investigated using KPFM, which is mounted in the SPM system. Figures 6.20 (a), (b), and (c) show the height mapping, and Figures 6.20 (d), (e), and (f) show the surface potential of the planar, valley region of pyramidal texture, and tip region of pyramidal texture, respectively. The planar surface and valley region of pyramidal texture showed a comparable surface potential of −0.72 V and −0.75 V, respectively. However, the tip region of pyramidal texture showed a lower surface potential of −0.98 V. Since the used probe was Pt-Ir coated Sb highly doped Si with a work function of 4.86 V [9], which is very close to the valence band edge of Si, Al-doped SiO_x formed n-type Si surface bands are strongly bent upward, especially in the tip region of the pyramidal textured surface. The tip of a pyramidal textured Si surface can be recognized as a nano-sized structure due to opposite side surfaces with highly negative charges within a nano-scale distance. Therefore, the lower surface potential on the pyramid's tip demonstrated that such a nano-sized structure enhances hole concentration, causing strong upward band bending.

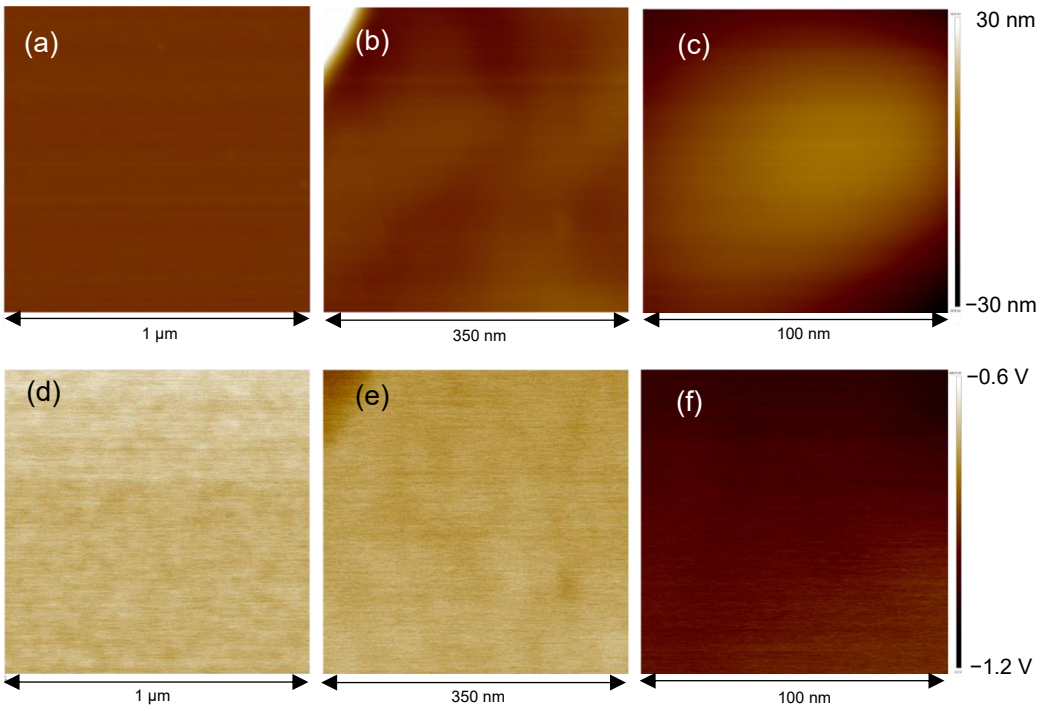

Fig. 6.20 **(a)**, **(b)**, and **(c)**: height mapping and **(d)**, **(e)**, and **(f)**: surface potential for the planar, valley region of pyramidal texture, and tip region of pyramidal texture, respectively.

Figure 6.21 shows simulated 2D mapping of surface hole density on a pyramidal textured Si surface with a high negative Q_f of 3.0×10^{13} cm^{-2} using PC3S [10] simulation. The simulation was performed under 1 sun illumination for a 2 μm size pyramidal texture with a base angle of 54.74° on a 15 μm thick n-type Si substrate with a doping concentration of 2.0×10^{15} cm^{-3}. This 2D simulation suggests that surface hole density on the tip and edge of the pyramidal structure is enhanced. Thus, 2D simulation assists the lower surface potential of the tip of the pyramidal structure. Therefore, sub-micrometer-sized typical pyramidal textured Si substrates have opposite side surfaces with highly negative charges within a nano-scale distance, which enhances the surface hole density. In such sufficiently high negative Q_f conditions, S_{eff} will be inversely proportional to the surface hole density, which realizes high surface passivation quality and hole selectivity. However, in such high negative Q_f conditions, the averaged surface hole density is almost the same as a planar surface. This would be one of the reasons for the higher surface passivation quality on a pyramidal textured Si surface in the low negative Q_f conditions, such as $Q_f = 10^{11} cm^{-2}$, a significant increase can be seen from 9.99×10^{10} to 4.80×10^{14} cm^{-3} by applying pyramidal texture, as shown in Figure. 6.22. When the estimated Q_f value was considered as -3.2×10^{12} cm^{-2}, pyramidal texture showed a slight increase of surface hole density from 9.52×10^{19}

to 1.08×10^{20} cm^{-3}. Assuming most of the surface orientations are (111), D_{it} increase is attributed to the ~1.73 times larger surface area of the pyramidal texture. Therefore, the 1.13 times higher surface hole density might not compensate for the increased D_{it}. Hence, the increase of carrier generation rate by enhanced light-trapping dominates the improvement of the surface passivation quality.

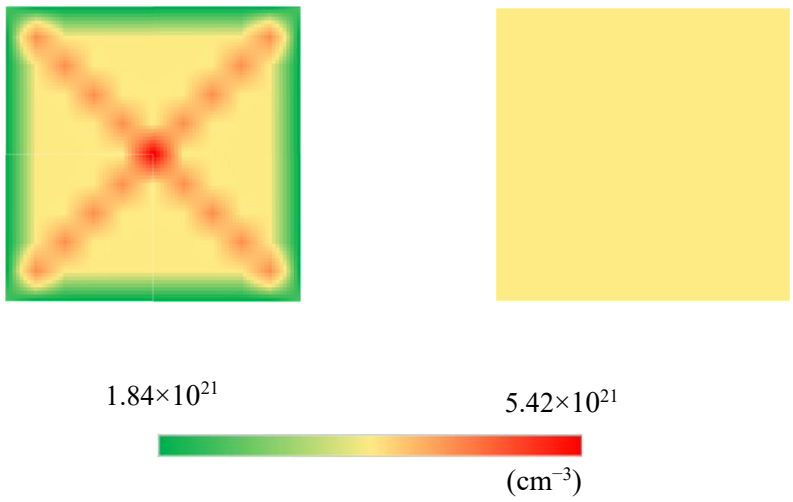

Fig. 6.21 PC3S simulated 2D mappings of surface hole density on **(a)** pyramidal textured and **(b)** planar Si surface with a high negative Q_f of $3.0\times10^{13}cm^{-3}$. The color scale is shown in percentile; the center value is shown as yellow.

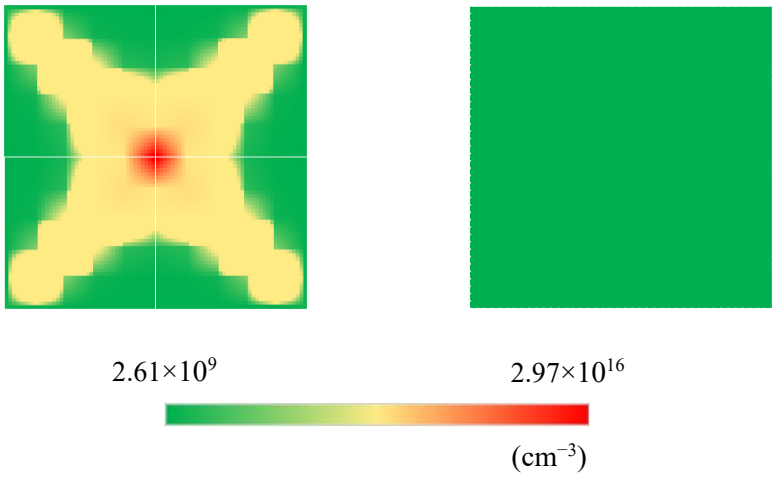

Fig. 6.22 PC3S simulated 2D mappings of surface hole density on **(a)** pyramidal textured and **(b)** planar Si surface with a high negative Q_f of 1.0×10^{11} cm^{-3}. The color scale is shown in percentile; the center value is shown as yellow.

6.9 Fabrication and evaluation of solar cells

6.9.1 Sample fabrication

The Ag finger electrode was deposited on the $Al(NO_3)_3$-treated sample through a mask by thermal evaporation in a vacuum chamber at a pressure of 9×10^{-4} Pa to evaluate solar cell performance. To form a grid electrode, after the deposition of the Ag finger electrode, the deposited sample was rotated 90°; subsequently, the Ag finger electrode was deposited. For the rear side of the sample, the full-area Mg followed by Al electrodes were thermally evaporated on the rear surfaces. The rear side of the Si band bends downwards because Mg is a low work function (3.66 eV [11]) material concerning n-type Si, resulting in the formation of electron selective contact by an accumulation layer. The fabrication process flow and the fabricated solar cell structure are shown in Figures 6.23 and 6.24, respectively.

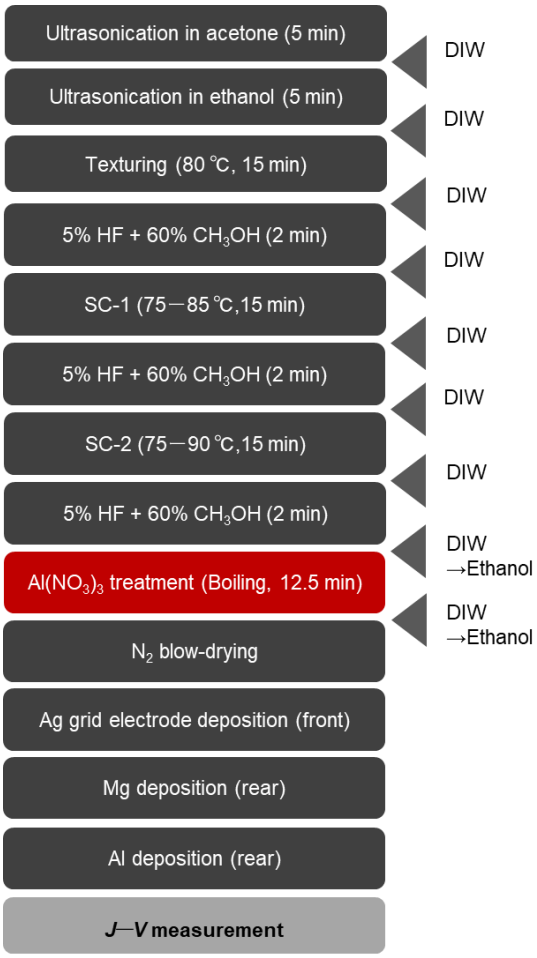

Fig. 6.23 Fabrication process flow of Al-COIL solar cell with a pyramidal textured surface.

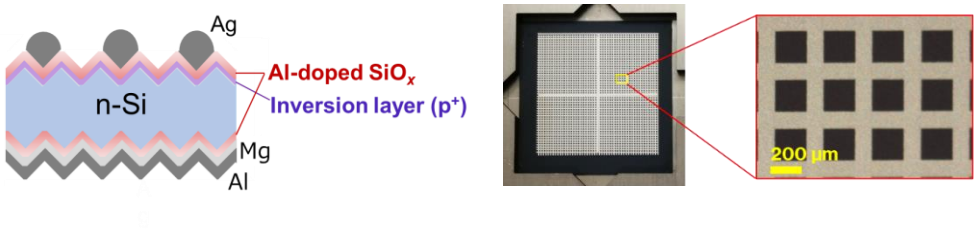

Fig. 6.24 Fabricated Al-COIL solar cell structure and front Ag grid electrode.

6.9.2 Sample evaluation

The current density–voltage (*J–V*) curves were acquired in the dark and under 1 sun illumination (AM 1.5 G). The light intensity was calibrated with a Si reference cell (Bunkoukeiki Co., Ltd., BS-500BK Si photodiode detector) to an irradiance of 0.1 W cm^{-2} at RT. The J_{sc} was calculated with an active area of 0.251 cm^2 after subtracting the estimated area of Ag front electrodes in an opened area of black-shade mask of 0.624 cm^2. During the measurement, one probe was placed on the Ag finger electrode, and the other was placed on the Cu plate, which was contacted on the Al electrode of the rear side of the test cell to collect the holes and electrons, respectively.

6.9.3 J–V characteristics of Al-COIL solar cells

Figure 6.25 shows *J–V* curves of the devices with AL-COIL structures on a pyramidal texture and a planar surface acquired in the dark (dotted line) and under 1 sun illumination (solid line). The solar cell performances are shown in Table 6.3. As a result, the device fabricated on a planar Si substrate led to a low η of 2.80%. In comparison, a significantly improved η of 12.13% was acquired for the device fabricated on a pyramidal textured Si substrate. In particular, a very high FF of 0.794 was achieved. The high FF was realized by a fine grid Ag electrode on an emitter side with a larger surface area of pyramidal textured surface. This can mitigate a low lateral conductivity in the emitter induced by Al-COIL. However, the V_{oc} is still lower than the analyzed iV_{oc} of 682 mV. The low V_{oc} might be attributed to the V_{bi} reduction under the Ag grid electrode due to a low work function of Ag, as discussed in Chapter 4. In addition, the J_{sc} also showed a significant increase, but still lower than the theoretical value of 40.03 mA cm^{-2}. This J_{sc}

degradation might have originated from the carrier recombination at the front emitter surface, as discussed in Chapter 4. If there are many carrier recombination centers at the emitter side and a degradation of charged oxide as a low negative Q_f, the J_{sc} degradation occurs as shown in the *J–V* curves of Figure 6.26 acquired from PC1D simulation.

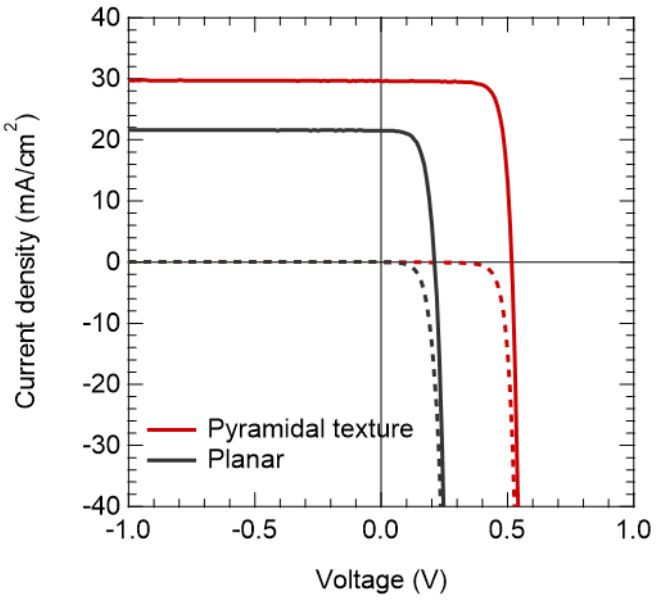

Fig. 6.25 *J–V* curves of the fabricated solar cells with Al-COIL structures on a pyramidal texture and a planar surface.

Table 6.3 Solar cell performances of the AL-COIL on a pyramidal texture and a planar surface.

	J_{sc} (mA cm^{-2})	V_{oc} (V)	FF	η (%)
Pyramidal texture	29.63	0.516	0.794	12.13
Planar n-Si(111)	21.50	0.210	0.622	2.80

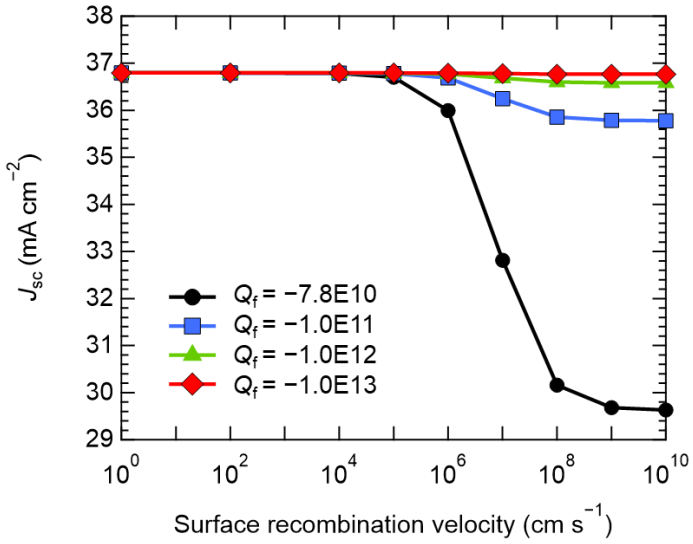

Fig. 6.26 PC1D simulated J_{sc} as a function of surface recombination velocity (SRV) with varying surface Q_f values.

6.10 Anti-reflective coating on Al-COIL structure

One possible solution to increase the J_{sc} of Al-COIL solar cells is through the use of ARC, which can enhance light trapping by gradually changing the refractive index (n) between air (n=1) and the Si substrate (n = 3.88 at a wavelength of 630 nm) [12]. The reflection can be calculated using the Fresnel equations. If the light incidents are perpendicular to the surface, the reflectance is expressed by

$$R = \left(\frac{n_1 - n_2}{n_1 + n_2}\right)^2 \tag{6.9}$$

Where n_1 is the refractive index of the first media and n_2 is the refractive index of the second media, respectively.

The optimal value of n is produced by the geometric mean of the two surrounding indices, as described below.

$$n_{\mathrm{ARC}} = \sqrt{n_{\mathrm{air}} n_{\mathrm{sub.}}} \tag{6.10}$$

Therefore, by inserting a layer with an n value of 1.97, the reflection of light can be mitigated, and SiN_y is commonly used for this purpose due to its n value. Furthermore, the key to reducing reflection is to ensure that the reflected waves from these two interfaces between air/ARC and ARC/Si have a path difference of $\lambda/2$ (half-wavelength). This path difference is crucial for destructive interference to occur, where the peaks of one wave align with the troughs of the other, resulting in minimal reflected light. To achieve a path difference of $\lambda/2$, the film should be $\lambda/4$ thick, corresponding to a quarter-wavelength. Hence, the optimal thickness of ARC is given by the equation below.

$$d_{\mathrm{ARC}} = \frac{\lambda}{4 n_{\mathrm{ARC}}} \tag{6.11}$$

Hence, the thickness of ARC should be 80 nm to minimize the reflection of light. Typically, SiN_y is deposited using plasma-enhanced chemical vapor deposition (PECVD), but this method can damage ultrathin layers on Si substrates and affect surface passivation quality and solar cell performance [13]. As an alternative, catalytic chemical vapor deposition (Cat-CVD) offers a gentler approach to deposit, using catalytically generated radicals on a hot wire with a high temperature of approximately 1800 °C, without plasma. A previous study demonstrated the Cat-CVD-grown SiN_y layer has an optical transparency with n~2 and excellent surface passivation quality [14]. Therefore, SiN_y /Al-doped SiO_x stacks were investigated to determine whether the stacks show excellent surface passivation quality and optical properties.

6.10.1 Sample fabrication

Double-side-polished n-type FZ Si(100) wafers with a thickness of 280 μm, a resistivity of 2.5 Ωcm, and a size of 50×50 mm^2 and 20×20 mm^2 were used in this research. The Al-doped SiO_x layers were formed on the Si surfaces through the processes described in Chapter 4; the treatments were performed for 1 to 30 min. In addition, as a reference, after an RCA cleaning followed by 1% diluted hydrofluoric acid (HF) treatment for 1 min and rinse with DIW, these pieces were immersed in the 70wt.% nitric acid (HNO_3) aqueous solutions at room temperature (RT) for 10 min. Right after the HNO_3 treatment and DIW rinse for 2 min, 80-nm-thick SiN_y layers were

deposited on both sides or one side of samples by Cat-CVD at a substrate temperature of 100 °C, SiH_4 and NH_3 flow rates of 4 and 250 sccm, respectively, under a pressure of 3.2 Pa. A tungsten (W) wire heated at 1800 °C was used as a catalyzer for decomposing those precursors into each radical species. After the deposition for 700 s, the samples were placed in the quartz tube furnace heated at 350 °C and annealed for 30 min in N_2 gas under a flow rate of 1.0 L min^{-1} as the post-deposition annealing (PDA). In addition, the Cat-CVD SiN_y layer was deposited on the fabricated pyramidal textured Si substrate to demonstrate an excellent optical property at the same deposition condition except for the processing time because it takes a longer time to deposit a same thickness of ~80 nm on the pyramidal textured Si surface due to slopes with the base angle.

6.10.2 Sample evaluation

To evaluate the surface passivation, τ_{eff} and iV_{oc} were analyzed as a function of Δn using a Sinton lifetime tester (Sinton Instruments, WCT-120) for 50×50 mm^2-sized pieces. Moreover, each Q_f was calculated from the *C–V* curves using the following equations [15] with obtained flat-band voltage (V_{FB}). For the calculation of Q_f, the *C–V* curves have large hysteresis, which might be related to the trapped charge in the Al-doped SiO_x layer. Therefore, we determined V_{FB} from the average of V_{FB} values obtained by the forward and reverse scans.

$$Q_f = \frac{C_i}{qA}(\Delta\Phi_{ms} - V_{FB}) \tag{6.12}$$

$$V_{FB} = \frac{(V_{FB,forward} + V_{FB,reverse})}{2} \tag{6.13}$$

$$C_i = \frac{A\,\varepsilon_r\,\varepsilon_0}{d} \tag{6.14}$$

Where C_i is the insulator's capacitance, $\Delta\Phi_{ms}$ is the work function difference between metal and Si, A is the electrode area, and V_{FB} is the flat band voltage. The electrode area, i.e., the contacted mercury (Hg) probe area of 0.0040–0.0043 cm^2, was estimated from the measured C_i, the insulator thickness (d) of 80 nm, ε_r, and ε_0 for each measurement.

6.10.3 Surface passivation of SiN_y/Al-doped SiO_x stacks

Figure 6.27 (a) shows the τ_{eff} of samples treated with $Al(NO_3)_3$ concerning Δn at each treatment time. The results indicate that τ_{eff} increases as treatment time increases, particularly in the low Δn region of around 10^{14} cm^{-3}. This suggests that the Al-doped SiO_x layer contains fixed charges. According to several papers [16–18], electron capture at the Al-induced acceptor states creates tetrahedrally four coordinated Al oxide (AlO_4^-) with negative fixed charges. This AlO_4^- induces the inversion layer by accumulating large holes at the Al-doped SiO_x/Si interface, which leads to good surface passivation. However, in the SiN_y/Al-doped SiO_x stacks configuration, significant degradation of τ_{eff} was observed in the low Δn region with increasing treatment time, as shown in Figure 6.27 (b). In this case, the opposite tendency can be attributed to the charge compensation of the positive fixed charges present in the SiN_y layers on top of the samples by the negative fixed charges in the Al-doped SiO_x layers.

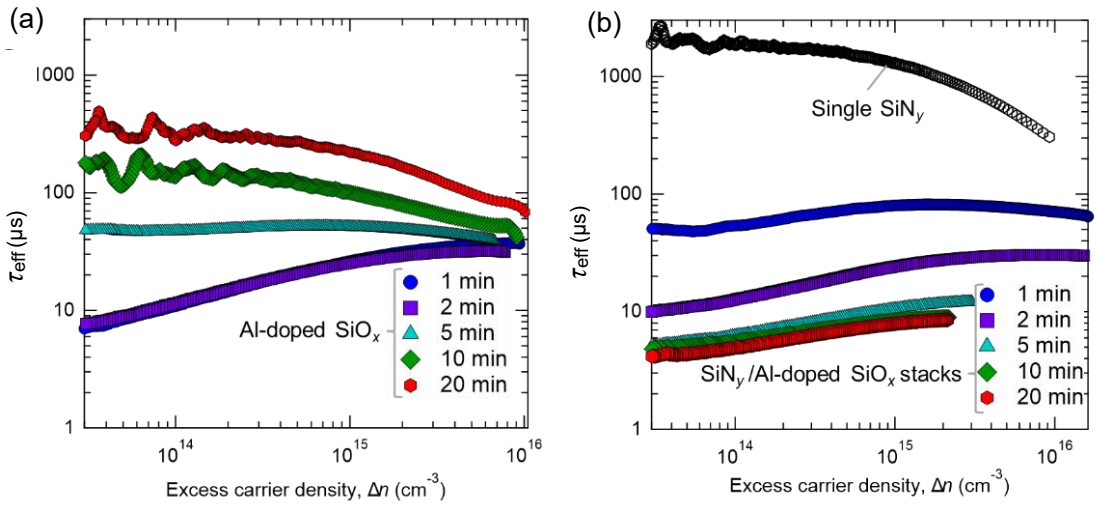

Fig. 6.27 **(a)** τ_{eff} as a function of Δn for the $Al(NO_3)_3$-treated samples at the various treatment time conditions. **(b)** τ_{eff} as a function of Δn for the samples with a single SiN_y layer and SiN_y/Al-doped SiO_x stacks formed at various treatment times.

6.10.4 Fixed charge density of SiN_y/Al-doped SiO_x stacks

Figures 6.28 (a) and (b) depict the *C–V* curves for samples with single SiN_y or SiN_y/Al-doped SiO_x stacks formed at various $Al(NO_3)_3$ treatment times. The curves were acquired by sweeping forward and reverse directions. The Al-doped SiO_x layer significantly impacts the positive charge reduction in the SiN_y layer. This is evident from the *C–V* curves of the stacks, which are shifted considerably to the positive voltage. Figure 6.29 shows the calculated Q_f values as a function of $Al(NO_3)_3$ treatment time. In the calculation, we used Eqs. (6.8) and (6.9), and the contacted Hg electrode areas were estimated to be 0.0040–0.0043 cm^2 from Eq. (6.10). The single SiN_y layer has a high positive Q_f value of about 2×10^{12} cm^{-2}. This value gradually decreases with increasing the $Al(NO_3)_3$ treatment time in the SiN_y/Al-doped SiO_x stacks. Furthermore, negative Q_f values are confirmed for samples treated for more than 5 minutes. This implies that the Al-doped SiO_x layer is highly negatively charged and overcompensates the positive fixed charges in the SiN_y layer. The negative fixed charges can explain the surface passivation improvement and degradation for the single Al-doped SiO_x layer and the SiN_y/Al-doped SiO_x stacks shown in Figure 6.27 (a) and (b). The improvement of τ_{eff} for the single Al-doped SiO_x layer with increasing $Al(NO_3)_3$ treatment time is due to the increase of negative fixed charges in the layer. On the other hand, the degradation of τ_{eff} for the SiN_y/Al-doped SiO_x stacks with increasing $Al(NO_3)_3$ treatment time might be due to the charge compensation. Such a charge-compensated-related degradation has also been reported. In the range of Δn as low as $< 5\times10^{13}$ cm^{-3}, the passivation with a single layer of Al_2O_3 showed a substantial decrease of τ_{eff}, which could be compensated by inserting an HfO_2 layer [19]. Moreover, in the case of Al_2O_3/SiO_2 stacks, the negative Q_f in Al_2O_3 was compensated to 'zero' by ten cycles of ALD-SiO_2 with the same order of magnitude of positive Q_f [19]. Therefore, the increased negative fixed charges overcompensate the positive fixed charges localized in the SiN_y layer, turning to the negative Q_f from the positive Q_f. Thus, these experimental results demonstrate the existence of high negative fixed charges in the Al-doped SiO_x layers. However, the estimated negative values of 10^{10}–10^{11} cm^{-2} are insufficient to obtain the surface passivation effect. SRV is rather increased around the low Q_f values because holes still exist as minority carriers near the n-Si surface, and carrier recombination actively occurs there. Hence, the degradation mechanism can explain the extremely low τ_{eff} of the SiN_y/Al-doped SiO_x stacks with low Q_f values.

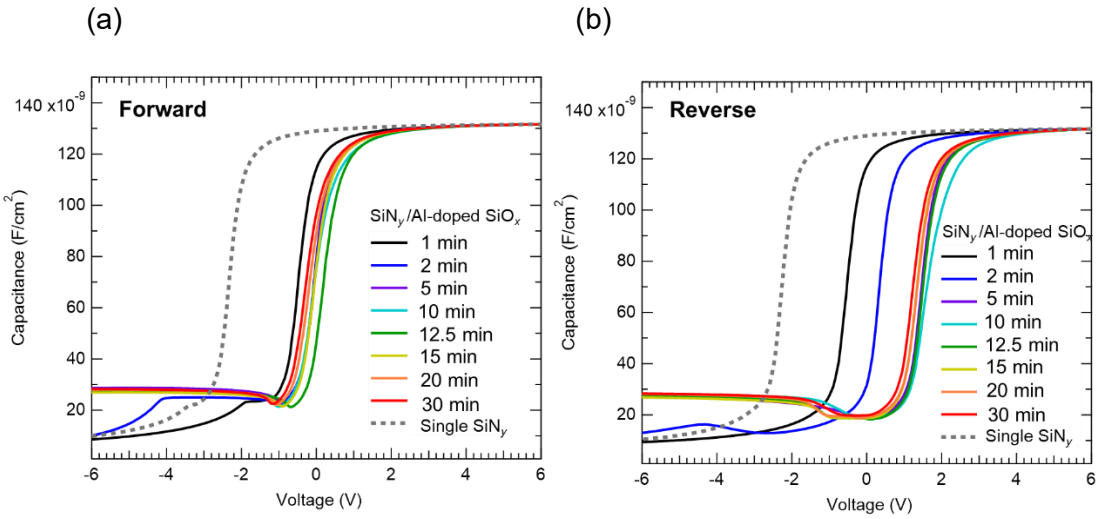

Fig. 6.28 **(a)** Forward- and **(b)** reverse-direction *C–V* curves for the samples with a single SiN_y layer and SiN_y/Al-doped SiO_x stacks prepared by $Al(NO_3)_3$ treatment for various treatment times.

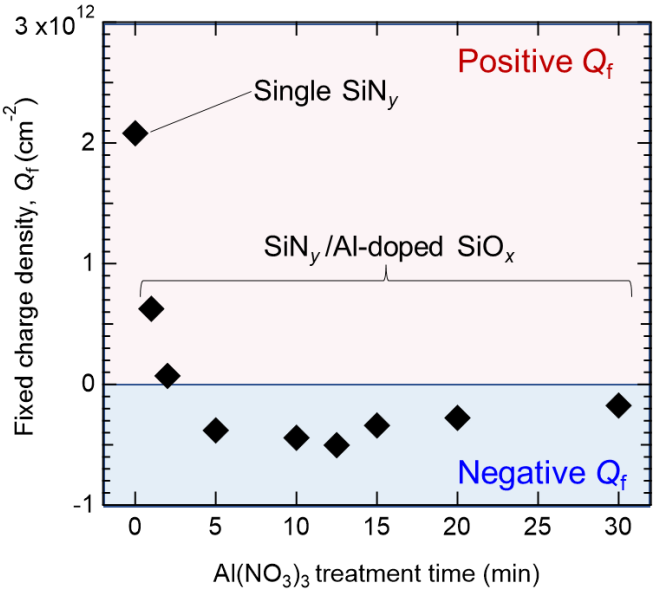

Fig. 6.29 Q_f for the samples with a single SiN_y layer and SiN_y/Al-doped SiO_x stacks prepared by $Al(NO_3)_3$ treatment as a function of treatment time.

In addition, the effect of the non-doped SiO_x interlayer underneath the SiN_y was also investigated. The τ_{eff} of SiN_y/Al-doped SiO_x and SiN_y/non-doped SiO_x as a function of Δn are shown in Figure 6.30. Aside from the significant τ_{eff} degradation for SiN_y/Al-doped SiO_x, a dramatic improvement of τ_{eff} can be seen for SiN_y/non-doped SiO_x. Excellent τ_{eff} of 8.9 ms was confirmed, corresponding iV_{oc} of 730 mV and $S_{eff,\,max}$ of 1.6 cm s^{-1}. Given that the oxides have a similar thickness and SiO_2 (Si^{4+}) content, as shown in Figure 6.31 of fitted Si 2*p* core-level XPS spectra and Table 6.4, charge compensation is likely responsible for the significant degradation of the τ_{eff} in SiN_y/Al-doped SiO_x stacks and damage to the ultrathin layer is not the reason for the degradation. To address this issue, a promising solution would be to deposit an ARC with a negative Q_f, such as aluminum nitride (AlN) [20].

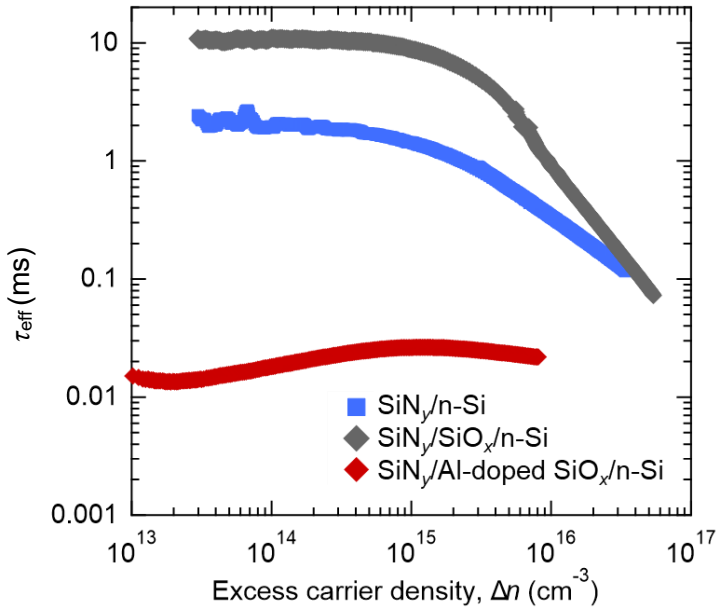

Fig. 6.30 τ_{eff} of SiN_y/n-Si, SiN_y/non-doped SiO_x/n-Si, and SiN_y/Al-doped SiO_x/n-Si as a function of Δn after 350 °C PDA.

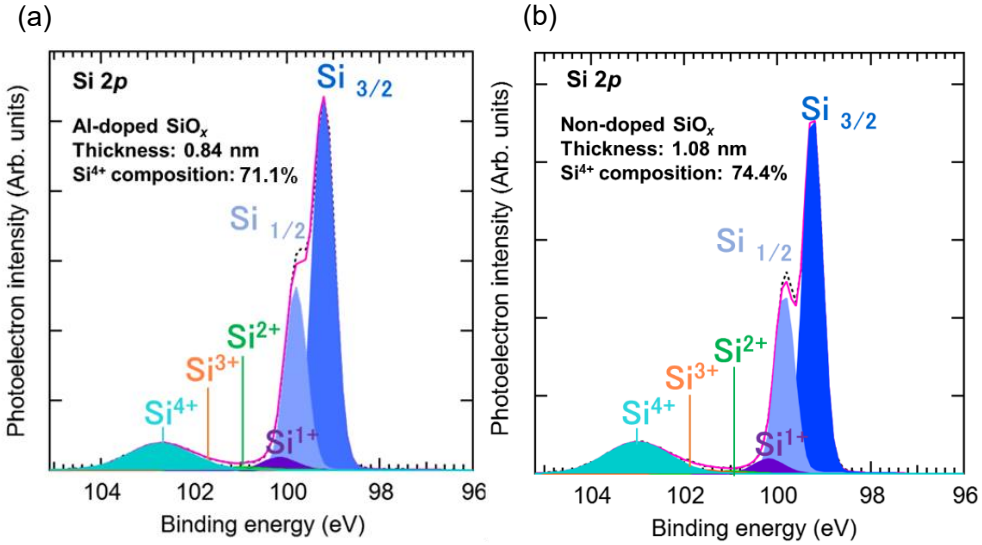

Fig. 6.31 Si 2p core-level XPS spectra for **(a)** a SiN_y/Al-doped SiO_x stack and **(b)** a SiN_y/non-doped SiO_x stack.

Table 6.4 SiO_x thickness and composition of the sub-oxides (Si^{1+}, Si^{2+}, and Si^{3+}) and SiO_2 (Si^{4+}) components.

	Thickness (nm)	Si^{1+} (%)	Si^{2+} (%)	Si^{3+} (%)	Si^{4+} (%)
Al-doped SiO_x	0.84	16.5	8.4	4.0	71.1
Non-doped SiO_x	1.08	15.8	3.4	6.4	74.4

6.10.5 Optical properties of Cat-CVD SiN_y on pyramidal textured Si

Figures 6.32 (a), (b), and 6.33 show reflectance, transmittance, and calculated absorbance spectra of Cat-CVD SiN_y on pyramidal textured Si substrate, varying deposition time from 950 to 1100 s. The estimated J_G values are listed in Table 6.5. The deposition time was optimized at 975 s to obtain the highest J_G value of 43.13 mA cm^{-2}. This value demonstrated a significant increase in the anti-reflective effect on Cat-CVD SiN_y on pyramidal textured Si substrate, which realizes a drastic increase of carrier generation compared to other configurations of the front surface and expected higher surface passivation quality by the Q_f enhancement due to the increment of the generated carrier trapping. However, due to the charge compensation, SiN_y on Al-doped SiO_x degrades the surface passivation quality. To enable excellent surface passivation, non-charged or negative-charged ARC should be deposited.

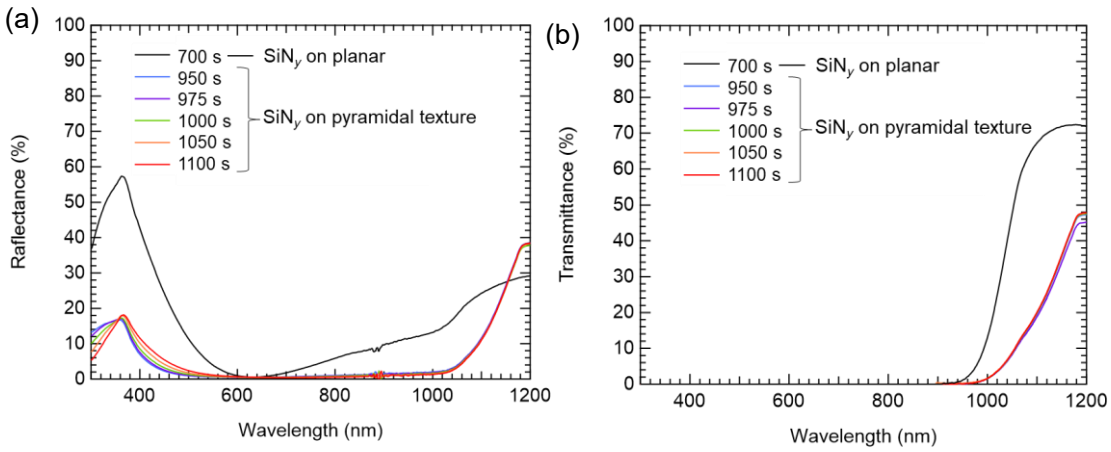

Fig. 6.32 **(a)** Reflectance and **(b)** transmittance spectra of Cat-CVD SiN_y on planar and pyramidal textured Si substrate.

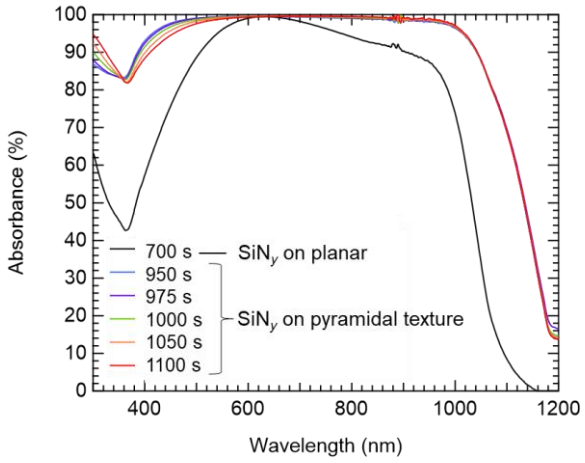

Fig. 6.33 Absorbance spectra of Cat-CVD SiN_y on planar and pyramidal textured Si substrate.

Table 6.5 Photon current density (J_G) for Cat-CVD SiN_y on pyramidal textured Si substrate, varying deposition time from 950 to 1100 s.

	SiN_y deposition time (s)	J_G (mA cm^{-2})
SiN_y on planar Si substrate	700	36.44
SiN_y on pyramidal textured Si substrate	950	43.05
	975	43.13
	1000	43.06
	1050	43.00
	1100	42.94

6.11 Summary

In this chapter, I investigated the effectiveness of antireflective structures and layers on Al-COIL architecture. The findings revealed that the Al-COIL on a pyramidal textured Si substrate showed a higher surface passivation quality and photon current density, leading to improved solar cell performance. The elevated surface passivation quality could be attributed to the improved light-trapping effect. 1.54 times higher J_G value implies that Q_f might be enlarged by the electron trapping in Al-induced acceptor states due to the increased carrier generation, causing an improvement of surface passivation quality. Cat-CVD SiN_y/ultrathin non-doped SiO_x showed an excellent surface passivation quality with a τ_{eff} of 8.9 ms corresponding to an iV_{oc} of 730 mV and optical properties with photon current density of >43 mA cm^{-2}. Hence, Cat-CVD is a suitable ARC deposition method for an ultrathin layer, as demonstrated experimentally. However, the deposition of SiN_y degraded the surface passivation of Al-COIL due to charge compensation. Therefore, different ARCs without positive charges will be considered a promising solution. For implementing device structure, the deposited ARC layer must be locally opened to make the contact like a PERC structure. Hence, to remain Al-doped SiO_x at the locally opened area, it is needed to apply some complicated process such as laser ablation or masking and etching process followed by further $Al(NO_3)_3$ treatment for the opened area. In order to pursue the low-cost production, It should be realized by an alternative simple process in the future work.

References

[1] K. R. McIntosh and S. C. Baker-Finch, "OPAL 2: Rapid optical simulation of silicon solar cells," In: Proceedings of the 38th IEEE Photovoltaic Specialists Conference, Austin, pp. 000265–000271 (2012).

[2] M. A. Green, "Lambertian light trapping in textured solar cells and light-emitting diodes: analytical solutions," Prog. Photovolt. **10**, 235 (2002).

[3] K. R. McIntosh, and L. E. Black, "On effective surface recombination parameters," J. Appl. Phys. **116**, 014503 (2014).

[4] C. T. Nguyen, K. Koyama, K. Higashimine, S. Terashima, C. Okamoto, S. Sugiyama, K. Ohdaira, and H. Matsumura, "Novel chemical cleaning of textured crystalline silicon for realizing surface recombination velocity <0.2 cm/s using passivation catalytic CVD SiN_x/amorphous silicon stacked layers," Jpn. J. Appl. Phys. **56**, 056502 (2017).

[5] G. von Gastrow, R. Alcubilla, P. Ortega, M. Yli-Koski, S. Conesa-Boj, A. F i Morral, H. Savin, "Analysis of the Atomic Layer Deposited Al_2O_3 field-effect passivation in black silicon," Sol. Ener. Mater. Sol. Cells **142**, 29 (2015).

[6] H. Savin, P. Repo, G. von Gastrow, P. Ortega, E. Calle, M. Garín, and R. Alcubilla, "Black silicon solar cells with interdigitated back-contacts achieve 22.1% efficiency," Nat. Nanotechnol. **10**, 624 (2015).

[7] S. Wang, X. Wu, F.-J. Ma, Y. Zhang, G. Scardera, D. Payne, M. Abbott, and B. Hoex, "Understanding field-effect passivation of black silicon: Modeling charge carrier population control in compressed space charge regions," In: Proceedings of IEEE 47th Photovoltaic Specialists Conference, Online, pp. 590–594 (2020).

[8] S. Wang, X. Wu, F.-J. Ma, D. Payne, M. Abbott, and B. Hoex, "Field-effect passivation of undiffused black silicon surfaces," IEEE J. Photovolt. **11**, 897 (2021).

[9] J. J. Kopanski, M. Y. Afridi, S. Jeliazkov, W. Jiang, and T. R. Walker, "Scanning kelvin force microscopy for characterizing nanostructures in atmosphere," AIP Conf. Proc. **931**, 530 (2007).

[10] P. A. Basore, "3D numerical solutions inside the pyramid of textured silicon solar cells," AIP Conf. Proc. **2487**, 040001 (2022).

[11] J. Hölzl and F. K. Schulte, "Work Functions of Metals" in Solid Surface Physics, Springer-Verlag, Berlin (1979).

[12] A. Goetzberger, J. Knobloch, and B. Voß, Crystalline Silicon Solar Cells (John Wiley & Sons, 1998).

[13] B. Mojrová, H. Chu, C. Peter, P. Preis, J. Lossen, V. D. Mihailetchi, and R. Kopecek, "A comparison study of boron emitter passivation by silicon oxide and a PECVD silicon nitride stack," Energy Procedia **124**, 288 (2017).

[14] H. T. C. Tu, K. Koyama, C. T. Nguyen, K. Ohdaira, and H. Matsumura, "High-quality surface passivation of crystalline silicon with chemical resistance and optical transparency by using catalytic chemical vapor deposition SiN_x layers and an ultrathin SiO_x film," Jpn. J. Appl. Phys. **57** 08RB17 (2018).

[15] S. M. Sze, and Kwok K. Ng, Physics of Semiconductor Devices, 3rd edition (John Wiley & Sons, 2007).

[16] D. Hiller, J. Göttlicher, R. Steininger, T. Huthwelker, J. Julin, F. Munnik, M. Wahl, W. Bock, B. Schoenaers, A. Stesmans, and D. König, "Structural properties of Al−O monolayers in SiO_2 on silicon and the maximization of their negative fixed charge density", ACS Appl. Mater. Interfaces **10**, 30495 (2018).

[17] D. Hiller, P. M. Jordan, K Ding, M. Pomaska, T. Mikolajick, and D. König, "Deactivation of silicon surface states by Al-induced acceptor states from Al–O monolayers in SiO_2," J. Appl. Phys. **125**, 015301 (2019).

[18] B. Hoex, M. Bosman, N. Nandakumar, and W.M.M. Kessels, "C-Si surface passivation by aluminum oxide studied with electron energy loss spectroscopy," In: Proceedings of IEEE 39th Photovoltaic Specialists Conference, Tampa, Florida, pp. 3333–3336 (2013).

[19] D. K. Simon, Paul M. Jordan, I. Dirnstorfer, F. Benner, C. Richter, and T. Mikolajick, "Symmetrical Al2O3-based passivation layers for p- and n-type silicon," Sol Ener. Mater. Sol. Cells **131**, 72 (2014).

[20] G. Krugel, A. Sharma, W. Wolke, J. Rentsch, and R. Preu, "Study of hydrogenated AlN as an anti-reflective coating and for the effective surface passivation of silicon," Phys. Status Solidi RRL **7**, 457 (2013).

CHAPTER 7

CONCLUSION

In this study, novel hole-selective passivating contact was developed using a simple wet chemical process. The study demonstrated that $Al(NO_3)_3$ treatment can form an ultrathin Al-doped SiO_x layer on Si substrates, which has an excellent surface passivation quality with hole-selectivity. On a planar n-Si surface, the $S_{eff,\,max}$ reached as low as 16 cm s^{-1}, corresponding to iV_{oc} of 670 mV and J_0 of 65 fA cm^{-2}. The hole selectivity (S_{10}) value could be estimated to be 13.3 using the J_0 and the analyzed ρ_c of 20 mΩ cm^2, which is competitive to other selective contacts. XPS revealed that the ultrathin Al-doped SiO_x layer consists of a bilayer of AlO_y/SiO_x on Si substrates with an Al surface atomic concentration of ~1 at.% and a SiO_x thickness of ~1 nm. *C–V* measurement revealed that intensely upward band bending at the ultrathin Al-doped SiO_x is formed on the n-Si surface.

The simplified SRH formalism and the analyzed V_{bi} estimated a Q_f value of -3.21×10^{12} cm^{-2} and a N_{it} value of 1.43×10^{12} cm^{-2}. The estimated values indicate that the surface passivation mechanism originated from field-effect and chemical passivation. In particular, the primary origin of the surface passivation is attributed to the field effect passivation induced by a highly negatively charged oxide, which provides strong upward band bending of the Si surface with an excellent hole-selective contact property. The photoconductance measurement implies that the surface passivation quality is enhanced by light illumination. The excited electron might be trapped in the Al-induced acceptor states existing in the Al-doped SiO_x layer, forming negatively charged AlO_4^- structures and enhancing field effect passivation induced by the fixed charges. The light-induced surface passivation effectively occurred at the surface of pyramidal textured Si

substrates. Even though the larger surface area leads to higher N_{it} on the pyramidal textured Si surface, the surface passivation quality was higher than that of mirror-polished Si surfaces. The $S_{eff,\ max}$ reached as low as 13.3 cm s^{-1}, corresponding to iV_{oc} of 682 mV and J_0 of 59 fA cm^{-2}. By enhancing the excited electron trapping due to the light absorbance increase in the pyramidal textured Si and the slight increase of the space charge compression in the structure, the lower S_{eff} is realized. The ARC layer on the ultrathin Al-doped SiO_x is also considered an initiator of surface passivation, but the fixed charge in the ARC layer highly affects the surface passivation quality. The uncharged or negatively charged ARC layer should be deposited on the ultrathin Al-doped SiO_x.

The light illumination also affects the R_{sheet}. Significant R_{sheet} reduction of two order magnitude was confirmed for Si(111) surface as low as 317 Ω sq^{-1} under the 1 sun illumination. The enhanced negative charges due to the enlargement of the electron trapping induce more surface hole density, leading to the lower R_{sheet}. Hence, the light illumination activates the hole-selective passivating contact property on the ultrathin Al-doped SiO_x.

In addition, the solar cell performance demonstrated the device operation of Al-COIL solar cells. The demonstration revealed that the induced inversion layer acts as a p^+ layer on the n-type Si substrates. However, the low performance in the η of 3.35%, especially in low J_{sc} and V_{oc} values, originated from the high surface recombination with the reduction of the Q_f value as simulated. Since the fine grid electrodes are applied on the emitter surface, and FF is improved, the low FF originated from a still high sheet resistance. Furthermore, the pyramidal textured Si surface improved all parameters of solar cell performance. The light-trapping enhances light absorbance, resulting in a higher solar cell performance. However, the still low V_{oc} might be due to surface recombination caused by the reduction of Q_f under the front side electrode. The light-illumination effect cannot appear due to the shadow of the electrode and the low work function material of Ag compared to the Si valence band edge.

To overcome this problem, applying a buffer layer or an Al-diffused layer will be a promising solution under the finger Ag electrode with a fine structure. In addition, to enhance the space charge region compression effect, nano-sized texture surface such as black Si should be tested as a surface structure underneath an ultrathin Al-doped SiO_x layer, which possibly decreases the s R_{sheet} of emitter surface, leading to the reduction of the front Ag area. Also, the novel solar cell that fully exploits both n and p doping via electrostatic charges in an inversion layer solar cell will be tested in the near future.

APPENDIX

Appendix 1: Simulation parameters for PC1D

The simulation parameters for the PC1D are shown in Figure A-1.1. The parameters were set to obtain the depth profile of carrier densities **(Fig. 4.24)** and the depth profile of energy bands **(Fig. 4.25)** for the negatively charged n-type Si surface.

DEVICE
Device area: 1 cm^2
No surface texturing
Front surface charge: -3.21×10^{12} cm^{-2}
Rear surface neutral
No Exterior Front Reflectance
No Exterior Rear Reflectance
No internal optical reflectance
All contacts disabled
No internal shunt elements
REGION 1
Thickness: 200 µm
Material from program defaults
Carrier mobilities from internal model
Dielectric constant: 11.9
Band gap: 1.124 eV
Intrinsic conc. at 300 K: 1×10^{10} cm^{-3}
Refractive index: 3.58
Absorption coeff. from internal model
Free carrier absorption enabled
N-type background doping: 2×10^{15} cm^{-3}
No front diffusion
No rear diffusion
Bulk recombination: $\tau_n = \tau_p = 10000$ µs
No Front-surface recombination
No Rear-surface recombination
EXCITATION
Excitation mode: Equilibrium
Temperature: 300 K
Base circuit: Zero
Collector circuit: Zero
Light sources disabled

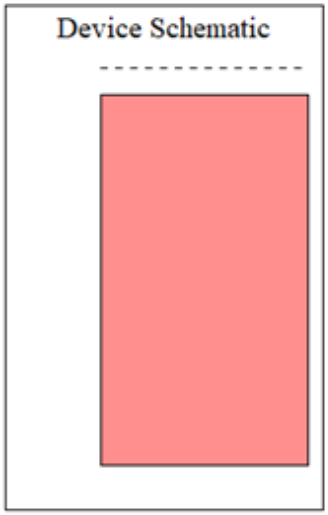

Fig. A-1.1 Simulation parameters for the PC1D to obtain the depth profile of carrier densities and the depth profile of energy bands for the negatively charged n-type Si surface.

The simulation parameters for the PC1D are shown in Figure A-1.2. The parameters were set to obtain the photo *J–V* characteristics for the devices with surface charge-induced emitters assuming various Q_f values in the range of -8.8×10^{10} – -1.0×10^{13} cm^{-2}, enormous front-SRV of 1×10^{10} cm s^{-1} **(Fig. 5.15)** and without front-surface recombination **(Fig. 5.16)**.

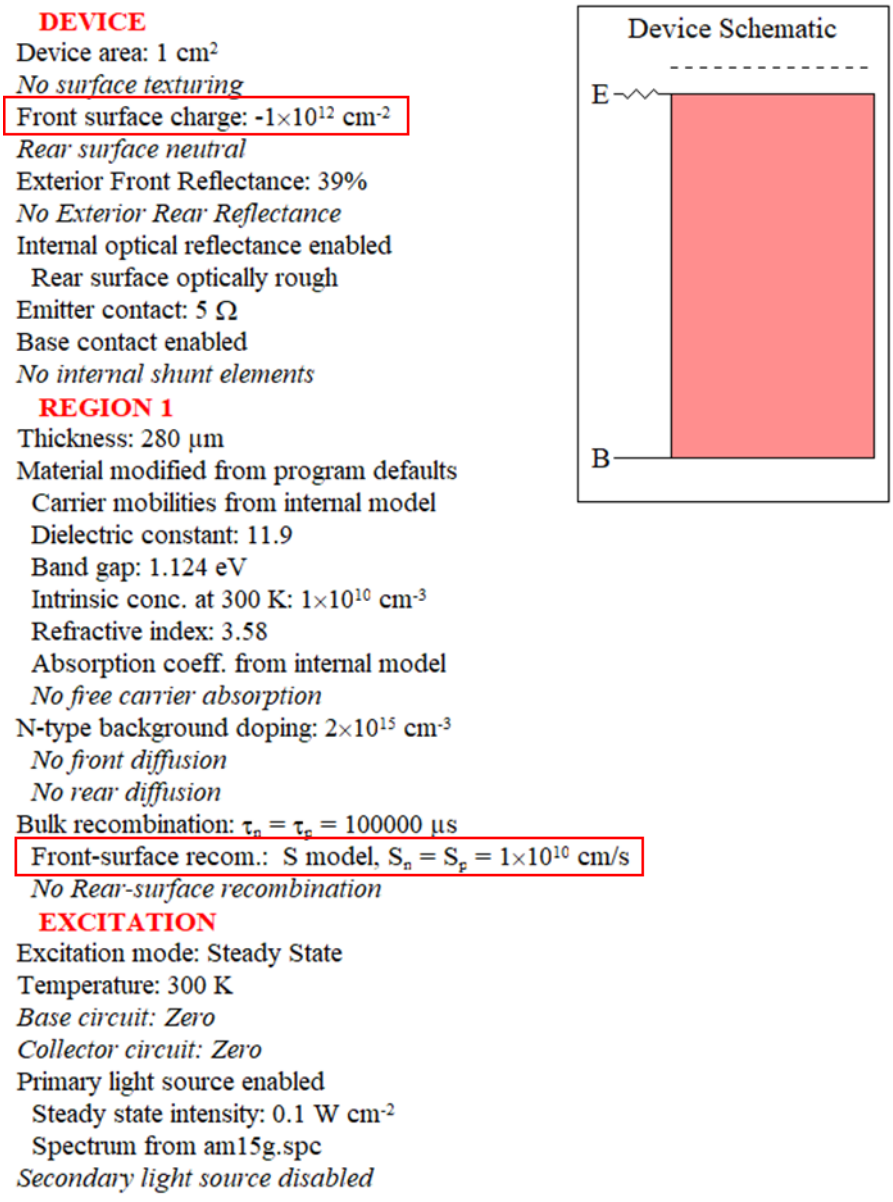

Fig. A-1.2 Simulation parameter for the PC1D to obtain the photo *J–V* characteristics for the devices with surface charge-induced emitters.

The simulation parameters for the PC1D are shown in Figure A-1.3. The parameters were set to obtain the depth profile of carrier densities of face-to-face structure with variable distances of 10 nm to 1 μm between both sides with highly negative Q_f of 1×10^{13} cm^{-2} **(Fig. 6.5)**. These results provided information about the enhancement of carrier densities by a space charge region compression.

DEVICE
Device area: 1 cm^2
No surface texturing
Front surface charge: -1×10^{13} cm^{-2}
Rear surface charge: -1×10^{13} cm^{-2}
No Exterior Front Reflectance
No Exterior Rear Reflectance
No internal optical reflectance
All contacts disabled
No internal shunt elements
REGION 1
Thickness: 0.01 μm
Material modified from program defaults
Carrier mobilities from internal model
Dielectric constant: 11.9
Band gap: 1.124 eV
Intrinsic conc. at 300 K: 1×10^{10} cm^{-3}
Refractive index: 3.58
Absorption coeff. from internal model
Free carrier absorption enabled
N-type background doping: 2×10^{15} cm^{-3}
No front diffusion
No rear diffusion
Bulk recombination: $\tau_n = \tau_p = 10000$ μs
No Front-surface recombination
No Rear-surface recombination
EXCITATION
Excitation mode: Steady State
Temperature: 300 K
Base circuit: Zero
Collector circuit: Zero
Primary light source enabled
Steady state intensity: 0.1 W cm^{-2}
Spectrum from am15g.spc
Secondary light source enabled
Steady state intensity: 0.1 W cm^{-2}
Spectrum from am15g.spc

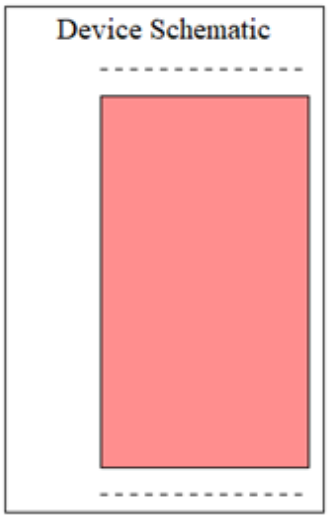

Fig. A-1.3 Simulation parameters to obtain depth profile of carrier densities of face-to-face structure.

Appendix 2: Simulation parameters for PC3S

The simulation parameters for the PC3S are shown in Figure A-2.1. The parameters were set to obtain a 2D mapping of surface hole density on **(a)** pyramidal textured and **(b)** planar Si surface with a negative Q_f of 1.0×10^{11} cm^{-3} (**Fig. 6.21**), 3.2×10^{12} cm^{-2}, and 3.0×10^{13}cm^{-3} (**Fig. 6.22**). The "SURFACE CHARGE" was variable, and "TEXTURE" was selected to "Pyramids" or "Planar." These results provided information about enhancing carrier densities by a space charge region compression in tiny structures on pyramidal textured Si surfaces.

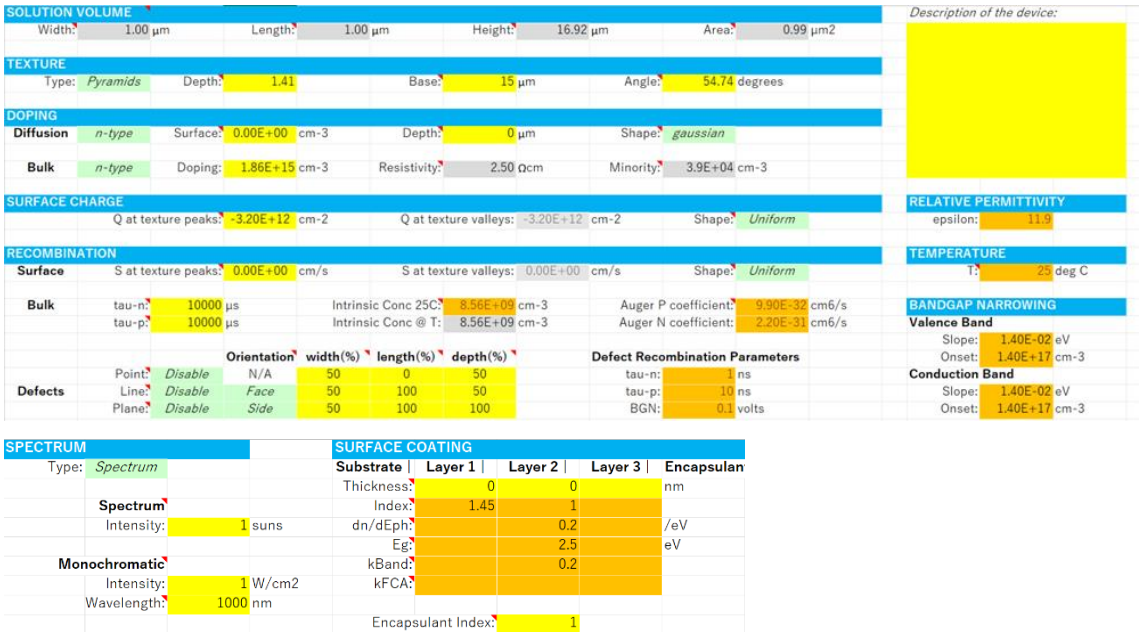

Fig. A-2.1 Simulation parameters to obtain a 2D mapping of surface hole density on pyramidal textured Si with negative surface charges of 3.2×10^{12} cm^{-2}.

Appendix 3: Simulation parameters for OPAL 2

The simulation parameter for the OPAL 2 to obtain generation rate (**Fig. 6.2)** and reflectance **(Fig. 6.3)**. The "**Surface morphology**" was varied, Planar, upright random pyramids with a normal angle of 54.74° or upright regular texture with a steeper angle of 80° were applied. The PECVD SiN_x (n=1.99) [1] was used from the data library as an ARC, and the thickness was optimized for each surface morphology. One of the input parameters is shown in Figure A-3.1.

Fig. A-3.1 Simulation parameters to obtain generation rate and reflectance for the surface morphology of upright random pyramids with a normal angle of 54.74° applied an optimized PECVD SiN_x (n=1.99).

Appendix 4: Photon flux spectrum of solar radiation

AM 1.5 G spectrum was used to calculate photon current density (J_G) in each Si substrate with each surface structure, such as planar and pyramidal texture. The used photon flux as a function of wavelength [2] is shown in Figure A-4.1. The AM 1.5 G spectrum is a standard solar spectrum designed for terrestrial flat plate modules and has an integrated power of 0.1 W cm^{-2}.

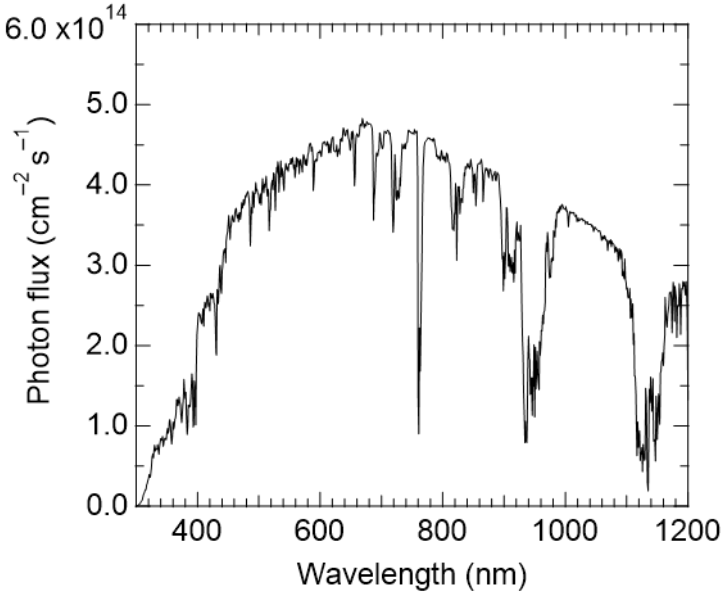

Fig. A-4.1 Photon flux as a function of wavelength.

Appendix 5: Absorption coefficient of c-Si and penetration length in c-Si

The absorption coefficient (α) of c-Si [3] and penetration length in c-Si are shown in Figure A-5.1 (a) and (b), respectively. The penetration length is defined as the decay length to be 1/e intensity. Hence, from Eq. (3.32), the penetration length can be described as $1/\alpha$. For the light with a wavelength of 350 nm, the penetration length would be ~0.0096 μm. On the other hand, for the light with a wavelength of 900 nm, the penetration length would be ~32.67 μm. Hence, Short-wavelength light can absorb the surface of the c-Si substrate, but long-wavelength light can absorb in bulk. Therefore, homogeneous generation requires a long wavelength of light illumination. For the effective lifetime measurement, the light should be manipulated by cutting short-wavelength or monochromatic laser light with a long wavelength. However, short-wavelength light should be used to achieve high generation at the surface region. In this study, laser light with a wavelength of 349 nm was also used to activate the surface passivation.

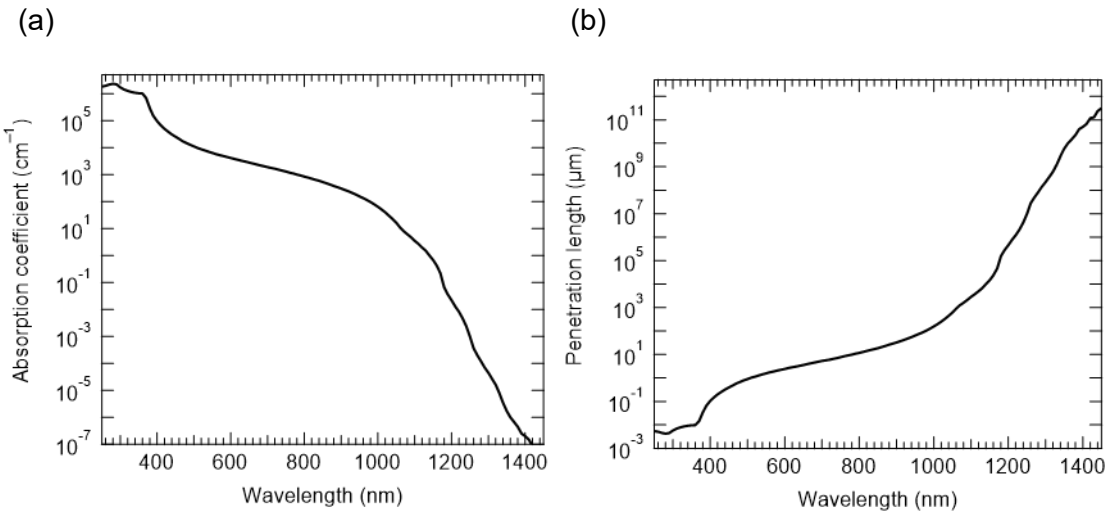

Fig. A-5.1 **(a)** Absorption coefficient (α) of c-Si and **(b)** penetration length in c-Si.

Appendix 6: Inelastic mean free path (IMFP)

In the material, the inelastic collision of electrons occurs, and their energy will be lost. The inelastic mean free path (IMFP) is the distance that decays 1/e signal intensity by inelastic scattering. IMFP can be calculated using the TPP-2M equation [4] described below.

$$\lambda = \frac{E}{E_p^2\{\beta \ln(\gamma E) - C/E + D/E^2} \tag{A-6.1}$$

$$E_p = 28.8\sqrt{N_v \rho / M} \tag{A-6.2}$$

$$\beta = -1.0 + 9.44\left(E_p^2 + E_g^2\right)^{-0.5} + 0.69\,\rho^{0.1} \tag{A-6.3}$$

$$\gamma = 0.191\,\rho^{-0.50} \tag{A-6.4}$$

$$C = 19.7 - 9.1\,U \tag{A-6.5}$$

$$D = 534 - 208\,U \tag{A-6.6}$$

$$U = \frac{N_v \rho}{M} = \frac{E_p^2}{829.4} \tag{A-6.7}$$

Where β, γ, C, and D are the parameters, E is the electron energy, Eg is the band gap energy, Nv is the number of valence electrons, ρ is the density, and M is the atomic weight. IMFP can be calculated to be 3.07 nm for the Si using Eqs. (A-6.1) – (A-6.7) and below parameters. Hence, the escape depth of photoelectrons can be estimated to be 8.35 nm.

Table A-6.1 Parameters of the Si for IMFP calculation

Parameters	Units	Values
E	eV	1387.5
E_g	eV	1.12
N_v	-	4
ρ	g cm^{-3}	2.33
M	-	28.08

Appendix 7: τ_{eff} measurement using low excitation laser light photon density

Figure A-7 shows τ_{eff} measured using μ-PCD (PV-2000A, Semilab Co. Ltd.) with a low areal laser photon density from 1.0×10^{11} to 1.5×10^{13} cm^{-2} and a wavelength of 904 nm. The τ_{eff} was gradually decreased with increasing the areal photon density in the range of relatively low injection levels between 1.0×10^{11} and 1.0×10^{12} cm^{-2}. Since such significant improvement does not appear without Si band bending, the high τ_{eff} at the lower injection level is attributable to field-effect passivation due to the band bending of the Si surface. The generation of the minority carrier concentration and the carrier recombination is significantly reduced by using an excitation laser of lower areal photon density. Hence, this τ_{eff} dependence on carrier excitation density implies that the surface passivation mechanism is ascribed to the field-effect passivation. However, the direction of the band bending cannot be determined by considering only this result. To elucidate the polarity of the fixed charge density in the ultrathin Al-doped SiO_x layer, *C–V* measurements were conducted, as investigated in 6.10.4. However, τ_{eff} increased with the injection level from 1.0×10^{12} to 1.5×10^{13} cm^{-2}. As shown in Figure 4.34(a) and described in 4.7.4, this increase might be attributable to the enhancement of the negative Q_f induced by electron trapping in the Al-induced acceptor states due to the instantly increased Δn by the illumination of the pulsed laser light, increasing the upward band bending and enhancement of field-effect passivation. The μ-PCD measurements were performed at the Fukushima Renewable Energy Institute, AIST.

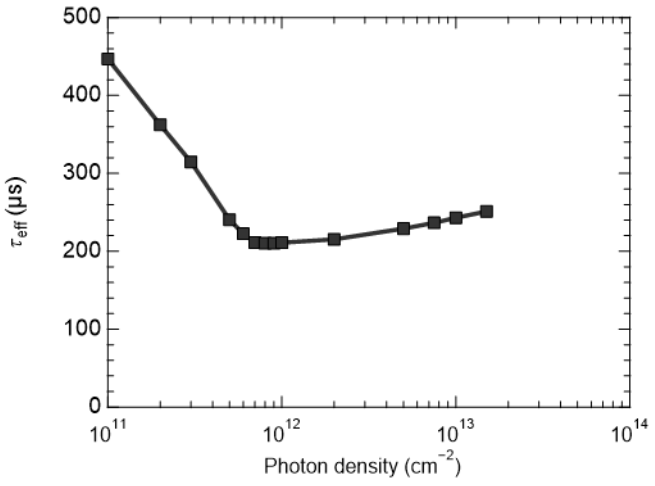

Fig. A-7. τ_{eff} measured using μ-PCD with a low areal laser photon density from 1.0×10^{11} to 1.5×10^{13} cm^{-2} and a wavelength of 904 nm.

Appendix 8: Surface passivation by different aluminum precursor

To reveal the effectiveness of $Al(NO_3)_3$ aqueous solution to form ultrathin Al-doped SiO_x layers on c-Si substrates, the different aluminum precursor was tested to determine whether they could realize the excellent surface passivation of the c-Si surface. In this study, aluminum sulfide ($Al_2(SO_4)_3$) was used for the Al doping and oxidant. The aluminum sulfide hydroxide ($Al_2(SO_4)_316H_2O$) was dissolved in DIW to make 0.5 M $Al_2(SO_4)_3$ aqueous solution, and the boiled $Al_2(SO_4)_3$ aqueous solution was used. HF-treated n-Si substrates were immersed in the boiled $Al_2(SO_4)_3$ aqueous solution for 3 to 30 min. After the DIW rinse followed by N_2 blow dry, τ_{eff} measurements were performed for each sample. Figure A-8 shows the τ_{eff} of $Al_2(SO_4)_3$-treated samples for each process time, as well as the τ_{eff} of $Al(NO_3)_3$-treated samples. As shown in Figure A-8, apart from $Al(NO_3)_3$-treated samples, the τ_{eff} of $Al_2(SO_4)_3$-treated samples remained low, around 13 to 18 μs in the entire range of the processing time. As an observation of the hydrophobicity on the Al-treated c-Si surface, hydrophobic surfaces were still observed for all of the samples. This implies that sufficient oxidation did not occur for the $Al_2(SO_4)_3$-treated samples, leading to low surface passivation.

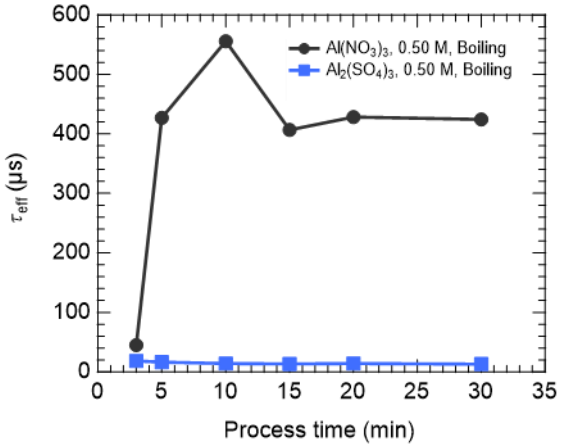

Fig. A-8. τ_{eff} of $Al_2(SO_4)_3$- and $Al(NO_3)_3$-treated samples for each process time.

Appendix 9: Stability and recovery of surface passivation quality

The stability of the ultrathin Al-doped SiO_x layer on n-Si(100) was investigated. Figure A-9-1 shows the time-related τ_{eff} transition through 30 days of the samples after $Al(NO_3)_3$ treatment with a boiling temperature and concentration of 0.25 M for 5–30 min. 5 min treated sample was stabilized at a low τ_{eff}. However, the samples with relatively high initial τ_{eff} showed gradual degradation with passing the elapsed time after the surface passivation. A peculiar increase feature was confirmed on a 10 min-treated sample. However, this sample also showed a gradual degradation after 3 days later. The lack of initial surface passivation quality was compensated with further oxidation in the ambient air, resulting in higher surface passivation. Another crucial finding was the τ_{eff} recovery by the light illumination. Figure A-9-2 (a) shows τ_{eff} mapping after the time-related degradation, and (b) shows τ_{eff} mapping after the 1 sun illumination for 5 min on the degraded sample. 1 sun illumination not fully but recovered at a certain level of surface passivation quality with a τ_{eff} of 393 μs, as shown in Table A-9. This result implies that the surface passivation induced by the ultrathin Al-doped SiO_x layer can retain the surface passivation quality even in the ambient air but under light illumination (carrier excitation). The possible reason for the τ_{eff} recovery is Q_f recovery. The slight reduction from the initial τ_{eff} might be attributable to the further interfacial SiO_x growth, leading to the mitigation of electron traps in the Al-induced acceptor states owing to the less tunneling probability through the thickened SiO_x layer during the storing in the air ambient.

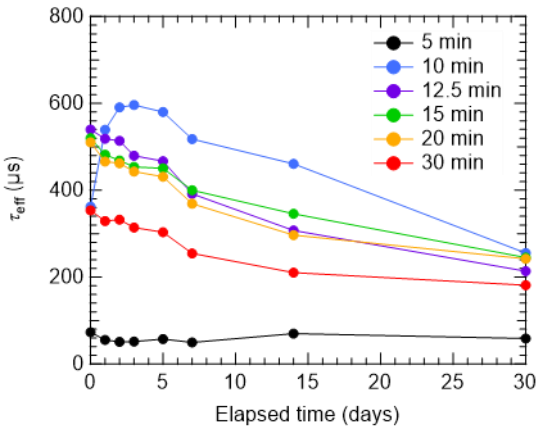

Fig. A-9-1. Time-related τ_{eff} transition through 30 days of the samples after $Al(NO_3)_3$ treatment with a boiling temperature and concentration of 0.25 M for 5–30 min.

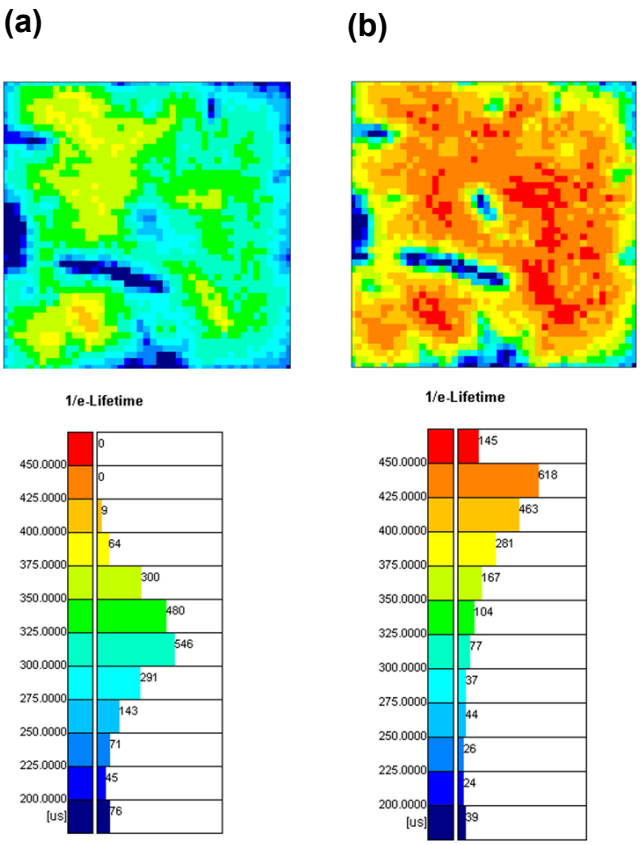

Fig. A-9-2. (a) τ_{eff} mapping after the time-related degradation, (b) τ_{eff} mapping after the 1 sun illumination for 5 min on the degraded sample.

Table A-9 Mean and maximum τ_{eff} of after the degradation and after the 1 sun illumination

Substrate	Mean τ_{eff}	Maximum τ_{eff}
After degradation	311	416
After 1 sun illumination	393	491

Appendix 10: Surface passivation quality on p-type c-Si

Surface passivation quality on p-type c-Si (p-Si) was also investigated as performed on n-Si in this study. The same process has proceeded as described in 4.3.1. The ultrathin Al-doped SiO_x layers were formed on the RCA-cleaned and HF-treated p-Si(100) substrates by immersing in the boiled $Al(NO_3)_3$ aqueous solution with a molar concentration of 0.25 M for several processing time conditions in the range of 5–30 min. Figure A-10 shows the τ_{eff} of the $Al(NO_3)_3$-treated samples on p-Si(100) as a function of the $Al(NO_3)_3$ processing time. Up to 15 min, τ_{eff} improved with increasing the processing time. However, after 15 min, τ_{eff} gradually decreased with increasing the processing time. The optimized time condition of 15 min realized 406 μs as a mean τ_{eff}. The tendency of the increment and decrease with respect to the processing time can be explained as described in 4.4.3. Considering the induction of negative Q_f originated from AlO_4 structures formed by trapping the excited electrons in Al-induced acceptor states, more adjacent to stoichiometric SiO_2 stabilizes to create this AlO_4 structure with increasing the processing time. However, further oxidation makes further oxide growth at the interface, which suppresses the electron tunneling through the oxide and trapping in the Al-induced acceptor states. Hence, further oxide growth inhibits the negative Q_f induction, causing the τ_{eff} degradation.

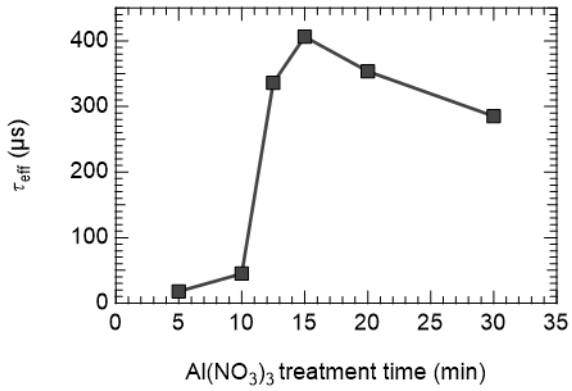

Fig. A-10. τ_{eff} of the $Al(NO_3)_3$-treated samples on p-Si(100) as a function of the $Al(NO_3)_3$ processing time.

Appendix 11: Frequency dependence of *C–V* measurements

The *C–V* characteristics of the ultrathin Al-doped SiO_x/n-Si interface were investigated. To mitigate a leakage current, ~80 nm-thick SiN_y layers were deposited as capping layers on the Al-doped SiO_x layer. The sample fabrication process and evaluation method are shown in 6.10.1 and 6.10.2, respectively. During the *C–V* measurements, the frequency was varied in the range of 100 Hz to 1 MHz. Figure A-11 (a) shows *C–V* curves measured with the frequency of 100 Hz to 1 MHz for 1 min $Al(NO_3)_3$-treated samples and Figure A-11 (b) for 12.5 min $Al(NO_3)_3$-treated samples. As shown in Figure A-11 (a), inversion capacitances were not observed for a 1 min $Al(NO_3)_3$-treated sample. On the other hand, inversion capacitances were observed for a 12.5 min $Al(NO_3)_3$-treated sample, as shown in Figure A-11 (b). Furthermore, the inversion capacitances were significantly increased with decreasing measurement frequency. Considering negative Q_f induction in a 12.5 min-treated sample but still positive Q_f induction in a 1 min-treated sample, these results suggest that negative Q_f induces an inversion layer at the surface of the n-Si substrate. The inversion capacitances can be observed by electron trapping at the inversion condition by applying a negative bias to the top electrodes. The lower frequency measurements increase inversion capacitance owing to the increment of the interface trap response. Hence, a sufficient $Al(NO_3)_3$-treated sample creates an inversion layer induced by highly negatively charged Al-doped SiO_x with electron-trapped Al-induced acceptor states.

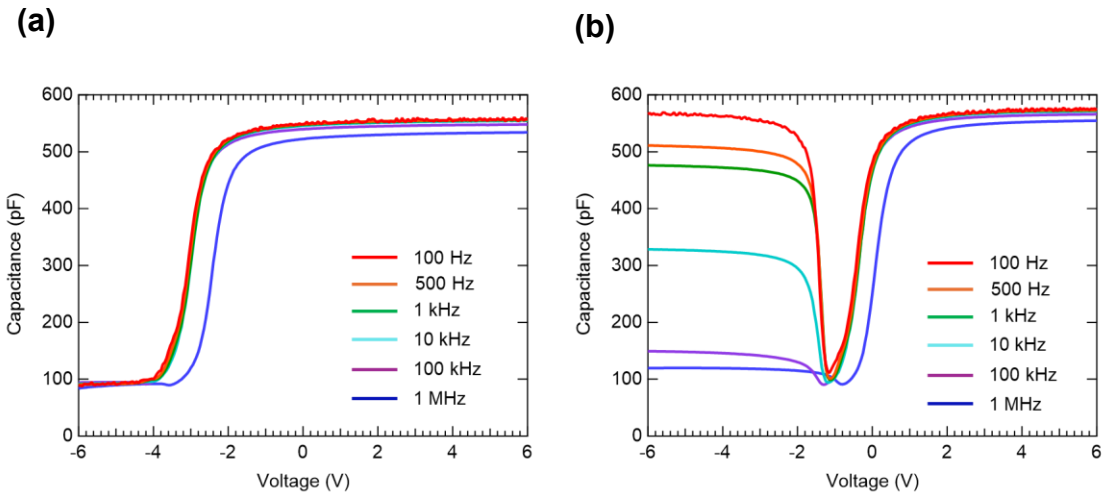

Fig. A-11. *C–V* curves **(a)** for 1 min $Al(NO_3)_3$-treated sample and **(b)** for 12.5 min $Al(NO_3)_3$-treated sample measured with the frequency of 100 Hz to 1 MHz.

Appendix 12: τ_{eff} degradation by residual water

The $Al(NO_3)_3$ treatment increases τ_{eff} to ~550 μs at one of the best conditions (0.25 M, Boiling temperature, 12.5 min) acquired by μ-PCD. However, sometimes, such a high τ_{eff} could not be obtained just after the surface passivation. Figure A-12-1 shows τ_{eff} mapping just after the Al-doped SiO_x formation. As shown in Figure A-12-1, the τ_{eff} was one order lower than successfully well-passivated the Si surface at the same condition of $Al(NO_3)_3$ treatment. The data was acquired just after the DIW rinse, followed by the N_2 blow. The N_2 dry process might not completely remove the water molecules from the sample surface. To investigate the reason for the low τ_{eff}, the confirmed well-passivated sample was immersed in the DIW in a transparent plastic bag and measured τ_{eff} using μ-PCD. Figure A-12-2 shows the τ_{eff} (a) after N_2 dried and (b) during immersing in DIW. These results suggest that water significantly affects the τ_{eff} degradation: ~300 μs was decreased to ~10 μs. The experimental fact implies that one of the reasons for the τ_{eff} degradation is residual water on the surface passivation layer. Considering that the oxidation-reduction potential of H_2O ($H_2O + e^- \rightarrow 1/2H_2 + OH^-$) is −0.83 eV, the trapped electrons in the Al-induced acceptor states occur a reduction reaction of the residual water, resulting in reducing the upward band bending.

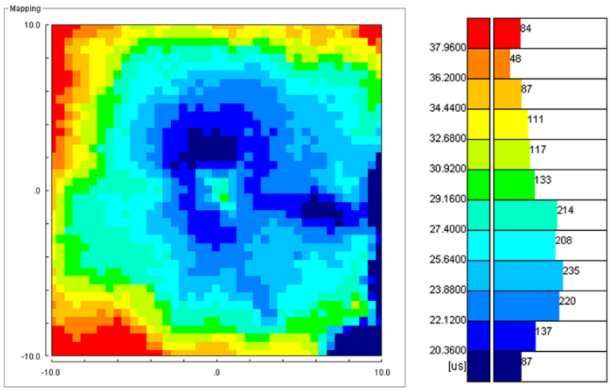

Fig. A-12-1 τ_{eff} mapping just after the Al-doped SiO_x formation. The N_2 dry process might not completely remove the water molecules from the sample surface.

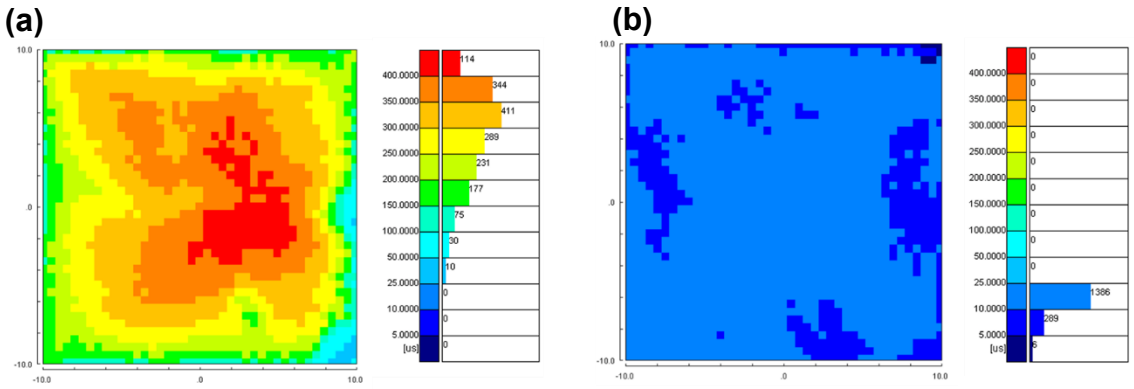

Fig. A-12-2 τ_{eff} of $Al(NO_3)_3$-treated n-Si(100) (a) after N_2 dried and (b) during immersing in DIW.

In addition, the τ_{eff} during immersing in ethanol was investigated. Since the sample immersed in ethanol did not show significant τ_{eff} degradation as a mean τ_{eff} of 431 μs, the ethanol could replace the residual H_2O, mitigating the reduction reaction of H_2O and the τ_{eff} degradation. Hence, the rinse process with ethanol improves the issue of τ_{eff} degradation due to the residual water.

Appendix 13: Fabrication of inverted pyramidal texture

The inverted pyramidal-textured c-Si substrates were formed using a wet chemical process by referring to the reported literature [5]. The etching solution was prepared (the mixture of 0.04 M copper (II) nitrate trihydrate $Cu(NO_3)_3$, 4.6 M HF, 0.55 M H_2O_2, and 2 mM polyethylene glycol (PEG) with an average molecular weight of 200) and then immersed in the etching solution for 15 min at 50 °C with stirring at 1000 rpm. The experimental setup for fabricating the inverted pyramidal textured c-Si substrates is shown in Figure A-13-1. The residual Cu precipitates were removed by immersing in 70 wt.% HNO_3 aqueous solution for 20 min with ultrasonication. In this study, the effectiveness of PEG was investigated. Figure A-13-2 shows the reflectance spectra of the formed inverted pyramidal texture by immersing in the etching solution w/ or w/o PEG. In the wide range of wavelengths, the reflectance was slightly decreased. At a wavelength of 630 nm, the w/ PEG sample showed a lower reflectance of 3.0% compared with the w/o PEG sample of 4.2%. These reflectance values were exceptionally low compared with the conventional upright pyramidal texture with a reflectance of 7.8% at a wavelength of 630 nm. As shown in the SEM images of Figure A-13-3, the size of the inverted pyramidal texture is almost the same, but the w/ PEG sample surface seems smoother than that of the w/o PEG sample. Further surface etching on the inverted pyramidal texture surface using NH_4OH aqueous solution was necessary to obtain an excellent surface passivation quality, as described in Appendix 14.

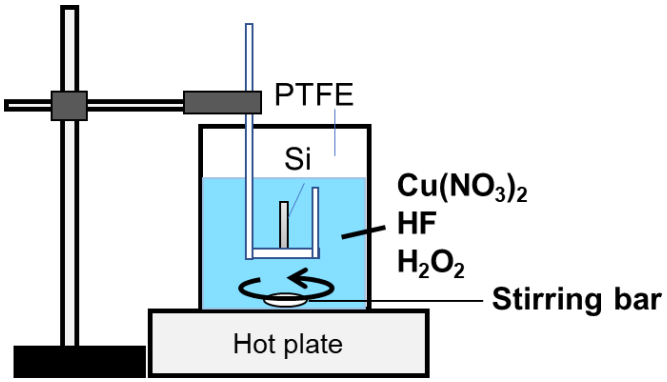

Fig. A-13-1. Experimental setup for the fabrication of the inverted pyramidal textured c-Si substrates.

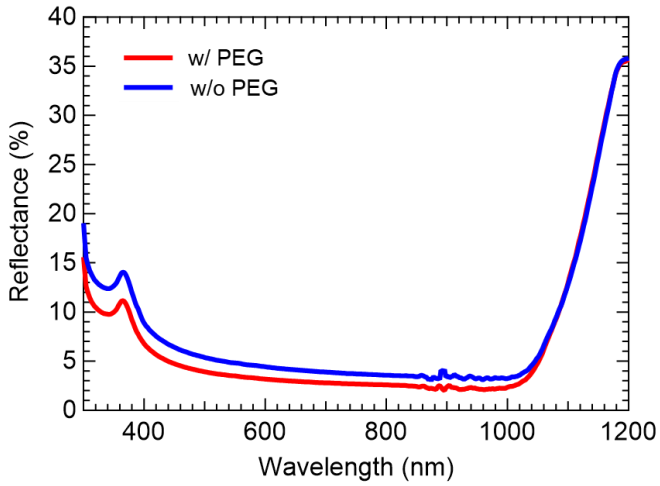

Fig. A-13-2. Reflectance spectra of the formed inverted pyramidal texture by immersing in the etching solution w/ or w/o PEG.

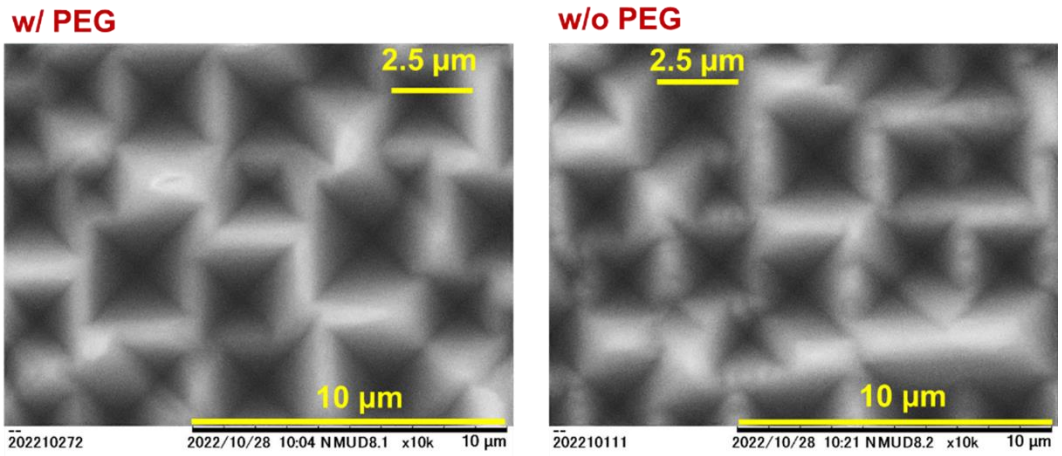

Fig. A-13-3. SEM image of the formed inverted pyramidal texture by immersing in the etching solution w/ or w/o PEG.

However, the additional surface etching increased reflectance, as shown in Figure A-13-3. To obtain lower reflectance compared with the conventional upright pyramidal texture, the surface etching process time should be less than 2 min. Further etching is considered to destroy the shape of the inverted pyramidal texture by the isotopic alkaline etching, deteriorating the optical property with higher reflectance.

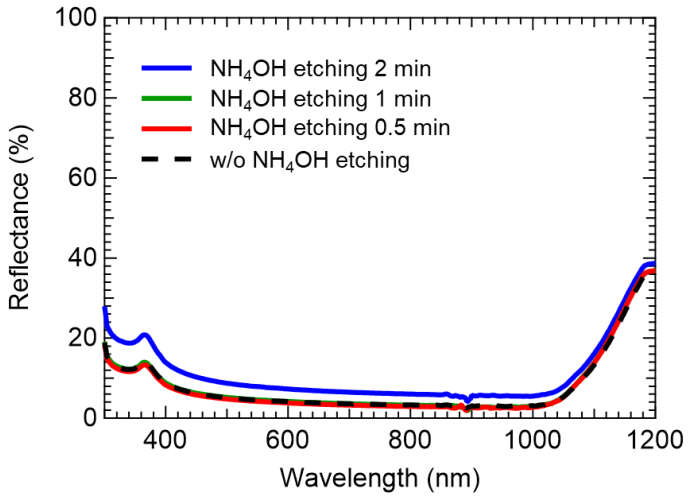

Fig. A-13-3. Reflectance spectra of the formed inverted pyramidal texture by immersing in the etching solution w/ or w/o additional etching using NH_4OH aqueous solution.

Appendix 14: Surface passivation on inverted pyramidal texture

The etching solution was prepared (the mixture of 0.04 M copper (II) nitrate trihydrate $Cu(NO_3)_3$, 4.6 M HF, 0.55 M H_2O_2) and then immersed in the etching solution for 15 min at 50 °C with stirring at 1000 rpm. After the residual Cu precipitates removal by immersing in 70 wt.% HNO_3 aqueous solution for 20 min with ultrasonication followed by oxide removal using a mixture of 40% CH_3OH and 5% HF for 5 min, the slight surface etching was performed using 28% NH_4OH for 0.5–2 min at RT. After oxide removal by immersion in a 5% HF aqueous solution, SC-2 cleaning was conducted at 80 °C for 10 min. After 5% HF treatment, ultrathin Al-doped SiO_x was formed by immersing in 0.25 M $Al(NO_3)_3$ aqueous solution at boiling temperature for 12.5 min. As shown in Figure 14-1 and Table A-14, the τ_{eff} was gradually increased with increasing the additional surface etching time using NH_4OH aqueous solution. Hence, additional surface etching on the inverted pyramidal texture was essential to obtain excellent surface passivation quality. However, as displayed in the surface images, the blackness is slightly reduced with the increase in additional etching time. This is due to the reflectance change as described in Appendix 13 and shown in Figure 13-3.

	w/o NH_4OH etching	w/ NH_4OH etching (0.5 min)	w/ NH_4OH etching (1 min)	w/ NH_4OH etching (2 min)
Surface image				
τ_{eff} mapping	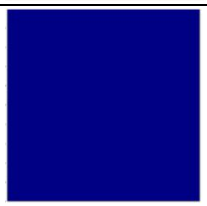	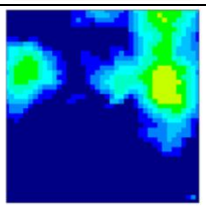	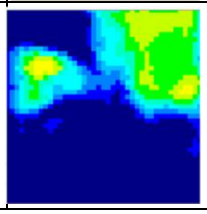	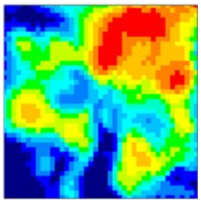

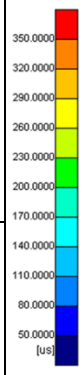

Fig.A-14-1. Surface images and τ_{eff} mappings after the surface passivation by Al-doped SiO_x of the formed inverted pyramidal textured c-Si w/ or w/o additional etching using NH_4OH aqueous solution.

Table A-14 τ_{eff} of w/ and w/o additional etching of inverted pyramidal texture using NH_4OH

Substrate	w/o NH_4OH etching	w/ NH_4OH etching (0.5 min)	w/ NH_4OH etching (1 min)	w/ NH_4OH etching (2 min)
Mean τ_{eff} (μs)	6	70	83	189
Maximum τ_{eff} (μs)	14	257	287	392

PEG was added to the etching solution to form an inverted pyramidal texture, as described in Appendix 13. After performing the same cleaning processes, ultrathin Al-doped SiO_x was formed on the inverted pyramidal texture by immersing in 0.25 M $Al(NO_3)_3$ aqueous solution at boiling temperature for 20 min. The mean τ_{eff} was 300 μs, and the maximum τ_{eff} was 421 μs. Hence, this result demonstrated an excellent surface passivation quality can be realized on inverted pyramidal textured c-Si surfaces. However, the additional etching process was essential to obtain excellent surface passivation quality, but it increased reflectance. Therefore, this trade-off between surface passivation quality and reflectance must be overcome to realize higher properties at the same time.

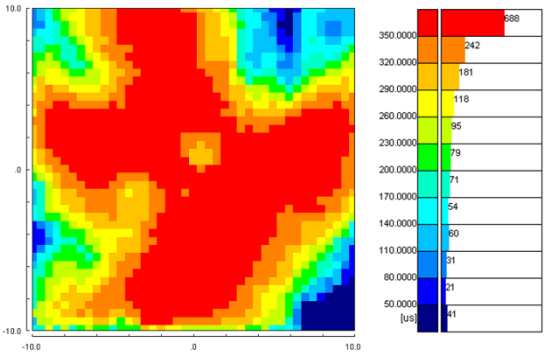

Fig. A-14-2. τ_{eff} mapping after the surface passivation by Al-doped SiO_x of the inverted pyramidal textured c-Si formed in PEG added etching solution and w/ additional etching for 2 min using NH_4OH aqueous solution.

Appendix 15: PEDOT:PSS on ultrathin Al-doped SiO_x

Poly(3,4-ethylenedioxythiophene) polystyrene sulfonate (PEDOT:PSS) is known as a hole transport layer with high conductivity and high work function. By using PEDOT:PSS dispersion solution, a thin film can be formed on a substrate surface. As described in 4.7.3, the R_{sheet} of Al-doped SiO_x/n-Si is still high to obtain an excellent solar cell performance with a sufficient FF. One of the promising solutions for the issue is utilizing a high-hole conductive layer on the ultrathin Al-doped SiO_x layer. Thus, to overcome this issue, PEDOT:PSS on the ultrathin Al-doped SiO_x layer was investigated to determine whether it can realize a low R_{sheet} while keeping an excellent surface passivation quality. In this experiment, 280 µm-thick FZ-grown n-Si(100) substrate with a resistivity of 2.5 Ωcm was used. After cleaning in acetone followed by ethanol solvent with ultrasonication for 5 min, respectively, and 1% HF treatment for 1 min at RT, ultrathin Al-doped SiO_x was formed by immersing in 0.25 M $Al(NO_3)_3$ aqueous solution at boiling temperature for 12.5 min. Subsequently, PEDOT:PSS (Heraeus Deutschland GmbH & Co. KG, Clevios PH1000) was spin-coated on the ultrathin Al-doped SiO_x/n-Si(100) using spin coater (MIKASA Co., Ltd., 1H-DX) following the process, as shown in Figure A-15-1. Figure A-15-2 shows τ_{eff} after the spin coating of PEDOT:PSS at various spin speeds (2000–5000 rpm). Since the high τ_{eff} of 420 µs before the spin coating significantly degraded to less than 90 µs, PEDOT:PSS layer degraded the surface passivation of ultrathin Al-doped SiO_x. The reason is not fully revealed but the acid of PEDOT:PSS might destroy the ultrathin Al-doped SiO_x layer, deteriorating the surface passivation. As shown in Figure A-15-3, R_{sheet} was gradually decreased with reducing spin speed due to the thickening of the PEDOT:PSS layer. However, a sufficient low R_{sheet} could not obtained. Hence, this experiment concluded different approaches should be investigated to increase the lateral conductivity of the ultrathin Al-doped SiO_x layer/n-Si.

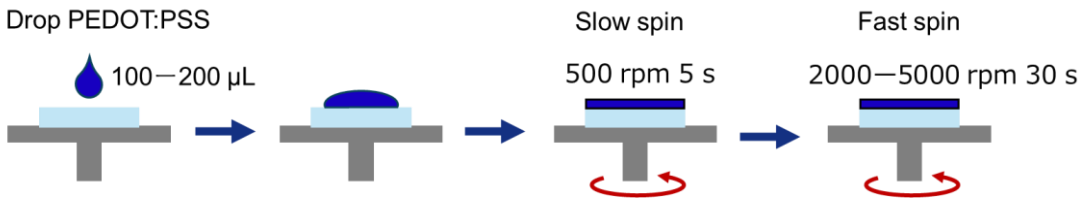

Fig. A-15-1. Spin coating process flow to form PEDOT:PSS thin film on the Al-doped SiO_x.

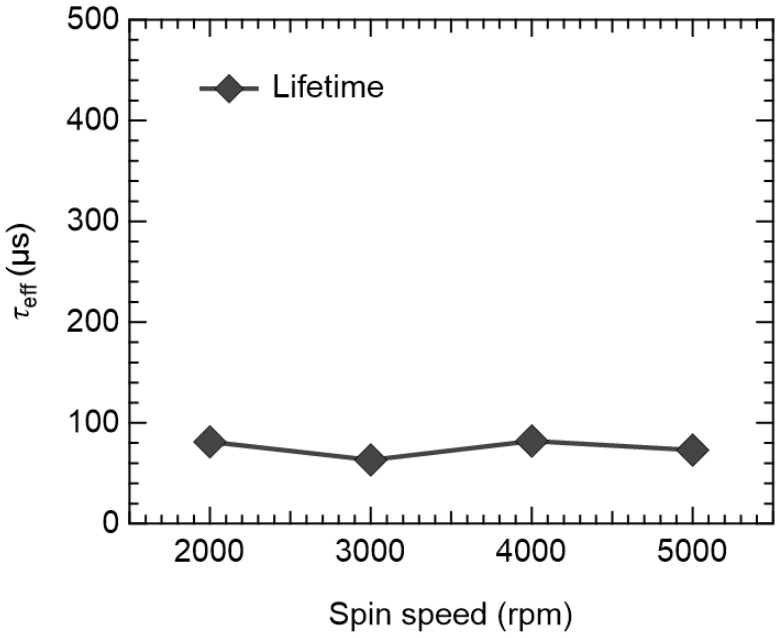

Fig. A-15-2. τ_{eff} after the spin coating of PEDOT:PSS at various spin speeds (2000–5000 rpm).

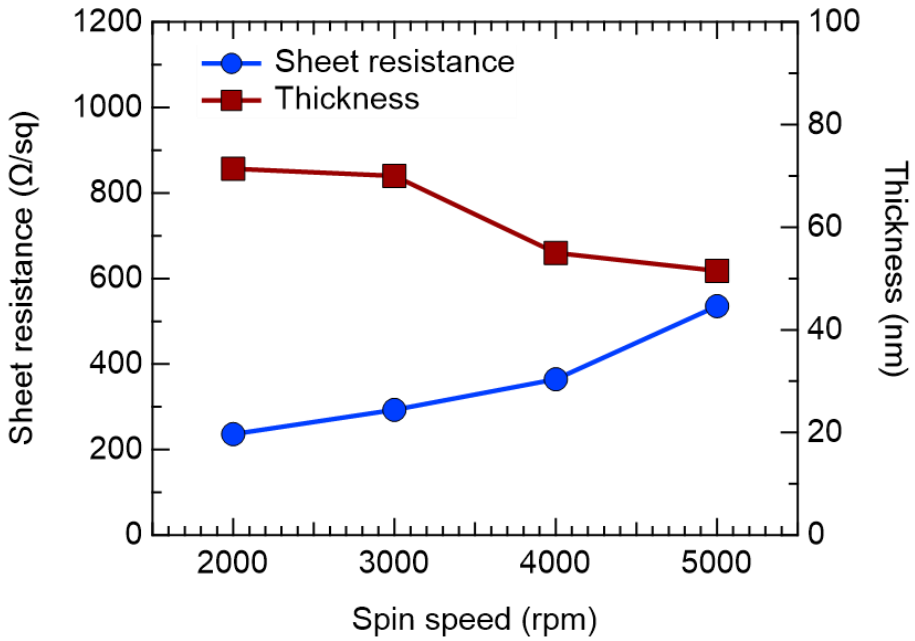

Fig. A-15-3. R_{sheet} and thickness of PEDOT:PSS layer formed at various spin speeds (2000–5000 rpm).

Appendix 16: Al/Mg/ultrathin Al-doped SiO_x stacks

As shown in Figure 6.24, the Al-COIL solar cell was tested as a rear structure of Al/Mg/ultrathin Al-doped SiO_x stacks. As described in this thesis, since the Al-doped SiO_x layer is revealed to be a hole-selective contact, the rear Al-doped SiO_x layer must be removed or transformed the layer into electron-selective contact. The removal of Al-doped SiO_x makes direct metal contact with the Si surface, resulting in high recombination at the rear surface. Hence, a better solution is the transformation of the carrier selectivity of the Al-doped SiO_x layer. In order to change the carrier selectivity, we should make contact with a low-work function metal. Magnesium (Mg) is one of the low-work function metals (3.66 eV) with respect to an electron affinity in Si of 4.05 eV. The concept is shown in Figure A-16; when the low-work function metal is in contact with the surface of Al-doped SiO_x/n-Si, the Si surface band is bent downwards by creating an accumulation layer. Hence, the Al-induced acceptor states transform into the donor states which can provide electron-selective contacts.

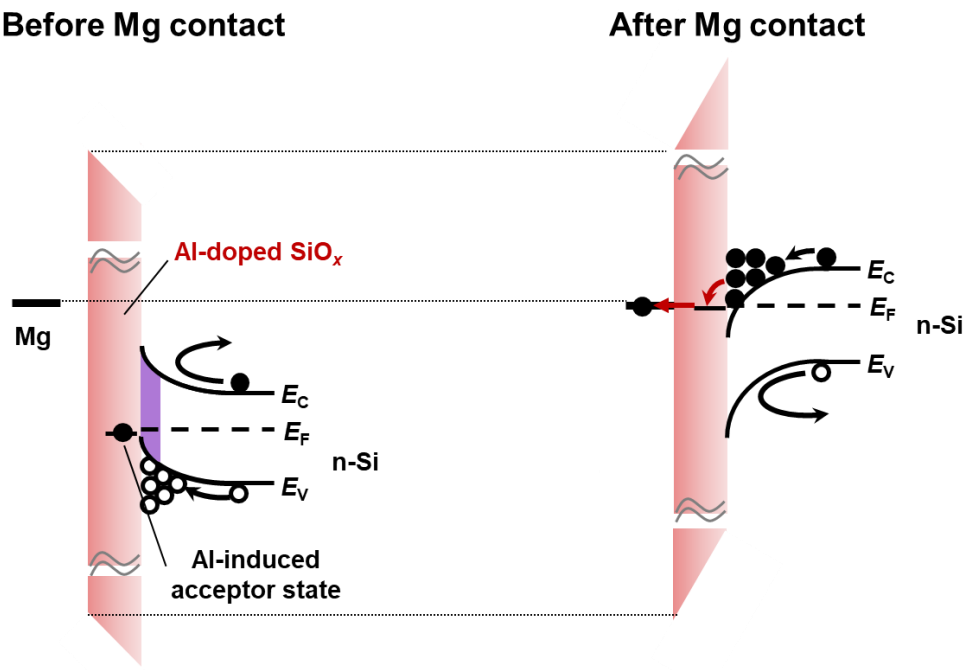

Fig. A-16-1. Band diagram before and after Mg contact with ultrathin Al-doped SiO_x/n-Si

The tunneling current density of the Al/Mg/Al-doped SiO_x/n-Si structure was evaluated. The ultrathin Al-doped SiO_x layers were formed on the RCA-cleaned and HF-treated n-Si(100) substrates by immersing in the boiled $Al(NO_3)_3$ aqueous solution with a molar concentration of 0.25 M for 12.5 min. A Mg wire with a diameter of 0.5 mm (Nilaco Corporation, 99.95%) was used to deposit Mg. After

the Mg electrode formation, Al was subsequently thermally deposited on the Mg/Al-doped SiO_x/n-Si through the mask with a diameter of 0.0028 cm^2 to form circular Al/Mg stack electrodes without breaking the vacuum condition with a pressure of < 9×10^{-4} Pa. After the deposition, the oxide of the rear side was removed using 5% HF and by scratching. Subsequently, full-area Al film was deposited on the rear side of the sample to form an Ohmic contact. To compare the Al/Mg stacks and only Al as a top electrode, the Al/Al-doped SiO_x/n-Si/Al structure was also fabricated and tested. Figure A-16-2 shows dark *J–V* characteristics of the samples with the MOS structures with Al/Mg/Al-doped SiO_x /n-Si/Al (w/ Mg) and Al/Al-doped SiO_x/n-Si/Al (w/o Mg). The *J–V* characteristics of the w/ Mg sample indicate an increase in the tunneling current density with more Ohmic properties compared with the w/o Mg sample. This implies that Mg contact transforms the Al-doped SiO_x/n-Si into electron-selective contact owing to the downward band bending of the Si surface due to the low-work function of Mg.

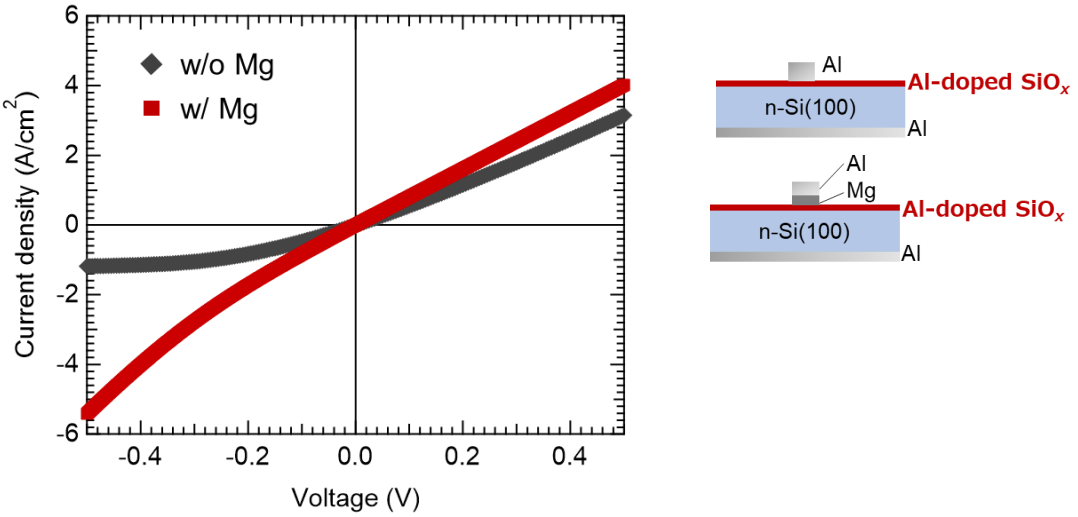

Fig. A-16-2. Dark *J–V* characteristics and the device structure of the samples with Al/Mg/Al-doped SiO_x /n-Si/Al (w/ Mg) and Al/Al-doped SiO_x/n-Si/Al (w/o Mg).

Appendix 17: Surface passivation on rough Si surface

The effectiveness of the rough Si surface on surface passivation by ultrathin Al-doped SiO_x was investigated. An acid etching process was performed to make a rough surface of Si substrates, as reported in the literature [6]. A 280 μm-thick n-Si(100) wafer with a resistivity of 2.5 Ωcm was immersed in the acid mixture of 96.67% HCl, 0.83% HF, and 2.5% H_2O_2 at RT for 60 min to form a rough Si surface. After the etching process, the treated substrates were cleaned using acetone and ethanol with an ultrasonication. Subsequently, 1% HF treatment was performed for 1 min. After DIW rinse, the hydrophobic Si substrates were immersed in the boiled $Al(NO_3)_3$ aqueous solution with a molar concentration of 0.25 M for 12.5 min. After the N_2 blow, τ_{eff} values were measured by μ-PCD using an excitation laser with a wavelength of 904 nm and an areal photon density of 5×10^{13} cm^{-2}. By the acid etching process, the Si substrates were 10 μm thinned. Hence, the measured τ_{eff} values were converted into $S_{eff,\,max}$ to compare the surface passivation quality on the mirror-polished Si surface. As shown in Figure A-17 of the optical microscope image of the c-Si surface after the acid etching process, ~10 μm-size bubble-like textures were observed.

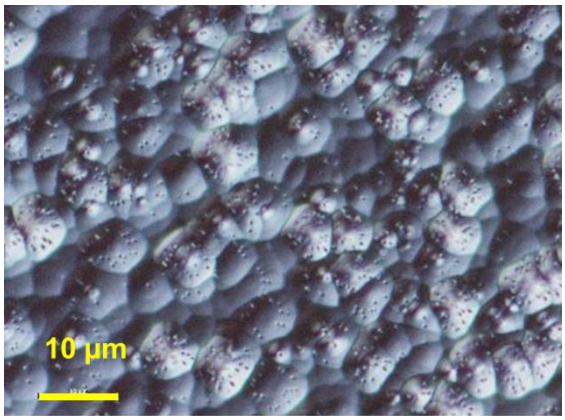

Fig. A-17. Optical microscope image of the c-Si surface after the acid etching process.

Table A-17 shows the average mean τ_{eff} and $S_{eff,\ max}$ of the $Al(NO_3)_3$-treated sample with and without the bubble-like textures. For each sample, four samples were tested and evaluated as their average values. The bubble-like textures increase the surface defect states corresponding to the surface area of Si. Nevertheless, the $S_{eff,\ max}$ was slightly decreased compared with the mirror-polished Si surface. Hence, the surface roughness would be an advantage of the surface passivation by the ultrathin Al-doped SiO_x. One possible reason is that effective negative Q_f is increased owing to the increment of the surface area, enhancing the field-effect passivation.

Table A-17 average mean τ_{eff} and $S_{eff,\ max}$ of the $Al(NO_3)_3$-treated sample with and without the bubble-like textures

Substrate	Average mean τ_{eff}	Average mean $S_{eff,\ max}$
w/ bubble-like textures	550	25.5
w/o bubble-like textures	476	30.2

Appendix 18: PMMA on Al-doped SiO_x for anti-reflection coating

The ultrathin Al-doped SiO_x cannot functionalize as an anti-reflection coating. Hence, an anti-reflection coating is essential to boost photocurrent density. In general, the PECVD-SiN_y layer or indium tin oxide (ITO) is widely used. However, the plasma or the sputtering causes the degradation of the ultrathin Al-doped SiO_x layer, leading to poor interface properties. In this thesis, the Cat-CVD SiN_y layer was tested for the anti-reflection coating on Al-doped SiO_x, but the surface passivation was significantly degraded, as described in 6.10.3. The degradation is considered to be due to Q_f compensation by the high positive Q_f in the Cat-CVD SiN_y layer. Therefore, to avoid such damage to the ultrathin layer and Q_f compensation, a wet deposition process using a material with a refractive index of ~2 increases optical properties. According to the optical simulation results using OPAL 2, as shown in Figure A-18-1, poly(methyl 2-methyl propanoate) (PMMA) is one of the promising materials. PMMA expects the reflected photon current density loss to be as low as 1.16 mA cm^{-2} when the thickness was optimized as 109 nm. In this experiment, PMMA (Sigma-Aldrich GmbH, 182230) was dissolved in acetone to prepare 2 wt.% PMMA solution. The PMMA dispersive solution was spin-coated on the ultrathin Al-doped SiO_x/n-Si(100) with a spin speed of 500 rpm for 5 s followed by 2500 rpm for 30 s, as illustrated in Figure A-18-2. The τ_{eff} was measured by μ-PCD before and after spin-coating. The τ_{eff} was 443 μs before pain-coating but degraded to 53 μs after spin-coating of PMMA. The τ_{eff} degradation mechanism has not been revealed yet, but acrylic resin might be related to the degradation because attaching scotch tape consisting of acrylic resin also caused degradation as low as 8 μs, but attaching cello tape without acrylic resin did not cause such degradation. As shown in Figure A-18-3, the reflectance of PMMA-coated Al-doped SiO_x/Si was lower than that of the sample without PMMA layer. However, the anti-reflection effect is insufficient due to the still unoptimized thickness. Although the reflectance can be optimized by adjusting the concentration of the PMMA solution and spin speed during the spin coating process, the τ_{eff} degradation issue cannot be solved as long as it is not replaced with other materials.

INPUTS

Surface morphology

Random

Upright pyramids

Charact. angle, ω 54.74 °

Planar fraction 0 %

Incident illumination

Spectrum AM1.5g [Gue9

Zenith angle, θ 0 °

Light trapping model

Z = 4n²

Substrate width, W 180 µm

Layer	t (nm)	Optim.	Material	
Superstrate			Air	[]
x Film 1	109	☑	PMMA	Cast [McI09b]
x Film 2	1	☐	SiO2	Thermal [Pal85e]
Substrate			Si	Crystalline, 300 K [Gre08]

+ Add Film 3 ↕ Flip layers → Visit RI library

Optimisation goal: Maximise — Photon current absorbed in substrate

OUTPUTS

Reflections	Unique paths	Fraction
1 reflection	0	0.0%
2 reflections	1	68.3%
3 reflections	3	25.6%
4+ reflections	3	6.1%
Total	7	100.0%

Photon current		mA/cm²	Fraction
Incident	J_{Inc}	44.49	100.0%
Reflected	J_R	1.16	2.6%
Absorbed in films	J_A	0.00	0.0%
Absorbed in substrate	J_G	43.33	97.4%

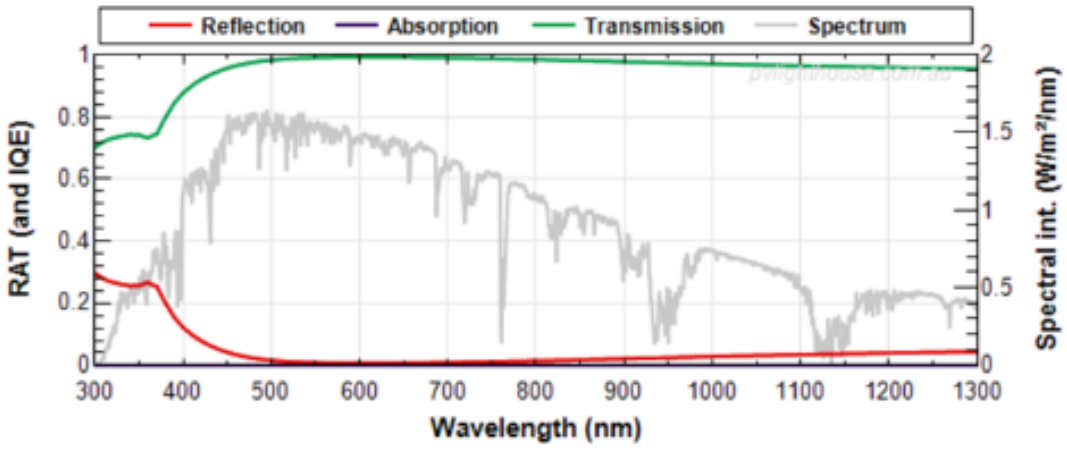

Fig. A-18-1. Optical simulation results using OPAL 2 for the structure with PMMA/SiO_2/Si.

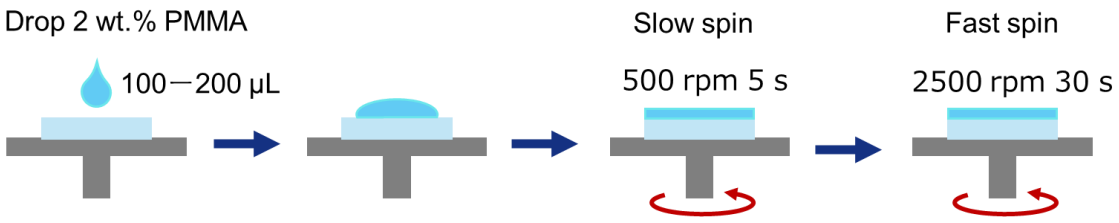

Fig. A-18-2. Spin coating process for the formation of PMMA anti-reflection coating.

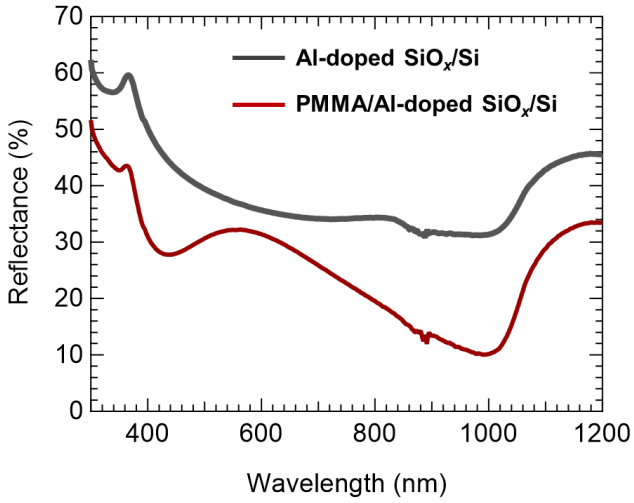

Fig. A-18-3. Reflectance spectra of PMMA-coated Al-doped SiO_x/Si and Al-doped SiO_x/Si.

Appendix 19: WO_z on Al-doped SiO_x for anti-reflection coating

As described in Appendix 18, forming an anti-reflection coating by wet deposition process is crucial to realize higher Al-COIL solar cell performance due to the boosted photocurrent density. In addition, high-work function materials can be hole-transport layers owing to the band alignment by receiving electrons from the Si surface and enhancing the upward band bending of the Si surface with strong inversion layers. Furthermore, the enhanced carrier generation by the anti-reflection coating is considered to increase the excited electron trapping in the Al-induced acceptor states, resulting in enhancing negative Q_f in the Al-doped SiO_x followed by field-effect passivation and hole-lateral conductivity. The concept of the enhancement of hole-selective passivating contact properties originating from boosting the light trapping effect is illustrated in Figure A-19-1.

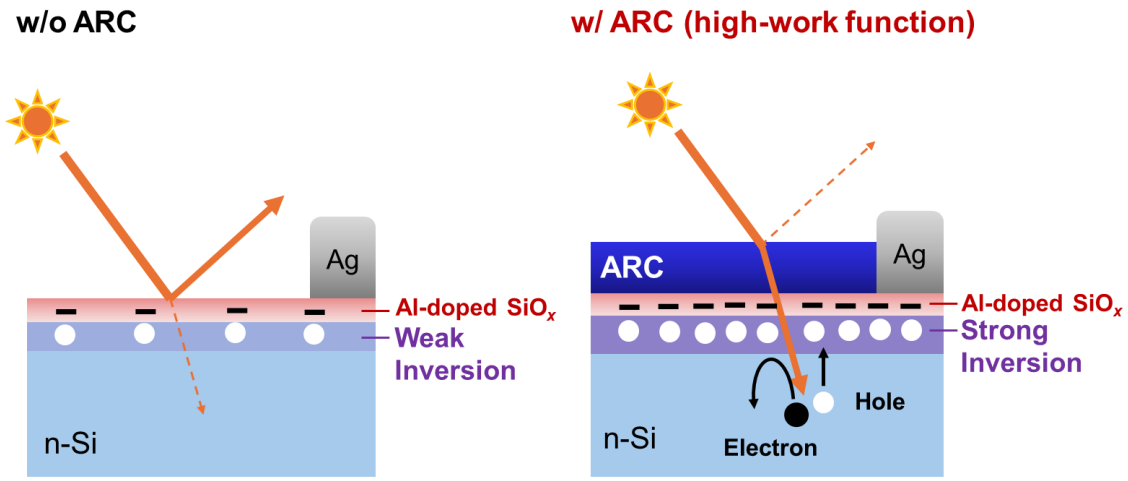

Fig. A-19-1. Concept of the enhancement of hole-selective passivating contact properties originating from boosting the light trapping effect.

For the material with anti-reflection and high-work function properties, WO_z was selected because the material has an adequate refractive index of 2.45 and a work function of ~6.7 eV. The optical simulation was conducted using OPAL2 to analyze the loss due to the reflectance. WO_z expects the reflected photon current density loss as low as 1.41 mA cm^{-2} when the thickness was optimized as 56 nm.

Fig. A-19-2. Optical simulation results using OPAL 2 for the structure with $WO_3/SiO_2/Si$.

In this experiment, cubic WO_z (c-WO_z) nanoparticles dispersed in a xylene solution were used. The WO_z dispersed solution was spin-coated on ultrathin Al-doped SiO_x/n-Si(100). Subsequently, the reflectance spectra and τ_{eff} were measured using UV-vis NIR and µ-PCD, respectively. Figure A-19-3 shows the reflectance spectra of spin-coated c-WO_z/Al-doped SiO_x/n-Si. Consequently, c-WO_z effectively reduced reflectance with respect to the bare-Si surface, and the bluish surface can be seen

in the inset of the figure. The lowest reflectance was still a slightly longer wavelength compared with the optimal wavelength. The thickness and refractive index should be adjusted by investigating the spin coating conditions to obtain higher optical properties. Figure A-19-4 shows τ_{eff} after the deposition of the WO_z layer measured by μ-PCD at each measurement time to investigate the time-related change of τ_{eff}. Although the τ_{eff} degraded just after the deposition, τ_{eff} gradually recovered to the initial value while storing in the air ambient at RT but slightly degraded in 24 h and stabilized at ~390 μs. However, higher τ_{eff} could not be realized by depositing WO_z on Al-doped SiO_x/n-Si. This concluded that the expectation of the high τ_{eff} owing to the higher band bending due to the high-work function of c-WO_z formed by the spin-coating process could not be realized. The spin-coated c-WO might not have a high-work function, resulting in reducing the upward band bending. In addition, spectroscopic ellipsometry measurement and analysis using the Cauchy model revealed the c-WO_z layer thickness was 100 nm, and the refractive index at 630 nm was 1.66. The refractive index was not far from the theoretical value of 2.45 for WO_3 crystallite.

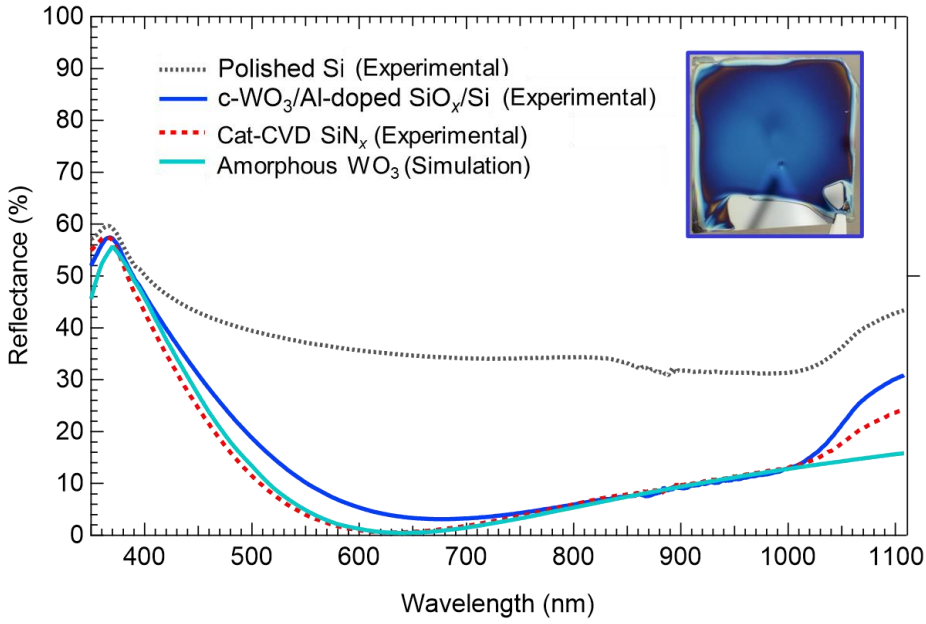

Fig. A-19-3. Reflectance spectra of spin-coated c-WO_z/Al-doped SiO_x/n-Si. As references, the reflectance spectra of mirror-polished Si, Cat-CVD SiN_x, and simulated amorphous WO_3 are also displayed.

	Before depo.	After depo.	After depo. 3 h later	After depo. 24 h later	After depo. 48 h later
τ_{eff} mapping	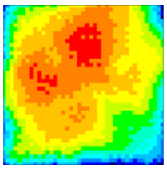	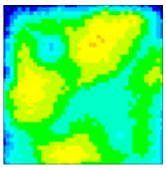	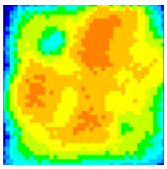	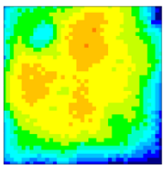	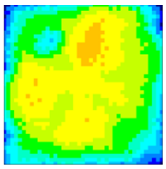
Mean τ_{eff} (μs)	453	356	435	393	387

Fig. A-19-4. τ_{eff} after the deposition of c-WO_z measured by μ-PCD at each measurement time.

In addition, WO_z was deposited using an electron beam evaporation system on ultrathin Al-doped SiO_x for both sides. The thickness of WO_z was determined to be ~36 nm by spectroscopic ellipsometry measurement and analysis using the Cathey model. As a result, the deposition of WO_z significantly degraded the τ_{eff} of n-Si(100) passivated by Al-doped SiO_x from ~400 μs to 15 μs. Since the *C–V* measurement revealed the V_{bi} reduction from 0.87 to < 0.8 eV, the deterioration is mainly due to the reduction of the upward band bending. The work function of deposited WO_z was not so higher than the expected value of ~6.7 eV. Therefore, WO_z/Al-doped SiO_x stacks could not be a solution for the excellent hole-selective passivation contact on n-Si substrates. However, the surface passivation quality may depend on the thickness of WO_z and may need to be optimized.

Appendix 20: Fabrication of nano-sized pyramidal textured c-Si surface

Space charge region compression in the narrow n-Si with the faced negatively charged oxides increases hole density. Figure A-20-1 shows the PC3S simulated surface hole density increase ratio of the pyramidal texture surface with respect to the planar surface as a function of the texture depth. The Q_f of -3×10^{12} cm^{-2}, the texture angle of 54.7°, and the doping concentration of base Si of 2×10^{15} cm^{-3} without impurity diffusion concentration were set and simulated in the region of the base thickness of 15 μm. As shown in Figure A-20-1, the surface hole density is gradually enhanced by decreasing the texture depth. The texture size of 0.5 μm makes the surface hole density increase ratio with respect to the planar surface > 1.4 times higher. Since the surface recombination velocity and sheet resistance are inversely proportional to the surface hole density, forming nano-sized pyramidal texture is one of the solutions to improve hole selective passivating contact properties. Hence, in this study, nano-sized pyramidal textures were fabricated using a conventional alkaline wet chemical etching process with additives as an etching mask to enhance the hole-selective passivating contact properties.

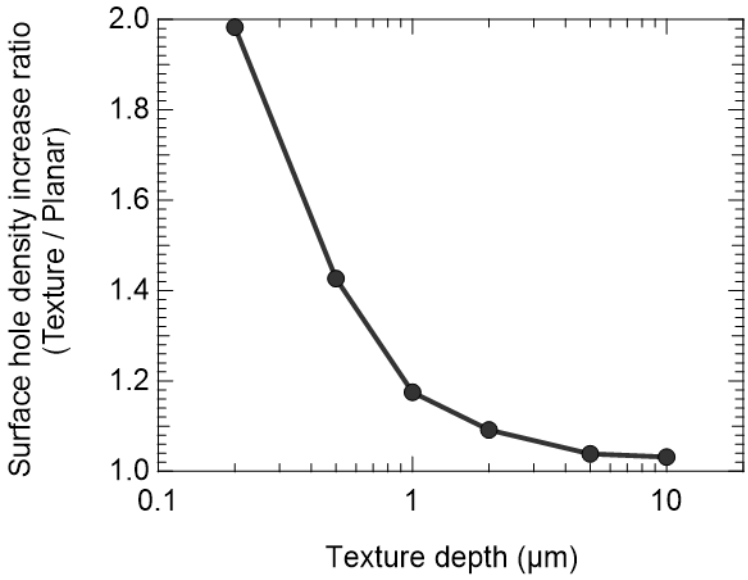

Fig. A-20-1. Surface hole density increase ratio with respect to planar surface as a function of texture depth.

In this experiment, 280 μm-thick n-Si(100) with a resistivity of 2.5 Ω cm was used as substrates. After cleaning the cleaved substrates in acetone followed by ethanol with ultrasonication for 5 min, the substrates were immersed in the heated KOH solution with additives (TP101, Hayashi Pure Chemical) to form pyramidal textures on the Si substrates. The details of the texturing conditions are shown in Table A-20.

Table A-20. Conditions for the formation of nano-sized pyramidal textures

Conditions	Temperature (°C)	Time (min)	Additives (wt.%)	Ultrasonication
Ref.	80	15	0.3	-
Low temp.	55	45	0.3	-
Low temp. w/ US	55	45	0.3	Applied
Low temp., ×2 additives w/ US	55	45	0.6	Applied
Low temp.,×4 additives w/ US	55	45	1.2	Applied

Figure A-20-2 shows the SEM images of the fabricated pyramidal textures for each condition. Two main factors were process temperature and additives concentration to fabricate the nano-sized pyramidal textures. As compared to the ref. (a) and (b) decreasing the process temperature from 80 to 55 °C significantly decreased the pyramidal texture size. The ultrasonication effect on the texture size was also investigated, but almost no effect was confirmed, as compared to (b) and (c). However, a further increase of additives concentration from 0.3 to 1.2 wt.% decreased the pyramidal texture size from ~1 μm to ~500 nm. Hence, the significant reduction of the pyramidal texture size from ~2 μm to ~500 nm was caused by lower process temperature and increasing additives concentration. However, the decreasing pyramidal textures slightly increased the reflectance in the wide range of wavelengths except for the short wavelength region of the smallest pyramidal textures, as shown in Figure A-20-3. This increase of the reflectance might be related to decreasing texture depth. Assuming this model, the higher aspect ratio of nano-sized pyramidal textures is considered to be a solution to realize both nano-size structure and lower reflectance.

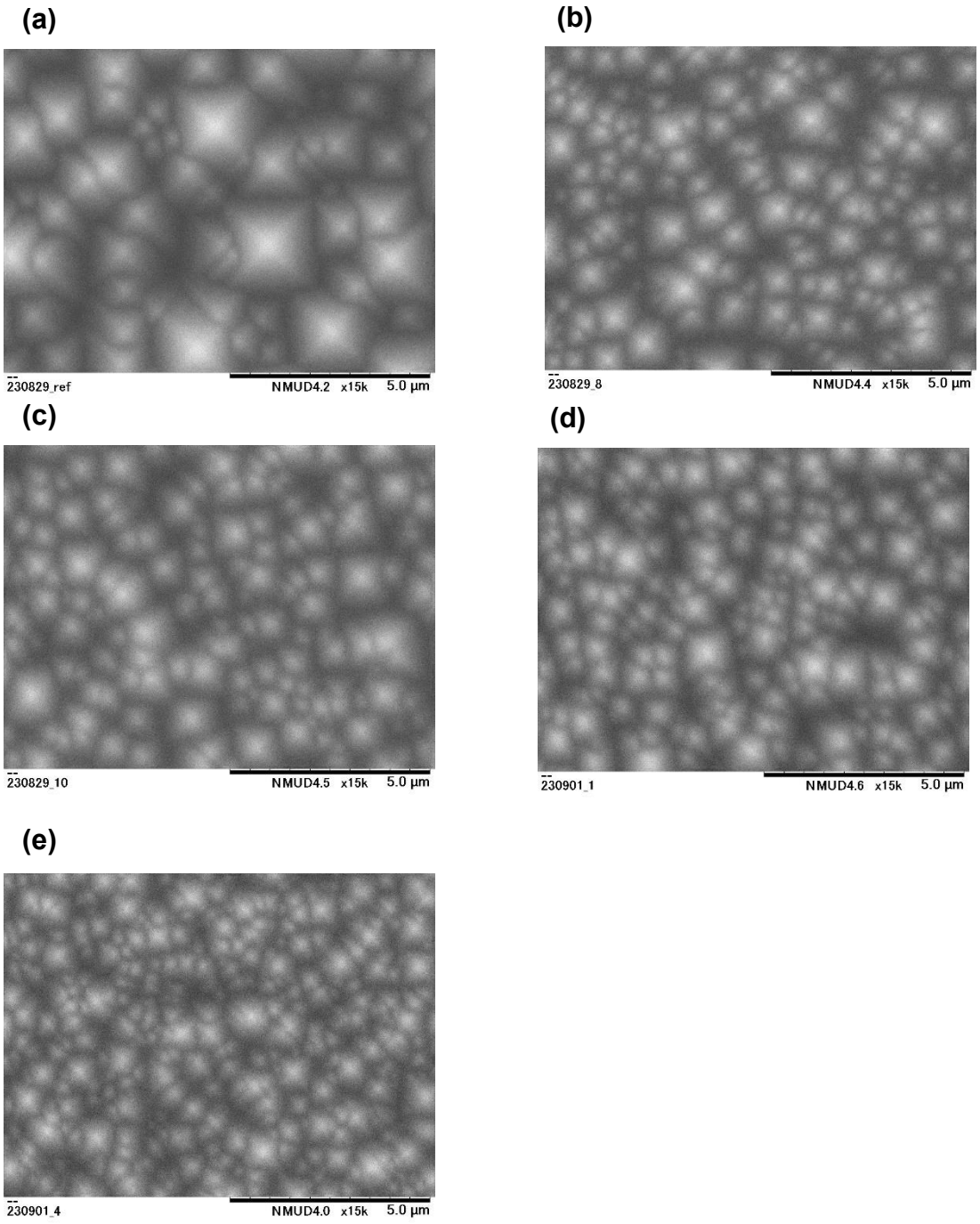

Fig. A-20-2. SEM images of the surface of the fabricated pyramidal textures for each condition. (a) reference, (b) 55 °C condition, (c) 55 °C w/ ultrasonication, (d) 55 °C, 0.6 wt.% additives w/ ultrasonication, and (e) 55 °C, 1.2 wt.% additives w/ ultrasonication.

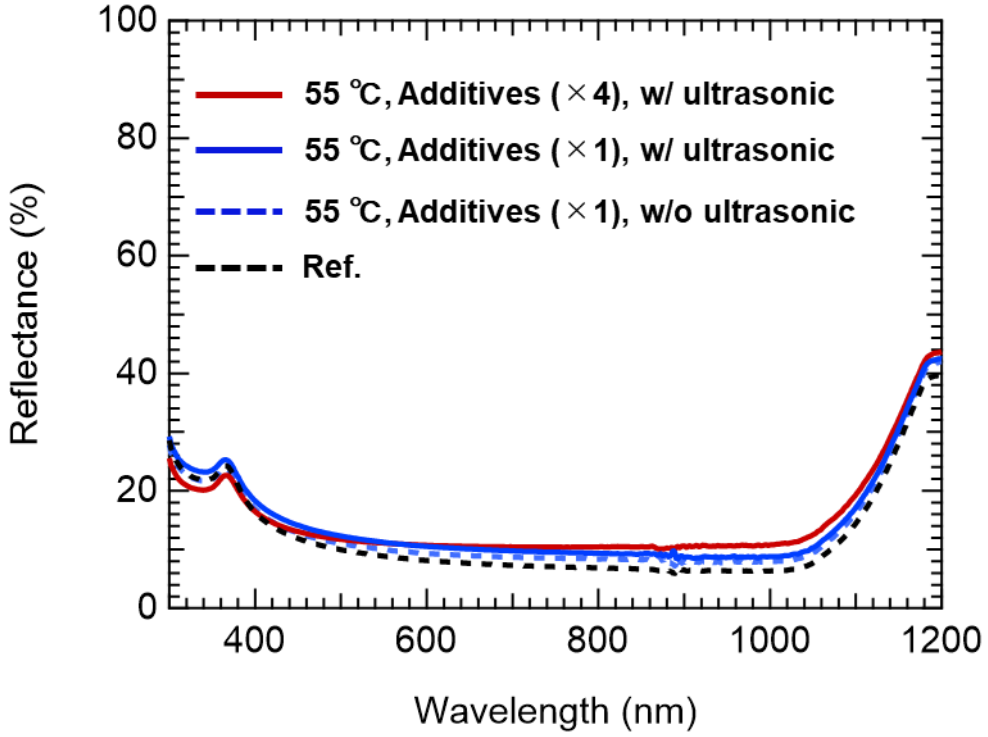

Fig. A-20-3. Reflectance spectra of the fabricated pyramidal textures for each condition.

Appendix 21: Potassium nitrate (KNO_3) treatment on c-Si surface

As described in this thesis, the $Al(NO_3)_3$ treatment boosts the surface passivation quality on c-Si surfaces. Other metal nitrates may oxidize the Si surface, and the included metal acts as a field-effect passivation as a formation of metal oxide with a low or high work function compared to an electron affinity of c-Si or metal ion with a positive charge. Hence, in this experiment, potassium nitrate (KNO_3) was investigated to determine whether it could improve the surface passivation quality on the c-Si surface. Cleaved 280 µm-thick FZ n-Si(100) substrates with a resistivity of 2.5 Ω cm were cleaned using RCA cleaning and treated in 1% HF solution. The hydrophobic c-Si substrates were immersed in 0.5 mol L^{-1} KNO_3 aqueous solution at RT for 8 h. The τ_{eff} mapping of Figure A-21-1 (a) shows that a slightly increased spot was observed up to ~8 µs. Hence, since the KNO_3 treatment passivates the Si surface, and the surface passivation quality surpassed the passivated surface by HNO_3 (τ_{eff} ~5 µs), the surface passivation might be attributable to the field-effect passivation owing to the included metal potassium as a formation of ion. Moreover, to improve the surface passivation quality by KNO_3 treatment, the KNO_3 concentration condition of 2.0 mol L^{-1} for 2 h increased to τ_{eff} of 28 µs and using 2.0 mol L^{-1} KNO_3 aqueous solution prepared by SC-1 solution for 10 min further increased to 111 µs, as shown in Figure A-21-2. The positive ion of K^+ might be attracted and attached by the negatively charged Si or SiO_x surface in the alkaline solution, resulting in the induction of field-effect passivation owing to the higher positive K^+ surface. The proposed surface passivation model is shown in Figure A-21-3.

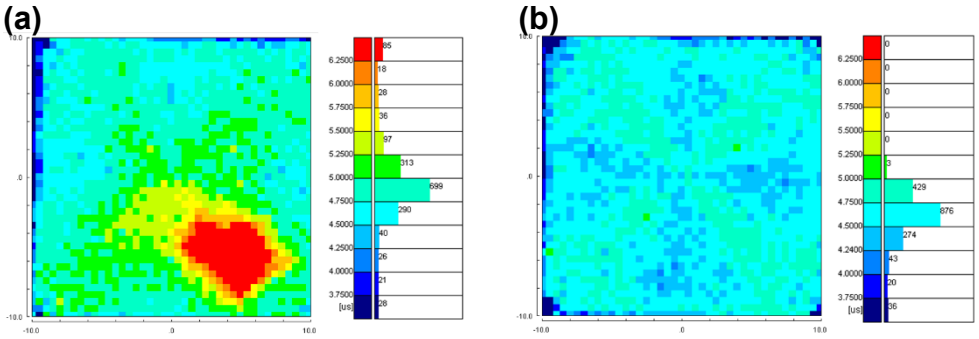

Fig. A-21-1. τ_{eff} mapping of (a) 0.5 mol L^{-1} KNO_3 treated sample and (b) 70 wt.% HNO_3 treated sample.

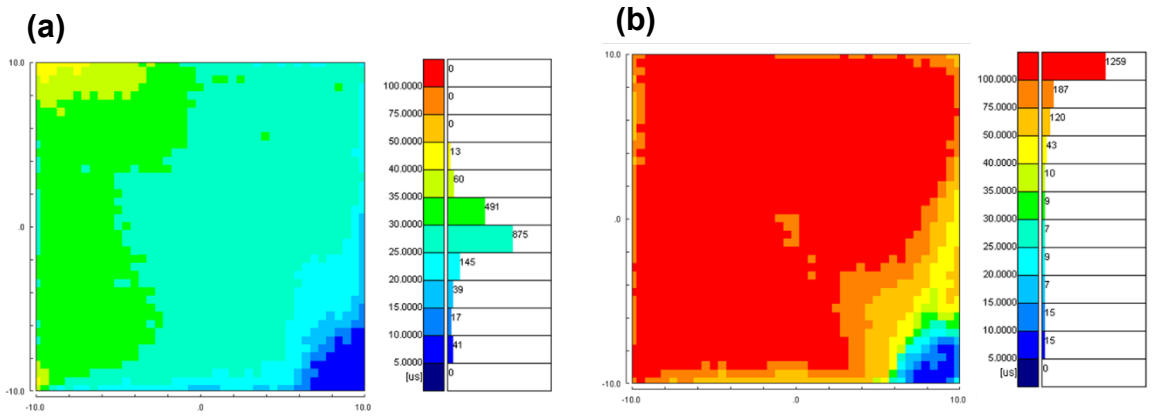

Fig. A-21-2. τ_{eff} mapping of (a) 2.0 mol L^{-1} KNO_3 treated sample and (b) 2.0 mol L^{-1} KNO_3 in SC-1 solution treated sample.

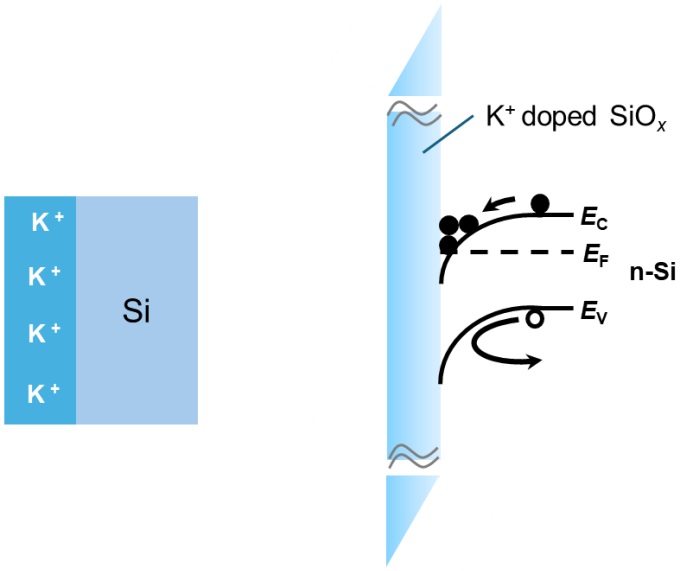

Fig. A-21-3. Surface passivation model by formed ultrathın K^+ doped SiO_x layer formed by KNO_3 treatment.

References

[1] S. Duttagupta, F. Ma, B. Hoex, T. Mueller, and A. G. Aberle, “Optimised antireflection coatings using silicon nitride on textured silicon surfaces based on measurements and multidimensional modelling,” Energy Procedia **15**, 78 (2012).

[2] C. A. Gueymard, "SMARTS2, A simple model of the atmospheric radiative transfer of sunshine: Algorithms and performance assessment," Florida Solar Energy Center Report (1995).

[3] M. A. Green, “Self-consistent optical parameters of intrinsic silicon at 300 K including temperature coefficients,” Sol. Energy Mater. Sol. Cells **92**, 1305 (2008).

[4] S. Tanuma, C. J. Powell, and D. R. Penn, “Calculations of electron inelastic mean free paths. V. Data for 14 organic compounds over the 50–2000 eV range,” Surf. Interface Anal. **21**, 165 (1994).

[5] Y. Wang, L. Yang, Y. Liu, Z. Mei, W. Chen, J. Li, H. Liang, A. Kuznetsov, and D. Xiaolong, “Maskless inverted pyramid texturization of silicon,” Sci. Rep. **5**, 10843 (2015).

[6] A. Stapf, F. Honeit, C. Gondek, and E. Kroke, “Texturing of monocrystalline silicon wafers by HF-HCl-H_2O_2 mixtures: Generation of random inverted pyramids and simulation of light trapping in PERC solar cells,” Sol. Energy Mater. Sol. Cells **159**, 112 (2017).

LIST OF PUBLICATION

Journal articles

[1] Hiroki Nakajima, Huynh Thi Cam Tu, and Keisuke Ohdaira, "Surface orientation dependence on hole-selective passivating contacts of ultrathin Al-doped SiO_x layers formed on n-type crystalline Si surfaces using an aluminum nitrate oxidation treatment," Appl. Surf. Sci. (Submitted)

[2] Hiroki Nakajima, Huynh Thi Cam Tu, and Keisuke Ohdaira, "Effectiveness of the Pyramidal Textured Crystalline Silicon Surfaces on Hole-Selective Passivating Contacts Induced by Wet Chemically Grown Ultrathin Al-doped SiO_x layers," Solar RRL (Submitted)

[3] Hiroki Nakajima, Huynh Thi Cam Tu, and Keisuke Ohdaira, "Significant role of an ultrathin SiO_x interlayer in Cat-CVD SiN_y/SiO_x stacks for the surface passivation of n-type crystalline silicon," Prog. Photovolt. (Submitted)

[4] Hiroki Nakajima, Huynh Thi Cam Tu, and Keisuke Ohdaira, "Ultrathin Al-doped SiO_x passivating hole-selective contacts formed by a simple wet process," Jpn. J. Appl. Phys. **62**, SK1040 (2023).

[5] Hiroki Nakajima, Huynh Thi Cam Tu, and Keisuke Ohdaira, "Hole-Selective Ultrathin Al-Doped SiO_x Passivation Layer Formed by Immersing in Aluminum Nitrate Aqueous Solution," Phys. Status Solidi (RRL) **16**, 2200052 (2022).

International Conference

[1] Hiroki Nakajima, Huynh Thi Cam Tu, and Keisuke Ohdaira, "Effectiveness of Al-induced charged oxide inversion layer on pyramidal textured Si surfaces," 34th International Photovoltaic Science and Engineering Conference (PVSEC-34), Shenzhen, China (6–10th Nov. 2023) (**Poster presentation**)

[2] Hiroki Nakajima, Huynh Thi Cam Tu, and Keisuke Ohdaira, "Excellent Surface Passivation on a Pyramidal Textured Si Surface by Wet Chemically Grown Al-induced Charged Oxide Inversion Layer," 40th European Photovoltaic Solar Energy Conference and Exhibition (EU PVSEC), Lisbon, Portugal (18–22nd Sep. 2023) (**Oral presentation**)

[3] Hiroki Nakajima, Huynh Thi Cam Tu, and Keisuke Ohdaira, "The significant role of an ultrathin SiO_x interlayer underneath a Cat-CVD SiN_y passivation layer for the high-efficiency n-type crystalline Si solar cells," 11th International Conference on Hot-Wire Chemical Vapor Deposition (11th HWCVD), Jülich, Germany (17–19th Apr. 2023) (**Oral presentation**)

[4] Hiroki Nakajima, Huynh Thi Cam Tu, and Keisuke Ohdaira, "Ultrathin Al-doped SiO_x passivating hole-selective contacts formed by a simple wet process," 33rd International Photovoltaic Science and Engineering Conference (PVSEC-33), Nagoya, Japan (13–17th Nov. 2022) (**Oral presentation**)

[5] Hiroki Nakajima, Huynh Thi Cam Tu, and Keisuke Ohdaira, "Cat-CVD SiN_x /ultrathin SiO_x passivation stacks for high-efficiency crystalline Si solar cells," 31st International Photovoltaic Science and Engineering Conference (PVSEC-31), Online (13–15th Dec. 2021) (**Poster presentation**)

Domestic Conference

[1] Hiroki Nakajima, Huynh Thi Cam Tu, and Keisuke Ohdaira, "The effectiveness of the p^+ inversion layer on an n-type crystalline Si surface with a pyramidal texture formed by aluminum nitrate oxidation treatment," The 3rd Japan Photovoltaic Society Conference, Kyoto, Japan (29–30th Jun. 2023) (**Oral presentation**)

[2] Hiroki Nakajima, Huynh Thi Cam Tu, and Keisuke Ohdaira, "Surface passivation of pyramidal textured Si surfaces by Cat-CVD SiN_y/ultrathin SiO_x stack layers," 20th Cat-CVD research meeting, Kitakyushu, Japan (22–23rd Jun. 2023) (**Poster presentation**)

[3] Hiroki Nakajima, Huynh Thi Cam Tu, and Keisuke Ohdaira, "The application of the inversion layers induced by the ultrathin Al-doped SiO_x layers for the front-emitter n-type crystalline Si solar cells," The 70th JSAP Spring Meeting 2023, Tokyo, Japan (15–18th Mar. 2023) (**Oral presentation**)

[4] Hiroki Nakajima, Huynh Thi Cam Tu, and Keisuke Ohdaira, "Surface passivation mechanism on Si surfaces by Al-doped ultrathin SiO_x formed by immersing in aluminum nitrate aqueous solution," The 83th JSAP Autumn Meeting 2022, Sendai, Japan (20–23rd Sep. 2022) (**Oral presentation**)

[5] Hiroki Nakajima, Huynh Thi Cam Tu, and Keisuke Ohdaira, "Effectiveness of Cat-CVD on Al-doped ultrathin SiO_x layers," 19th Cat-CVD research meeting, Tosu, Japan (14–15th Jul. 2022) (**Poster presentation**)

[6] Hiroki Nakajima, Huynh Thi Cam Tu, and Keisuke Ohdaira, "Orientation dependence of Si surface passivation for an ultrathin Al-doped SiO_x layer," The 2nd Japan Photovoltaic Society Conference, Kanazawa, Japan (28–29th Jun. 2022) (**Poster presentation**)

[7] Hiroki Nakajima, Huynh Thi Cam Tu, and Keisuke Ohdaira, "Surface passivation on Si surfaces by Al-doped ultrathin SiO_x formed by wet process," The 69th JSAP Spring Meeting 2022, Kanagawa, Japan (22–26th Mar. 2022) (**Oral presentation**)

[8] Hiroki Nakajima, Huynh Thi Cam Tu, and Keisuke Ohdaira, "Surface passivation mechanism in Cat-CVD SiN_x/ultra-thin SiO_x stacks," JSAP Hokuriku-Shinetsu Branch Meeting 2021, Shinshu, Japan (4th Dec. 2021) (**Oral presentation**)

[9] Hiroki Nakajima, Huynh Thi Cam Tu, and Keisuke Ohdaira, "Surface passivation on crystalline silicon surfaces by Cat-CVD SiN_x/NAOS-SiO_x stacks," The 1st Japan Photovoltaic Society Conference, Online (14–15th Oct. 2021) (**Oral presentation**)

[10] Hiroki Nakajima, Huynh Thi Cam Tu, and Keisuke Ohdaira, "Surface passivation on crystalline silicon surfaces by SiN_x/SiO_x stacks formed by catalytic chemical vapor deposition and nitric acid oxidation," The 82nd JSAP Autumn Meeting 2021, Online (10–13th Sep. 2021) (**Oral presentation**)

[11] Hiroki Nakajima, Huynh Thi Cam Tu, and Keisuke Ohdaira, "Effect of ultra-thin silicon oxide film formed at the Cat-CVD SiN_x/Si(100) interface on surface passivation," 18th Cat-CVD research meeting, Nomi, Japan (9–10th Jul. 2021) (**Poster presentation**)

Award

Innovative Photovoltaic Young Researcher's Award

Hiroki Nakajima, Huynh Thi Cam Tu, and Keisuke Ohdaira, "The effectiveness of the p^+ inversion layer on an n-type crystalline Si surface with a pyramidal texture formed by aluminum nitrate oxidation treatment," The 3rd Japan Photovoltaic Society Conference, Kyoto, Japan (29–30th Jun. 2023) (**Oral presentation**)

Grant

JST SPRING: Support for Pioneering Research Initiated by the Next Generation, Grant Number JPMJSP2102